Anisotropic Parameter Estimation from PP and PS Waves in 4-Component Data

Bärbel M. Traub
Diplom in Geophysics 1999
Universität Karlsruhe (TH), Germany

Thesis submitted in fulfilment of
the requirements for the degree of
Doctor of Philosophy

School of GeoSciences
University of Edinburgh
2004

Declaration

I declare that this thesis has been composed solely by myself and that it has not been submitted, either in whole or in part, in any previous application for a degree. Except where otherwise acknowledged, the work presented is entirely my own.

Bärbel Traub
July, 2004

Abstract

The estimation of anisotropic parameters in the shallow subsurface becomes increasingly important for 4C seismic data processing in order to obtain accurate images in both time and depth domain. I focus on two approaches to evaluate anisotropy in seismic data: using P-wave data and PS-converted (C-wave) data. To gain better insight into the accuracy and sensitivity of anisotropic parameters to for instance layering and compaction gradients, I undertake numerical modelling studies and verify the results with full-wave modelling as well as findings from the real data from a 4C data set from the Alba field.

The focus of this thesis is on vertical transverse isotropy (VTI) which widely occurs in marine sediments and cannot be neglected in seismic processing. P-wave data alone cannot constrain the vertical velocity and the depth scale of the earth model for a VTI medium. Therefore, the joint inversion of non-hyperbolic P- and converted wave (C-wave) or S-wave data from long offsets has been suggested. I carried out a detailed analysis of the resolution and accuracy of non-hyperbolic moveout inversion for P-, S- and C-waves for a single VTI layer in two parts. First, I introduce the concept of the inherited error Δ_{inh} as a measure of the possible resolution of the moveout approximations for the different wave types. The range of this error stays constant regardless of the magnitude of the anisotropic parameter for each wave type. Second, I analyse the accuracy of non-hyperbolic moveout inversion. I find that for anisotropy parameter η the error of estimation from C-wave data is in most cases about half that from P-wave data. Inversion of non-hyperbolic S-wave moveout data does not resolve the anisotropy parameter due to the presence of cusps in the data.

The study is then extended to a multilayered medium considering only P- and

C-waves. The results confirm the findings from the single layer case. Furthermore, I investigate phase effects on parameter estimation for P- and C-waves. It is suggested that η estimated from C-wave data gives a better description of the anisotropy found in a medium than the η values picked from P-wave data.

To verify the above findings near-surface effects are studied on the 4C data from the Alba field and accompanied by a full-waveform modelling study. I find that the picked η values from P-wave data are distinctly larger than the η values from C-wave data and also larger than the η values from VSP data. The full-wave modelling study shows that picked η values from P-wave data may account for influence of structure such as velocity gradients in the near-surface and are influenced by high velocity ratios and phase reversals.

Finally, I have carried out an integrated analysis of the Alba 4C data to demonstrate how seismic anisotropy can be estimated from 4C seismic data and how such information can be used to improve subsurface imaging. The results are presented in two parts. The first part deals with non-hyperbolic moveout analysis for estimating anisotropic parameters to gain improved stacked sections. The second part describes migration model building and final imaging. The models are evaluated by comparison with VSP data results and with a synthetic modelling study for three events of the overburden. The evaluation confirms that the anisotropy parameter obtained from C-wave moveout corresponds better with the VSP data than the values directly estimated from P-wave data.

Acknowledgements

First of all, I would like to express my gratitude to my supervisor Dr. Xiang-Yang Li and thank him for the opportunity to work in this exciting subject and his continious support and guidance. Thank you very much to my supervisor Dr. Roger Scrutton for reviewing my work and helpful discussions.
I would like to thank all the members of the Edinburgh Anisotropy Project for their cordiality and help with the day to day problems in geophysics. I am also grateful to the Sponsors of the EAP for keeping this research group going and supplying the data I showed in this work.
I am thankful to all the members of the BGS computer support for their help with all sorts of computing problems.

A special thanks goes to Andy D. ("I just run another program"), Sonja M. (*let's go to Patagonia*), Fabio M., Shaggy, Serafeim V., Jinghua Z. and Lifeng W., my office mates. You truly made all the time spent in the office enjoyable with sharing your knowledge about geophysics/computers, chocolate or just a giggle.

A big thank you goes to Magnus H., who shared his knowledge about linux and latex and for proof reading this thesis.
I am very grateful for all the friends I found in Edinburgh: Lynette R., Fahad A., Heidi G., Rowan H., Ira O. just to name a few. I had an unforgettable time and enjoyed all the trips to the hills, cinema, pubs, cooking sessions or just meeting for a horrible coffee in KB union.

A big thank you goes to all my friends back home in Germany and other parts of the world. Especially Hanna-Maria R. and Maren S. for their continuous support

and exchange of views about life as a Ph.D. student and all the rest. Katharina F., Flo L., Anke O., Martin O., Armin S., Marcus R., Gabi L. and Wolfram M. for cheering me up with emails and keeping me informed about life on the continent and having great holidays together. There are many more I would like to acknowledge for staying in touch, you know who you are.

Last but not least I want to express my deep gratitude to my parents and siblings, Martin, Claudia, Birgit and Hans-Jörg and their families. I owe you a lot. Without your understanding, patience and support I could not have done this.

Von ganzem Herzen möchte ich mich bei meinen Eltern und Geschwistern, Martin, Claudia, Birgit und Hans-Jörg und deren Familien bedanken. Ohne Euer Verständnis, Geduld und Unterstützung wäre diese Arbeit nicht gelungen.

für meine Eltern

Contents

List of Tables

List of Figures

List of Symbols

$t_{c/p/s}$	moveout traveltime of C-/P-/S-wave
Θ	phase angle
C_{ij}	elastic constants
ρ	density
$\epsilon, \delta, \gamma^{'}$	Thomsen's parameter
ϵ	$\epsilon = \frac{C_{11}-C_{33}}{2C_{33}}$
δ	$\delta = \frac{(C_{13}+C_{44})^2-(C_{33}-C_{44})^2}{2C_{33}(C_{33}-C_{44})}$
$\gamma^{'}$	Thomsen's parameter $\gamma^{'} = \frac{C_{66}-C_{44}}{2C_{44}}$
$\sigma, \eta, \chi, \zeta$	anisotropy parameters based on Thomsen's parameters
γ_0	vertical velocity ratio V_{p0}/V_{s0}
γ_2	stacking velocity ratio V_{p2}/V_{s2}
γ_{eff}	effective velocity ratio γ_2^2/γ_0
γ_{bin}	depth-constant effective velocity ratio used to bin C-wave data
x	source-receiver offset
x_c	conversion point
$V_{c/p/s}$	C-/P-/S-wave velocity
V_{ph}	horizontal P-wave velocity
$\Delta\eta/\chi$	difference between reference model parameter and its variation in chapter 4
Δ_p	difference between model and picked value
$\Delta t_{\max} t$	maximum difference between exact and approximated traveltimes
Δ_{inh}	inherited error
$\Delta_{\text{km}} t$	kinematic model
z	reflector depth

Glossary

4C data: 4-component data: hydrophone, vertical, inline and crossline component

C-wave: P-SV converted wave at the reflector

CCP/ACP: Common Conversion Point/ Asymptotic Conversion Point

CDP: Common Depth Point

CIP: Common Image Point

DMO: Dip Moveout

DSR: double-square-root

INMO-CIP: Inverse NMO applied to CIP gather

km: kilometres

ms: milliseconds

NMO: Normal Moveout

Notation: The notation used throughout this thesis follows Thomsen (1999) notation where subscripts P, S and C denote $P-$, $S-$ and $C-$waves respectively. Subscripts i, 2 and 0 denote interval, root-mean-square (RMS) and vertical or average quantities, respectively. t stands for traveltime, V for velocity and γ for velocity ratio

OBC: Ocean Bottom Cable to record 4C data

OWC: Oil-Water-Contact

PSTM: Kirchhoff Pre-Stack Time Migration

RMS: root-mean-square

VSP: Vertical Seismic Profiling

VTI: Transverse isotropy with a vertical axis of symmetry.

Chapter 1

Introduction

1.1 Motivation

Our Earth is a complex system made up of different layers of material which have undergone various tectonic processes such as compression and folding. Invariably, the Earth's crust is anisotropic. In the context of seismic wave propagation anisotropy means the variation of seismic velocity with direction. There are many types of seismic anisotropy such as transverse isotropy or orthorhombic anisotropy. In this thesis the focus is on the simple case of transverse isotropy with a vertical symmetry axis (VTI) which often occurs in marine sediments (Thomsen, 1986). In seismic data processing the assumption of an isotropic medium is usually used and often gives satisfactory results when used for compressional (P-) waves. For a long time, exploration methods have concentrated on P-waves as an easy and effective tool, especially in a marine environment. However, in recent years, research has shown that anisotropy may not always be ignored. This is the case in two areas in particular. Firstly, including anisotropy in processing routines can improve subsurface images and correct for mis-positioning of reflectors for reservoir characterisation (e.g. Larner and Tsvankin, 1995; Alkhalifah and Larner, 1994). Secondly, using shear-waves which are more sensitive to anisotropy (e.g. Winterstein and Paulsson, 1990) can provide information about the internal structure of a reservoir, including fracture density and orientation by shear-wave splitting analysis (e.g. Crampin, 1985; Li, 1997).

Recent advances in seismic technology, especially in the field of 4-component (4C) ocean-bottom-cable (OBC) data, have shown that the P-to-SV converted wave (or simply C-wave) can provide further valuable insight into earth properties compared to pressure waves. This wave type is, due to its shear wave content, more sensitive to the internal structure of subsurface media than the pure pressure wave and is easier to acquire and of better quality than pure shear wave data. Furthermore, it can be used to acquire dense 3D data in well-explored regions populated with producing platforms and pipelines which would make a streamer survey difficult. 4C OBC data has been successfully used to get improved images from reservoirs with gas clouds (e.g. Thomsen et al., 1997; Li et al., 2001a) and to make low impedance contrast reservoirs visible (e.g. MacLeod et al., 1999).
However, the C-wave of 4C data is more affected by anisotropy due to its S-wave leg. P-waves only show anisotropic effects in the far-offset, therefore, anisotropy can be ignored to a certain extent for this wave type. In contrast, converted waves show anisotropic effects in mid offsets and thus anisotropy often needs to be included in processing routines.

Intense efforts to include transverse isotropy in seismic processing for both P- and C-wave data have lead to several approaches. After investigating the effect of anisotropy on P-waves, Alkhalifah (1997) proposed an anisotropy parameter η. Working on S- and C-waves, Yuan et al. (2001) introduced the new anisotropic parameters ζ for S-waves and χ for C-waves which combines the P- and S-wave anisotropy parameters. Thus, η describes the P-wave anisotropy and χ the C-wave anisotropy. Non-hyperbolic moveout for both wave types has been expressed in terms of a Taylor series expansion, incorporating the anisotropy parameters into the higher order terms. As a result, parameter estimation for the anisotropic parameter and stacking velocity can be performed by means of double scanning semblance analysis over non-hyperbolic moveout for both P- and C-waves. These estimated parameters can be used in time processing of each wave type, i.e. NMO/DMO correction, stacking and migration.
Despite these efforts some fundamental issues remain unresolved. There is a lack of understanding of the uncertainties in these parameters as well as their accuracy and sensitivity with regard to the effect of layering, near surface compaction (vertical gradients), processing errors (inherited or induced) estimation methods

and robustness. All these play an important role for better use of converted wave anisotropy.

1.2 Aim and objectives

The primary focus of this thesis is to investigate the accuracy and sensitivity of anisotropic parameter estimation using 4C data. To address this question, I will focus on anisotropy, where it comes from, how to get the best estimate of it and how it can be included in the processing flow. In order to understand the effect of anisotropy on different wave types it is necessary to review the C-wave and P-wave moveout methods for anisotropic media and their use in current processing techniques.
Other practical issues regarding the better understanding of anisotropy parameters in seismic data are:

- How is anisotropy represented?
- Is it feasible to use converted waves for anisotropy estimation?
- Is there an advantage in using converted wave over pressure wave data for anisotropy quantification?
- How sensitive is seismic data processing to errors in anisotropic parameters?
- Does full anisotropic processing of converted wave data give an improved subsurface model?
- What is the relationship between the different anisotropy parameters η, ζ and χ?

Li and Yuan (2001b) discuss dependencies and sensitivity for the double scanning technique between the four parameters $\gamma_0, \gamma_{\text{eff}}, \chi$ and V_{c2} (see List of symbols) and give a validation of the offset-to-depth ratio (x/z) for which different traveltime approximations are accurate. Nevertheless, the accuracy of the moveout inversion itself and of the parameters obtained subsequently have not been investigated. A single layer synthetic study will be used for this part of the research. The investigation will then be extended to a multilayered medium in which the effect

of layering and consequent phase effects are studied.
For a VTI medium, P-wave data alone cannot constrain the vertical velocity and the depth scale of the earth model (Tsvankin, 1996), i.e. not all the necessary parameters can be estimated from P-wave data alone to build a satisfactory anisotropic model. Therefore, joint inversion of non-hyperbolic P- and C-wave or S-wave data from long offsets has been suggested. Due to error propagation, it has been a point of debate in the literature as to whether or not the additional C-wave or S-wave data may provide sufficient constraints. Therefore, I will investigate the possibility of joint moveout inversion for anisotropic model building.
For this purpose, I will estimate the anisotropy parameter η using two approaches: using η extracted from P-wave data and χ from C-wave data which will then be used to calculate η. I will compare the accuracy of both methods to find the most accurate anisotropic value.
Finally, I use a field data set to study near-surface effects and explain them with findings from the synthetic studies. I show a complete anisotropic model building routine for a 4C data set and discuss the final image results. The 4C data set from the sand-shale Alba field (MacLeod et al., 1999) with horizontally layered overburden will be used. VSP and well log data are also available.

1.3 Outline of the thesis

The layout of my thesis with a short description of the contents of each chapter is:

Chapter 2 In this chapter I give a summary of the background of converted waves and anisotropic media on which my work is based. I will give examples of cases in which it was beneficial to use converted waves instead of P-waves and of where the limitations are. Further, I summarise the main theories which have been developed to describe the converted wave propagation in anisotropic media.

Chapter 3 This chapter introduces the data from the Alba field in the North Sea comprising surface 4C data, VSP data and well logs. In particular I will show the characteristics of the 4C data set, such as amplitude behaviour,

frequency content and evidence of polar anisotropy and why the data set is ideal for this study.

Chapter 4 In this chapter I investigate the feasibility of using moveout equations for P- and C-waves for parameter estimation in a single VTI layer. I study the conditions under which one can differentiate between different anisotropy contents of models. P- and C-wave analyses are used and their practical implementation is introduced. Further, I will investigate the error propagation of the estimated parameters when used for processing and finally study the possibility of using S-wave moveout analysis.

Chapter 5 Here, I extend the modelling study from a single to multi-layered VTI medium and examine the influence of layering on parameter estimation. I also study the phase behaviour for different scenarios to explain observed amplitude and phase effects.

Chapter 6 In this chapter, I focus on near-surface characteristics and compare parameter estimation in the light of these from P- and C-wave data. I analyse findings from real data and explain them with a near-surface modelling study.

Chapters 7 & 8 Here, I focus on parameter estimation and the use of anisotropic parameters in processing the Alba 4C data set and present the results in two chapters.

I incorporate the knowledge gained from the previous chapters and process the data with isotropic and anisotropic work flows in chapter 7. In chapter 8 the anisotropic work flow is extended to a full pre-stack time migration. The resulting anisotropic subsurface model is then supported by a synthetic model of the overburden and then applied to the data to obtain the final image results.

Chapter 9 Here I discuss and conclude the results from the previous chapters and give an outlook of what questions remain unanswered and where progress can still be made.

Chapter 2

A review of basic converted wave theory in anisotropic media

2.1 Introduction

Common approximations for conventional seismic processing are that the medium is isotropic, targets are flat, all receiver and sources are on the same level and that there are no converted waves. Combined, these approximations justify the hyperbolic moveout approximation for a single wave mode as a Taylor series expansion without higher order terms:

$$t^2 = \frac{4z^2}{V^2} + \frac{x^2}{V^2} = t_0^2 + \frac{x^2}{V^2}, \tag{2.1}$$

where x is the offset, z the depth to the reflector, V the velocity of the layer and t_0 the vertical traveltime assuming a single layer above the reflector.
In the case of converted waves (C-waves) recorded on the sea bed these approximations do not hold anymore. Therefore, in this chapter I will introduce in more detail the C-wave and the main theories about its propagation in anisotropic media. The notation I use throughout this thesis follows the notation of Thomsen (1999) where subscripts P, S and C denote $P-$, $S-$ and $C-$waves respectively. Subscripts i, 2 and 0 denote interval, root-mean-square (RMS) and vertical or average quantities, respectively. t stands for traveltime, V for velocity and γ for velocity ratio.

2.2 Converted wave exploration and Ocean Bottom Cable (OBC) survey

In contrast to single wave mode reflection data such as P- or S-waves a C-wave consists of a wave which converts from one wave mode to another at the subsurface reflection point. Recording of this wave type is of interest as it mirrors properties of both its P- and S-wave leg. P-wave propagation is affected by the matrix of the rock it passes through and its fluid/gas content in pore spaces. In contrast, S-waves are only affected by the solid part of the rock (i.e. the matrix): they travel approximately half the speed of P-waves and cannot travel through fluids. Figure 2.1 illustrates the ray paths for a single mode reflection on a subsurface point (P-wave) and a converted wave (C-wave) which converts at the reflection point from a P- to a S-wave. The C-wave consists of a P-wave travelling to a subsurface reflector where it reflects and converts into a S-wave which propagates to the receiver unit. The conversion point (CP) location is shifted towards the receiver compared with the midpoint (MP) where the reflection of the single mode wave happens. Mode conversions occur on any interface between two media.

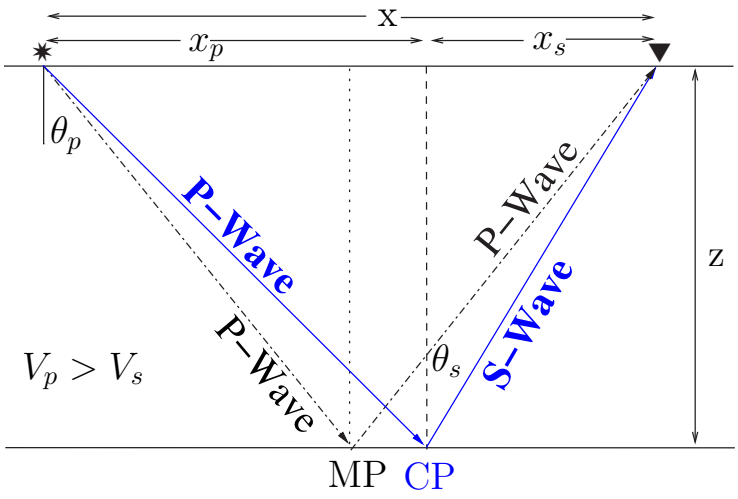

Figure 2.1: Ray paths for a single mode (PP) reflected wave and a converted wave (PS) in a single layer of depth z showing that the conversion point (CP) of the converted wave is no longer identical with the mid point (MP). The offset x between source and receiver is divided in x_p and x_s corresponding to the P-and S-wave leg of the converted wave. θ_p is the incidence angle and θ_s the reflected angle of the S-wave.

Although marine multicomponent technology is relatively new, work and knowledge of shear-wave analysis and its usefulness has a long history (e.g. Stewart et al., 2002) but has long been neglected due to its higher costs. P-S converted waves analysis itself has a history of about 20 years first mainly focusing on land data acquisition. In the late 1970s P-S surveys on land were proposed and tried. However, fundamental processing was only developed in the 1980s and early 1990s. Marine P-S converted analysis became more popular after the invention of the so called ocean bottom cables allowing an easy and cost effective way to record C-waves in a marine environment.

In a marine environment C-waves are recorded using an ocean bottom cable

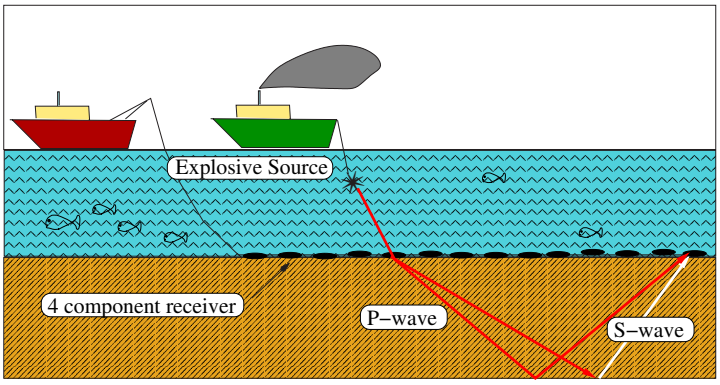

Figure 2.2: Schematic plot showing the acquisition geometry for a four component Ocean Bottom Cable (OBC) survey. Each receiver unit in the cable consists of a hydrophone and 3 orthogonal geophones recording P-waves (red) and C-waves (red-white).

(OBC) survey as shown in Figure 2.2. The ocean bottom cable (OBC) technique consists of a cable which is lowered down on the seafloor. In each cable there are receiver points consisting of one hydrophone and three orthogonal geophones which allow the recording of particle motion due to shear and pressure waves. The energy source is an airgun towed behind the second ship. The figure shows a two P-waves propagating from the source through the water and into the earth. These waves are reflected at an impedance boundary and one also converts into a S-wave. The reflected waves will be recorded with the OBC receiver unit. Because the source is in the water the down-going wave has to be a P-wave and as the cable is installed on the seafloor this technique allows to record the S-wave leg of the converted wave.

Usually in an OBC survey the cable is laid on the sea floor and stays connected to the ship. A second vessel sails over the cable and fires the source at time intervals. When all shot lines are recorded the receiver cable is moved to the next position.

Transmission, reflection and conversion occurs whenever energy is incident on an interface. The angles of reflection and transmission and thus the ray path is governed by Snell's law. The exact partitioning of the energy is described by the Zoeppritz equations. According to Sheriff and Geldart (1995) only 1% of the incident energy on an interface is reflected if the density and velocity contrast is small. Reflection/conversions at layer interfaces with small density/velocity differences undergo a substantial loss of energy at each conversion and do not appear as strong events in the data. Also, Stewart et al. (2002) states that multiple conversions or transmissions have mostly a lower amplitude than primary P-S reflections. Thus, reflection and conversion occurs with the strongest impact at strong reflectors.

2.2.1 Successful applications of OBC data

C-wave data is more costly to acquire than conventional streamer data. Hence, it is usually applied in areas where single mode P-wave gives unsatisfactory results. Typically these problems are that P-waves

- may identify the target but may not clearly delineate it due to a very low P-wave impedance contrast.
- are disrupted even by small quantities of gas and thus underlying targets are obscured.
- are less sensitive to aligned fractures or rock textures that impose azimuthal variations of velocity or other types of anisotropy.
- may not be able to distinguish between changes in lithology and changes in fluid content or pressure.

Because of the S-wave leg which is not affected by gas or liquid and reacts to different rock characteristics, an attempt can be made to overcome these problems with C-wave data. Stewart et al. (2003) gives a good overview of successful

application of C-wave analysis. In the following I want to list a few examples of successful application of C-wave data.

A prime example is the imaging of the Alba field. The reservoir is almost invisible to P-waves due to a low impedance contrast. S-wave reflectivity is high and the reservoir outline was found using C-waves (MacLeod et al., 1999). This data set will be discussed in more detail in Chapter 3.

Another well known example where P-waves do not give a clear subsurface picture is imaging through a gas cloud, for instance the Valhall field, North Sea. The Valhall field is a chalk reservoir and its crest is hard to image using P-wave data because gas in the overburden attenuates compressional energy and distorts the P-wave velocity. C-waves are not affected by the compressibility of pore fluids/gas and Thomsen et al. (1997) showed successful images of the reservoir using this data. Li et al. (2001a) improved the image by compensating for the so called diodic illumination effects, i.e. that the forward and reverse shooting directions give different C-wave stacking velocities. For the compensation, the data volume has to be separated into positive and negative offset and processed independently. Processing focuses on a data-driven approach based on using the C-wave data only to estimate the velocity ratios γ_0 and γ_{eff} and finally applying a Kirchhoff prestack migration which can handle vertical and lateral velocity variations.

Other successful cases of imaging through gas clouds are the Tommeliten Alpha field (Granli et al., 1999) and the Lomond field (Pope et al., 2000; Mancini, 2004). Kendall et al. (1998) showed that C-waves can be used in a similar way to improve the image of a sub-salt target like the Mahogany field in the Gulf of Mexico.

Further, various studies have examined the use of C-waves to gain fracture information of a reservoir such as direction and spatial frequency based on the analysis of shear-wave splitting. The S-wave bifringerence or S-wave splitting occurs when a shear-wave enters a medium with stress-aligned fractures which give rise to azimuthal anisotropy. The amount of splitting, i.e. anisotropy, is the time lag between the two S-waves. The faster one, polarised parallel to the alignment (fracture strike) is called S_1 while the slower one, S_2, is polarised perpendicular

to the strike. There are numerous examples of shear-wave splitting studies, but to here I mention only a few. Ata and Michelena (1995) presented an example based on land multicomponent data in Venezuela and Ronen et al. (2001) for the successful improvement of imaging on the Harding area in the North Sea when azimuthal anisotropy analysis and processing was applied. Vetri et al. (2002) applied azimuthal analysis to the 3D/4C data of the Emilio field in the Adriatic Sea. Variable anisotropy in the overburden in the case of the Emilio field complicates the processing and needs further research. Despite this, the results are in good agreement with the well data.

A different aspect of C-wave properties are used for identifying drilling hazard. Drilling wells is expensive and thus it is important to have as much pre-drill information as possible such as formation pore pressure. Too low a predicted pore pressure may lead to formation fluids entering the well and possibly loosing it. In the opposite case, higher pore pressure may lead to blow out. Sayers et al. (2001) used C-wave data from the Gulf of Mexico for a study to predict pore pressure. Using reflection tomography they gained a P- and S-wave velocity field which was then used to calculate pore pressure. As P-wave velocities are influenced by changes in lithology and fluid content the additional S-wave information helped to identify an ambiguity of variation in pore pressure or variation in lithology/fluid content, i.e. a shale body opposed to a possible change of pore fluid/gas.
In summary, these examples showed the possibility of using C-waves to determine lithology. P-wave velocity on its own may allow ambiguous interpretation of possible lithologies. For instance Garotta et al. (2002) showed that using the velocity ratio V_p/V_s from C-waves allows clearer lithology prediction, since the S-wave allows a tighter constraint on the interpretation. Furthermore, Margrave et al. (1998) also used the velocity ratio V_p/V_s successfully from land multicomponent data (Blackfoot field, Alberta, Canada) for lithology discrimination.

2.2.2 OBC and C-wave problems

Although there are many cases of successful application of C-waves in scenarios of failure from conventional P-wave data, there are still unresolved issues. On the acquisition side, there is the issue of vector fidelity. The P- and C-waves recorded

with an OBC survey tend to be naturally separated due to extremely low velocities in the near surface layers just below the receiver on the sea bed. Such low velocities cause the rays to bend upward to an almost vertical ray path as illustrated in Figure 2.3. S-waves especially are affected since they have by nature a lower velocity than P-waves. The vector fidelity of an acquisition system refers to the capacity to record accurately the magnitude and direction of a seismic wave in 3 dimensions. Tree (1999) stressed the importance of achieving this for OBC surveys, i.e. that the horizontal components of the direct arrivals are linearly polarised in the radial and transverse direction for all source azimuths. However,

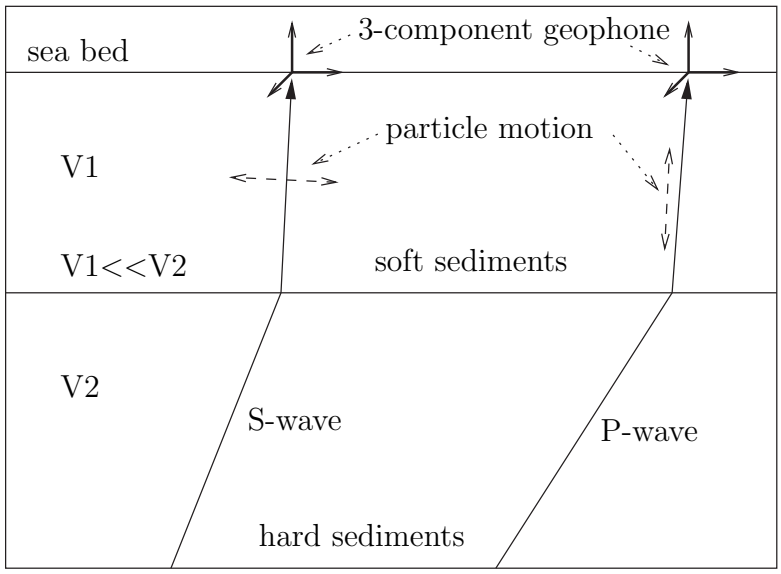

Figure 2.3: Diagram showing the effect of a low velocity layer, e.g. soft sediments on the sea floor, on P- and C-waves and how they tend to be recorded.

real OBC surveys do not always record the wavefield with such precision (Reid and MacBeth, 2000) and thus a term often found in literature is *infidelity* as described by Dellinger et al. (2001): "*failure of multicomponent ocean-bottom-seismic geophones to respond isotropically to incoming seismic energy.* " Infidelity includes problems with geophone orientation, gain and frequency mismatch and wave contamination. Various solutions to this problems haven been proposed such that geophones in OBC surveys are often gimballed, i.e. the vertical axis is fixed and thus, the vertical component represents true vertical. Hence, only the horizontal components needs to be adjusted to the radial and transverse direction Yilmaz (2001). Further literature shows different ways to rotate the components such that

the horizontal energies are in the radial and transverse directions, i.e. Dellinger et al. (2001) proposes the use of a recovery filter and Li and Yuan (1999b) rotation of the energy based on polarisation of water break and generally a more accurate geophone orientation.

Other issues which still need to be worked on include the asymmetric ray path of the C-wave and the consequent problems in binning. Unlike single mode data the C-wave data has to be sorted into common conversion point (CCP) gathers which even in a horizontal isotropic layer do not correspond with the common mid point, due to the asymmetric ray path. The location of the CCP depends on the velocity ratio which is usually unknown at the beginning of a processing sequence. Binning using wrong velocity ratios can lead to wrong CCP locations and hence to smeared images. In the next section, I will explain a few more details about the CCP binning.

Estimation of the velocity ratio between P- and S-waves is gained from event correlation of P- and C-wave sections. However, it is not trivial to be certain that the exact same event from a layer in the medium is picked in each section. P- and C-waves have different arrival times and frequency contents and also, P- and S-wave react differently when encountering gas and may have different impedance contrast which all leads to a different appearance in the P- and C-wave sections. As the velocity ratio is an important tool for lithology interpretation of C-waves the correctness of event correlation is crucial.

Last but not least, the C-waves are often more sensitive to anisotropy than P-waves. In reality, anisotropy, with seismic waves travelling with different speeds in different directions, is widely present in the Earth's subsurface, particularly in marine sedimentary basins. P-waves are mostly affected by anisotropy in the far offset and S-waves in the near offset. By contrast C-wave data senses anisotropy in mid-far offsets. Thus, P-wave processing may in many cases ignore the anisotropic nature of the medium because conventional processing neglects the far offset traces. However, the energy of C-waves is zero at zero offsets and then increases with the incidence angle (see also Section 3.2.2 in Chapter 3) and thus we cannot neglect far offset traces. Therefore, for C-wave processing anisotropy

cannot be ignored and it is important to find ways to compensate for it in order to enhance the image quality. As I focus in my project on the effects of anisotropy on C-waves and how one can get an accurate estimate of it, I will define the term "anisotropy" in more detail in Section 2.4.

2.3 Traveltime and conversion point in isotropic media

Figure 2.1 illustrates the ray paths for both, a single-mode (P-wave) and a converted wave reflection event. The black ray paths shows an incident P-wave which is reflected at a boundary and travels upwards to the surface as a P-wave. The travel path is symmetric and the reflection point is coincident with the midpoint (MP). The blue ray path illustrates another incident P-wave which converts after reflecting with the angle Θ_s into a mode converted SV waves. This is the P-SV or converted wave (C-wave). P and SV-wave travel with different velocities, with $V_p > V_s$. Owing to this difference, the ray path of the converted wave is asymmetric and the conversion point (CP) is no longer identical with the midpoint. The offset distances can be distinguished in x_p and x_s according to the P-wave or S-wave leg. Due to the asymmetrical ray path processing of converted waves requires more effort than single mode P- or S-waves. Symmetric ray paths have the advantage that source-receiver reciprocity can be assumed which is often used in algorithms for NMO correction, redatuming and migration. Binning is common for processing the reflection data. For C-waves this binning has to take into account the asymmetric reflection path and resulting non-hyperbolic moveout.

2.3.1 Single layer case

The correct traveltime for a single mode reflected wave in a single layer is given by

$$t = \frac{\sqrt{4z^2 + x^2}}{V}. \tag{2.2}$$

For the converted wave the traveltime is

$$t_c = t_p \downarrow + t_s \uparrow = \frac{\sqrt{x_c^2 + z^2}}{V_p} + \frac{\sqrt{(x - x_c)^2 + z^2}}{V_s} \tag{2.3}$$

$$\text{where} \qquad x_c = V_p t_p \sin\theta_p \tag{2.4}$$

is the location of the conversion point (CP), which coincides in Figure 2.1 with the offset corresponding to the P-wave leg x_p. It is obvious that Equation (2.3) is strongly influenced by the conversion point x_c. Considering the asymptotic limit of almost vertical travel $V_0 = z/t_0$, i.e. small offset to depth ratio x/z, the ratio of traveltimes become

$$\frac{t_s(x0)}{t_p(x0)} \rightarrow \frac{t_{s0}}{t_{p0}} = \frac{V_p}{V_s} = \gamma, \tag{2.5}$$

where γ is the velocity ratio V_p/V_s. In this limit the location of the conversion point can be approximated by

$$x_c = \frac{x\gamma}{1+\gamma}, \tag{2.6}$$

(after Fromm et al., 1985), and is now depending on the physical parameter γ of the ground. This velocity ratio, γ, varying with depth as shallow sediments tend to have lower S-wave velocities, i.e. γ tends to be high in the near-surface and decrease with depth. Equation (2.6) is also called an asymptotic approximation, as it represents the asymptote to the conversion point (ACP) in the limit of small offsets. Although derived for a single layer Equation (2.6) has been used for horizontally layered media. In multilayered media the conversion point changes its location with depth as shown in Figure 2.4 (Stewart et al., 2002) and thus may lead to large errors when Equation (2.6) is used for small reflector depths compared to the whole offset.

Tessmer and Behle (1988) introduced an accurate analytical expression to calculate the conversion point in a single isotropic layer

$$x_c = \frac{x}{2} + D, \tag{2.7}$$

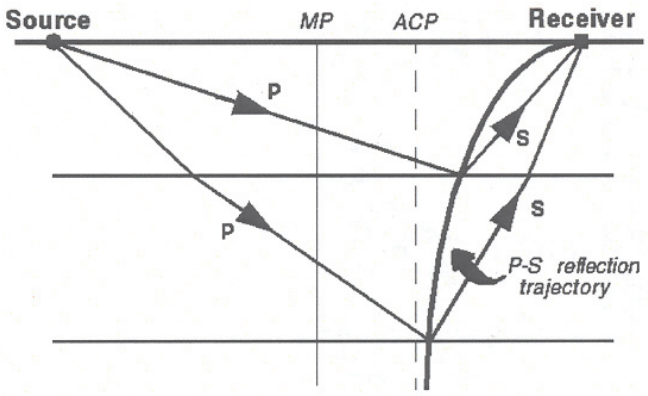

Figure 2.4: Schematic diagram showing that the location of the conversion point changes its location with depth. For small offset/depth ratios, i.e. small offsets and large depths, the conversion point is approximated with the asymptotic approximation (ACP), from Equation (2.6) (from Stewart et al., 2002).

where D is the horizontal distance between the mid-point (MP) and the conversion point (CP). D is then found by solving the fourth-order polynomial equation

$$D^4 + (z^2 - \frac{x^2}{2})D^2 - z^2 mxD + \frac{1}{16}(x^4 + 4x^2z^2) \;=\; 0$$

with $m = ((V_p/V_s)^2 + 1)/((V_p/V_s)^2 - 1)$.

Zhang and Robinson (1992) proposed an iterative approach to estimate the location of the conversion point:

$$x_c \;=\; \frac{\sqrt{1 + (\frac{x_c}{z})^2(1-\gamma^2)}}{\gamma + \sqrt{1 + (\frac{x_c}{z})^2(1-\gamma^2)}}x \tag{2.8}$$

with initial value $x_c^0 = x/(1+\gamma)$ and a constant γ the conversion point x_c can be found within a few iterations.

2.3.2 Multi-layer case

Another attempt to determine the traveltime and the location of the conversion point has been shown by Tsvankin and Thomsen (1994)and Thomsen (1999) by using Taylor series expansion and rational function approximation. For the single

layer case he found the expression for traveltimes

$$t_c = t_{c0} + \frac{x^2}{V_{c2}^2} + \frac{A_4 x^4}{1 + A_5 x^2}, \tag{2.9}$$

$$A_4 = \frac{-(\gamma - 1)^2}{4\gamma t_{c0}^2 V_c^4}, \tag{2.10}$$

$$A_5 = \frac{-A_4 V_c^2}{1 - V_c^2/V_p^2}, \tag{2.11}$$

and for the conversion point

$$x_c = x \left[C_0 + C_2 \frac{(x/z)^2}{1 + C_3 (x/z)^2} \right], \tag{2.12}$$

with

$$C_0 = \frac{\gamma}{1+\gamma}, \quad C_2 = \frac{\gamma(\gamma - 1)}{2(\gamma + 1)^3},$$

and $C_3 = C_2/(1 - C_0)$. The exact Equation (2.8) and this approximation have in common that they all depend upon the reflector depth z and the velocity ratio γ. However, Equations (2.3), (2.7) and (2.8) are both only valid in a single layer medium.

Further, Thomsen (1999) extend this equation to the case of horizontally multilayered media. In such a scenario there is no exact analytical solution to the traveltime equation and the location of the conversion point except by ray-tracing. Using a Taylor series expansion as seen for the single layer and taking account that in a multilayered medium the velocity ratio is expressed as vertical velocity ratio γ_0 and effective velocity ratio $\gamma_{\text{eff}} = \gamma_2^2/\gamma_0$ (which will be introduced in more detail later) he found an approximation for traveltimes similar to Equation (2.9) with the term A_4 changed to (as simplified written in Yuan (2001))

$$A_4 = \frac{-(\gamma_2 - 1)^2}{4(1 + \gamma_{\text{eff}})^2 \gamma_0 t_{c0}^2 V_{c2}^4}, \tag{2.13}$$

and with the conversion point

$$x_c = x \left[C_0 + \frac{C_2 x^2}{1 + C_3 x^2} \right], \tag{2.14}$$

where

$$C_0 = \frac{\gamma_{\text{eff}}}{1+\gamma_{\text{eff}}}, \quad C_2 = \frac{1}{2t_{c0}V_{c2}^2}\frac{\gamma_{\text{eff}}(\gamma_0+1)}{\gamma_0(\gamma_{\text{eff}}+1)^3}(\gamma_{\text{eff}}\gamma_0-1), \tag{2.15}$$

and $C_3 = C_2/(1-C_0)$. Note that z has now been replaced by $t_{c0}V_{c2}$ as the reflector depths are not known *a priori* in a more realistic case.

2.4 Anisotropy

A general definition of seismic anisotropy is given by Sheriff and Geldart (1995) as: *Anisotropy (seismic): Variation of seismic velocity depending on the direction in which it is measured.*

This dependency on direction is shown in Figure 2.5 by a snapshots of a wavefield propagating through (a) an isotropic and (b) a non-specific anisotropic media. In each case the top picture shows the result as recorded on the X- and in the bottom picture for the Z-Component. The isotropic wavefront are as expected circles where weak and strong amplitudes describe the energy distribution to the source pattern. In the anisotropic scenario the wavefront take a more elliptical shape with the vertical direction being slower than the horizontal due the variation of velocity with direction. To evaluate the effects of anisotropy on reflection moveout, anisotropy needs to be parameterised. In general, every anisotropic medium can be described by elastic constants. Although there is a large variety of anisotropic scenarios, I will introduce only azimuthal and polar anisotropy as they are common in exploration seismology. This is followed by the parameterisation of polar anisotropy as my thesis focuses on this type of anisotropy. Then, I will introduce conversion point and traveltime approximations to describe P- and C-wave propagation in polar anisotropic media.

2.4.1 Azimuthal anisotropy

Azimuthal anisotropy exists in most sedimentary rocks as a result of tectonic processes. It is commonly caused by systems of vertical fractures (see Figure 2.6) or tilted transversely isotropic layers with horizontal axis of symmetry (HTI). This means, that the seismic velocity varys in the horizontal plane with azimuth. Knowledge about fracture orientation, connectivity between them and

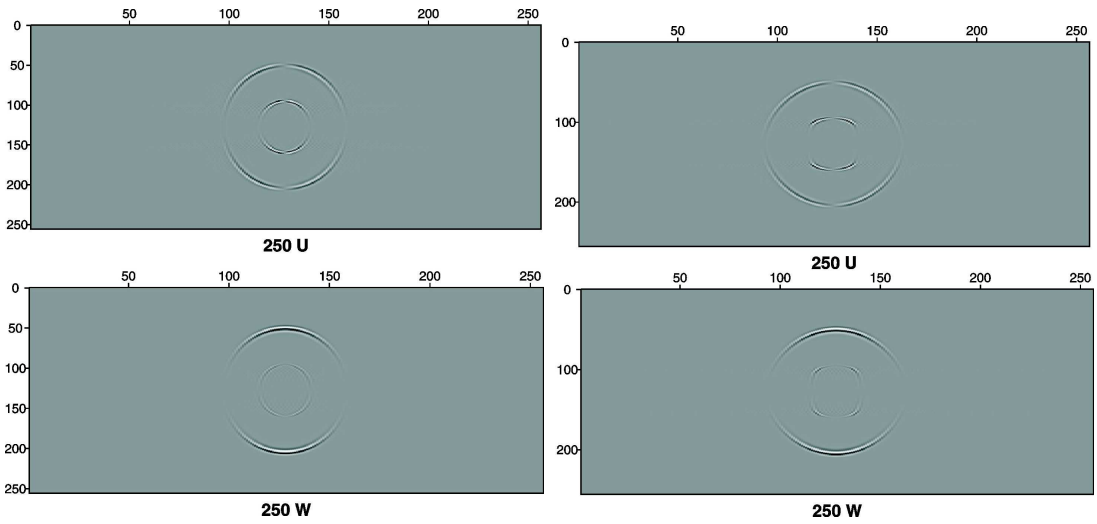

(a) isotropy (b) anisotropy

Figure 2.5: Snapshots of wavefield propagation in (a) isotropic and (b) anisotropic media. The top plot shows the X-component (label "u") and the bottom plot the Z-component (label "w").

Figure 2.6: Azimuthal anisotropy is typically caused by systems of vertical fractures, here seen on a granite surface.

spatial distribution are necessary for exploitation of a fractured reservoir. Seismic methods used to characterise fractures are mostly based on shear-wave analysis. S-waves split in the presence of azimuthal anisotropy with the fast wave, polarised parallel to the fracture strike and the slow one perpendicular to the fractures. In the same way the shear wave leg of the C-wave is affected by shear-wave splitting and can be utilised for azimuthal anisotropy analysis (Li, 1998).
Another method to extract principle directions of azimuthal anisotropy is to use the variation of P-wave seismic signatures over offset azimuth (Tsvankin and Lynn, 1999). There are numerous studies on the subject and readers are referred to Tsvankin and Lynn (1999) for more details.

2.4.2 Polar anisotropy or vertical transverse isotropy (VTI)

One of the main problems in seismic processing of C-waves is the wide presence of polar anisotropy in marine sediments. If this type of anisotropy is ignored in processing routines it may lead to mis-positioning of reflectors, depth errors (Banik, 1984) and may also give misleading results in AVO modelling. In this project I will focus purely on VTI and how one can quantify and estimate it.

A medium is transverse isotropic if its seismic velocity do not vary from one lateral direction to another but varys in the vertical direction, i.e. the velocity parallel to the bedding is faster than the one perpendicular to it, see Figure 2.7.

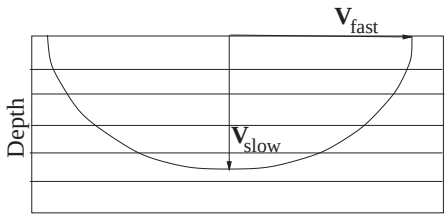

Figure 2.7: Vertical transverse isotropic media with a vertical axis of symmetry (VTI). Owing to the two seismic velocities in the media a wavefront has elliptical shape.

Polar anisotropy can be induced by thin horizontal layering such as found in sedimentary sequences (e.g. Backus, 1962), see Figure 2.8(a). Anisotropy caused

by layering is typical for a sedimentary basin containing flat-lying, shale interbedded sediments (Lawton and Isaac, 2001). Further, it can be intrinsic due to microscopic particle alignments of minerals as found in clay, see Figure 2.8(b) or clay-rich sediments such as shales (e.g. Winterstein and Paulsson, 1990).

(a) layering (b) particle alignment

Figure 2.8: Polar anisotropy can be caused by (a) fine layering or be intrinsic due to (b) preferential alignment of particles in minerals such as clay.

2.5 Parameterisation

2.5.1 Elastic parameters and Thomsen's parameters

Polar anisotropy can be described by five independent elastic constants:

$$\mathbf{C} = \begin{pmatrix} C_{11} & C_{11}-2C_{66} & C_{13} & 0 & 0 & 0 \\ & C_{11} & C_{13} & 0 & 0 & 0 \\ & & C_{33} & 0 & 0 & 0 \\ & & & C_{44} & 0 & 0 \\ & & & & C_{44} & 0 \\ & & & & & C_{66} \end{pmatrix} \tag{2.16}$$

However, estimation of the strength of anisotropy from traveltime analysis is cumbersome when the elastic constants are used. Therefore, it is more convenient to use the so-called Thomsen parameters (Thomsen, 1986):

$$V_{p0} \equiv \sqrt{\frac{C_{33}}{\rho}}, \tag{2.17}$$

$$V_{s0} \equiv \sqrt{\frac{C_{55}}{\rho}}, \tag{2.18}$$

$$\epsilon \equiv \frac{C_{11} - C_{33}}{2C_{33}}, \tag{2.19}$$

$$\delta \equiv \frac{(C_{13} + C_{55})^2 - (C_{33} - C_{55})^2}{2C_{33}(C_{33} - C_{55})}, \tag{2.20}$$

$$\gamma' \equiv \frac{C_{66} - C_{44}}{2C_{44}}, \tag{2.21}$$

where ϵ measures the amount of P-wave anisotropy, γ' the amount of S-wave anisotropy and δ relates to the shape of the wavefront. Note that following Yuan (2001), Thomsens's original notation γ has been changed to γ' since γ denotes the velocity ratio. When ϵ and δ are both less than 0.2 the medium is considered weakly anisotropic (Thomsen, 1986). Wang (2001) showed that most marine sediments show weakly anisotropic and thus can be described using above parameters.

Other useful parameters for traveltime analysis are the following combinations of Thomsen parameters which are used by Thomsen (1986) to express the P- and S-wave stacking velocities: P-wave stacking velocity and its relation to anisotropy is described by

$$V_{p2}^2 = V_{p0}^2(1 + 2\delta). \tag{2.22}$$

SV-wave stacking velocity in the presence of anisotropy takes the form:

$$V_{s2}^2 = V_{s0}^2(1 + 2\sigma) \tag{2.23}$$

$$\text{where } \sigma = \left(\frac{V_{p0}}{V_{s0}}\right)^2 (\epsilon - \delta). \tag{2.24}$$

In VTI media or the case of a multi-layered isotropic media, there are three different velocity ratios:

$$\gamma_0 = \frac{V_{p0}}{V_{s0}} = \frac{t_{s0}}{t_{p0}} \quad \text{vertical velocity ratio} \tag{2.25}$$

$$\gamma_2 = \frac{V_{p2}}{V_{s2}} \quad \text{stacking velocity ratio} \tag{2.26}$$

$$\gamma_{\text{eff}} = \frac{\gamma_2^2}{\gamma_0} \quad \text{effective velocity ratio} \tag{2.27}$$

where γ_{eff} is responsible for the correct lateral positioning of the seismic event when layering or anisotropy is present. γ_0 and γ_2 can be obtained by correlation of the same event in the C- and P-wave stacks. Using the Equation (2.27), γ_{eff} can be computed from these quantities.
The parameter σ is defined by Thomsen (1986) as the difference between the SV stacking and vertical velocity. This parameter can also be estimated by the difference between the vertical and effective velocity ratio

$$\sigma = \frac{V_{S2}^2 - V_{S0}^2}{2V_{S0}^2} \approx \frac{\gamma_0 - \gamma_{\text{eff}}}{2\gamma_{\text{eff}}}. \tag{2.28}$$

This difference is a good indicator of polar anisotropy (Dai et al., 2001) and can be used to quantify it in a data set by analysing both vertical and inline horizontal components, as I will show in Chapter 3, Section 3.5.

2.5.2 Processing parameters

In order to simplify expressions for traveltime approximations the following parameters were introduced to describe the effects of anisotropy on the moveout of different wavetypes. For a single VTI layer the following relationships are valid:

$$\eta = (\epsilon - \delta)/(1 + 2\delta), \quad \text{P-wave anisotropy parameter} \tag{2.29}$$

$$= \frac{\zeta}{\gamma_{\text{eff}}^2}, \tag{2.30}$$

$$\zeta = (\gamma_2^4/\gamma_0^2)\eta = \gamma_{\text{eff}}^2\eta, \quad \text{S-wave anisotropy parameter} \tag{2.31}$$

$$\chi = \gamma_0\gamma_{\text{eff}}^2\eta - \zeta = (\gamma_0 - 1)\gamma_{\text{eff}}^2\eta, \quad \text{C-wave anisotropy parameter} \tag{2.32}$$

where η describes the effect of anisotropy on the P-wave (Alkhalifah and Tsvankin, 1995) and ζ is the analogue for the effect on the S-wave or the S-wave leg of the C-wave (Yuan et al., 2001; Li and Yuan, 2003). χ controls the far-offset moveout behaviour of the non-hyperbolic C-wave moveout and describes the effect of anisotropy on C-waves which consists of both P- and S-wave anisotropy effects. Using χ and ζ, η can be rewritten as

$$\eta = \frac{\chi}{\gamma_{\text{eff}}^2(\gamma_0 - 1)}. \tag{2.33}$$

For a layered medium these parameters change to so called effective parameters which describe not only the anisotropy effects but also the influence of the layering.

$$\eta_{\text{eff}} = \frac{1}{8t_{p0}V_{p2}^4}\left(\sum V_{p2i}^4(1+8\eta_i)\Delta t_{p0i} - t_{p0}V_{p2}^4\right), \tag{2.34}$$

$$\zeta_{\text{eff}} = \frac{1}{8t_{s0}V_{s2}^4}\left(t_{s0}V_{s2}^4 - \sum V_{s2i}^4(1-8\zeta_i)\Delta t_{s0i}\right), \tag{2.35}$$

$$\chi_{\text{eff}} = \eta_{\text{eff}}\gamma_0\gamma_{\text{eff}}^2 - \zeta_{\text{eff}}, \tag{2.36}$$

where Δt is the interval traveltime. In a layered media with isotropic layers these anisotropic parameters do not vanish but reduce to

$$\eta_{\text{eff}} = \frac{1}{8t_{p0}V_{p2}^4}\left(\sum V_{p2i}^4\Delta t_{p0i} - t_{p0}V_{p2}^4\right), \tag{2.37}$$

$$\zeta_{\text{eff}} = \frac{1}{8t_{s0}V_{s2}^4}\left(t_{s0}V_{s2}^4 - \sum V_{s2i}^4\Delta t_{s0i}\right), \tag{2.38}$$

$$\chi_{\text{eff}} = \eta_{\text{eff}}\gamma_0\gamma_{\text{eff}}^2 - \zeta_{\text{eff}}. \tag{2.39}$$

2.5.3 Types of anisotropic measurements

Anisotropy in a medium can be analysed and quantified in various ways. I will give a short overview of the major methods:

Laboratory measurements Anisotropy of a material can be measured from core samples using ultrasonic measurements. Vernik and Liu (1997) mea-

sured the velocity of a sample on three differently cut core plugs which were normal (0° to the symmetry axis), 45° and 90° (parallel) to the bedding. They used different effective pressures and used dried and brine saturated plugs. From these velocities they were able to calculate the phase and group velocities and thus as a result Thomsen parameters.

Wang (2001) introduces the single-plug method. He measures elastic properties of transverse isotropic (TI) material by using a single 90° (to the symmetry axis) core plug sample. This is put into the transducer which has 2 transmitters and 2 receivers for P-waves built in. Finally, at either top or bottom are one P- and two orthogonal S-wave transducers. From the measured velocities and bulk density the elastic constants C_{11}, C_{44} and C_{66} can be calculated. From the elastic constants the Thomsen parameters are computed.

Wireline log measurements These measurements are obtained in situ in the borehole and are also called well logs. Typical well logs include the sonic velocities of P- and S-waves and density logs. These data, especially the sonic logs, are used for comparison with surface reflection data and the stacking velocities gained from them (Banik, 1984; Leaney et al., 2001b) in order to obtain anisotropy information. Anisotropy can be measured by cross-dipole logs, where sources and receivers are grouped in parallel and perpendicular combinations (Stewart et al., 2002).

VSP moveout analysis Miller and Spencer (1994) and Miller et al. (1994) describe a method to obtain phase slowness surfaces at the receiver depth of a VSP measurement and verify their results on real data. They use the direct arrival times and slownesses from wide-aperture walkaway VSP data to obtain the phase slowness surfaces which are then used to fit a VTI medium and extract the density-normalised elastic moduli for it. However, a prior estimate of the vertical shear velocity is necessary. Winterstein and Paulsson (1990) proved that in situ shale is intrinsicly polar anisotropic by using crosshole and VSP data to calculate the elastic properties of a subsurface formation.

Reflection moveout analysis Anisotropy parameters can also be estimated

using seismic reflection surface data. Alkhalifah and Tsvankin (1995) showed that the non-hyperbolic P-wave moveout, as it is observed for far-offsets in anisotropic media, can be used to extract the P-wave anisotropy parameter η and the stacking velocity V_{p2}.
Li and Yuan (2003) showed that for C-waves the non-hyperbolic moveout can be used already in mid-to-far offsets for estimation of the C-wave anisotropy parameter χ. The description of the non-hyperbolic moveout for both wave types is given in Section 2.7 and their implications for parameter estimation in Section 2.8. Investigation into the accuracy, sensitivity and reliability of these methods is the main purpose of this thesis.

2.6 Conversion point in anisotropic media

For completeness I will also list the expressions to approximate the conversion point in a single and multi-layered vertical transverse isotropic (VTI) medium here. Li and Yuan (2003) express the conversion point location in a single VTI layer as

$$x_c = x(C_0 + \frac{C_2 x^2}{1 + C_3 x^2}), \tag{2.40}$$

with (2.41)

$$\begin{aligned} C_0 &= \frac{\gamma_{\text{eff}}}{1+\gamma_{\text{eff}}}, \\ C_2 &= \frac{\gamma_{\text{eff}}(1+\gamma_0)}{2t_{c0}^2 V_{c2}^2 \gamma_0 (1+\gamma_{\text{eff}})^3}(\gamma_0\gamma_{\text{eff}} - 1 + 8(\gamma_0 + \gamma_{\text{eff}})\eta\gamma_{\text{eff}}) \\ C_3 &= \frac{C_2}{1-C_0}. \end{aligned} \tag{2.42}$$

For the more realistic case of a multi-layered VTI medium the coefficients C_0 and C_3 are the same as listed for Equation (2.14). The influence of anisotropy shows in the the coefficient C_2 with the P-wave anisotropy parameter η_{eff} and S-wave parameter ζ_{eff} (see Section 2.5).

$$C_2 = \frac{\gamma_{\text{eff}}(1+\gamma_0)}{2t_{c0}^2 V_{c2}^2 \gamma_0 (1+\gamma_{\text{eff}})^3}(\gamma_0\gamma_{\text{eff}} - 1 + 8(\gamma_0\gamma_{\text{eff}}\eta_{\text{eff}} + \zeta_{\text{eff}})). \tag{2.43}$$

The asymptotic conversion point approximation, Equation (2.6), is often used as initial processing step for some common conversion point (CCP) (or then asymptotic conversion point (ACP)) binning.

2.7 Traveltime approximations in anisotropic media

Velocity analysis is one of the most important steps in data processing. Taner and Koehler (1969) showed that traveltimes of PP and SS reflected waves in horizontally layered media can be approximated using truncated power series and utilised to calculate velocity spectra. This is true for isotropic media but in an anisotropic surrounding the moveout is inherently non-hyperbolic. Hake et al. (1984) approximated the $t^2 - x^2$-curves over a VTI medium with a three-term Taylor series as a function of the elastic parameters in order to take the non-hyperbolic moveout into account.

2.7.1 Model and definitions

Here, I want to introduce the model on which the definitions are based. Consider an n-layered VTI medium and a C-wave converted at the bottom of the n^{th}-layer with a down-going P-wave leg and an upgoing S-wave leg (see for example Figure 2.4). Within this model each layer is homogeneous and has the interval properties for the i^{th}-layer ($i = 1, 2, \ldots, n$): P- and S-wave short-spread NMO velocities V_{p2i} and V_{s2i}, vertical one-way traveltimes Δt_{p0i} and Δt_{s0i} and Thomsen (1986) parameter ϵ_i and δ_i.
Using the notation of Thomsen (1999) the velocity ratios are defined as

$$\gamma_{0i} = \frac{V_{p0i}}{V_{s0i}}; \qquad \gamma_{2i} = \frac{V_{p2i}}{V_{s2i}}; \qquad \gamma_{\text{eff}i} = \frac{\gamma_{2i}^2}{\gamma_{0i}}, \tag{2.44}$$

and the interval and RMS quantities obey the relationships,

$$t_{p0} = \sum_{i=1}^{n} \Delta t_{\mathrm{p0}i}, \qquad t_{s0} = \sum_{i=1}^{n} \Delta t_{\mathrm{s0}i}, \tag{2.45}$$

$$V_{p2}^2 = \frac{1}{t_{\mathrm{p0}}} \sum_{i=1}^{n} V_{\mathrm{p2}i}^2 \Delta t_{\mathrm{p0}i}, \qquad V_{s2}^2 = \frac{1}{t_{\mathrm{s0}}} \sum_{i=1}^{n} V_{\mathrm{s2}i}^2 \Delta t_{\mathrm{s0}i}. \tag{2.46}$$

From these relationships and the definition of the RMS velocity ratios, Equations (2.25), (2.26) and (2.27), the C-wave connections can be expressed as (Thomsen, 1999)

$$t_{c0} = t_{p0} + t_{s0}, \tag{2.47}$$

$$V_{c2}^2 t_{c0} = V_{p2}^2 t_{p0} + V_{s2}^2 t_{s0}. \tag{2.48}$$

With γ_0 this gives

$$V_{c2}^2 = \frac{V_{p2}^2}{1+\gamma_0} + \frac{V_{s2}^2}{1+1/\gamma_0}, \tag{2.49}$$

which simplifies for a single layer to

$$V_{c2}^2 = V_{p2} V_{s2} = V_{p2}^2 \gamma_0. \tag{2.50}$$

From the above definitions the following relationships between velocity ratios and stacking velocities can be found

$$\gamma_{\mathrm{eff}}^2 = \frac{V_{p2}^2}{V_{c2}^2(1+\gamma_0) - V_{p2}^2} \tag{2.51}$$

$$V_{p2}^2 = V_{c2}^2 \frac{\gamma_{\mathrm{eff}}(1+\gamma_0)}{1+\gamma_{\mathrm{eff}}} \tag{2.52}$$

and

$$V_{s2}^2 = V_{c2}^2 \frac{1+\gamma_0}{(1+\gamma_{\mathrm{eff}})\gamma_0} \tag{2.53}$$

Based on these equations a number of traveltime approximations have been

proposed to describe the moveout from P-, C- and S-waves. These equations are of particular interest for NMO correction and migration.

2.7.2 P-wave

The non-hyperbolic P-wave moveout in a VTI media was first described by a fourth-order Taylor series expansion by Tsvankin and Thomsen (1994). As their equations were complicated they have later been simplified by Alkhalifah (1997) depending on the P-wave parameter η to:

$$t_{p2}^2 = t_{p0}^2 + \frac{x^2}{V_{p2}^2} - \frac{2\eta x^4}{t_{p0}^2 V_{p2}^4 (1 + Ax^2)}, \tag{2.54}$$

$$\text{with} \qquad A = -\frac{2\eta}{t_{p0}^2 V_{p2}^4 (1/V_{ph}^2 - 1/V_{p2}^2)}, \tag{2.55}$$

where the horizontal P-wave velocity is given by

$$V_{ph} = V_{p2}\sqrt{1 + 2\eta}, \tag{2.56}$$

and this reduces the traveltime expression to

$$t_{p2}^2 = t_{p0}^2 + \frac{x^2}{V_{p2}^2} - \frac{2\eta x^4}{V_{p2}^2 \left[t_{p0}^2 V_{p2}^2 + (1 + 2\eta)x^2\right]}, \tag{2.57}$$

which is valid for large offset-to-depth ratios. This equation allows us to describe the moveout as a function of only V_{p2} and η_{eff} and can be used for semblance double scanning.

2.7.3 C-wave

The C-wave moveout is inherently non-hyperbolic due to its asymmetric ray path even in isotropic media. In a VTI media this effect becomes stronger so already mid-far offsets are affected. In order to describe the C-wave moveout there are two different approaches. Firstly, the traditional Taylor series expansion and secondly, a so called Double Square Root equation, where the P- and S-wave nature of the C-wave is taken account of.

Taylor series expansion

Methods to quantify polar anisotropy and to compensate for it are mostly based on Taylor series expansion. First, Tsvankin and Thomsen (1994) introduced an equation to describe the non-hyperbolic three-term Taylor series expansion in multi-layered media which is accurate to an offset-to-depth ratio of $x/z = 2$. This equation is very complicated. Thomsen (1999) gave a simplified version of it depending on the effective velocity ratio γ_{eff}, the vertical velocity ratio γ_0 and the P-wave anisotropy parameter η:

$$t_c^2(x) = t_{c0}^2 + A_2 x^2 + \frac{A_4 x^4}{1 + A_5 x^2}, \tag{2.58}$$

$$\text{with} \quad \frac{1}{A_2} = V_{c2}^2, \tag{2.59}$$

$$A_4 = \frac{\frac{-1}{(\gamma_{\text{eff}}+1)}\left[2\eta\frac{(\gamma_0^2-1)}{\gamma_0}\gamma_{\text{eff}}^2 + \frac{(\gamma_2^2-1)^2}{4(\gamma_0+1)}\right]}{V_{c2}^2 t_{c0}^2}, \tag{2.60}$$

$$A_5 = \frac{A_4 V_{c2}^2}{1 - \frac{V_{c2}^2}{V_{p2}^2(1+2\eta)}}. \tag{2.61}$$

However, this equations are less accurate and only valid for an $x/z = 1.0$.
A simpler form of a three-term Taylor series expansion was developed by Cheret et al. (2000) depending on the three parameters V_{c2}, V_{ch} and coefficient κ. Although the accuracy of this approach is similar to the original one above, its parameter V_{ch}, the horizontal converted wave velocity, is not very well defined and hard to determine.
Following Thomsen (1999), Yuan et al. (2001) derived a traveltime approximation for C-waves in a multi-layered VTI medium with dependency on the newly introduced C-wave anisotropy parameter χ_{eff}:

$$t_c^2(x) = t_{c0}^2 + \frac{x^2}{V_{c2}^2} + \frac{A_4 x^4}{1 + A_5 x^2} \tag{2.62}$$

$$\text{with} \quad A_4 = -\frac{(\gamma_0\gamma_{\text{eff}} - 1)^2 + 8(1+\gamma_0)\chi_{\text{eff}}}{4t_{c0}^2 V_{c2}^4 \gamma_0 (1+\gamma_{\text{eff}})^2}, \tag{2.63}$$

$$A_5 = \frac{A_4}{\frac{1}{V_{ph}^2} - \frac{1}{V_{c2}^2}}, \tag{2.64}$$

where V_{ph} is the horizontal P-wave velocity and the equation has the same accuracy as the original one from Thomsen (1999), $x/z = 2.0$ (Yuan et al., 2001). The horizontal P-wave velocity is defined as seen for the P-waves and extended for the empirical relationship between V_{ph} and χ_{eff}

$$V_{ph}^2 = V_{p2}(1+2\eta) \approx V_{p2}\sqrt{1+\frac{2\chi_{\text{eff}}}{(\gamma_0-1)\gamma_{\text{eff}}^2}}. \tag{2.65}$$

Note that the Equation (2.65) for V_{ph} is only strictly valid for a single layer. However, it has been found through numerical tests that it is a good approximation for multi-layered media.

Using this approximation the C-wave moveout in multi-layered VTI media can be described by the 4 parameters $V_{c2}, \gamma_0, \gamma_{\text{eff}}$ and χ_{eff}. The three terms of the Taylor series can also be differentiated into the hyperbolic moveout term which is controlled by the C-wave velocity V_{c2}, the non-hyperbolic moveout term related to the asymmetric ray path which corresponds to the velocity ratios $\gamma_0, \gamma_{\text{eff}}$ and the non-hyperbolic moveout due to the influence of anisotropy which is represented by the parameter χ_{eff}. However, not all parameters can be inverted accurately using this moveout equation. For example, Li and Yuan (2001b), showed that there is no resolution when trying to invert the parameters $\gamma_0, \gamma_{\text{eff}}$ by non-hyperbolic moveout inversion. On the other hand, the double scanning procedure searching for $V_{c2} - \chi_{\text{eff}}$ is robust and relatively insensitive to errors of the velocity ratios.

Double Square Root (DSR) Equation

An alternative approach to describe the non-hyperbolic moveout of C-waves uses a Double Square Root (DSR) equation, just as Equation (2.3) describes it for a single isotropic layer. Zhang (1996) proposed the use of such a DSR equation to describe the non-hyperbolic moveout and Li and Yuan (1999a) expanded it for anisotropic media. In Li et al. (2001b) the DSR equation for a stack of VTI layers is given in the following form:

$$t_c(x) = \sqrt{(\frac{t_{c0}}{1+2\gamma_0})^2 + \frac{(x+h)^2}{V_{p2}^2} - 2\eta_{\text{eff}}\Delta t_p^2} + \sqrt{(\frac{\gamma_0 t_{c0}}{1+\gamma_0})^2 + \frac{(x-h)^2}{V_{s2}^2} + 2\zeta_{\text{eff}}\Delta t_s^2} \tag{2.66}$$

where

$$\Delta t_p^2(x) = \frac{(x+h)^4}{V_{p2}^2[t_{c2}^2 V_{p2}^2/(1+\gamma_0)^2 + (1+2\eta_{\text{eff}})(x+h)^2]} \tag{2.67}$$

$$\Delta t_s^2(x) = \frac{(x-h)^4}{V_{s2}^2[t_{c2}^2 V_{s2}^2/(1+\gamma_0)^2 + (x-h)^2]} \tag{2.68}$$

and h is the half source-receiver offset. Although this is an approximation the equation is very accurate up to $x/z = 3$ for a constant velocity ratio and otherwise at least up to $x/z = 2$. Note, that although this equation is very accurate it needs 5 parameters to describe the anisotropic non-hyperbolic C-wave moveout: $V_{c2}, \gamma_0, \gamma_{\text{eff}}, \eta_{\text{eff}}$ and ζ_{eff}. Therefore, this equation is not ideal for parameter estimation. However, it can be used to describe the diffraction C-wave curve from a scatter point (x, z) located below a stack of VTI layers and thus be utilised for migration.

For anisotropic model building and Pre-Stack Time Migration Equations (2.35) and (2.34) can be re-written in terms of χ and the velocity ratios:

$$\zeta_{\text{eff}} = \frac{-(1+\gamma_0)}{8\gamma_0 t_{c0} V_{s2}^4}\left[\sum_{i=1}^{n} V_{s2i}^4 \frac{\Delta t_{c0i}^2 \gamma_{0i}}{1+\gamma_{0i}}\left(1 - \frac{8\chi_i}{\gamma_{0i}-1}\right) - \frac{\gamma_0 t_{c0}}{1+\gamma_0} V_{s2}^4\right] \tag{2.69}$$

$$\eta_{\text{eff}} = \frac{(1+\gamma_0)}{8\gamma_0 t_{c0} V_{p2}^4}\left[\sum_{i=1}^{n} V_{p2i}^4 \frac{\Delta t_{c0i}^2}{1+\gamma_{0i}}\left(1 + \frac{8\chi + i}{(\gamma_{0i}-1)\gamma_{\text{eff}i}^2} - \frac{t_{c0}}{1+\gamma_0} V_{p2}^4\right]\right. \tag{2.70}$$

(from Dai and Li, 2001).

2.7.4 S-wave

Tsvankin and Thomsen (1994) introduced a three-term Taylor series expansion for S-SV reflection moveout for a single VTI layer. Yuan (2001) modified and simplified this equation by introducing the S-wave anisotropy parameter ζ

$$t_{s2}^2(x) = t_{s0}^2 + \frac{x^2}{V_{s2}^2} + \frac{2\zeta x^4}{V_{s2}^2(t_{s0}^2 V_{s2}^2 + x^2)}. \tag{2.71}$$

This moveout equation is less accurate than its P- and C-wave counterpart (Equation 2.57 and 2.62) and limited to an $x/z = 1.5$.

For the multi-layered VTI case Yuan (2001) modified the corresponding equations

with the coefficients from the Taylor series expansion after Hake et al. (1984); Tsvankin and Thomsen (1994) by including the effective S-wave anisotropy parameter ζ_{eff} and found that the traveltime equation takes the same form as for a single layer:

$$t_{s2}^2(x) = t_{s0}^2 + \frac{x^2}{V_{s2}^2} + \frac{2\zeta_{\text{eff}} x^4}{V_{s2}^2(t_{s0}^2 V_{s2}^2 + x^2)}. \tag{2.72}$$

2.8 Semblance analysis and parameter dependency

2.8.1 Semblance analysis

The parameters introduced above can be extracted from data using semblance analysis or traveltime inversion. However, semblance analysis is more stable and less sensitive to traveltime errors and thus widely used. Semblance is the measure of coherence of many traces. The semblance coefficient is defined as the ratio of the output energy over a window of stacked traces to the input energy in the unstacked traces.

2.8.2 Parameter dependency

Li and Yuan (2001a) perform a sensitivity analysis to investigate which C-wave parameters can be extracted reliably from C-wave data. For this study, they use a single VTI layer of Dog Creek shale with the parameters $V_{p0} = 1.875$ km/s, $V_{s0} = 0.826$ km/s, $\epsilon = 0.225$, $\delta = 0.1$ and of depth $z = 1.0$ km. The Taylor series expansion for VTI media, as listed in Equation (2.62), shows that V_{c2} acts on the quartic term and controls the near-offset. The other three parameters, $\gamma_0, \gamma_{\text{eff}}$ and χ_{eff} influence the quartic term only. I will focus on these parameters in order to understand the dependencies between them and their sensitivity.

Figure 2.9 (a) shows the synthetic seismogram for the C-wave in Dog Creek shale. Figure 2.9 (b) shows the result from semblance double-scanning for γ_0 and γ_{eff} for fixed $V_{c2} = 1.54$ km/s and $\chi_{\text{eff}} = 0.187$. Inversion for the velocity ratios, γ_0 and γ_{eff}, show poor resolution. This means in terms of the vertical velocity ratio, that the moveout is insensitive to the variation in γ_0. When the offset increases

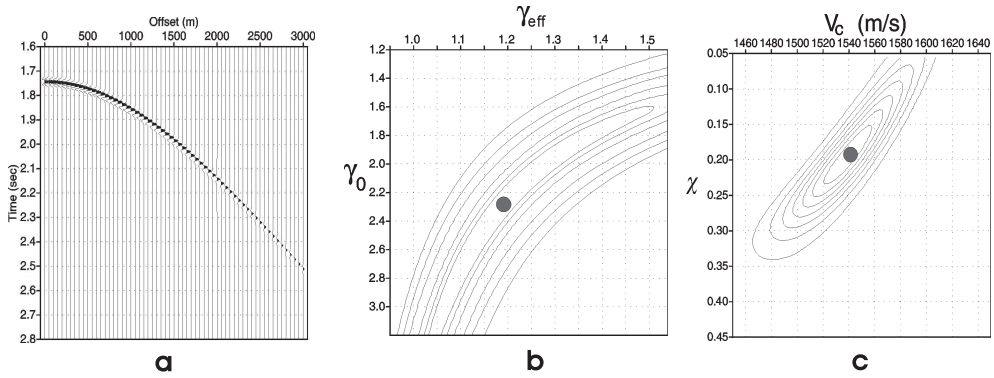

Figure 2.9: Sensitivity analysis for a single VTI layer. (a) Synthetic seismogram. (b) Double-scanning semblance analysis for γ_0 and γ_{eff} for fixed V_{c2} and χ_{eff}. (c) Double-scanning semblance analysis for V_{c2} and χ_{eff} with fixed velocity ratios. The dots indicate model values.

the influence of γ_0 decreases. Changes in γ_0 up to 15% have little effect on the moveout when the other parameters are fixed. Therefore, inversion for γ_0 shows a poor resolution.

In Figure 2.9 (c) double scanning is used to estimate V_{c2} and χ_{eff} with fixed velocity ratios $\gamma_0 = 2.27$ and $\gamma_{\text{eff}} = 1.191$. In contrast to (b) the semblance analysis shows good resolution for both parameters V_{c2} and χ_{eff} and thus can be inverted with sufficient accuracy.

Error analysis

A second analysis focuses on the sensitivity of C-wave moveout over the intermediate spread ($x/z = 1.5$) to the variation in the background velocity ratio γ using Taylor series expansion. Unlike P-waves, the non-hyperbolic moveout for C-waves is not neglectable for spreads up to $x/z = 1.0$. However, Figure 2.10 shows that the non-hyperbolic term is significant but relatively insensitive to the variation of γ for offsets up to $x/z = 1.0$. Thus, the Taylor-series expansion with a non-hyperbolic correction controlled by the background γ may be used to determine V_{c2}. In practise, for the non-hyperbolic analysis the vertical velocity ratio γ_0 is fixed as background parameter γ.

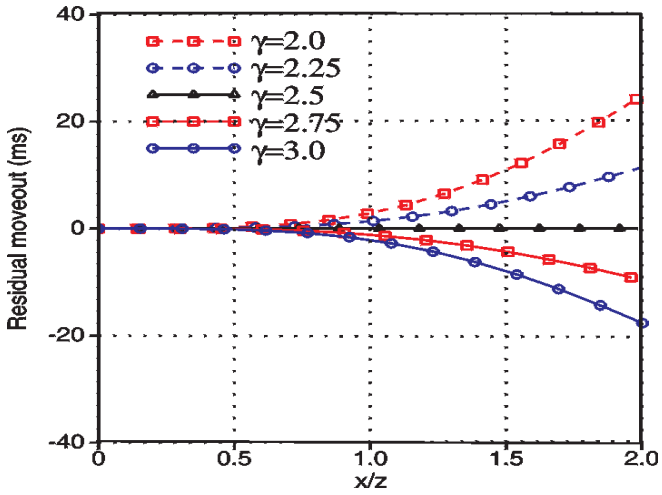

Figure 2.10: Analysis of sensitivity of C-wave moveout to the variation in the background velocity ratio γ using Taylor series expansion. The model curve is defined with $t_{c0} = 1.5$ seconds, $V_{c2} = 1.5$ km/s and $\gamma = 2.5$. The residual moveout is the difference between the model curve and the curves calculated using five other ratios from 2.0 to 3.0 while V_{c2} and t_{c0} are fixed.

2.9 Summary

In this chapter I have presented an overview of converted waves in terms of how they differ from single wave modes and the implication for the acquisition, i.e. the Ocean Bottom Cable survey technique. I have explained in which scenarios it is useful to record C-waves and mentioned some case studies. Further, I gave a short introduction to anisotropy and its effect on wave propagation and ways to parameterise it. Finally I gave an overview of how the conversion point of a C-wave can be expressed mathematically and of how traveltimes are approximated in anisotropic media for P-, S- and C-waves. Next, I want to continue with an introduction to the Alba data set.

Chapter 3

The Alba data: A multicomponent experiment

In my studies I used a multicomponent data set from the Alba Field. In this chapter I give a brief overview of the geological setup, the acquisition of the data, its characteristics and published processing results. Furthermore, I introduce well log data and results from VSP analysis which I used for model building as well as evidence of polar anisotropy in the Alba field. Finally, I will discuss some unresolved issues and why this data set is ideal for my study.

3.1 Location and Geology

The Alba Field is located about 225 km northeast of Aberdeen in Block 16/26 of the UK North Sea (see Figure 3.1) and was discovered in 1984 through Well 16/26-5 while drilling for a Lower Cretaceous discovery (Britannia Field). The Alba reservoir is an Eocene sand reservoir at an average depth of about 1.9 km. The main field is approximately 9 km long and is oriented in a northwest to southeast direction. Its width is about 1.5 - 3 km and it has a thickness of up to 100 m. The second and minor field is located northwest of the main field and has a length of 3 km and a width of again up to 3 km. Located underneath the Alba field is another reservoir, the Britannia Field (MacLeod et al., 1999). Alba is overlain by mainly flat overburden of low-permeability shales showing polar anisotropy.

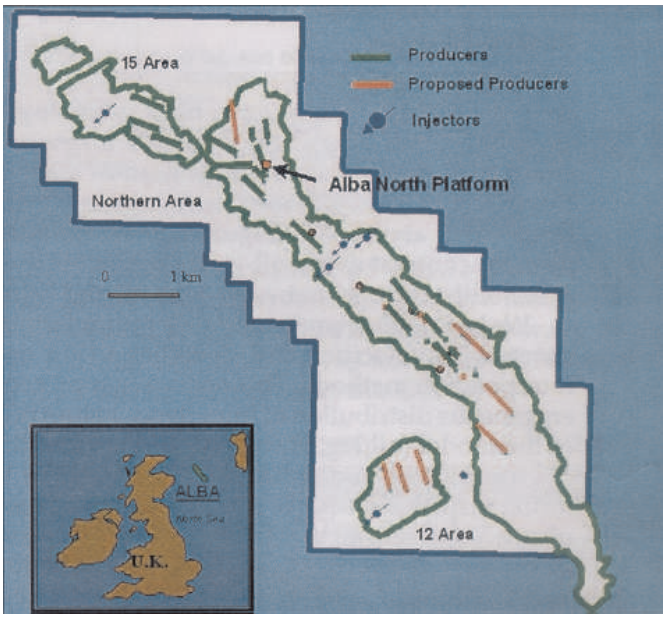

Figure 3.1: Location and shape of the Alba Field in the North Sea, from MacLeod et al. (1999).

The Alba Field overlies the Mesozoic Witch Ground Graben, south of the Fladen Ground Spur and north of the Renee Ridge. The Alba reservoir consists of Eocene-age high-porosity, unconsolidated turbidite channel sands which are sealed by low-permeability shales (caprock). Figure 3.2 shows a cross-section with typical off-field and in-field wells, and the sequence subdivision of the Eocene. The oil-bearing Middle Eocene sands display remarkable petrographic uniformity and are thought to have been deposited by high-density turbidity currents. The presence of water-escape structures and sand injection features suggest rapid deposition and burial. Newton and Flanagan (1993) interpret this as deposition in a previously eroded channel-like structure. This structure was then filled by large volumes of petrographically uniform sands which were rapidly deposited by high-density turbidity currents. Later, Hanson et al. (1999) and Duranti et al. (2000) provided evidence of post-depositional fluidisation and remobilisation of sandstones with injections in the surrounding sands. Fluidised and re-mobilised sands are oil-saturated above the oil-water-contact (OWC) and believed to hold substantial reserves of hydrocarbons (Duranti et al., 2002).

Knowledge about the extension of the channel sands is vital for the oil-industry as the oil exploitation is carried out by horizontal wells. These wells for the

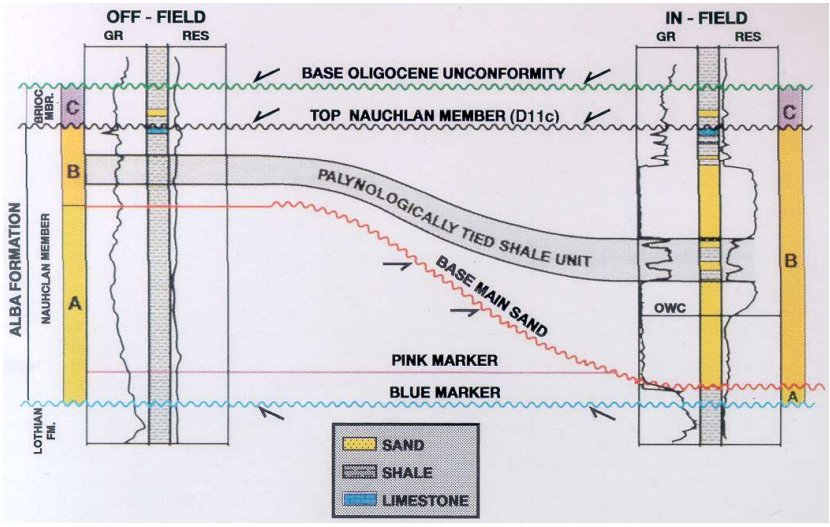

Figure 3.2: Schematic cross-section showing typical off-field and in-field wells, and the sequence subdivision of the Eocene (from Newton and Flanagan, 1993).

reservoir drainage need to be as close as possible to the top of the reservoir. Moreover, the channel contains discrete bodies of intrareservoir shales that can cause significant drilling and production problems. Thus, it is desired to locate these intrareservoir shales. Several seismic surveys have been carried out over the Alba Field, for example a 2D survey in 1988 and a 3D streamer survey in 1989. These data and rock physical studies showed that the velocity and density in the reservoir interval sand and shale formations result in generally low P-wave impedance contrasts (see Figure 3.16(b)). Thus, picking the top of the reservoir is difficult because of the weak and often inconsistent seismic event. The intrareservoir shales are often seismically invisible. On the basis of these observations a 4-component (4C) seismic survey was conducted using the ocean bottom cable (OBC) technique. The main objectives were

- Improving the structural image of the reservoir sands, especially location of top and bottom for better well positioning.

- Time-lapse monitoring of fluids to predict water saturation changes.

- Mapping of intra-reservoir lithology.

3.2 Acquisition and data characteristic

The data were acquired during March and April 1998. A total of 67 km^2 of sea bed data was recorded incorporating 14 swaths. The swath geometry was chosen to produce a data set which could easily be used together with the 1989 streamer data set for time-lapse analysis (MacLeod et al., 1999). Each swath consists of two 6-km-cables (Nessie 4, 4C Multiwave array) which are positioned 400 m apart from each other on the sea bed at a depth of approximately 140 metres. Each cable consists of 240 receiver points, with a 25 metre distance between them. Each receiver point has four components, consisting of one hydrophone and 3 orthogonal geophones (X,Y,Z), the inline, crossline and vertical, components. When the first ship deployed the cable on the sea bed in the designated position the source vessel shot 12 km lines parallel to the sea bed cables. For each swath 21 lines were shot, each 100 metre distant from the next (McHugo et al., 1999). The shot lines were acquired using a flip-flop configuration with the source lines being 50 m apart and thus resulting in a 25 m inline pop interval. The sampling rate was $\Delta t = 2$ ms and record length 8.19 seconds (Underwood and Tilling, 1999). Figure 3.3 illustrates the acquisition geometry for swath 05 of the 4C ocean-bottom-cable survey over the reservoir. The yellow lines indicate the position of the ocean bottom cables and the blue lines the shotlines (sail lines). The data used in this study is the 2D Line 1194 (i.e. cable 1194 recorded shots from all shotlines). Furthermore, the map indicates the position of boreholes 28 and 28z, from which well log data is available.

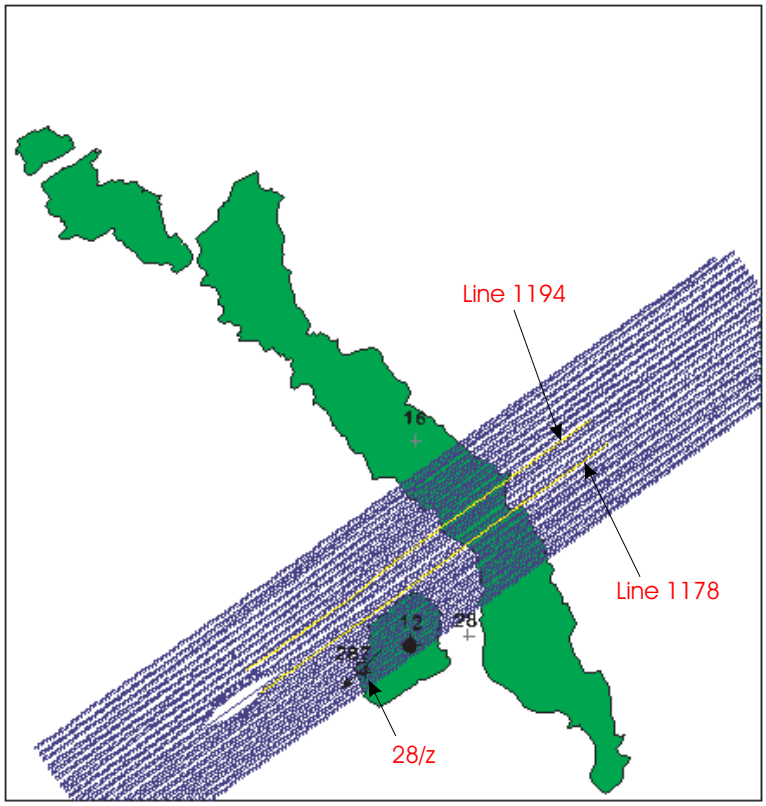

Figure 3.3: The Alba field with acquisition geometry for swath 05. Highlighted are the two cables which coincide with shotlines 1194 (cable 1) and 1178 (cable 2). The wells 16/26-28 and 16/26-28z are also shown.

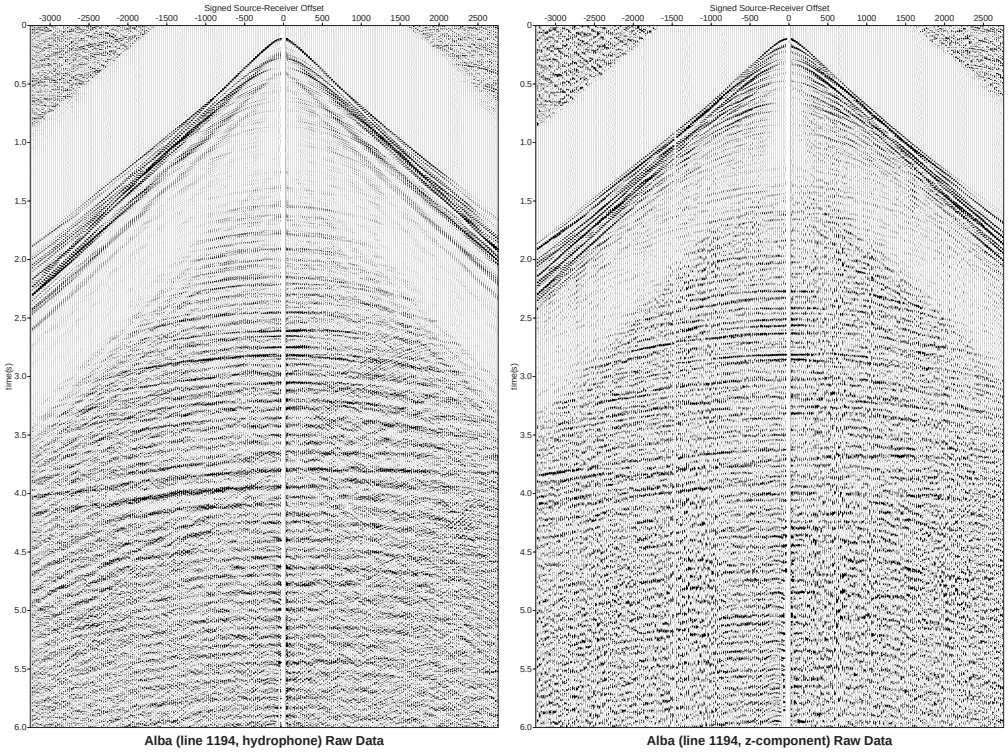

(a) H (b) Z

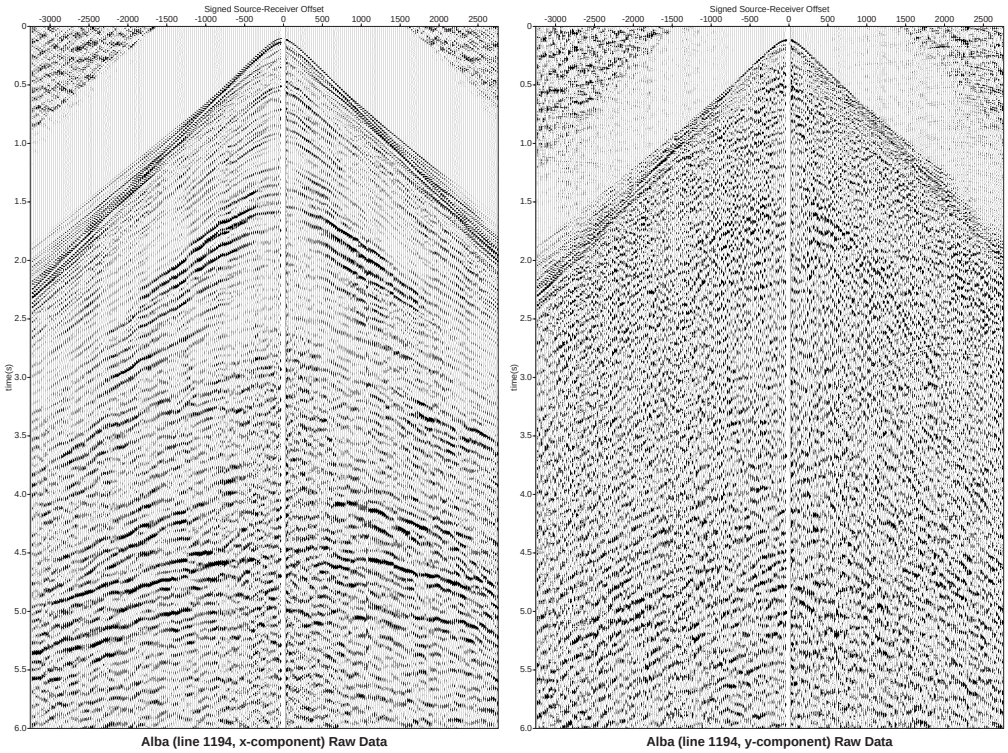

(c) X (d) Y

Figure 3.4: Example of the raw data quality from the Alba data set. Displayed are a receiver gather of each, the hydrophone and vertical component on the top, and the inline and crossline component on the bottom.

Figure 3.4 shows an example of the raw data: a receiver gather for each of the 4 components of cable 1, shotline 1194, swath 05. Displayed are, on the top, the receiver gather for the hydrophone and vertical components, and on the bottom, the inline and crossline components. Overall, the data quality is good and this is explained in the following subsections.

3.2.1 General characteristics

The natural separation of P- and C-wave can be clearly identified on the vertical and inline components. The P-wave events are characterised by a gentle moveout (i.e. high velocity) and C-wave events by a steep moveout (i.e. low velocity). This wavefield separation can be explained remembering Figure 2.3 in Chapter 2 which shows the effect of a low velocity near-surface layer on P- and C-waves. Well log and VSP results (see the next section) indicate a low S-wave velocity in the Alba data. No further analysis of wavefield separation has been performed for this reason. A more detailed study about the effects of S-wave velocity on near-surface events follows in Chapter 5. Generally speaking, the fidelity of the data is good for 3 reasons:

- good signal-to-noise ratio,
- good separation of P- and C-wave, and no leakage,
- no leakage between X- and Y-component.

The hydrophone (pressure) and vertical geophone (particle motion) show clear P-wave events up to 4 seconds. Both wave types are acquired in OBC surveys and utilised to suppress water-column reverberation. The hydrophone shows a negative trough for the water reverberation while the vertical geophone shows a positive peak (Barr and Sanders, 1989). Combining the data sets will remove this receiver ghost. For the Alba data the water reverberation is expected at 187 milliseconds due to a water depth of 140 metres. The second multiple is therefore predicted at a lag of 374 milliseconds. Figure 3.5 shows the diagrams for the autocorrelation of (a) the hydrophone and (b) the vertical geophone. The negative trough is very clearly visible on the hydrophone as well as the positive peak of the second multiple. In contrast, the vertical geophone does not show such

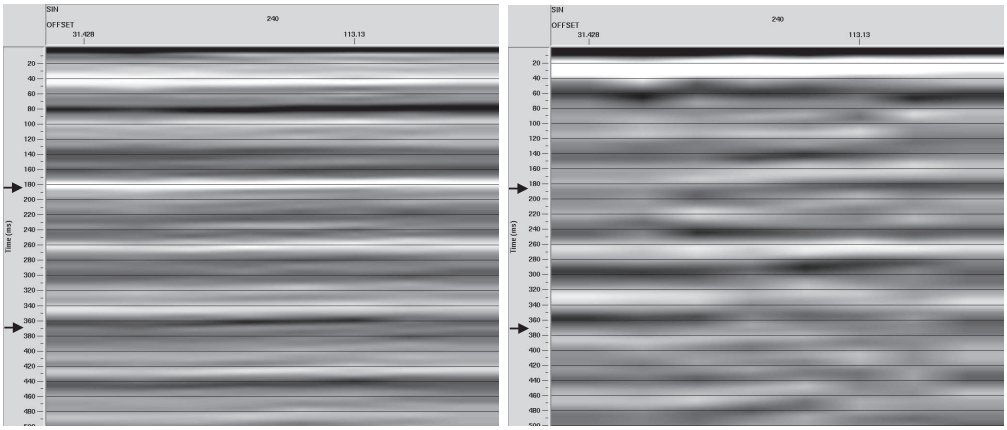

(a) H (b) Z

Figure 3.5: Autocorrelation diagrams for (a) Hydrophone and (b) vertical geophone of the Alba data. The receiver ghost is expected at 187 milliseconds, as indicated by the top arrow, because the water depth is 140 metres. The data are pre-processed by applying true amplitude recovery, first break mute and a bandpass filter.

a clear positive peak for the water reverberation or its second multiple. Yuan (2001) explains the lack of water reverberation on the vertical geophone with a S-wave gradient at the sea bed. If the sea bed is nearly flat and the reflectivity is larger than 0.3 the multiple on the geophone data will be very weak and negligible due to the cancelling effect of both source- and receiver-side reverberations in the geophone component. Furthermore, if the vertical geophone shows no water reverberations the combination of hydrophone and geophone data may not be necessary. Hence, in this study the vertical geophone has been processed without the summation with the hydrophone data.

The inline component shows converted wave events up to about 5.5 seconds while the crossline component shows very little energy indicating that there is no S-wave splitting. This is expected as the shotlines were parallel to the receiver cables and thus the energy should be visible on the inline component only if there is no azimuthal anisotropy. Further, the lack of energy on the Y-component is an indication that there is no HTI anisotropy but possibly only VTI (which I will discuss later in this chapter). However, the bad data quality of the crossline component may also be due to the chosen instrumentation.

3.2.2 Amplitude and frequency characteristics

C-wave data shows some different amplitude and frequency characteristics compared to P-wave data. In order to illustrate this I calculate the reflected energy of P- and C-wave on a horizontal, isotropic layer with the properties listed in Table 3.1. For the calculation of the amplitude for these wave types the equations from

V_p [km/s]	V_s [km/s]	ρ [g/cm^3]
2.0	1.0	2.0
3.0	1.5	2.0

Table 3.1: Isotropic model for calculation of reflection energy of P- and C-wave.

Aki and Richards (2002) were used. The algorithm is explained in more detail in Chapter 5. Figure 3.6 shows the normalised amplitude against incidence angle for (a) P-wave and (b) C-wave. Of interest are angles between 0 and 40 degrees. The energy of the P-wave has a maximum at zero-offset, or zero incidence angle, and decreases slightly for higher angles until it approaches the critical angle. The C-wave has zero energy at zero-offset and increases with higher incidence angles up to an angle of about 25 degrees. After that it decreases again until the angle which corresponds to the critical angle of this P-wave. In the raw data gathers of Figure 3.4 the following energy distribution can be observed: the main energy of the vertical component is found in the near offset. However, the horizontal or inline component shows its main energy in the mid-to-far offset and almost no energy around zero-offset. Considering data processing this is ideal, as the effect of non-hyperbolic moveout from C-waves which is used for processing is only visible at mid-to-far offsets while P-wave processing routines are based on the near-offset.

The frequency content of P- and C-wave shows differences too. Figure 3.7 shows for (a) the P-wave and (b) the C-wave corresponding amplitude spectra for the used data (0-4.5 s and 0-6.0 s, respectively). The plots show on the left the input data, i.e. a raw receiver gather, with a blue box defining the selected area. The data has been only pre-processed, i.e. mute and amplitude recovery was applied. The middle part displays the zoom of the selected data field on top and the F-X power spectrum below. The diagram on the right hand side is the corresponding average power spectrum in percentage of power. Comparing the power spectra of the two waves it is clear, that the C-wave shows lower frequen-

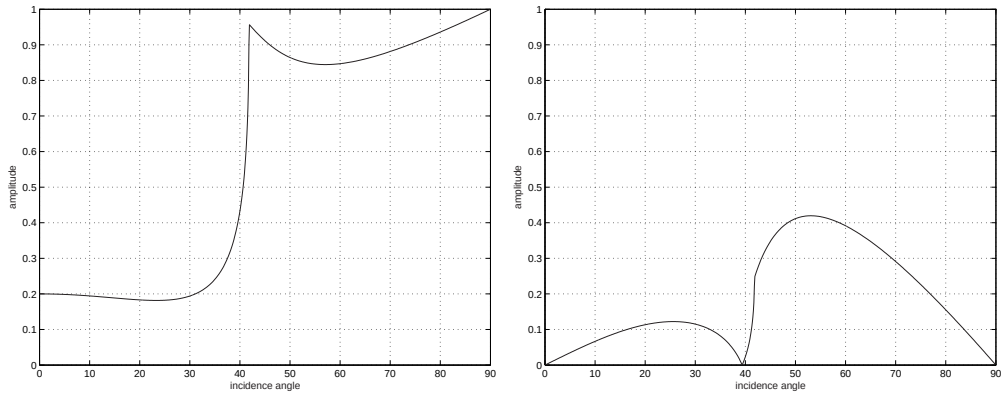

(a) P-wave (b) C-wave

Figure 3.6: Reflected energy for P- and C-wave displayed as the reflected amplitude for a single isotropic interface (see Table 3.1).

cies than the P-wave possibly due to greater attenuation of the S-wave leg of a C-wave path. The peaks of the spectra are 17 Hz for the P-wave and only 13 Hz for the C-wave. Next, the power spectra has been calculated for the reservoir arrival times (2.0 s for P-wave and 3.6 s for C-wave). Figure 3.8 displays again in (a) the result for the P-wave and in (b) for the C-wave. The frequencies are slightly higher for the P-wave with a peak at 15.6 Hz and only a bit lower for the C-wave with 13.8 Hz. Moreover, in both cases at all arrival times and in the reservoir area, the frequency band of the P-wave is broader than that of the C-wave. After (isotropic) processing the amplitude spectra from the stacked sections show hardly a change of the maximum frequency. However, the frequency bands are narrower (see Figure A.1 and Figure A.2 in Appendix A). This behaviour is confirmed by Hanson et al. (1999) who also state that the dominant frequency of the C-wave is half as large as the P-wave for the Alba data. The difference in frequency is a potential problem for event correlation between the two data sets.

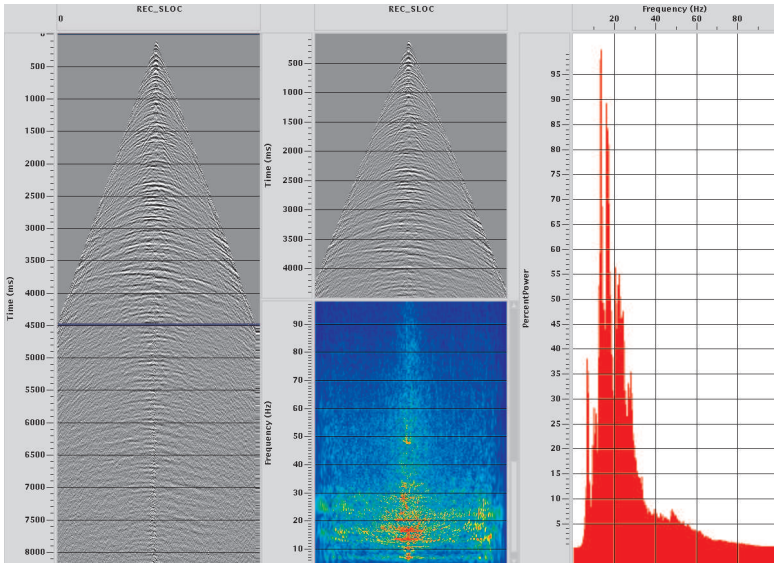

(a) P-wave

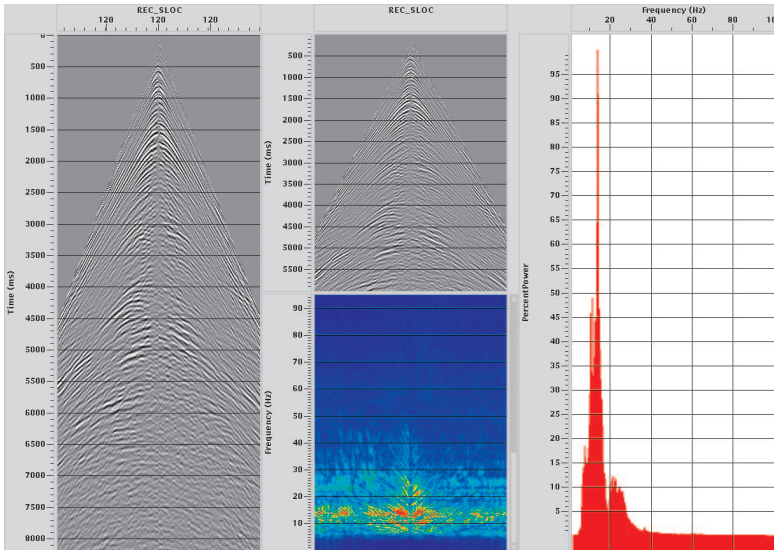

(b) C-wave

Figure 3.7: Amplitude spectrum for a receiver gather of (a) P-wave (0-4.5 seconds) and (b) C-wave (0-6.0 seconds). On the left is the receiver gather displayed, in the middle on top the zoom of the selected area (here the main part of the data), on the bottom the F-X power spectrum and on the right the average power spectrum.

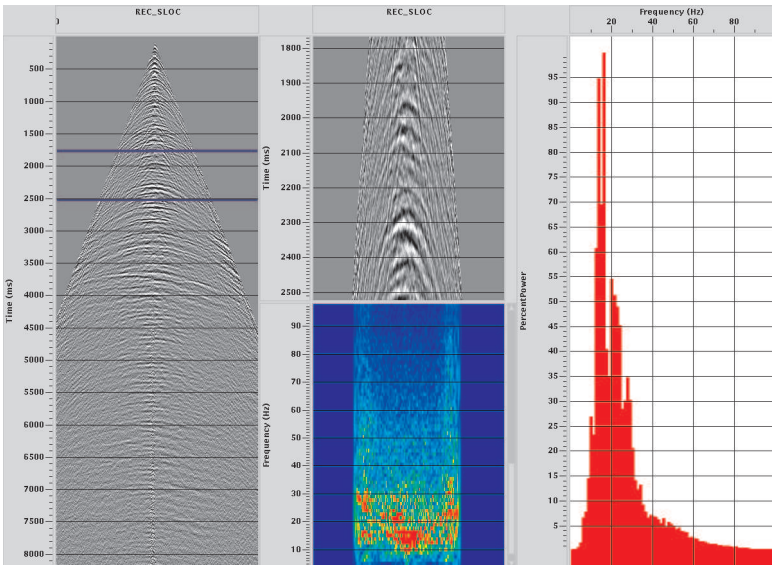

(a) P-wave

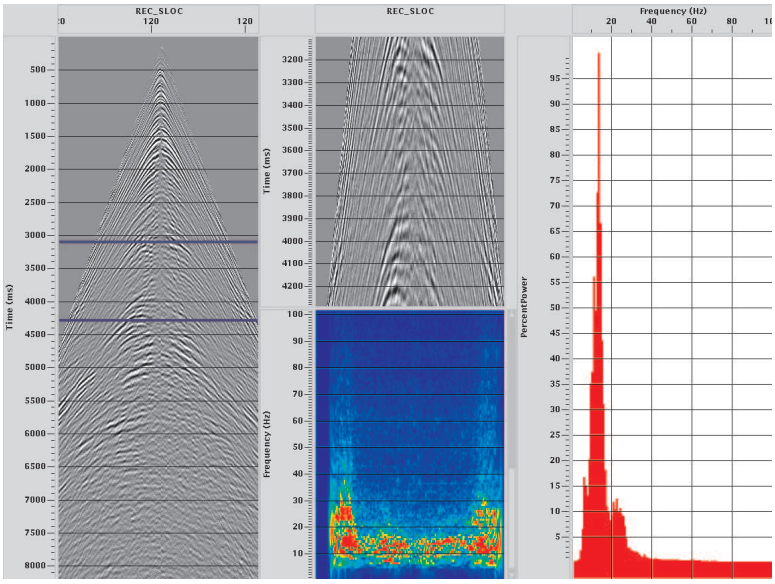

(b) C-wave

Figure 3.8: Amplitude spectrum for the same receiver gather as in Figure 3.7 focusing on the reservoir events of (a) P-wave and (b) C-wave.

3.2.3 P-to-S conversion

For C-wave data it is important to know where the conversion takes place. As the sea floor is a strong reflector the conversion may take place there or at another reflector. In most cases of 4C surveys it has been observed that the conversion takes place at the reflector. There are two lines of evidence for this. Firstly, in shot gathers the events in the vertical geophone and hydrophone are continuous while they appear wobbly in the horizontal components. This is due to a shear wave static problem. These static shifts are not caused by the elevation of the receiver but by S-wave velocity variations in the near-surface sediments. In Chapter 7, I show this shear static and its correction for the inline component.

Secondly, the non-hyperbolic moveout of the horizontal component confirms that

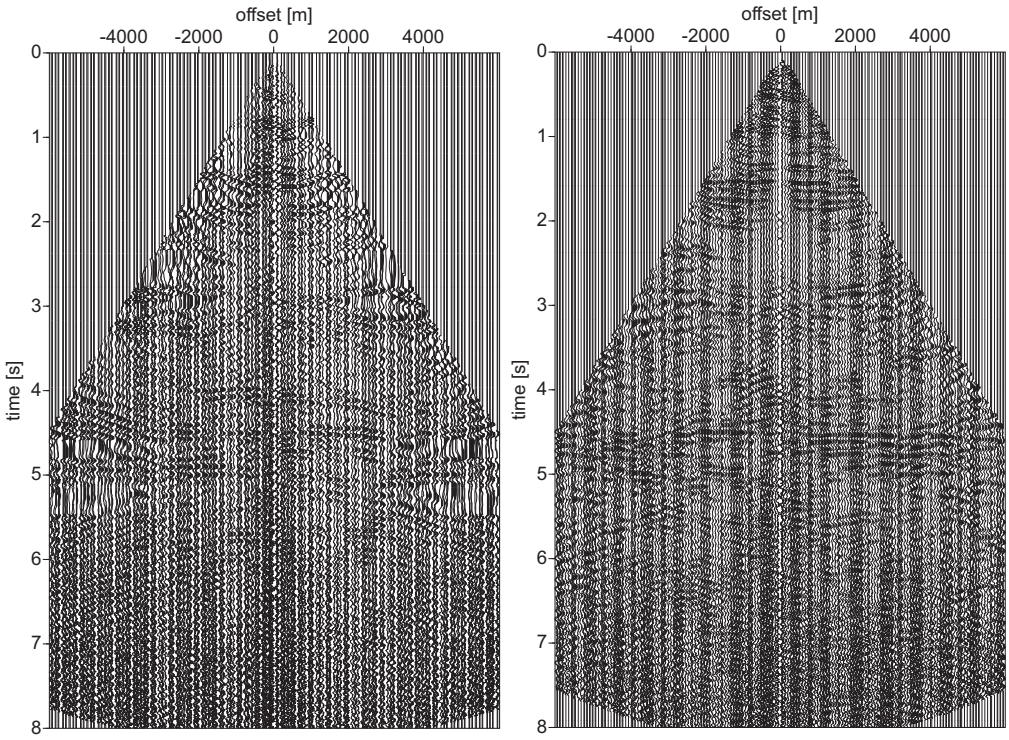

(a) hyperbolic (b) non-hyperbolic

Figure 3.9: Comparison of hyperbolic and non-hyperbolic moveout correction on an ACP gather: (a) after hyperbolic NMO and (b) after non-hyperbolic anisotropic NMO. Hyperbolic NMO correction causes overcorrection at events between 2-3 seconds and 4.5-5.5 seconds.

the conversion takes place at the reflector. The $P-S-S$ type which is converted

at the seafloor should show a hyperbolic traveltime curve if the water is not very deep. Figure 3.9 shows a data example from Alba with (a) the gather corrected using a hyperbolic NMO correction and in (b) with a non-hyperbolic anisotropic NMO correction. For all gathers the same mute was used. The hyperbolic NMO corrected gather shows over-correction for events between 2-3 seconds and 4.5-5.5 seconds. Using the non-hyperbolic NMO correction this overcorrection is mostly compensated.
These two arguments show that P-to-S conversion in the Alba data set occurs as desired at the target reflector.

3.3 VSP and well log data

3.3.1 VSP data

Vertical seismic profiling (VSP) measures the response of a geophone at various depths in a borehole to sources on the surface. The so called walkaway VSPs are acquired when the source is moved away from the well. VSP data is known to be very useful for calibrating recorded reflection events in surface data with the geology of a subsurface reflector. Furthermore, they are most important for modelling, as they show whether or not a horizon returns a detectable reflection to the surface. Also, because VSP displays both the down- and upgoing ray, the reflector depth can be estimated from the intersection of the downgoing and its corresponding reflection event.
In January 1998, a multiazimuthal walkaway VSP survey was acquired in the deviated well 16/26-28z in the Alba field, North Sea (for location in relation to the OBC data see Figure 3.3). For the acquisition an ASI (Array Seismic Imager) tool consisting of 5 receiver points with a spacing of 15.12 m was used. Each receiver point consists of 3C non-gimballed geophones. Five walkaway lines were acquired for each of the two tool settings at the depth of 2773-2712 m (measured depth, MD) and 1371-1310 m (MD). The source was an airgun deployed from a supply boat. The walkaway lines are regularly separated in azimuth and the lines for the tool setting at 1371-1310 m are displayed in Figure 3.10. As an example for the data quality Figure 3.11 shows a VSP seismogram for the x-, y- and z-component from the top tool position at 1310 m. Initial editing has been applied

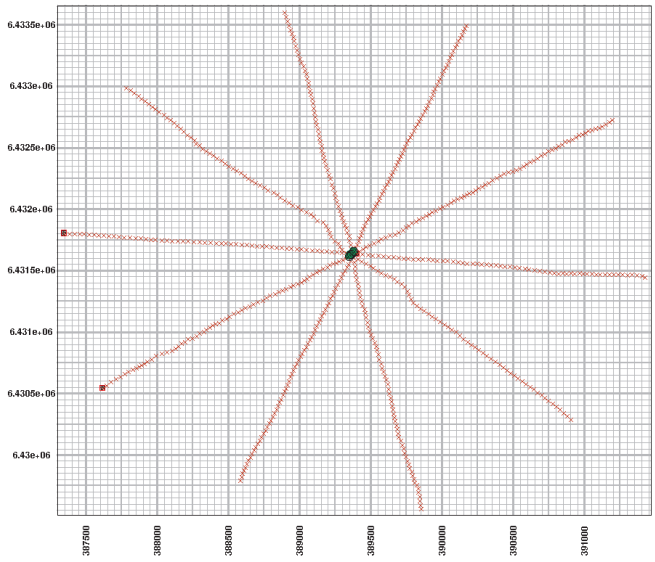

Figure 3.10: Walkaway VSP pattern of shot locations for one tool setting at 1310 m.

to the data such as removal of acquisition delay, static shift to MSL (mean sea level) and broadband filter (Leaney et al., 2001a).

In addition to the walkaway VSP a vertical incidence VSP was recorded from 2795-244 m (MD) and sonic data was acquired. All data was used by Western-Geco during walkaway processing. Leaney (2000) showed that walkaway VSP data can be used to build a 1D model for polar anisotropy media. The results from the VSP analysis from S. Leaney (courtesy of ChevronTexaco) for the estimated velocities and Thomsen parameter ϵ and δ are displayed in Figure 3.12. These results provide the starting point for parameter estimation using the reflection data. Further, I have used these VSP results for model building in Chapter 5 and anisotropic forward modelling.

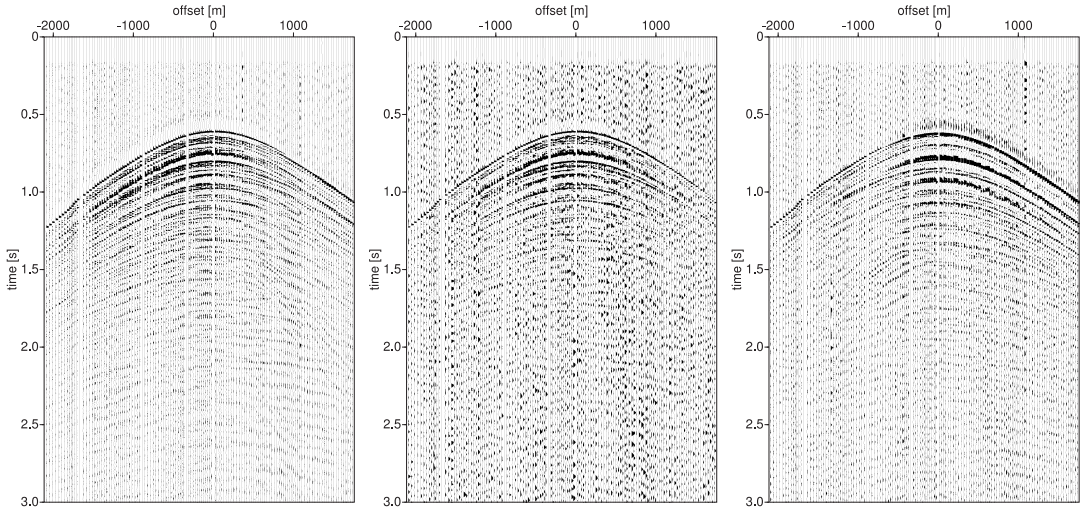

(a) X (b) Y (c) Z

Figure 3.11: VSP seismograms for (a) x-component, (b) y-component and (c) z-component from the top tool at a depth of 1310 metres. Initial editing has been applied to the data such as removal of acquisition delays and static shift to MSL (mean sea level).

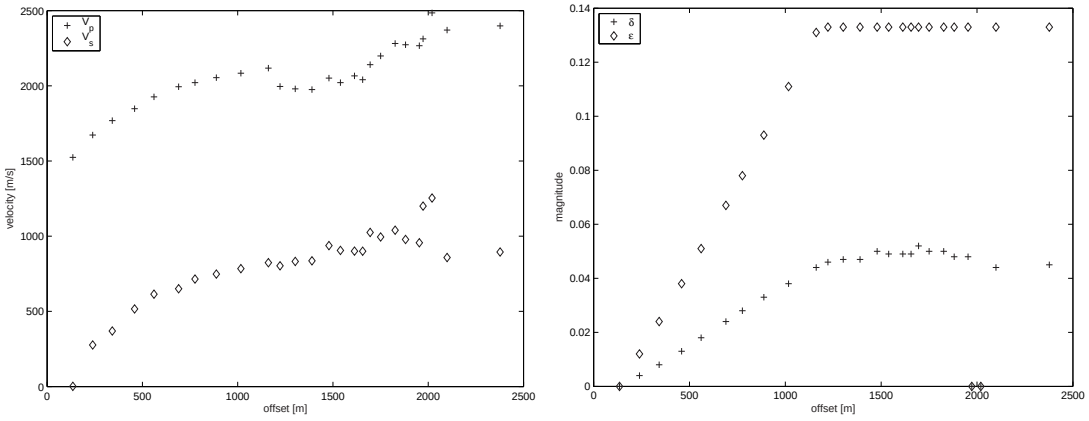

Figure 3.12: (a) V_p and V_s determined from VSP analysis. (b) Thomsen's parameters δ and ϵ determined from VSP data. Both analyses were performed by S. Leaney.

3.3.2 Wireline log data

Well logs are records of one or more physical parameters as a function of depth in a borehole. They are essential for determination of lithology and linking rock types. Furthermore, they are used for estimation of fluid contact locations and the identification of geological environments. Without well control, i.e. well logs and VSP data, accurate estimation of rock properties and lithology analysis is uncertain. Focusing on converted wave analysis, the correlation between P-wave and C-wave events needs confirmation from well log and VSP data to correct for possible mis-ties. Thus, for accurate processing and interpretation of converted wave data the integrated analysis of different data sets is important. Figure 3.13 shows a sonic, porosity, gamma-ray and caliper log for the depth interval from 1000 to 2200 metres. My interpretation of the layering sequences is drawn on the plot. Figure 3.14 highlights the depth segment of 1800-2100 metres which includes the

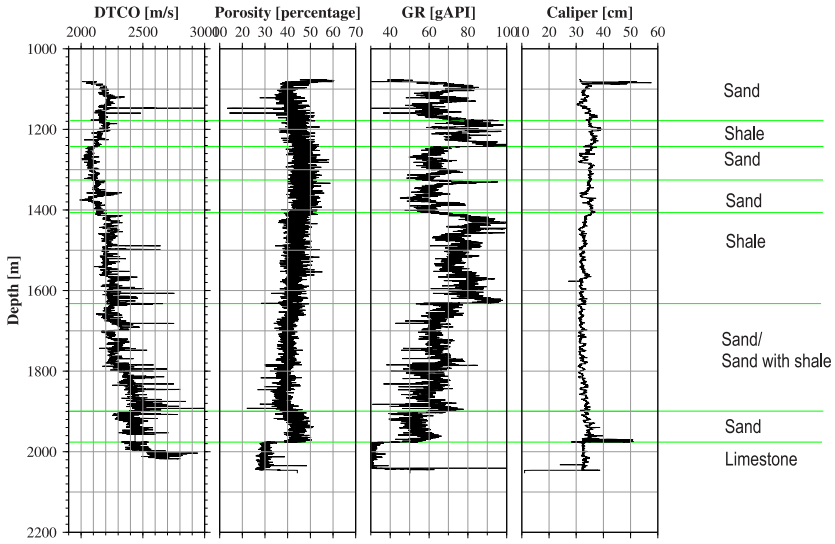

Figure 3.13: Sonic log, porosity, gamma-ray, caliper log for a depth of 1000-2200 m depth from borehole 28z. Interpretation of layering sequence is printed to the right of the well logs.

reservoir layer. The well logs displayed are two shallow and one deep resistivity log, a sonic and density log. In particular, the location of the hydrocarbon is indicated by the regions of high resistivity on the resistivity logs. MacLeod et al. (1999) indicated that the depth of the reservoir is approximately 1900 metres which agrees with the information from the logs. Figure 3.15(a) displays once more gamma-ray, caliper and shallow and deep resistivity logs, restricted to the

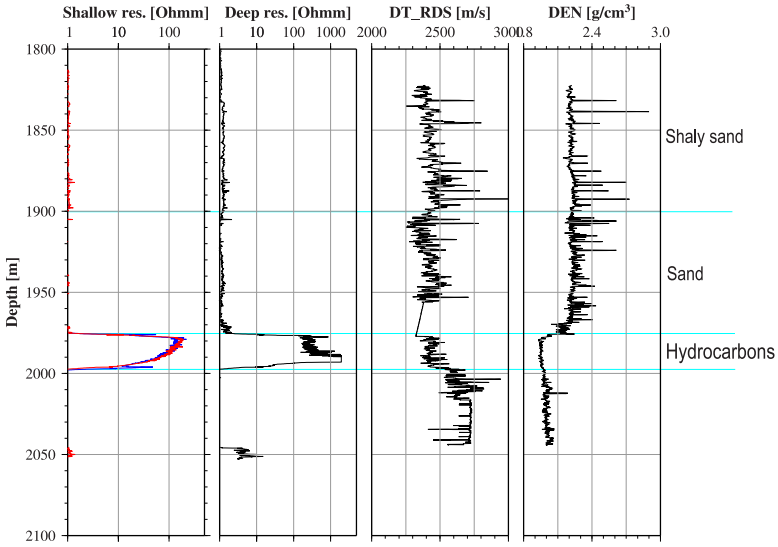

Figure 3.14: Shallow (blue), middle (red) and deep resistivity, sonic log, density for reservoir level. Interpretation of the location of hydrocarbons are drawn to the right of the logs.

depth of the reservoir. Both gamma-ray and resistivity indicate well the top of the hydrocarbons and from the resistivity log an estimate of the bottom can be made. Finally, Figure 3.15(b) shows the curves for the total water saturation (SWT) and the volume of shale (VSH). These logs are also used to identify the exact location of the hydrocarbon bearing horizons. Both curves show the same depth for the top of the reservoir but only the SWT indicates the bottom too. The VSH-curve does not differentiate between limestone and sand, and therefore the bottom boundary of the reservoir can not be located.

3.4 Review of published results

MacLeod et al. (1999) showed that the use of converted waves has helped to successfully image the extension and thickness of the Alba reservoir sands, which was not possible before. Figure 3.16(a) shows the strong improvement comparing P-wave and C-wave images. However, both wave types show different information about the reservoir. The P-wave image indicates the oil-water-contact (OWC) in the reservoir is as confirmed by rock physics modelling (Hanson et al., 2003). The C-wave image shows a clearer picture of the top and bottom of the reservoir and its wing features (i.e. sand-body geometry). The dipole sonic log in Figure 3.16(b)

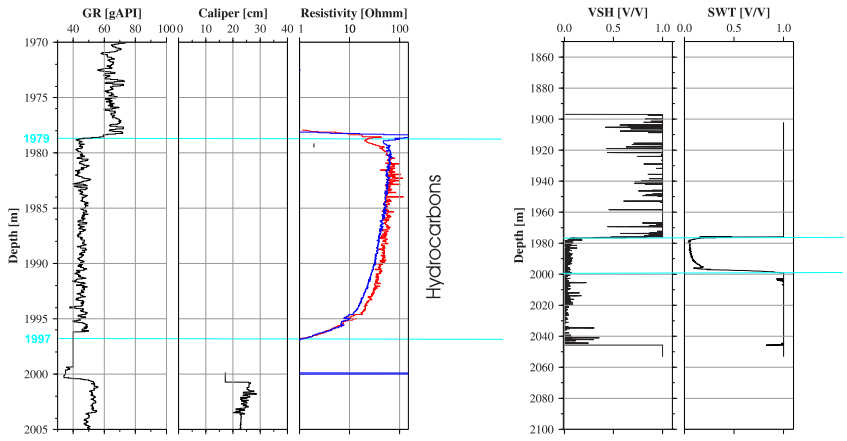

Figure 3.15: (a) Gamma-ray, caliper, shallow (blue) and middle (red) resistivity logs at the reservoir depth. (b) Diagrams of SWT (total water saturation) and VSH (volume of shale). Again, the interpretation of the reservoir location is marked on the logs.

illustrates clearly the large contrast in S-wave velocity and the small contrast in P-wave velocity between the reservoir sands and the surrounding shales causing the different images. Following this success the interpretation of the Alba Field sand distribution and its origins were re-examined and changed (Duranti et al., 2000, 2002). The revised Alba model (Figure 3.17,right) shows an irregular top and wing-like sand injections at the flanks of the reservoir. The change in the geological model is significant for well log planning as the old model would have only needed one production well but the new model may require wells to be drilled at local crests and along marginal intrusions to drain the reservoir (Huuse et al., 2003).

Other studies showed that using AVO analysis from both P- and C-wave data increases the success rate of classification of facies from $\sim 64\%$ to$\sim 98\%$ compared with using only P-wave AVO attributes (Mukerji et al., 2000).

Time-lapse analysis shows that amplitude differences between OBC and streamer data can be related to production. However, it is only a quantitative guide for reservoir modelling and well placement. The reservoir is a complex, irregularly shaped sandbody containing shales which may control fluid flow. Therefore change in OWC around shale bodies due to reservoir geometry may cause time-lapse impedance changes that interfere with those created due to production

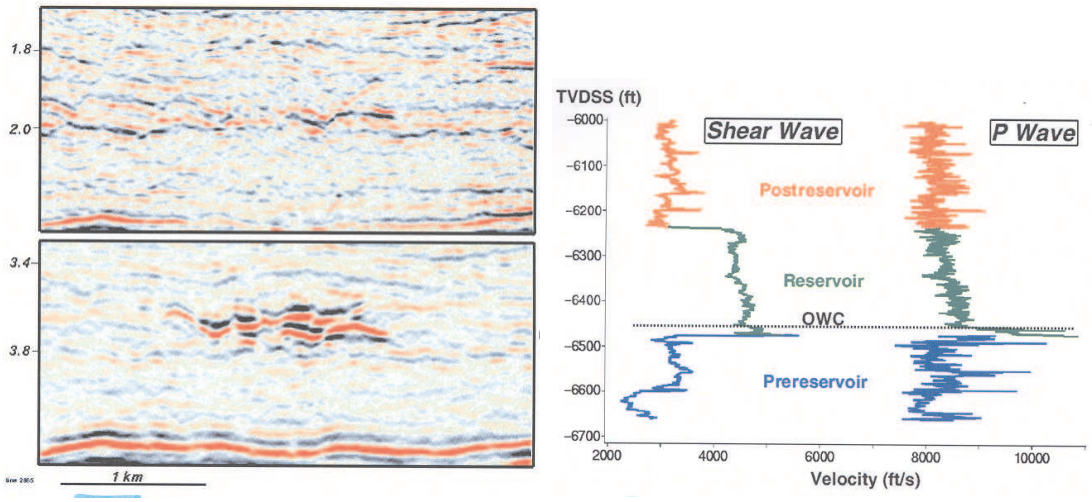

(a) (b)

Figure 3.16: (a) Top: Image from streamer P-wave data. Bottom: Improved image of the reservoir outline from C-wave data. (b) Dipole sonic log through reservoir sand showing a large contrast in S-wave velocity and a small contrast in P-wave velocity with the surrounding shales. (Both pictures taken from MacLeod et al. (1999).)

(Hanson et al., 2003). Furthermore, Dai et al. (2001) shows evidence for polar and some azimuthal anisotropy in the Alba data from a neighbouring sailing line to the one I use here.

3.5 Evidence for Polar Anisotropy

In this section I want to show that the Alba field is seismically anisotropic. Hence, in order to obtain a valuable image of the subsurface from seismic data, anisotropy needs to be quantified in the data and taken in account during processing. For example, neglecting of the effects of anisotropy might lead to mis-positioning of reflectors. The first line of evidence for polar anisotropy or VTI can be found from the geology and stratigraphy of the Alba field. Newton and Flanagan (1993) published the cross-section in Figure 3.2 showing shale in the overburden and shale and interbedded sands in the reservoir depth. Huuse et al. (2003) and Duranti et al. (2002) discuss borehole and core data from the Alba field in context of sandstone intrusions but also stating that shale encloses the sand-rich reservoir facies. Figure 3.18 shows a gamma-ray log and photographs of cores from a re-mobilised

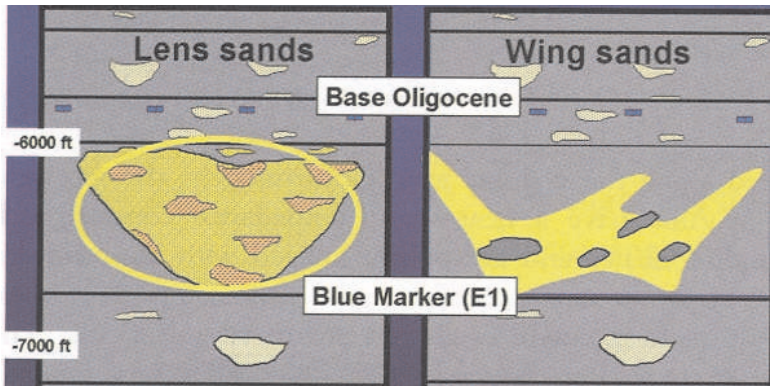

Figure 3.17: The improved C-wave image leads to changes in the geological model of the Alba field. On the left, the original model. On the right, the model with "wings" explains the missing sand along the channel axis and high sands at channel edges (from Hanson et al., 2003).

turbidite reservoir from the northern North Sea, which is typical for the Alba field. The diagram shows clearly the overlaying shale, thin "ratty" sand layers and the main sand body of the reservoir. I also found evidence for shale and sand interbedded structure from the well log data displayed in Figure 3.13. Wang (2001) published results from measurements on several hundred core samples estimating seismic velocities and anisotropy. He mainly investigated lithologies with shales, sands and carbonates. He found that essentially all shales are highly anisotropic while sands are intrinsically isotropic if they are not fractured. Shales are a source of polar anisotropy due to their laminar structure and preferential alignment of minerals. Anisotropy in shales ranges from 6% to 33 % for P-waves and 2% to 55% for S-waves. Fine layering is also a reason for occurrence of polar anisotropy. As I have shown that the overburden of the Alba field contains shale and thus is likely to be highly anisotropic (see Section 3.3). Hence, anisotropy cannot be ignored in processing the Alba data.

A second way to establish anisotropy in seismic data is the comparison of the vertical and stacking velocity ratios. In theory, in isotropic media they are identical. In an anisotropic media they differ due to the definition of stacking P- and S-wave velocities, $V_{p2}^2 = V_{p0}^2(1+2\delta)$ and $V_{s2}^2 = V_{s0}^2(1+2\sigma)$, including anisotropy parameters δ and σ. These equations indicate that in a VTI medium the stacking velocities are generally higher than the vertical velocities for positive δ and σ.

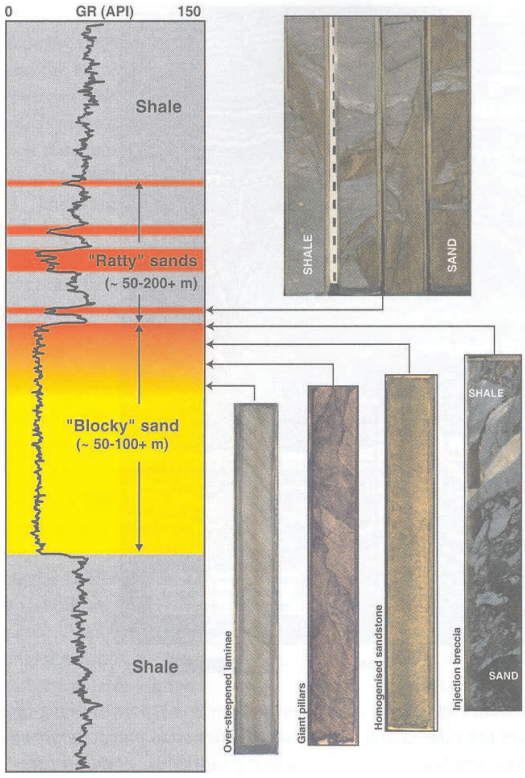

Figure 3.18: Diagram of a borehole section through a lower Paleogene turbidite reservoir from the northern North Sea (close to the Alba Field) from Huuse et al. (2003). The diagram shows gamma-ray (GR) log and lithology with core photographs. The diagram shows clearly the shale in the reservoir overburden.

In marine sediments often $\sigma > \delta$ (Wang, 2001) and both parameters are usually positive while the stacking velocity ratio $\gamma_2 = V_{p2}/V_{s2}$ is expected to be lower than the vertical ratio $\gamma_0 = V_{p0}/V_{s0}$.
Figure 3.19(a) shows the vertical velocity ratio γ_0 and Figure 3.19(b) the stacking velocity ratio γ_2 both with the C-wave arrival time on the vertical axis. The estimation of the velocity ratios is explained in more detail in Chapter 7. As expected, the stacking velocity ratio is generally smaller than the vertical velocity ratio. As an example of the difference between the ratios in the overburden of the reservoir (0 to about 3.8 seconds C-wave arrival time), at $t_{c0} = 2.3$ s we see $\gamma_0 = 3.183$ and $\gamma_2 = 2.47$ which corresponds to a difference of 29%. The difference between the two ratios is a good indicator of the presence of polar anisotropy.

The stacking S-wave velocity differs from its vertical counterpart due to the S-wave anisotropy parameter σ (see Equation 2.23). This parameter can be approximated

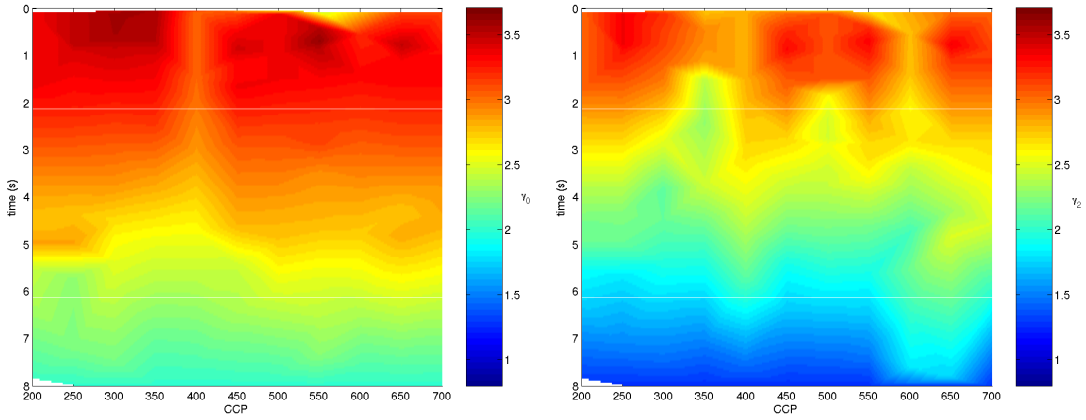

(a) γ_0 (b) γ_2

Figure 3.19: (a) Vertical velocity ratio γ_0 from Alba data. (b) Stacking velocity ratio γ_2 from Alba data. Both diagrams show C-wave arrival time. Comparing the velocity ratios shows differences which are an indication for polar anisotropy.

by the fractional difference between the vertical and effective velocity ratio (see Chapter 2 Equation 2.28)

$$\sigma \approx \frac{\gamma_0 - \gamma_{\text{eff}}}{2\gamma_{\text{eff}}}$$

which is strictly speaking only valid for a single horizontal layer when δ is reduced to zero. However, assuming that δ is usually very small for marine sediments and the Alba field has a mainly horizontally layered overburden this equation can be used to get a feel for the magnitude of anisotropy in the data. The approximated σ values range from 0.1 to 0.75. These values are too high to be neglected and indicate S-wave anisotropy. However, it has to be kept in mind that the value of σ represents processing anisotropy, e.g. fractional difference between the vertical and stacking velocity.

In summary, I found geological evidence of shale in the overburden and interbedded shale in sand in the reservoir layer of the Alba field. Shale is known to be highly anisotropic. Comparing vertical and stacking velocity ratios confirms the appearance of polar anisotropy. In order to get a feel for the magnitude of the anisotropy, I approximate the S-wave anisotropy parameter σ from the velocity ratios and find, that the anisotropy is too strong to be neglected. Finally, VSP

processing results allows the estimation the Thomsen's parameters ϵ and δ which confirm polar anisotropy. Thus, seismic anisotropy is present in the Alba field and the dominant type is VTI. The magnitude of anisotropy is significant and cannot be neglected during processing the Alba field data.

3.6 Conclusions

The purpose of my study is to investigate the feasibility of using 4C data for anisotropic parameter estimation. For this purpose the Alba data set is ideal for the following reasons:

- the data set consists of good quality moveout reflection data, VSP and well log data.
- the overburden of the Alba reservoir is a simple structure of mainly horizontal layers.
- it is evident that the overburden contains polar anisotropy.
- VSP and well log data offer a "ground truth" to verify the processing and inversion results.

Therefore, in this study I will use the Alba field data to investigate the sensitivity and accuracy of anisotropic parameter estimation of VTI media. I will also analyse and quantify the anisotropy in the Alba data and perform anisotropic imaging on the data which will hopefully lead to an improved imaging of the field structures. Using this benchmark data set I will show that the anisotropic data processing workflow for C-waves is sufficient to estimate meaningful anisotropic parameters χ and η for model building and Kirchhoff pre-stack time migration (PSTM).

Chapter 4

Feasibility study of moveout inversion for a single VTI layer

Assuming a single-layered medium with vertical transverse isotropy (VTI), as shown in Chapter 2, Figure 2.1, I investigate the possibility of inverting the VTI parameters from PP, PS and SS traveltimes by moveout inversion. The traveltime equations for a single VTI layer have been reviewed in Chapter 2. Alkhalifah and Tsvankin (1995) have shown that inversion of reflection traveltimes in VTI media can provide estimates of anisotropic parameter η for P-waves. The issue now is whether these estimates of anisotropy parameters are sufficiently accurate to constrain the VTI model when both P- and C-wave data are available. For this, I carry out a detailed analysis of the accuracy of non-hyperbolic moveout inversion. Firstly, I investigate the influence of varying anisotropy parameters and stacking velocities as well as the spread-length on the accuracy of moveout approximations for both P- and C-wave data. Secondly, I study the error of moveout inversion for a set of models consisting of a single VTI layer for both PP and PS wave types. Thirdly, I discuss analyses for the S-wave moveout of the same model. Fourthly, the findings are confirmed by performing the same analyses on a second set of models with a low S-wave velocity leading to small values of the anisotropy parameter η. Finally, I analyse the error propagation when estimated parameters are used to compute other related parameters.

4.1 Concept of joint moveout inversion

4.1.1 Problems arising

In exploration seismology P-wave data are acquired. For VTI media the P-wave propagation has to be expressed in terms of Thomsen's parameters ϵ and δ as described in Chapter 2 Equation (2.22) and (2.29):

$$\begin{aligned} V_{p2}^2 &= V_{p0}^2(1+2\delta), \\ \eta &= \frac{\epsilon-\delta}{1+2\delta}. \end{aligned}$$

The moveout velocity V_{p2} and anisotropy parameter η can be extracted from P-wave moveout data as demonstrated in Alkhalifah and Tsvankin (1995). However, all four Thomsen parameters V_{p0}, V_{s0}, ϵ and δ are needed to constrain the VTI model, which cannot be extracted from P-wave data alone. Thus it is necessary to use other data to gain these information. There are two other types of reflection data available in the industry: S-wave data and PS-converted data.

Let's look at S-wave data first. SV-wave propagation is strongly affected by anisotropy. Equations (2.23) and (2.24) are available:

$$\begin{aligned} V_{s2}^2 &= V_{s0}^2(1+2\sigma), \\ \sigma &= (\frac{V_{p0}}{V_{s0}})^2(\epsilon-\delta) = \gamma_0^2(\epsilon-\delta) = \gamma_0^2\eta(1+2\delta). \end{aligned}$$

Although SV-waves could be used to extract the remaining Thomsen's parameters, they have the disadvantage of possible bad data quality due to statics on land surveys, and moreover, they cannot be acquired in a marine setting.

How about PS converted or C-wave data? From C-wave data, one can at least recover the converted wave stacking velocities based on Equation (2.1). With the knowledge of P- and C-wave NMO velocities the S-wave NMO velocity can be calculated as follows my Equation (2.48) (Seriff and Sriram, 1991):

$$t_{c0}V_{c2}^2 = t_{p0}V_{p2}^2 + t_{s0}V_{s2}^2. \tag{4.1}$$

In principle all four unknown parameters $(V_{p0}, V_{s0}, \epsilon, \delta)$ can be calculated as follows:

$$t_{c0} = t_{p0} + t_{s0} \tag{4.2}$$

$$\frac{V_{p0}}{V_{s0}} = \frac{t_{s0}}{t_{p0}} = \gamma_0. \tag{4.3}$$

Using Equation (2.29) and inserting σ as defined in Equation (2.24), η can be expressed as

$$\eta = \frac{\epsilon - \delta}{1 + 2\delta} = \frac{\sigma}{\gamma_0^2} \frac{1}{1 + 2\delta}. \tag{4.4}$$

Recalling the relationship of the P- and S-wave stacking velocities, Equations (2.22) and (2.23), the stacking velocity ratio γ_2 can be rewritten as

$$\gamma_2 = \frac{V_{p0}}{V_{s0}} \frac{\sqrt{1 + 2\delta}}{\sqrt{1 + 2\sigma}}, \tag{4.5}$$

$$\text{which implies} \qquad \gamma_0 = \gamma_2 \frac{\sqrt{1 + 2\sigma}}{\sqrt{1 + 2\delta}}. \tag{4.6}$$

Finally, I substitute Equation (4.6) into Equation (4.4), η then satisfies

$$\eta \gamma_2^2 = \frac{\sigma}{1 + 2\sigma}. \tag{4.7}$$

Thus, knowing the P-wave anisotropy parameter η and the stacking velocity ratio γ_2 one can calculate the anisotropic parameter σ. Together with the S-wave stacking velocity V_{s2} (from Equation (4.1)), the vertical S-wave velocity V_{s0} can be calculated from Equation (2.23). Now, knowing V_{s0} and γ_0 the vertical P-wave velocity can be calculated according to Equation (4.3). Recalling the definition of the P-wave stacking velocity V_{p2}, Equation (2.22), one can now compute the anisotropy parameter δ from the known vertical and stacking P-wave velocity. Finally, using the obtained values for η and δ we are able to compute the missing Thomsen parameter ϵ with Equation (2.29).

However, is the inversion procedure described above stable? Picking errors from the input data get amplified to non-negligible size when inverted, for example, from P-wave anisotropy parameter η into Thomsen parameters ϵ and δ. I illus-

trate this with an example. Equation (2.24) shows that the square of the vertical velocity ratio, $(V_{p0}/V_{s0})^2$, acts as a multiplier of the error from ϵ and δ when calculating σ. For instance, if $(\epsilon - \delta)$ has a small error of $\Delta = 0.03$ and the vertical velocity ratio is $\gamma_0 = 2.5$ as found in the model in Table 4.1, the error in σ is as large as 0.188. The propagation of this error into the computation of V_{s0} and subsequently V_{p0} can lead to a distortion of 19% from the model velocity value.

In order to keep the errors as small as possible one needs to find the most accurate way to estimate the anisotropy parameters. In summary, acquiring η from P-wave data is not ideal due to the insensitivity towards anisotropy and the large error margins. Obtaining this parameter from S-waves is problematic, as cusps can occur, and the data is expensive to acquire and may have a bad signal-to-noise ratio. Thus, the question is, is it possible to get a better constraint on η from converted waves?

4.1.2 Elements of the C-wave moveout

The C-wave raypath consists of a P-wave and a S-wave leg, and thus the C-wave moveout is a combination of P- and SV-wave moveout. One intriguing question to be asked is, what is the relevant contribution of P- and S-moveout on the C-wave moveout signature? Is the C-wave moveout dominated by P- or by S-wave or a simple combination of both? I will discuss this issue here with its important implications for parameter estimation.

In Chapter 2, Figure 2.1 illustrates a reflection from a P-wave and a P-SV conversion at the reflection point. In order to find out about the ratio between P- and S-wave legs I calculate the conversion point x_c with Equation (2.40). Figure 4.1 illustrates the result for a basic single VTI layer of 1 km depth (for model properties see Table 4.1). The properties used consists of some typical VTI values. For comparison, the width of the S-wave leg is plotted in the same diagram (dash-dotted line) as calculated from $(x - x_c)$ and the midpoint $(x/2)$ or reflection point from a P-wave (dashed line). Up to an offset-to-depth ratio of 1 there is not a large difference between midpoint and conversion point. However, up to a ratio of 2 this changes rapidly such that the S-wave leg (and its associate part

of the offset) does not increase anymore for larger offsets ($x/z > 2$). I find this confirmed in Figure 4.1(b) showing the S-wave group angle $\Theta_s = \arctan(x_s/z)$ displayed against offset with a constant angle of 35°-37° after 2 km offset. The meaning of this is that the P-wave part of the C-wave is constantly increasing with increasing offset. Thus, for the same offset a C-wave has a larger incident P-wave leg (i.e. corresponding offset) than a pure P-wave reflection. Hence, this simple analysis shows that long-offset C-wave moveout is more influenced by the anisotropy parameter η.

How about the near-offset moveout? In order to do this I examine the difference between the traveltime curves of this model in isotropy and anisotropy in Figure 4.2 and compare these differences for different wave types. The isotropic traveltimes are displayed as dashed lines while the anisotropic times are solid. As expected, the P-wave times show only a clear difference after an offset of about 2000 metres (i.e. $x/z = 2$) while the S-wave shows a difference from an offset of 500 metres but also has a cusp at about 1700 metres. The C-wave difference is strong after an offset of about 1000 metres. Hence, the C-wave represents a good compromise between the extremes of the diverging S-wave and the P-wave which is only affected in the long offset. In Figure 4.3 I concentrate on the C-wave and plot again the isotropic and anisotropic traveltime curves. I also add for comparison a hyperbolic curve using the C-wave velocity.
Because the C-wave consists of a P- and a S-wave part, the moveout is inherently non-hyperbolic. However, for an offset-to-depth ratio of $x/z = 1$ the conversion point between the wave types is almost identical with the midpoint in these models. Hence, it is clear that the non-hyperbolic moveout due to the asymmetric raypath is very small within the first 1000 metres. However, in this figure the moveout still differs strongly from the hyperbolic shape within the first 500 metres. Thus, this difference should be mainly caused by anisotropy. This must therefore be due to the fact that S-waves are more strongly affected by anisotropy than P-waves. In summary, for the C-wave case I find

- for offsets larger than $x/z = 1$ the P-wave incident leg is larger than in pure mode P-wave data.

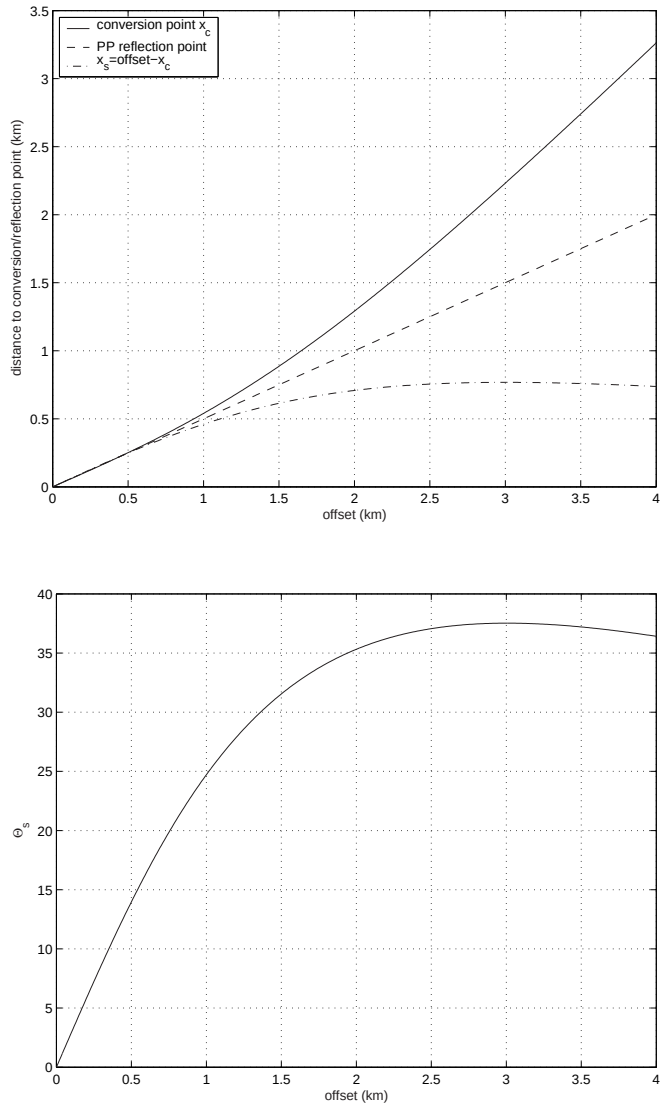

Figure 4.1: (a) In a single VTI layer the conversion point x_c for C-wave and the reflection point for P-wave diverge with increasing offset. x_c also gives the width of the offset related to the P-wave leg of the C-wave. The offset minus conversion point gives the offset corresponding to the S-wave leg x_s. (b) S-wave reflection angle from the C-wave against offset.

- from near-offset observations, $x/z < 1$, it is found that the non-hyperbolic moveout is due to the S-wave leg and has increased sensitivity to anisotropy.

Therefore, in theory C-wave data is the best option for estimating anisotropy parameters. This forms the basic idea of my thesis where I propose to use C-wave data to estimate anisotropy parameters.

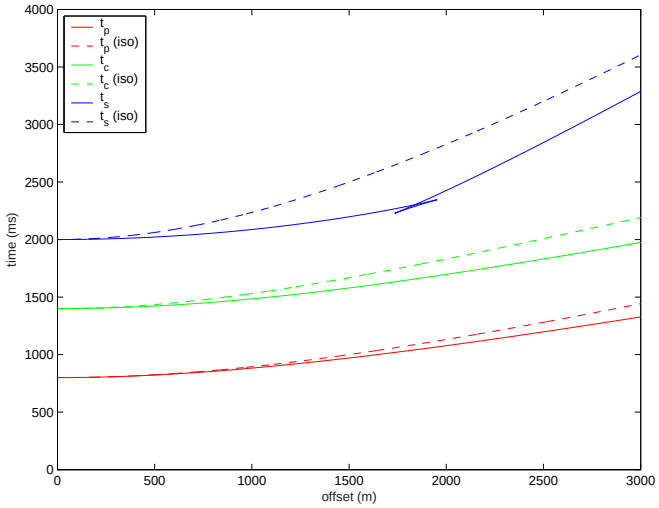

Figure 4.2: Isotropic and anisotropic calculated traveltimes for P-, S- and C-waves for the reference model.

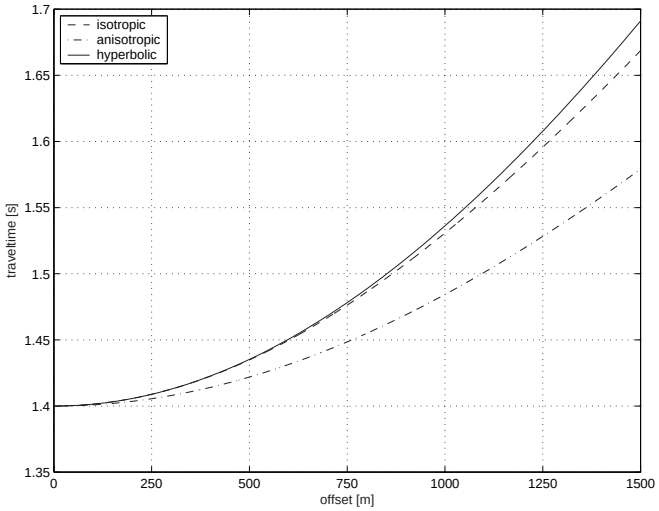

Figure 4.3: Traveltime curves for the C-wave in isotropic (dashed) and anisotropic (dash-dot) media compared to a hyperbolic moveout (solid). For the calculation of the hyperbolic curve the relation $V_{c2}^2 = V_{p2}V_{s2}$ was used. Traveltime curves are displayed for offsets up to 1.5 km.

4.1.3 Estimating η from C-waves

As discussed in Chapter 2, the effects of anisotropy on C-wave is described by the anisotropic parameter χ. The purpose of C-wave moveout inversion is to invert χ from the moveout data, then convert χ into η. Note, Equation (2.33), $\eta = \chi/(\gamma_{\text{eff}}^2(\gamma_0 - 1))$, shows this relation. Errors will not be amplified as long as $\gamma_{\text{eff}}^2(\gamma_0 - 1) > 1$, i.e. the process of calculating η from χ is a stable process. From the above, one can see that C-waves seem more suitable for anisotropic parameter estimation then either P- or S-waves. However, in practice, can we estimate a better η from C-waves and the C-wave anisotropy parameter χ? This is one of the issues that will be addressed in this chapter. Another issue is, how well can actual changes in η be resolved by moveout data? In the following, I will perform numerical analysis to explore these questions.

4.2 Analysis of resolution and the inherited errors in moveout inversion in VTI media

In this section, I will discuss the issue of resolution, e.g. how well can actual changes in η be resolved by moveout inversion. This will lead to an investigation about usable offsets for moveout inversion and introduction of the inherited error, which is a measure for the power of resolution between different models.

4.2.1 η resolution

Table 4.1 lists the properties of the reference model I used in this study including the Thomsen parameters ϵ, δ, the combination σ, the P-wave anisotropy parameter η, C-wave parameter χ, the S-wave parameter ζ and the vertical and stacking velocities (Grechka and Tsvankin (2002a) used similar values). In order to investigate the effect of small variations in the anisotropy parameters η and χ the model values have been perturbed, but the vertical traveltimes kept constant as well as the stacking S-wave velocity. Therefore, the change in moveout is minimal. Although the anisotropy parameters vary only slightly the change in depth cannot be neglected. Table 4.2 lists the model depth, the vertical velocities and anisotropy parameters of the 6 model variations while Table B.1 in Appendix

B lists the stacking velocities. The quantities $\Delta\eta_{\text{eff}}$ and $\Delta\chi_{\text{eff}}$ are the differences between the reference model parameter and its variation. These values give a feel for the extent of anisotropy in each model. For model variations V1-V4 they are small, in the range ± 0.02. However, for models V5 and V6 they are more significant, up to ± 0.04.

V_{p0}	V_{s0}	ϵ	δ	σ	η	χ	t_{p0}
2.5 km/s	1. km/s	0.2	0.05	0.938	0.136	0.187	0.8 s
t_{c0}	t_{s0}	V_{p2}	V_{c2}	V_{s2}	γ_0	γ_{eff}	ζ
1.4s	2 s	2.622 km/s	2.004 km/s	1.696 km/s	2.5	0.957	0.125

Table 4.1: Properties of reference model for feasibility study including C-wave parameters. Grechka and Tsvankin (2002a) used similar values.

Model	depth	V_{p0}	V_{s0}	ϵ	δ	η_{eff}	$\Delta\eta_{\text{eff}}$	χ_{eff}	$\Delta\chi_{\text{eff}}$
exact	1.	2.5	1.0	0.2	0.05	0.136	-	0.187	-
V1	1.115	2.787	1.115	0.057	-0.049	0.118	-0.018	0.166	-0.021
V2	1.058	2.646	1.058	0.121	-0.004	0.126	-0.01	0.177	-0.01
V3	0.939	2.349	0.939	0.298	0.117	0.147	0.011	0.197	0.01
V4	0.876	2.19	0.876	0.421	0.202	0.156	0.02	0.206	0.019
V5	0.711	1.778	0.711	0.939	0.565	0.176	-0.04	0.232	-0.044
V6	1.171	2.927	1.171	0.0024	-0.085	0.106	0.03	0.155	0.032

Table 4.2: In order to study small variations in η and χ between different models, although the change in moveout between these models is very small (see Figure 4.4), the anisotropic parameters and stacking P-wave velocity (V_{p2}) of the reference model (Table 4.1) were altered slightly. $\Delta\eta_{\text{eff}}$ and $\Delta\chi_{\text{eff}}$ are the differences between the reference anisotropy parameters and the value from the model variations. Velocities are in km/s and depth in km. For variations in stacking velocities, effective velocity ratios and σ, see Table B.1 in appendix B.

For all models the traveltimes have been calculated with an anisotropic ray tracing algorithm which supplies kinematic properties only. The ray tracer also generated synthetic seismograms. The P-wave seismogram is displayed in Figure 4.12(a), the C-wave in Figure 4.14(a) and the S-wave in Figure 4.20(a). The small differences between the actual moveout times of the models are illustrated in Figure 4.4(a) for the P-wave and in Figure 4.4(b) for the C-wave in milliseconds against an offset of 3 km. It can be seen that the traveltime error hardly exceeds 1 milliseconds for P-waves and 1.5 milliseconds for C-waves for models V1-V4. The traveltime differences for model V6 increases for both wave types up to 2 milliseconds (light-

blue curves). For these 5 models the maximum traveltime difference actually occurs at an offset of about 1.5-2 km and decreases again after that. The largest differences are found for model V5 (pink curves). The traveltime differences here continuously increase with offset. Therefore one can conclude that it is not possible to resolve models with η differences of $\eta = \pm 0.02$ from either P- or C-wave moveout. Moveout inversion can only resolve η models with differences of $\eta = \pm 0.03$ or above.

4.2.2 Usable offset ranges

Restricting the traveltime difference to 4 milliseconds, the usual sampling rate in seismic processing, a maximum offset is found for P-waves of 2.25 km and for C-waves of 2.65 km. Alternatively, traveltimes are calculated using traveltime approximations as introduced in Chapter 2. Figure 4.5(a) displays P-wave traveltimes computed by ray tracer (solid line) and calculated using traveltime approximation, Equation (2.57) (dashed line). After an offset of about 1500 metres a small difference in traveltimes is noticeable. This difference is plotted against the offset-to-depth (x/z) ratio in Figure 4.5(b). Again the maximum acceptable difference between approximated and exact traveltimes is 4 ms. For this model the approximation works well for up to $x/z \approx 2.5$. Figure 4.6 shows the exact C-wave traveltime and the approximation after Equation (2.62) and the difference between them. Again, a $x/z \approx 2.5$ is acceptable for the use of the approximation for this model. The S-wave traveltime curve is displayed in Figure 4.7(a). At an offset of about 1.7 km it shows a cusp which is due to anisotropy (Tsvankin and Thomsen (1994), Helbig (1966)). We calculate the traveltimes up to the cusp since Equation (2.72) cannot account for the cusp. Hence, the inversion based on the traveltime approximation cannot handle the cusp and so the offset is due to this effect already restricted to $\sim$ 1.7 km. Figure 4.7(b) confirms this and the difference between exact and approximated traveltimes indicates the maximum usable offset of 1.6 km. This result suggests that S-wave moveout inversion can be problematic since cusps may occur. Therefore, S-waves are discussed separately in Section 4.6.

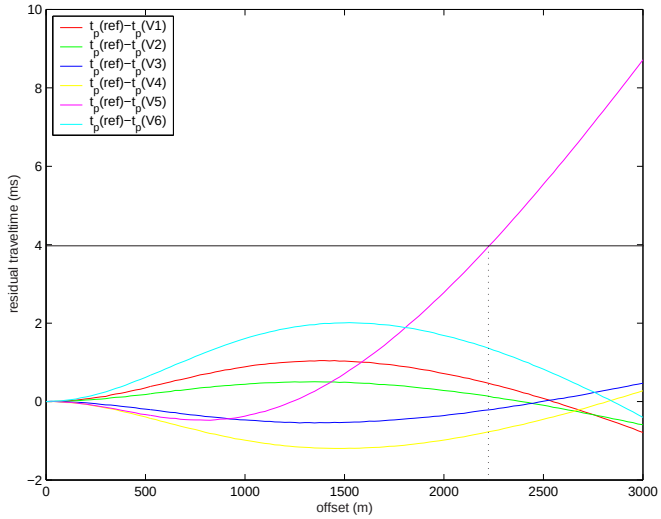

(a) P-wave

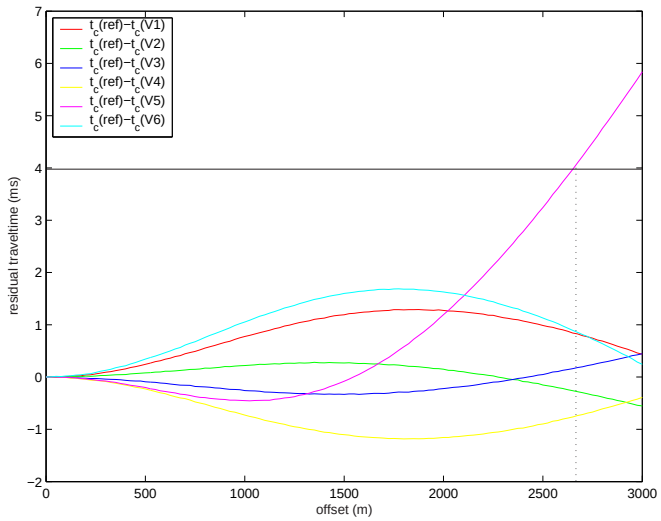

(b) C-wave

Figure 4.4: Traveltime differences between reference model and the 6 erroneous model variations for (a) P-wave and (b) C-wave against offset. Traveltimes have been calculated by ray tracing. Using a $\Delta t = 4$ milliseconds as maximum time difference the corresponding x/z ratio is for P-waves 2.25 and for C-waves 2.65.

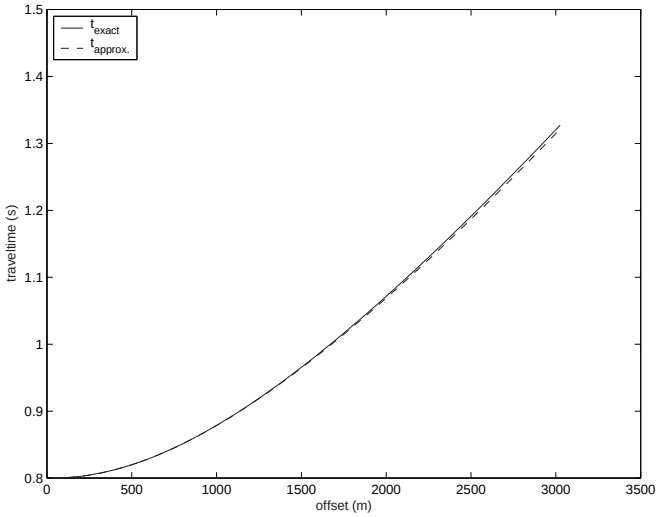

(a)

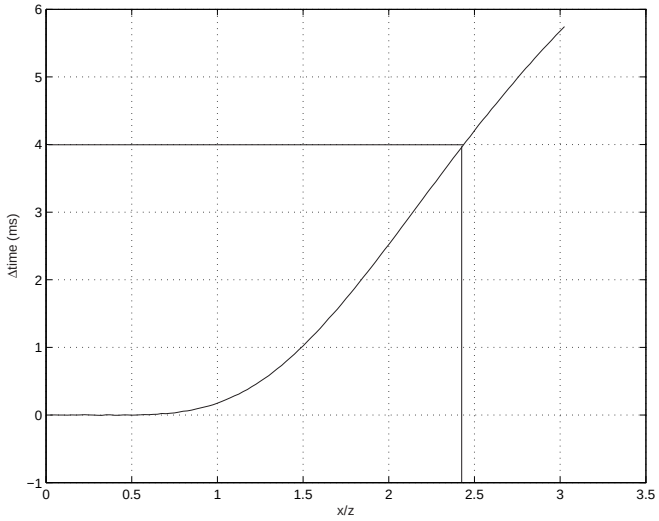

(b)

Figure 4.5: (a) P-wave traveltime curves for the reference model computed by ray tracing (solid) and approximated using Equation (2.57) (dashed). (b) The traveltime difference between exact and approximated traveltimes against x/z ratio. The maximum acceptable traveltime difference of 4 ms indicates the corresponding maximum x/z ratio for this approximation.

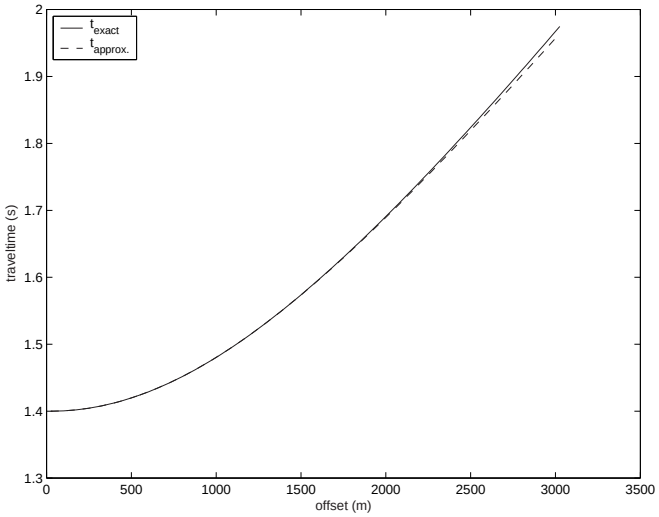

(a)

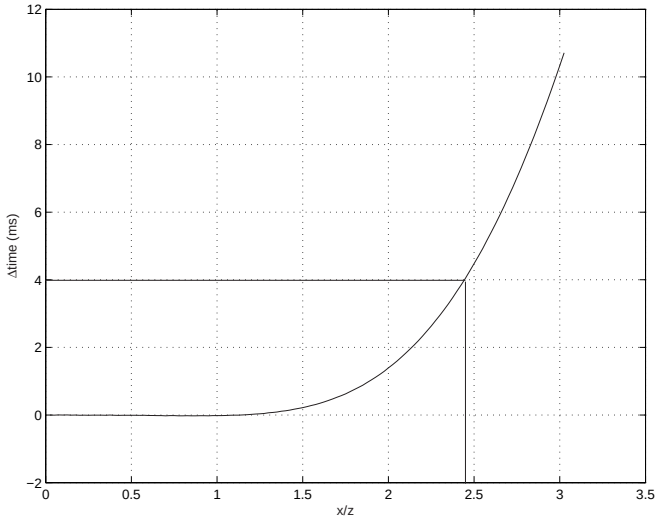

(b)

Figure 4.6: (a) C-wave traveltime curves for the reference model calculated by ray tracing (solid) and approximated with Equation (2.62) (dashed). (b) The traveltime difference between exact and approximated traveltimes against x/z ratio. The maximum acceptable traveltime difference of 4 ms indicates the corresponding maximum x/z ratio for this approximation.

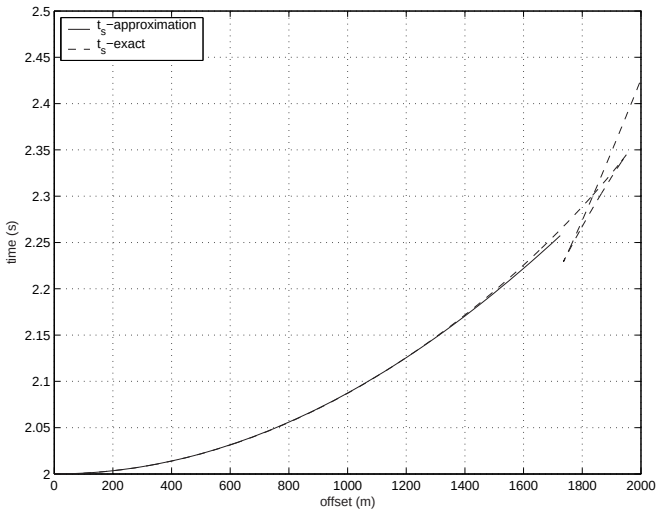

(a)

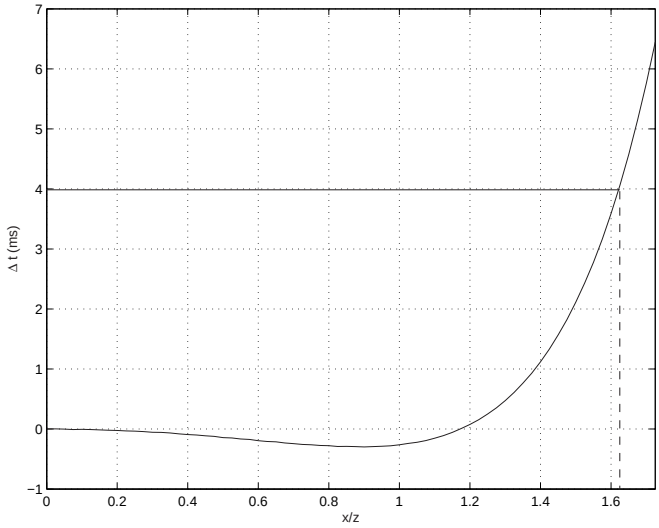

(b)

Figure 4.7: (a) S-wave traveltime curves for the reference model computed by ray tracing (solid) and approximated with Equation (2.72) (dashed). (b) The time difference between exact and approximated traveltimes over x/z ratio. The maximum acceptable traveltime difference of 4 ms indicates the corresponding maximum x/z ratio for this approximation.

4.2.3 Inherited errors

A numerical test was performed to understand the inherited error by examining the influence of the NMO velocity V_{p2}/V_{c2} and the horizontal P-wave velocity V_{ph} or the anisotropy parameter η/χ on the P-/C-wave moveout, respectively. The analysis is based on the method for P-waves described in Grechka and Tsvankin (1998). The long-spread P-wave moveout can be approximated as shown in Chapter 2, Equation (2.57). It can be rewritten as a function of the horizontal velocity V_{ph} instead of the anisotropy parameter by inserting Equation (2.56) in (2.57):

$$t_{p2}^2 = t_0^2 + \frac{x^2}{V_{p2}^2} - \frac{(V_{ph}^2 - V_{p2}^2)x^4}{V_{p2}^2(t_0^2 V_{p2}^4 + V_{ph}^2 x^2)}. \tag{4.8}$$

Then the exact traveltime of the reference model and its variations are computed by ray tracing and approximated by the traveltime equations introduced in Chapter 2. The maximum traveltime difference $\Delta t_{\max}$ between exact and approximated traveltimes from all differences over an offset range of 0 to 2 km is plotted for varying V_{ph}/η, V_{ph}/χ and V_{p2}/χ respectively. The contour lines illustrate the maximum traveltime differences $\Delta t_{\max}$ in milliseconds. The minimum ellipse is $\Delta t_{\max} = 2$ms and the model value is indicated by a black dot.

P-wave moveout

The P-wave traveltimes are calculated using the approximation in Equation (4.8) to see the influence of V_{ph} and V_{p2}. The resulting plot of maximum difference between exact and approximated traveltimes over on offset of 0-2 km is shown in Figure 4.8(a). Using the anisotropy parameter η instead of the horizontal velocity the traveltimes are calculated by Equation (2.57). Figure 4.8(b) shows the resulting $\Delta t_{\max}$. The contours of $\Delta t_{\max}$ form a narrow valley in both set of coordinates of $\Delta t_{\max}(V_{ph}, V_{p2})$ and $\Delta t_{\max}(\eta, V_{p2})$. The ellipses lie at an angle of about 45° in the coordinate system. This positioning indicates that the stacking velocity V_{p2} and the horizontal velocity V_{ph} or parameter η are not independent of each other. For example if the value for the stacking velocity is picked with a small error, this will lead to a larger error for the anisotropy parameter/horizontal velocity. Hence, this coupled situation between the parameters makes precise parameter estimation more difficult.

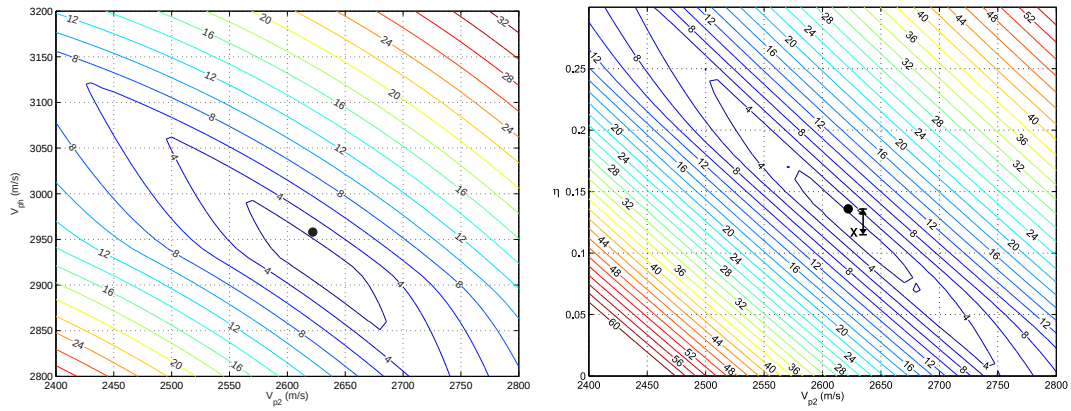

(a) $V_{ph} - V_{p2}$ (b) $\eta - V_{p2}$

Figure 4.8: The influence of (a) V_{ph} and V_{p2} and (b) η and V_{p2} on the traveltime moveout from a single horizontal VTI layer. Contours display the maximum traveltime difference in milliseconds between exact and approximated traveltimes $\Delta t_{\max}$ over an offset of 0-2000 metres. The black dot indicates the model values for the couples of V_{ph}, V_{p2} and η, V_{p2} from the reference model, respectively. The distance between the model value and the centre of the ellipse is called the inherited error ($\Delta_{\text{inh}}\eta$) and is indicated by the solid line between dot and "x" in (b).

Within each ellipse the traveltimes remain almost independent of the moveout parameters. This illustrates the range of kinematic equivalent models (km) for a certain combination of horizontal velocities or anisotropy parameters and stacking velocities. Figure 4.8(a) has a smaller long axis of the ellipse than Figure 4.8(b). This means, the uncertainty using the approximation with the anisotropy parameter η is larger than using V_{ph}. This behaviour can be explained because η can be expressed by the velocity ratio V_{ph}/V_{p2} (see Equation (2.56)). For this model, the kinematic equivalent model with a $\Delta_{\text{km}} t_{\max} = 2$ ms has a range of $\Delta_{\text{km}} V_{p2} = 100$ m/s, $\Delta_{\text{km}} V_{ph} = 150$ m/s and $\Delta_{\text{km}}\eta = 0.1$.

The exact model values are in both cases shifted from the centre of the ellipses. However, they are still within 3 ms for the (V_{ph}, V_{p2}) and 4 ms in the (η, V_{p2}) coordinates. This shift might be due to small deviations of the moveout from the ray tracing algorithm compared to the exact model values. For the same reason the minimum value of $\Delta t_{\max}$ is not zero. The shift, i.e. difference between the centre of the ellipse and the model value, is called the inherited error $\Delta_{\text{inh}}\eta$. For the P-wave of the reference model the $\Delta_{\text{inh}}\eta$ is displayed in Figure 4.8(b) and

has the value 0.02, i.e. $\eta = 0.14 \pm 0.02$. I have repeated this analysis for all 6 model variations. Because our interest lies in using the traveltime equation as a function of η for parameter estimation I concentrate on its influence on the moveout. The resulting plots of the maximum traveltime difference $\Delta t_{\max}$ are in Appendix B, Figure B.1(a)-(f). The estimated inherited errors of all models are listed in Table 4.3. I find that, regardless of magnitude of the anisotropy parameter, the inherited error stays in the same range. For P-waves this range is $\Delta_{\text{inh}}\eta = 0.02$. This agrees with the resolution analysis in Section 4.2.1.

C-wave moveout

Next, this analysis has been applied to C-waves calculated from the reference model. For the traveltime approximation Equation (2.62) was used. One can express χ with η and V_{ph} (using Equations (2.32) and (2.56)) as

$$\chi = (\gamma_0 - 1)\gamma_{\text{eff}}^2 \frac{1}{2}\left(\frac{V_{ph}^2}{V_{p2}^2} - 1\right). \tag{4.9}$$

Inserting this equation in the traveltime Equation (2.62) the traveltime can be calculated as a function of V_{c2} and V_{ph}. The maximum traveltime error $\Delta t_{\max}$ over an offset of 2 km is displayed in Figure 4.9(a) for V_{ph} against V_{c2} and Figure 4.9(b) for χ and V_{c2}. The ellipses in both cases are narrower and longer than the ones for the P-wave. The are aligned almost vertically in the coordinate system which means that the stacking velocity V_{c2} is almost completely decoupled from the horizontal velocity V_{ph} or the anisotropy parameter χ. In terms of parameter estimation this is a desired effect as it implies that the stacking velocity can be picked very exactly even if the anisotropy parameter is erroneous.
The minima (2 ms contour) in both cases have a range of equivalent models for $\Delta_{\text{km}}V_{c2} \approx 50$ m/s which is half of the range from $\Delta_{\text{km}}V_{p2}$. However, the range for $\Delta_{\text{km}}V_{ph}$ is 300 m/s and $\Delta_{\text{km}}\chi = 0.15$. This means that converted waves have a very restricted range of kinematic equivalent models of stacking velocities but both, horizontal velocity or corresponding anisotropy parameter appears to be less well defined. The centre of the minimum valley is again shifted relative to the model values (black dot) and not equal to zero. The inherited error for the reference model is $\Delta_{\text{inh}}\chi = 0.04$, i.e. $\chi = 0.19 \pm 0.04$ and about twice the P-wave

error. For both wave types, the anisotropy parameter varies quite strongly within the family of equivalent models. From $\eta = \frac{\chi}{\gamma_{\text{eff}}^2(\gamma_0 - 1)}$ (Equation 2.33) the error in χ of $\Delta_{\text{inh}}\chi = 0.04$ confirms roughly the equivalent value of $\Delta_{\text{inh}}\eta = 0.02$.
Verifying this result I computed the $\Delta t_{\max}$ for the influence of χ and V_{c2} for the 6 variations of the reference model. The results are displayed in Figure B.2(a)-(f) in Appendix B. The inherited errors are summarised in Table 4.3. As with the P-wave analysis, I find again that the inherited error is independent of the magnitude of the anisotropy parameter and has a value of $\Delta_{\text{inh}}\chi = 0.04$. This means that both P- and C-waves have the same power to resolve the parameters.

This indicates that for both wave types the analytical approximations (Equation (2.57) for the P-wave and Equation (2.62) for the C-wave) are sufficiently accurate for the purpose of the moveout inversion. Furthermore, I suggest that the inherited error gives an indication to what extent moveout inversion can differentiate between different anisotropic models. In the case of the reference model and its variations this means that the differences Δ_η and Δ_χ from Table 4.2 have to be larger than $\Delta_{\text{inh}}\eta = 0.02$ and $\Delta_{\text{inh}}\chi = 0.04$ respectively. For both wave types this is true for models V1-V4, i.e. it cannot be expected to get a good differentiation between the different models. However, model V5 and V6 satisfy the criterion and thus can be used to find out if moveout inversion can differentiate between these models.

model	reference	V1	V2	V3	V4	V5	V6
$\Delta_{\text{inh}}\eta$	0.02	0.02	0.02	0.02	0.02	0.03	0.01
$\Delta_{\text{inh}}\chi$	0.04	0.04	0.03	0.04	0.04	0.04	0.03

Table 4.3: Table of the inherited errors $\Delta_{\text{inh}}\eta$ and $\Delta_{\text{inh}}\chi$ for the reference model and its variations. The diagrams are displayed in Appendix B.

4.3 Influence of spread-length

According to Figure 4.5(b) the usable spread-length for inversion using the traveltime approximation Equation (2.57) for P-waves is valid up to an x/z ratio of 2.5. Similarly, Figure 4.6(b) also suggests that Equation (2.62) for C-waves is valid up to an $x/z = 2.5$ for inversion purposes in a single layer. With a layer

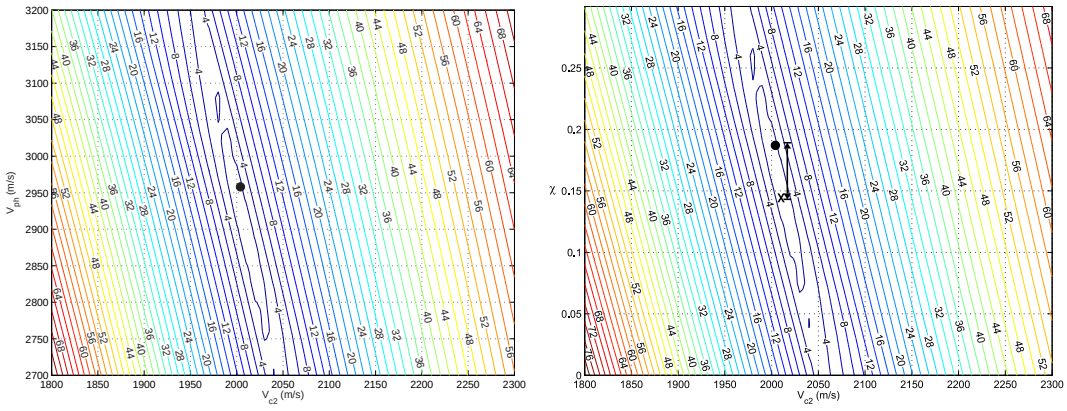

(a) $V_{ph} - V_{c2}$ (b) $\chi - V_{c2}$

Figure 4.9: The influence of (a) V_{ph} and V_{c2} and (b) χ and V_{c2} on the traveltime moveout from a horizontal VTI layer. Contours display the maximum traveltime difference $\Delta t_{\max}$ in milliseconds between exact and approximated traveltimes over an offset of 0-2000 metres. The black dot indicates the model values of V_{ph}, V_{c2} and χ, V_{c2} from the reference model, respectively. The distance between the model value and the centre of the ellipse is called the inherited error ($\Delta_{\text{inh}}\chi$) and is indicated by the solid line between dot and "x" in (b).

depth of 1000 metres this translates to an offset of 2500 metres. However, note that the study in Section 4.2 was carried out using a range of offsets of 0-2km to investigate the influence of varying anisotropy parameters and stacking velocities. In this section, I want to investigate the influence of different spread-length on this analysis varying the included offset length between 1 and 2.5 km. Again, the reference model with a depth of 1km has been used for the traveltime calculations.

4.3.1 P-waves

I have chosen four different spread lengths in addition to the previously shown $x/z = 2.0$: $x/z = 1.0$, $x/z = 1.5$, for $x/z = 2.3$ and $x/z = 2.5$. Figure 4.10 displays the results from the analysis of $\Delta t_{\max}$ for P-waves: Figure 4.10(a) displays the result for $x/z = 1.$, (b) for $x/z = 1.5$, (c) for $x/z = 2.3$ and (d) for $x/z = 2.5$. Figure 4.10 shows, that the ellipses of $\Delta t_{\max}$ become tighter and smaller with larger offsets. This can be explained by the fact that the anisotropy changes the moveout from the hyperbolic shape in the far offset for P-waves. It is also obvious, that with increasing offset the model value does not fall into the ellipse

of $\Delta t_{\max} = 2$ ms but still holds within 4ms for both, $x/z = 2.3$ and $x/z = 2.5$. However, as already mentioned, a time difference of 4 milliseconds is still good enough so the traveltime approximation can be used for inversion and an offset-to-depth ratio of $x/z = 2.5$ will be used for further studies. Nevertheless, this trend indicates that there is a trade off between accuracy of the minimum position and how well it is constrained by larger spread-length.

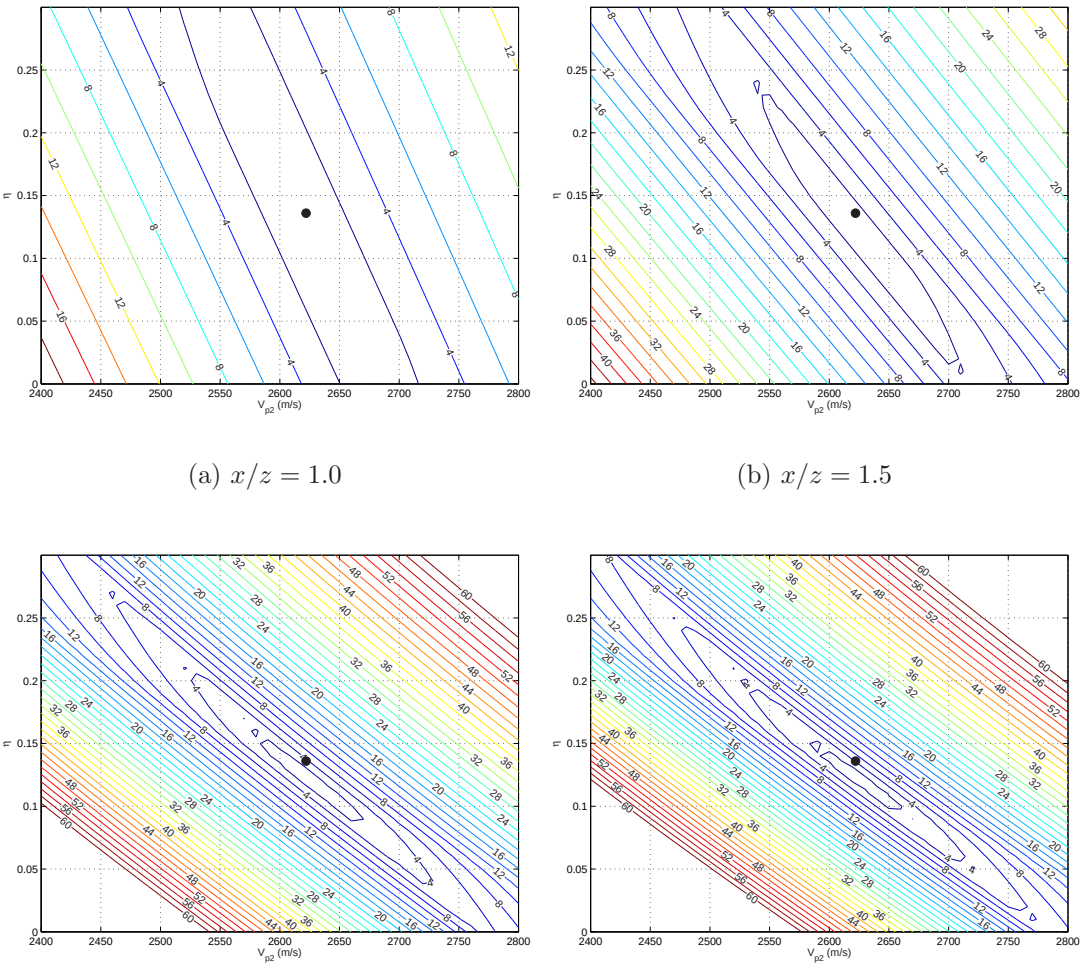

(a) $x/z = 1.0$ (b) $x/z = 1.5$

(c) $x/z = 2.3$ (d) $x/z = 2.5$

Figure 4.10: The influence of spread-length on the traveltime moveout shown for 4 different x/z ratios: (a) $x/z = 1.0$, (b) $x/z = 1.5$, (c) $x/z = 2.3$ and (d) $x/z = 2.5$. All plots show the maximum difference between accurate and approximated traveltimes $\Delta t_{\max}$ for varying η, V_{p2} for the reference model. The black dots indicate the model values.

4.3.2 C-waves

Figure 4.11 displays the results from the analysis of $\Delta t_{\max}$ for C-waves for different x/z ratios: Figure 4.11(a) is for $x/z = 1.0$, (b) for $x/z = 1.5$, (c) for $x/z = 2.3$ and (d) for $x/z = 2.5$. The influence of anisotropy on the moveout becomes more important with larger offset resulting in a stronger deviation from the hyperbolic shape of the traveltime curve. Therefore, an increase in resolution is expected from the inclusion of larger offsets in the analysis. Figure 4.11 confirms this expectation. The ellipses of $\Delta t_{\max}$ become tighter and smaller. In particular the anisotropy parameter χ becomes better constrained with increasing offset-to-depth ratio. However, it should be noted that for a $x/z = 2.5$ the minimum of the traveltime differences is not unique anymore and lies in the ellipse of $\Delta t_{\max} = 6$ ms. This series of 5 different offset-depth ratios shows that including a wider offset will lead to a better defined minimum of traveltime differences but at the same time the model value moves further away from the minimum ellipse. Again, this means that there is a trade-off between the exactness of the position of the minimum and how well it is constrained. As a consequence, an offset-to-depth ratio of $x/z = 2.$ has been used for further analyses.

Comparing Figure 4.10 and Figure 4.11 shows that for the same spread length the ellipses are tighter and steeper for C-waves than for P-waves. This means that C-waves are more sensitive and its parameters more decoupled. This confirms that C-waves are better suited for parameter estimation as discussed in Section 4.1.

4.4 Influence of small perturbations on accuracy and resolution of semblance analysis

So far, I have analysed the sensitivity and accuracy of moveout characteristics only. Now, I want to discuss the actual processing use. The common method in moveout inversion is semblance analysis. The anisotropic parameter and NMO velocity of a wave type can be found by a double semblance analysis incorporating Equation (2.57) for P-waves in VTI media. For C-waves the Equation (2.62) is

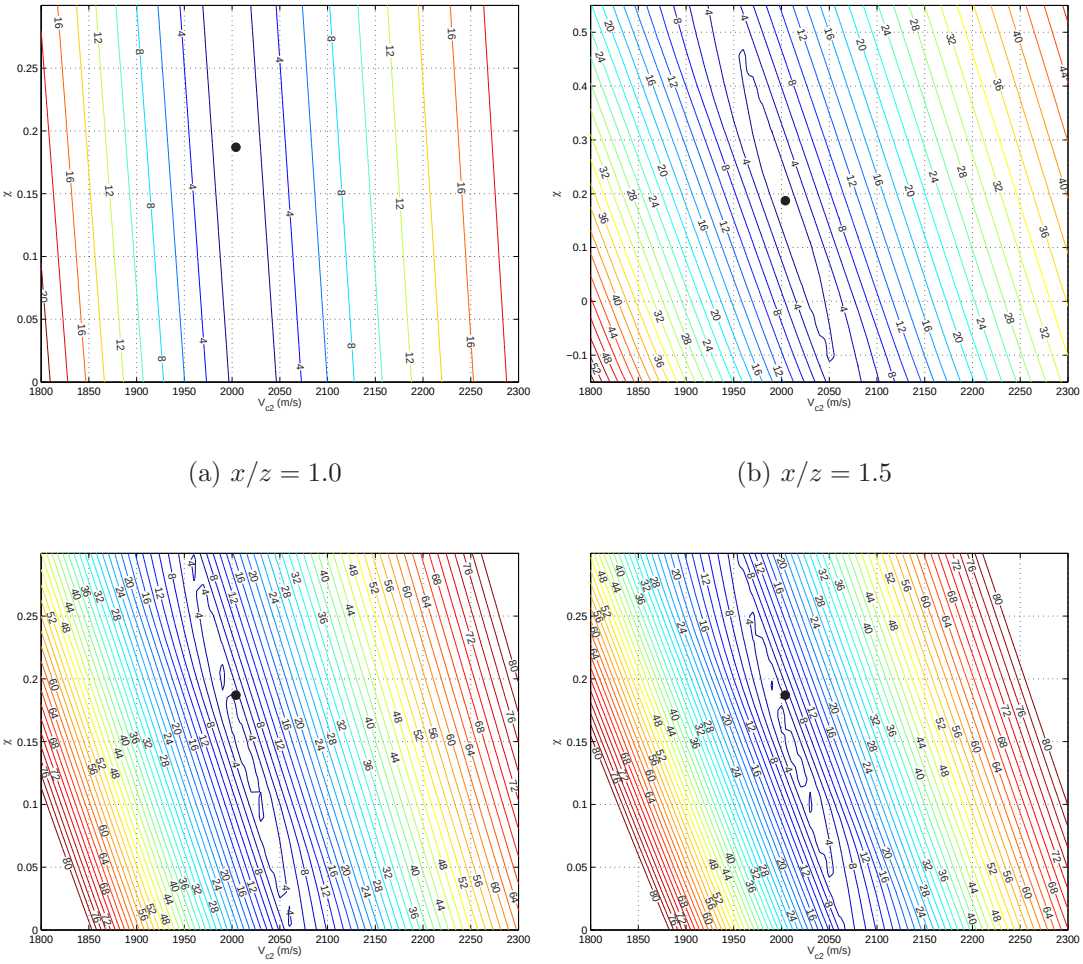

(a) $x/z = 1.0$ (b) $x/z = 1.5$

(c) $x/z = 2.3$ (d) $x/z = 2.5$

Figure 4.11: The influence of spread-length on the traveltime moveout shown for 4 different x/z ratios: (a) $x/z = 1.0$, (b) $x/z = 1.5$, (c) $x/z = 2.3$ and (d) $x/z = 2.5$. All plots show the maximum difference between accurate and approximated traveltimes Δt_{max} for varying χ, V_{c2} for the reference model. The black dots indicate the model values.

used to estimate χ and V_{c2}. I give detailed analyses of the accuracy and resolution of the semblance analysis for both wave types.

4.4.1 P-wave

For the P-wave the corresponding moveout inversion is displayed in Figure 4.12: (a) shows the P-wave seismogram from the reference model and (b) the result from double scanning semblance analysis for moveout inversion. The cross marks the model value for the model parameters. According to the previous analysis an offset-depth ratio of 2.5 has been used. The anisotropy parameter has been estimated with an absolute picking error of $\eta_{\text{ref}} = 0.136 \pm 0.016$. The velocity pick is almost exact with $V_{p2} = 2.622 \pm 0.002$km/s. I also applied the moveout

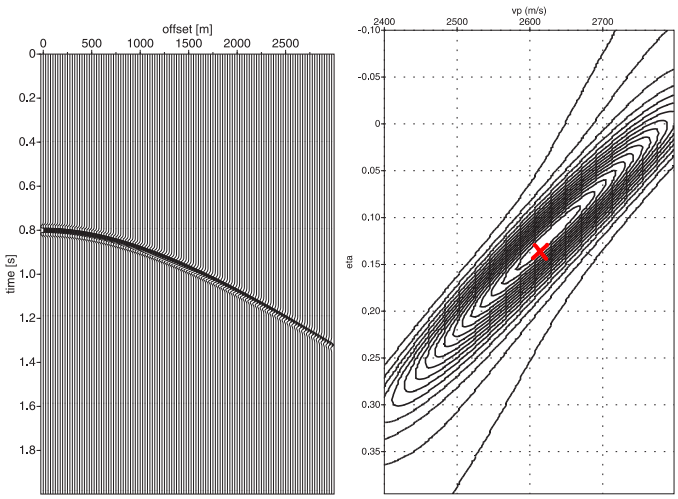

(a) P-wave (b) inversion

Figure 4.12: (a) Synthetic seismogram of the P-wave reflection on the bottom of a single VTI layer. (b) Semblance contours from inversion to estimate the parameters η and V_{p2} from the P-wave for a $x/z = 2.5$. The crosses mark the model values.

inversion to the 6 variations of the reference model. The double scanning results are displayed in Figure 4.13 and the picking results and corresponding errors are listed in Table 4.4 while the picked velocities are listed in Table B.2 in Appendix B. The double scanning results for the 6 models display the same good quality and resolution for picking. The picking errors are all in the same range and increase up to ± 0.023 for model V5. However, the model values of model V1-V4

lie within the error bars of the estimated parameters η, V_{p2} from the reference model. In contrast to this, model V5 and V6 are outside the error range of the reference model and thus can be distinguished. This agrees with earlier findings ($\Delta_{\text{inh}}\eta \leq \Delta\eta$). Both models (V5, V6) show that the picked parameters can be distinguished from the reference model parameter as the error bars of these models, $\eta_{\text{V5}} = 0.176 \pm 0.023$ and $\eta_{\text{V6}} = 0.106 \pm 0.012$, do not include the reference model value $\eta_{\text{ref}} = 0.136 \pm 0.016$. Thus between the reference model and its four variations V1-V4 cannot be distinguished from moveout inversion. The estimated velocities are all very good and almost exact. The largest absolute error is ± 0.005 km/s.

4.4.2 C-wave

In analogy to the P-wave, Figure 4.14(a) shows the seismogram for the C-wave of the reference model and Figure 4.14(b) the result from the double scanning moveout inversion. According to the previous analysis an offset-depth ratio of 2 has been used for this wave type. The picking error for the anisotropy parameter with $\chi = 0.187 \pm 0.014$ is in the same range as the one for the P-wave parameter η. However, calculating η from the picked C-wave parameter χ, I find a better constrained value of $\eta = 0.136 \pm 0.01$ than the one picked from the P-wave ($\eta = 0.136 \pm 0.016$). Again, the velocity pick for the C-wave is very good with an absolute error of $V_{c2} = 2.004 \pm 0.001$ km/s. The moveout inversion has also been applied to the C-wave of each variation of the reference model. The picking results are displayed in Figure 4.15 and are listed in Table 4.4 and velocities are listed in Table B.2 in Appendix B. I find that in general, the picking error for χ remains in the same range as for the reference model. As for the P-wave, the model values for models V1-V4 are within the error bars of the reference model estimates $\chi = 0.187 \pm 0.014$. Models V5 and V6 on the other hand are distinguishable from the reference model as their values lie outside the error bars from the reference model and the error bars from the model inversion ($\chi = 0.232 \pm 0.09$ for V5 and $\chi = 0.155 \pm 0.09$ for V6) exclude the reference model value. The velocities are estimated within an absolute error of ± 0.09 km/s. Furthermore, I have calculated η from the picked χ of each model. In general the calculated η is better constrained than the picked one from the P-wave. The absolute error for this calculated

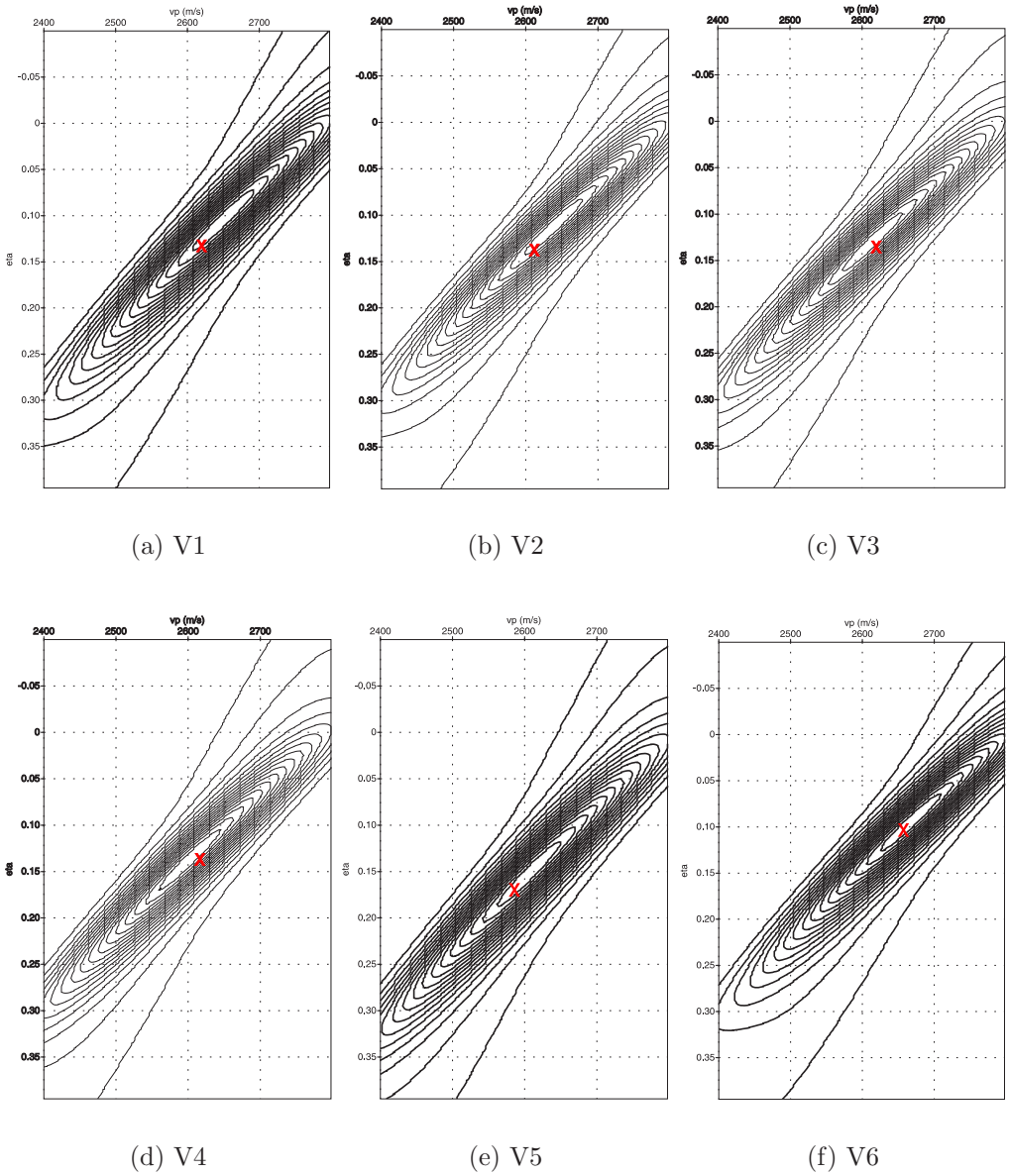

(a) V1 (b) V2 (c) V3

(d) V4 (e) V5 (f) V6

Figure 4.13: Inversion results for parameters η and V_{p2} using a $x/z = 2.5$ for model variation (a) V1, (b) V2, (c) V3, (d) V4, (e) V5 and (f) V6. The crosses mark the individual model values.

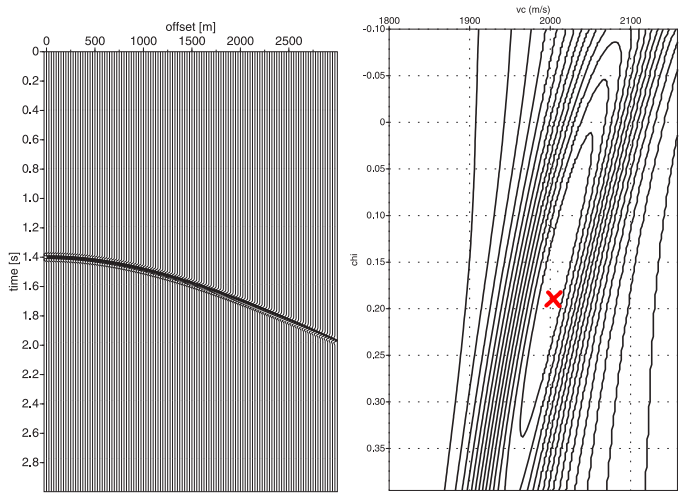

(a) C-wave (b) inversion

Figure 4.14: (a) Corresponding synthetic seismogram for C-wave. (b) Semblance contours from inversion to find χ and V_{c2} for a $x/z = 2.0$. The crosses mark the model values.

Model	η	χ	$\Delta_p\eta$	$\Delta_p\chi$	$\eta(\chi)$	$\Delta_p\eta(\chi)$
ref.	0.12	0.173	0.016	0.014	0.126	0.01
V1	0.106	0.157	0.012	0.009	0.114	0.004
V2	0.115	0.169	0.011	0.008	0.123	0.003
V3	0.13	0.181	0.017	0.016	0.132	0.015
V4	0.136	0.187	0.02	0.019	0.136	0.02
V5	0.153	0.223	0.023	0.009	0.1697	0.006
V6	0.094	0.146	0.012	0.009	0.1	0.006

Table 4.4: Summary of inversion results and their picking errors (Δ_p =model - picked value) compared with the model values. $\eta(\chi)$ is the value if η is calculated from the picked χ value. $\Delta_p\eta(\chi)$ is the difference between the model value for η and the calculated one. Results for the velocity inversion are listed in Table B.2 in Appendix B.

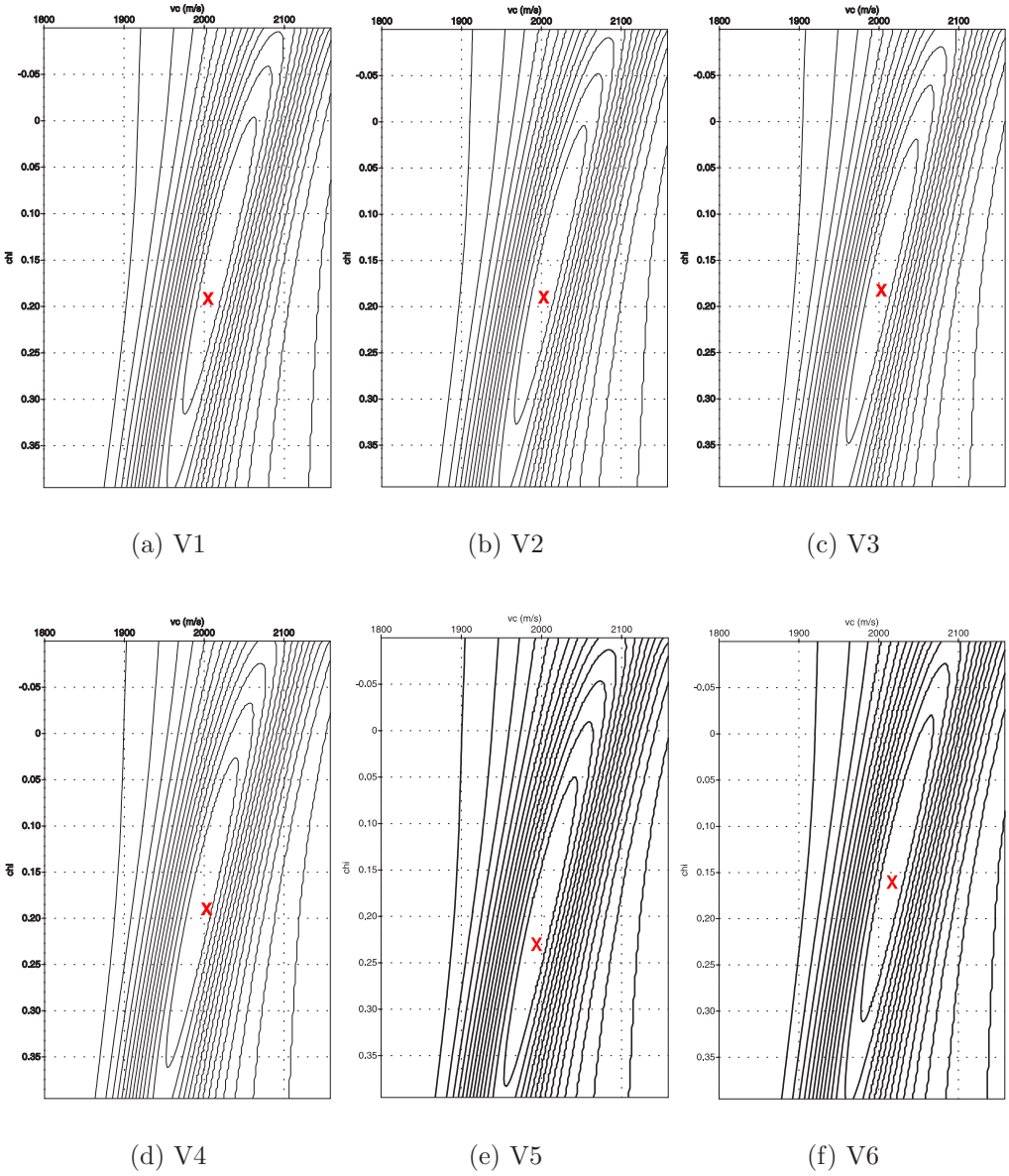

(a) V1 (b) V2 (c) V3

(d) V4 (e) V5 (f) V6

Figure 4.15: Inversion results parameters χ and V_{c2} using a $x/z = 2.0$ for model variation (a) V1, (b) V2, (c) V3, (d) V4, (e) V5 and (f) V6. The crosses mark the individual model values.

parameter is less than or equal to the picking error of the P-wave estimate and in most cases actually about half of that for $\Delta_p\eta$.

4.5 Influence of small perturbations in traveltime

In the above section, I have investigated the effect of small differences in anisotropy parameters on inversion. Here, the influence of traveltime distortions on C-wave inversion is studied. For this purpose a uniform noise function $\tau(x)$ was added to the traveltimes $t(x)$. Figure 4.16(a) illustrates the exact traveltime $t(x)$ from the reference model in blue, with added error $\tau(x)$, 0.25% noise in green and 1% noise in red. Figure 4.16(b) shows the magnitude of the differences between the exact and the noisy traveltimes. It shows that 0.25% noise leads to a maximum error of 3.5 ms and for 1% noise to 14 ms. The corresponding seismograms are

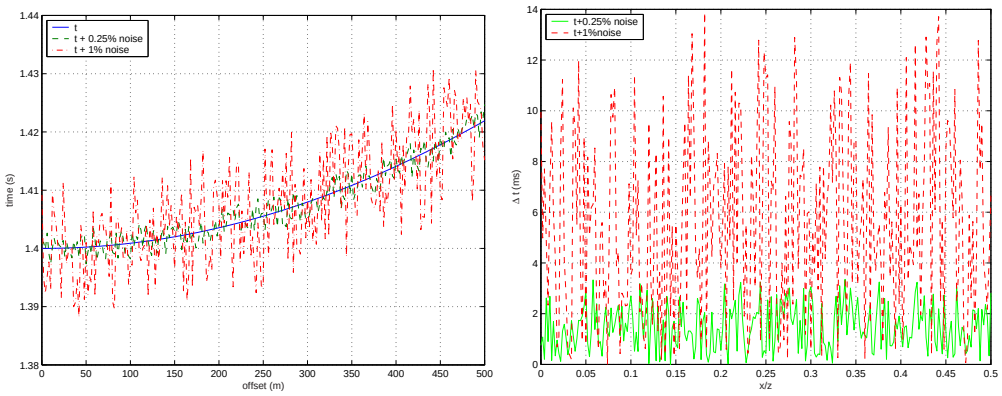

(a) (b)

Figure 4.16: The exact traveltimes are distorted with noise functions $\tau(x)$. (a) Noise traveltimes, 0.25% noise (green) and 1% noise (red), against the exact traveltime $t(x)$ of the reference model. (b) Magnitude of the differences between exact and noisy traveltimes in ms.

shown in Figure 4.17(a)+(c). In Figure 4.17(b), I also added Gaussian noise to the traveltimes with 0.25% noise. The semblance analysis has been applied to these three seismograms and the results of the inversion are displayed in Figure 4.18. It can be seen that for 0.25% traveltime noise with added Gaussian noise

the result is quite well defined and the pick would be in both cases $\chi = 0.158$ and $V_{c2} = 2$ km/s. This indicates that the non-hyperbolic moveout semblance analysis is hardly affected by Gaussian noise on the whole trace. If an error of 1% is added the semblance analysis of the inversion is not as well constrained. However, the pick is in the local minimum and gives the values of $\chi = 0.195$ and $V_{c2} = 1.99$ km/s which is closer to the reference values of $\chi = 0.187$ and $V_{c2} = 2.$ km/s. The semblance result of the reference model without any distortion gives a pick of $\chi = 0.173$ and $V_{c2} = 2.$ km/s. This means that the picking error with 0.25% noise is in the same range as the picking errors from the undistorted reference model and its variations. The picking error with 0.25% and $\Delta_p\chi = 0.028$ is slightly larger than these picking errors. However, in general the error due to small traveltime distortions are in the same range as the normal picking errors. Hence, the moveout inversion can be used on real data which will always show some noise.

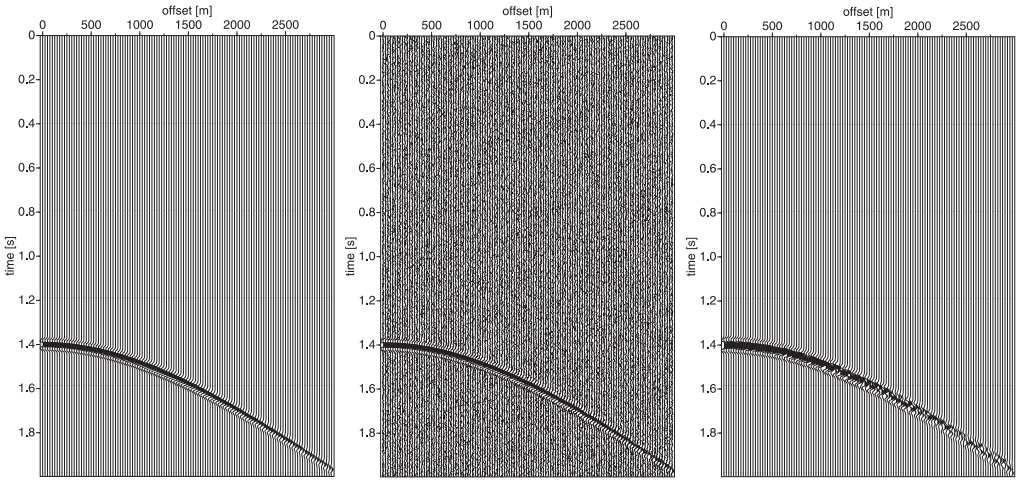

(a) 0.25% noise

(b) 0.25% noise + Gaussian noise

(c) 1% noise

Figure 4.17: Seismograms for traveltime curve of exact reference model distorted by adding an error function $\tau(x)$. (a) 0.25% error of is added to traveltimes as noise. (b) Similar to (a) but with a Gaussian noise distribution added to the whole trace. (c) 1% noise of traveltimes added as noise.

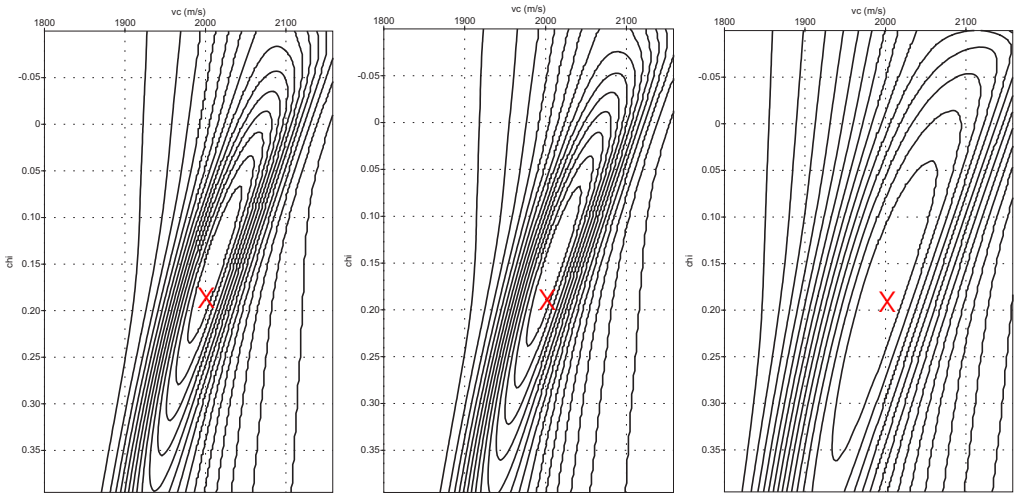

(a) 0.25% noise

(b) 0.25% noise + Gaussian noise

(c) 1% noise

Figure 4.18: Inversion results for χ and V_{c2} on the noisy seismograms (see Figure 4.17). (a) 0.25% noise, (b) 0.25% noise + Gaussian noise distribution on the whole trace and (c) 1% noise. The crosses mark the model values.

4.6 The use of S-waves moveout

In the previous sections I studied the feasibility of traveltime approximations for P- and C-wave data for anisotropic parameter estimation. However, S-waves are the wave type most strongly affected by anisotropy and therefore should be ideal for anisotropic parameter estimation. I recall Figure 4.2 which shows the traveltime curves for all 3 wave types for the reference model and its isotropic counterpart. Clearly, the difference between isotropic and anisotropic traveltimes are strongest for the S-wave. Furthermore, for example, Tsvankin and Thomsen (1995) showed that long-spread SV-waves ($x/z = 2$) can be used for traveltime inversion, depending on offset and degree of anisotropy. However, in most cases with moderate anisotropy, the S-wave moveout can form a cusp (Helbig (1966), Schoenberg and Daley (2003)) which impede anisotropic parameter estimation by means of non-hyperbolic moveout analysis. In the case of the reference model the S-wave moveout shows such cusps at an offset of about 1.7 km. In analogy to the P- and C-wave analysis, I estimate the inherited error for the S-wave. As the traveltime approximation, Equation (2.72), does not show the cusp, I restrict the offset for this analysis to 1.7 km, i.e. the maximum possible offset

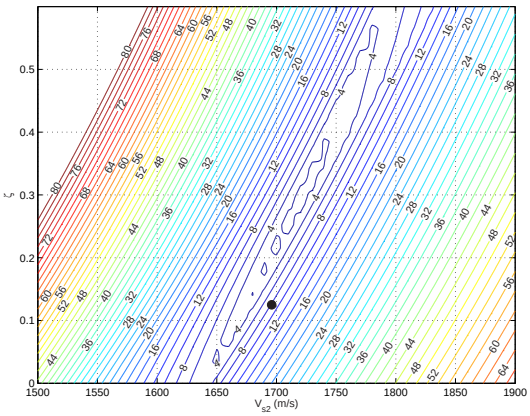

Figure 4.19: The influence of ζ and V_{s2} on the traveltime moveout from one horizontal VTI layer. Contours display the maximum traveltime difference $\Delta t_{\max}$ in ms between exact and approximated traveltimes against an offset of 0-1700 metres. The black dot indicates the model value of $\zeta - V_{s2}$ for the reference model.

before the cusp occurs. The influence of varying ζ and V_{s2} are displayed as contours of traveltime differences $\Delta t_{\max}$ in ms for an offset of 0-1.7 km in Figure 4.19. The black dot indicates the model value from the reference model. The ellipses of smallest traveltime difference $\Delta t_{\max}$ indicate again that the stacking velocity is well constrained while the anisotropy parameter has a larger error. The inherited error between model value and the pick of the centre of the ellipse of smallest $\Delta t_{\max}$ is $\Delta_{\text{inh}}\zeta = 0.181$. Compared to the actual model value, $\zeta = 0.125$, there is a very large error that indicates that the moveout from the exact and the approximated traveltimes differ strongly in some parts. In order to obtain the S-wave anisotropy parameter ζ and the stacking velocity V_{s2} the traveltime approximation Equation (2.72) has been implemented in a double semblance scanning technique similar to the P- and C-wave. As the semblance analysis breaks down when it encounters a cusp the offset has to be restricted to the part before the cusp for parameter estimation. The result of the inversion analysis is displayed together with the S-wave seismogram in Figure 4.20 and listed in Table 4.5. Note, that the anisotropy parameter is not well resolved and the picking error is as large as $\zeta = 0.125 \pm 0.18$. Again, η can be calculated from the anisotropy parameter using Equation (2.30). Due to the large picking error in ζ the calculated P-wave parameter η is not very exact either $\eta(\zeta) = 0.3$, which means a large error of $\Delta_p\eta(\zeta) = 0.175$. The low resolution of the anisotropic parameter might be due to the small x/z ratio of 1.7.

This finding may be problematic for the "PP+PS=SS" approach (Grechka and Tsvankin (2002b),Grechka and Dewangan (2003)) due to the limited S-wave offset.

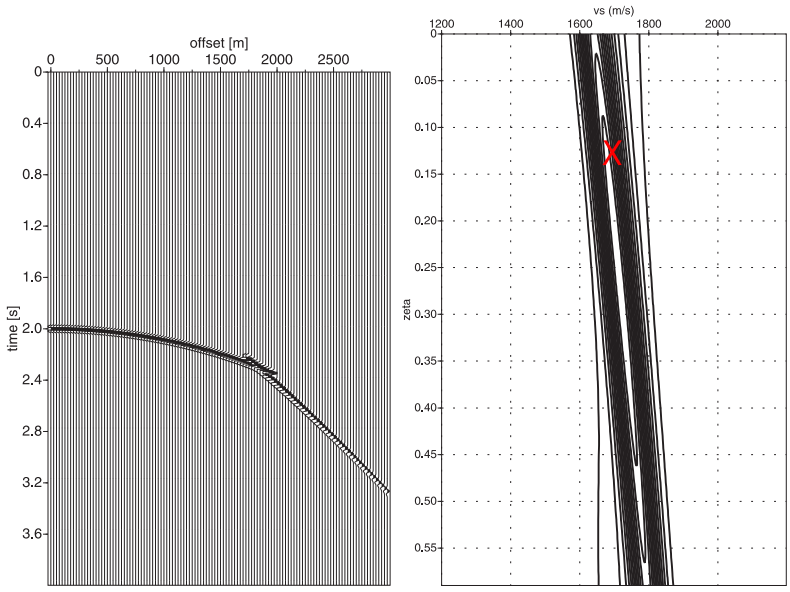

Figure 4.20: (a) S-wave seismogram from the reference model. (b) Inversion result using double semblance scanning technique searching for $\zeta - V_{s2}$ on S-waves for $x/z = 1.7$ (restricted due to cusp). The cross marks the model value.

ζ	$\Delta_p\zeta$	$\eta(\zeta)$	$\Delta_p\eta(\zeta)$	$\Delta_{\text{inh}}\zeta$
0.271	0.146	0.3	0.164	0.18

Table 4.5: Inversion result and its picking error from S-wave moveout. Δ_p is the picking error and Δ_{inh} the inherited error. $\eta(\zeta)$ is the value if η is calculated from ζ using Equation (2.30) and $\Delta_p\eta(\zeta)$ the corresponding error between calculated and model value.

The "PP+PS=SS" approach makes use of the property that pure S-waves can be processed using conventional velocity analysis tools without the problems of C-waves such as asymmetric moveout and phase reversal. Therefore, the S-wave moveout is reconstructed from P- and C-wave data by identifying PP and PS reflections originating from the same interface. In order to find the maximum possible S-wave offset gained from this method Figure 4.21 visualises the ray paths and the angles related to the P-wave and S-wave leg of a converted wave in a single isotropic layer. The maximum S-wave reflection angle is independent of the offset and is defined by Snell's law as $\Theta_{\mathrm{max}s} = \arcsin(V_s/V_p)$. For the reference model this leads to $\Theta = 23.6°$ which corresponds to $x_s = z \tan\Theta = 0.437$ km. From P- and C-waves this approach estimates the maximum offset for S-waves

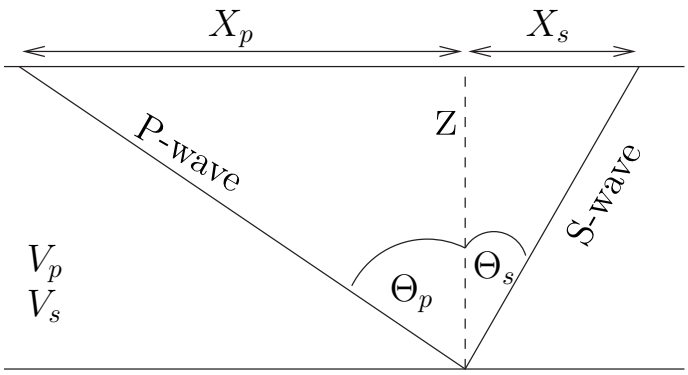

Figure 4.21: Raypath of C-wave in a single isotropic horizontal layer with velocities V_p, V_s and offsets X_p and X_s corresponding to the P- and S-wave leg, respectively and its reflection angles. Θ_p and Θ_s are the reflection angles.

from the known traveltimes using

$$t_c = t_p + t_s = \frac{\sqrt{(z^2 + x_p^2)}}{V_p} + \frac{\sqrt{(z^2 + (x - x_p)^2)}}{V_s}, \tag{4.10}$$

where z is the depth of the layer, $x = x_p + x_s$ is the total offset, x_p is the offset corresponding to P-wave leg and x_s = offset corresponding to S-wave leg. The equation for unknown x_p is solved by recursion, computing t_c for x_p ranging between $x/2$ and x and finding the difference between the calculated and known traveltime t_c from the ray tracer to be minimal. The corresponding value for the minimum is the searched x_p from which x_s can be calculated. For the reference model the result for $t_c = 1.975$ s and $x = 3$ km is $x_p = 2.598$ km and $x_s = 0.402$. Hence, the maximum offset for S-wave reflection from "PP+PS=SS" is $x_s = 0.804$ km. For a smaller offset, $x = 2.5$ km corresponding to a $x/z = 2.5$,

an offset related to the S-wave is found to be 0.389 km, i.e. a total of $x_s = 0.778$ km. These offsets are too small for parameter estimation with a good resolution as has been shown in Figure 4.19 and Figure 4.20(b) for this type of model.

4.7 Effects of low S-Wave velocity model

So far, I have used a model and its variations which had P- and C-wave parameters of the same order of magnitude. Now I will extend this analyses to a second set of models which reflects a scenario for near-surface sediments. The important changes to the first set of models are that it features a lower S-wave velocity and thus higher γ_0 and the P-wave anisotropy parameter is an order of magnitude lower with $\eta = 0.075$ while the C-wave is still in the range as before with $\chi = 0.338$. One variation, V1, will be studied, with differences in the anisotropy parameters of $\Delta\eta = 0.01$ and $\Delta\chi = 0.03$. As before, the vertical traveltimes and the stacking S-wave are constant while the P-wave stacking velocity and the depth of the layer vary slightly to compensate for the change in the anisotropy parameter in order to keep the moveout as constant as possible. Tables 4.6 and 4.7 list the properties of the new reference model with low S-wave velocity and its variation V1. The traveltimes for this model are shown in Figure 4.22(a).

Model	depth	V_{p0}	V_{s0}	ϵ	δ	η_{eff}	$\Delta\eta_{\text{eff}}$	χ_{eff}	$\Delta\chi_{\text{eff}}$
ref.	0.3	2.2	0.4	0.11	0.03	0.075	-	0.338	-
V1	0.213	1.560	0.284	0.71	0.53	0.085	0.01	0.366	0.028

Table 4.6: Properties of a new model with low S-wave velocity and its variation. $\Delta\eta_{\text{eff}}$ and $\Delta\chi_{\text{eff}}$ are the differences between the anisotropy parameters of the reference and the perpetuated model. Velocities are in km/s and depth in km.

Model	t_{p0}	t_{c0}	t_{s0}	V_{p2}	V_{c2}	V_{s2}	γ_0	γ_{eff}	ζ
ref.	0.273	0.886	1.5	2.265	1.257	0.967	5.5	0.998	0.075
V1	0.273	0.886	1.5	2.242	1.251	0.967	5.4	0.085	0.081

Table 4.7: More properties of the models in Table 4.6, where times are in seconds and velocities in km/s.

Although the anisotropy is smaller than in the first reference model, the S-wave traveltime curve still shows a cusp. For non-hyperbolic moveout semblance analysis the offset would therefore, be limited to 330 m for S-wave moveout analysis.

Figure 4.22(b) illustrates the traveltime difference between the original model and its variation V1 for the P- (solid line) and C-wave (dashed line). The time difference between both models for an offset up to 3 km is never larger than 2.5 ms, i.e. the moveout has hardly changed between the models. Each wave type is investigated by applying the inherited error analysis and the inversion.

Again seismograms have been calculated by ray tracing. Figure 4.23(a) il-

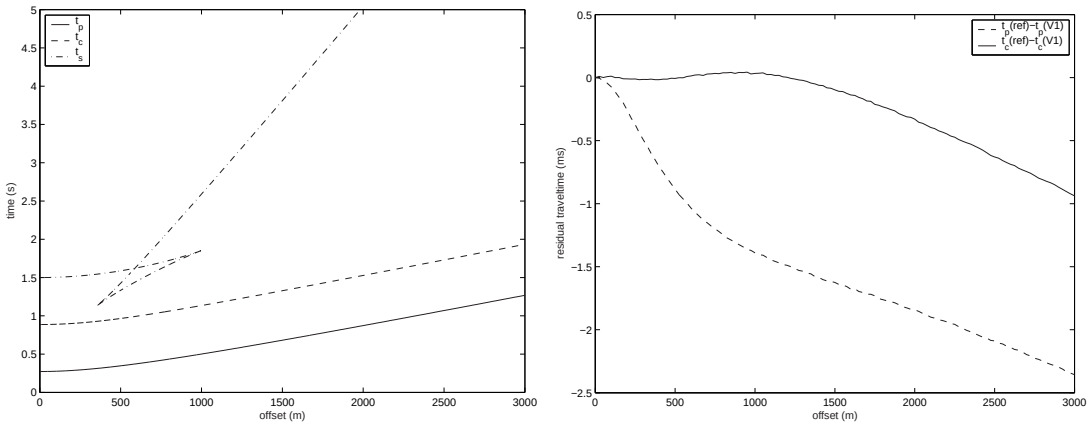

(a) (b)

Figure 4.22: (a) Traveltimes for P-, C- and S-waves in the low S-wave velocity model. (b) Traveltime difference between low S-wave velocity model and its variation (V1) for P- (solid) and C-wave (dashed) in ms.

lustrates the maximum traveltime differences $\Delta_{\max}$ as ellipses for varying η and V_{p2} for an offset of 0-750 m ($x/z = 2.5$). Figure 4.23(b) shows the same analysis for the C-wave with varying χ and V_{c2} over an offset of 0-600 metres which corresponds to an offset-to-depth ratio of 2. Although the ellipse of smallest traveltime difference for the P-wave is rather large the inherited error is only $\Delta_{\text{inh}}\eta = 0.012$. Although the C-wave shows a better constrained smallest ellipse, the model value already lies on the edge to the next higher time difference of 4 ms. However, the inherited error is found to be $\Delta_{\text{inh}}\chi = 0.045$. The results for the model V1 are shown in Appendix B, Figure B.5. The inherited errors found for this model ($\Delta_{\text{inh}}\eta = 0.014$, $\Delta_{\text{inh}}\chi = 0.03$) correspond as well with the reference model as with the values found from the first set of models. This strengthens the idea, that the inherited error stays in the same range for the different wave types and might

be used as an indication to what extent moveout inversion can differentiate between different anisotropic models. Comparing the inherited error Δ_{inh} with the difference of the anisotropy parameter between the different models (Δ in Table 4.6) I find that $\Delta\eta < \Delta_{\text{inh}}\eta$ and thus it might be hard to differentiate between the different models. In contrast, $\Delta\chi \geq \Delta_{\text{inh}}\chi$ so hopefully the different models can be resolved.

As already mentioned, the offset for the S-wave data has to be restricted to 330 metres, i.e. $x/z = 1.1$ and Figure 4.25(a) shows the influence of anisotropy parameter ζ and stacking velocity V_{s2} on the moveout. Only the velocity can be resolved and unfortunately there is no resolution for ζ. The result for the model variation V1 confirms these findings and is displayed in the Appendix B, Figure B.6(a).

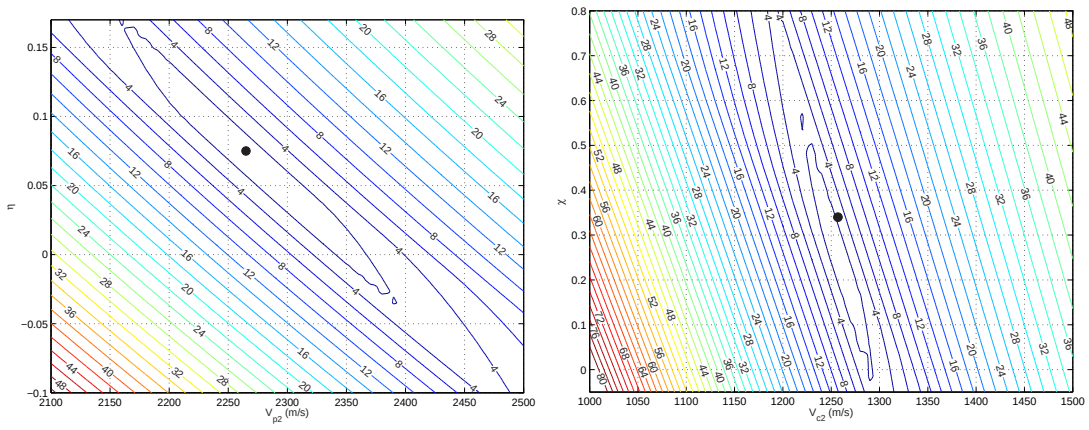

(a) $\Delta_{\text{inh}}\eta$ (b) $\Delta_{\text{inh}}\chi$

Figure 4.23: (a) Influence of varying $\eta - V_{p2}$ displayed as Δt_{max} for an offset of 0-750 metres ($x/z = 2.5$) for P-waves from the low S-wave velocity model. (b) Influence of varying $\chi - V_{c2}$ displayed as Δt_{max} for an offset of 0-600 metres ($x/z = 2.$) for C-waves The dots indicate the model values.

The non-hyperbolic moveout inversion for the P-waves of both, the original low S-velocity model and its variation V1, (Figure 4.24(a) and (b)) give an estimate of the anisotropy parameter with an absolute picking error of $\Delta_p\eta = 0.004$ and 0.006 respectively. The inversion result from the C-wave give χ estimates with picking errors of $\Delta_p\chi = 0.008$ and 0.004 for the original and variation, respectively. Table 4.8 summarises all picking results. The picking errors also confirm, that C-wave analysis can distinguish between the two model anisotropy param-

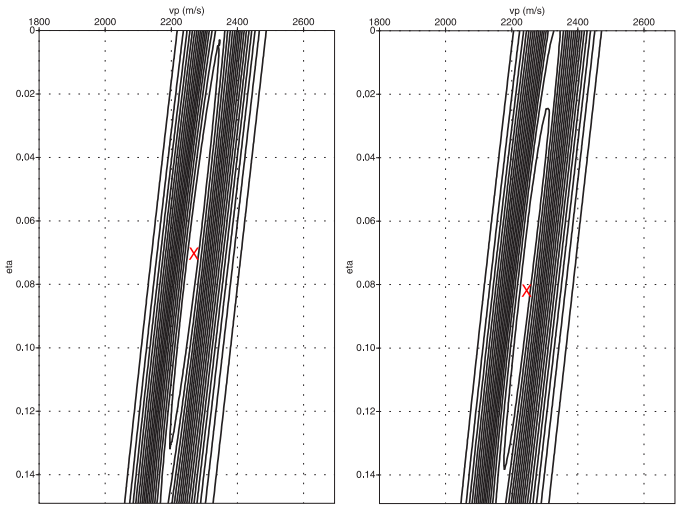

(a) $\eta - V_{p2}$ original (b) $\eta - V_{p2}$ V1

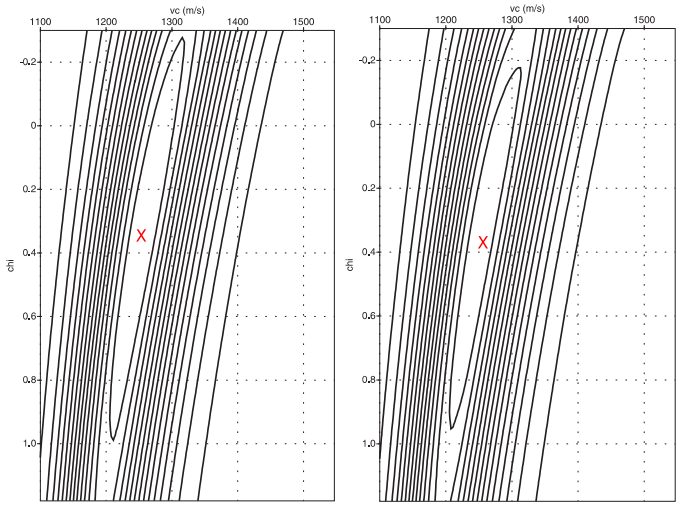

(c) $\chi - V_{c2}$ original (d) $\chi - V_{c2}$ V1

Figure 4.24: (a) Inversion results from double semblance analysis to estimate η and V_{p2} from P-wave data of the low S-wave velocity model. (b) Double scanning of $\eta - V_{p2}$ from P-wave data of variation V1. (c) Semblance analysis results for χ and V_{c2} from C-wave data of low S-wave velocity model. (d) Double scanning of $\chi - V_{c2}$ from C-wave data of variation V1. For P-wave analysis $x/z = 2.5$ was applied and for C-waves a $x/z = 2.$. The crosses indicate the model values.

eters. It is harder to differentiate between the P-wave parameters as their size is an order of magnitude smaller than the C-wave parameters. Furthermore, the V1 model values lie within the picking error bars of the reference model. In contrast, the C-wave reference model values have no overlap with the error bars of the V1 model. Calculating η from the C-wave parameter χ reduces the absolute error of the calculated η to the model value to $\Delta_p\eta(\chi) = 0.001$ for both models. This means that the error from the calculated η is smaller than the picking error from the P-wave. Parameter inversion from S-wave data alone cannot resolve the

	η	χ	$\Delta_p\eta$	$\Delta_p\chi$	$\eta(\chi)$	$\Delta_p\eta(\chi)$	$\Delta_{\text{inh}}\eta$	$\Delta_{\text{inh}}\chi$
picks ref.	0.069	0.33	0.006	0.008	0.074	0.001	0.012	0.045
picks V1	0.081	0.37	0.004	0.004	0.086	0.001	0.014	0.03

Table 4.8: Picked P- and C-wave anisotropy parameters and their corresponding picking errors (Δ_p). From the C-wave inversion results the parameter η can be calculated and $\Delta_p\eta(\chi)$ represents the corresponding error between model and calculated value. Δ_{inh} gives the inherited error for both wave types.

anisotropy parameter ζ for either of the models (see Figure 4.25(b) and Appendix B, Figure B.6(b)).

Finally, the maximum possible offset which could be achieved if the S-waves are obtained from P- and C-wave is calculated as introduced in Section 4.6. For this model the result is for $t_c = 3.6595$ s and $x = 2.5$ km $x_p = 2.826$ km and $x_s = 0.174$. Therefore, the maximum possible offset for S-wave reflection is $x_s = 0.348$ km. For an $x/z = 3$ the result is $x_p = 2.33$ km and $x_s = 0.17$. Hence, the maximum offset for S-wave reflection from PP+PS is $x_s = 0.34$ km, i.e. it differs only of 8 metres from the result using a smaller offset. Both these offsets are too small for parameter estimation.

4.8 Analysis of error propagation

To quantify the error propagation when quantities are calculated from parameters estimated from real data, I compare the error magnification when the anisotropy parameter σ is calculated from either η or χ in a single layer VTI medium.

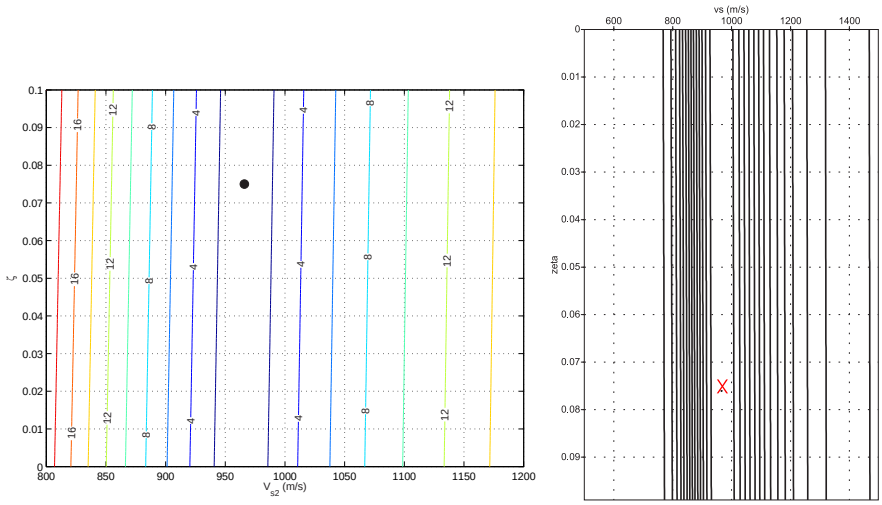

(a) $\Delta_{\text{inh}}\zeta$ (b) $\zeta - V_{s2}$ inversion

Figure 4.25: (a) Influence of varying $\zeta - V_{s2}$ displayed as Δt_{max} for an offset of 0-350 metres (due to cusp) for S-waves from the low S-wave velocity model. (b) Inversion using double semblance analysis to estimate ζ and V_{s2} from synthetic data. For both analyses a $x/z = 1.1$ were used. The dot/cross indicate the model values.

Equation (4.7) relates η to σ:

$$\eta\gamma_2^2 = \frac{\sigma}{1+2\sigma}.$$

The error of the picked value η will thus be magnified by γ_2^2 when σ is calculated.

For the C-waves I consider the relationship between C-wave anisotropy parameter $\chi = (\gamma_0 - 1)\eta\gamma_{\text{eff}}^2$ and σ. Firstly, I expand η with $\eta = (\sigma/(1+2\sigma))/\gamma_2^2$ to obtain

$$\chi = \frac{(\gamma_0 - 1)\gamma_{\text{eff}}^2}{\gamma_2^2}\frac{\sigma}{1+2\sigma}.$$

I use the definition of the effective velocity ratio $\gamma_{\text{eff}} = \gamma_2^2/\gamma_0$ and rearrange the equation to

$$\chi\frac{\gamma_0^2}{\gamma_2^2(\gamma_0 - 1)} = \frac{\sigma}{1+2\sigma} \tag{4.11}$$

Hence, one can see that σ may be calculated from the C-wave anisotropy parameter χ. The picking error in χ will thereby be magnified by a term consisting of

the vertical and the stacking velocity ratios.

To quantify the effects of Equations (4.7) and (4.11) I evaluate the error magnification factors for values of γ_2 in the range of between 1.2 and 2.4. Corresponding values for γ_0 are chosen to be 2.4, 2.8, 3.4 and 3.9, respectively. The range of γ_2 and γ_0 reflects values that I used for modelling and have been observed in data. Figure 4.26 illustrates the magnification factors of the picked anisotropy

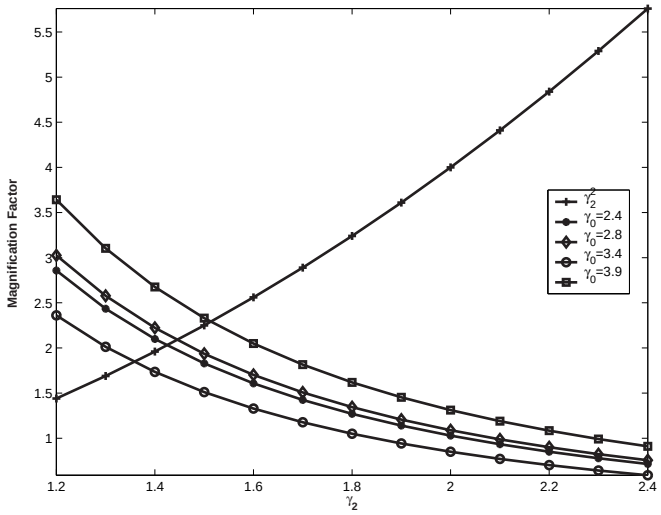

Figure 4.26: Magnification factor γ_2^2 for P-wave anisotropy parameter η, "+", and magnification factor $\gamma_0^2/(\gamma_2^2(\gamma_0-1))$ for C-wave anisotropy parameter χ (all other curves). It can be seen that for γ_2 values bigger than 1.5 the error magnification using the parameter χ is smaller than using the parameter η to calculate $\sigma/(1+2\sigma)$.

parameter when $\sigma/(1+2\sigma)$ is estimated. The diagram shows the factor γ_2^2 for P-wave anisotropy parameter η. The magnification factor increases with increasing γ_2. It shows the development of the factor $\gamma_0^2/(\gamma_2^2(\gamma_0-1))$ for different γ_0 values. It illustrates that the higher γ_0 the higher the magnification factor. There is a decrease of the magnification factor with increasing γ_2. For γ_2 greater than 1.5 the error magnification is much higher when σ is calculated from the P-wave parameter η than when the C-wave parameter χ is used. As a matter of fact, the γ_2 values of the models that I use are mostly greater than 1.6 and thus I suggest that the C-wave parameter χ for model building should be used.

The next question is, how big is the influence of an error in the anisotropy parameter on the traveltime calculation. The error propagation of an erroneous η into

distorted traveltimes is illustrated by using the parameters from the 300 metres thick reference model summarised in Section 4.7, Table 4.6, with a low S-wave velocity. This situation is closer to an observed velocity distribution and range of anisotropy parameters in the near-surface. Figure 4.27(a) illustrates the cor-

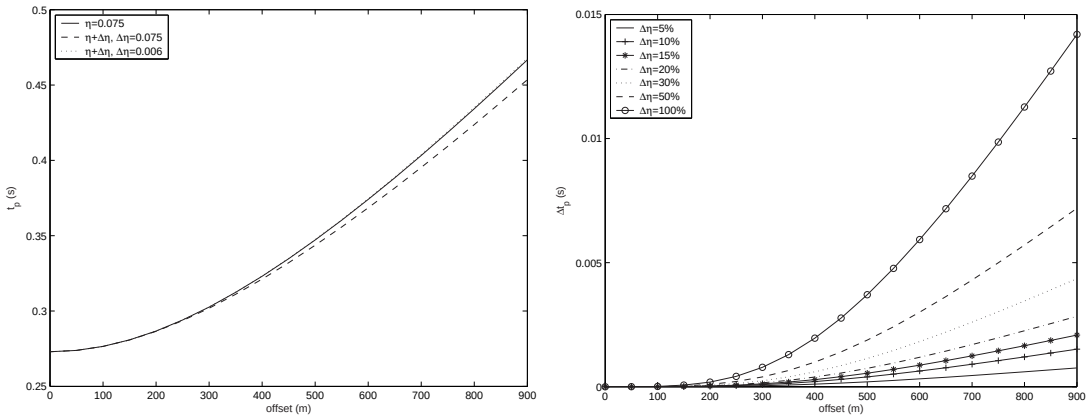

Figure 4.27: (a) P-wave traveltime curves for correct η (solid), $\eta + \Delta\eta = 0.006$ (dotted) and $\eta + \Delta\eta = 0.075$ (dashed). The resulting errors in traveltime are $\Delta t_p = 0.001$s and $\Delta t_p = 0.013$s for an offset of 900 metres (corresponds to x/z=3), respectively. (b) Error of traveltime t_p for various erroneous η.

responding P-wave traveltime curves. The solid curve represents the traveltimes calculated with the exact value of η. The dotted curve shows the traveltime curve using the actual picked error of $\Delta\eta = 0.006$ for this layer (see Table 4.8). Here, the resulting error in traveltime is only $t_p = 0.467 \pm 0.001$s. The dashed curve results from an error of $\Delta\eta = 0.075$ which is an error of 100%. This value has been chosen because $\eta = 0.15$ lies within the range of the typically picked values. Considering an offset-to-depth ratio of $x/z = 3$, or offset $x = 900$ metres, the resulting error is $t_p = 0.467 \pm 0.013$.

Figure 4.27(b) shows the error in traveltime over offset for 7 percentage changes in η and Table 4.9 lists the corresponding traveltime errors for t_p at an offset of $x = 900$ metres. The plot illustrates that the error in traveltime shows exponential increase after an offset of 300 m and at 900 m at 100% error in η leads to an error in t_p traveltime of about 14 ms. This is quite significant in time processing for shallow events and thus the error in η has to be minimised.

Previously in this chapter I have calculated η from χ to obtain a more accurate result than estimating η from data itself. The error propagation when calculating

η	$\Delta\eta$ [%]	$\Delta\eta$	t_p [s]	Δt_p [s]
0.075	5	0.004	0.467	0.00076
	10	0.008		0.00151
	15	0.011		0.00208
	20	0.015		0.00284
	30	0.023		0.00435
	50	0.038		0.00719
	100	0.075		0.0142

Table 4.9: Traveltime error from erroneous η for an offset of 900 metres.

η from picked χ-values is found as

$$|\Delta\eta| = \frac{1}{\gamma_{\text{eff}}^2(\gamma_0 - 1)}|\Delta\chi| \leq |\Delta\chi|/2. \tag{4.12}$$

For example the absolute error for the calculated parameters in Table 4.4 are less than or equal to the picking error of the P-wave estimate and in most cases actually about half of those from $\Delta_p\eta$ which can be explained by Equation (4.12) since γ_{eff} is often about 1.0 and γ_0 about 3.0. In the case for the low S-wave velocity model the magnification factor is much smaller than $1/(\gamma_{\text{eff}}^2(\gamma_0 - 1)) = 0.2231$. This is one of the reasons why I propose to use C-wave analysis to quantify η when the numerical stability criteria discussed in Section 4.1.3 are met.
Note, that the relative error of the calculated η, i.e. $\delta\eta = \Delta_p\eta/\eta$, stays the same as the corresponding $\delta\chi = \Delta_p\chi/\chi$.

4.9 Discussion and Conclusion

In this chapter I carried out a detailed analysis of the accuracy of moveout inversion from a single VTI layer. In the first part I investigated the influence of anisotropy parameters and stacking velocities on moveout approximations on P- and C-waves. I find that in general the stacking velocity is better constrained than the anisotropy parameter. However, the approximations are good enough to be used for moveout inversion. The spread-length influences the inversion: the constraints on the anisotropy parameer become stronger with increasing length of the included offset. However, there is a trade-off between strong constraints and exactness as the position of the centres of the ellipses shifts away from the

model value with increasing length of the offset. Thus, for the remaining investigations of this project I used an offset-to-depth ratio of $x/z = 2.5$ for the P-wave and $x/z = 2.0$ for the C-wave. Moreover, I introduced the concept of inherited error $\Delta_{\text{inh}}\eta$ and $\Delta_{\text{inh}}\chi$ which are the difference between the centre of the ellipse of smallest traveltime difference and the model value. I find, that regardless of the magnitude of the anisotropy parameter, the inherited error stays in the same range for each wave type, i.e. $\Delta_{\text{inh}}\eta = 0.02$ and $\Delta_{\text{inh}}\chi = 0.04$. Thus, it can be suggested that if the difference Δ between the anisotropy parameter of the reference model and the model under consideration is smaller than the inherited error ($\Delta < \Delta_{\text{inh}}$) one cannot differentiate between these models. Inversion from a set of models confirms this finding.

Furthermore, the anisotropic parameter η can be estimated from the C-wave moveout data more accurately than from P-wave data. In most cases the error is halved. Random errors, i.e. small perturbations in the traveltimes, show hardly any influence on the inversion. Obtaining pure S-wave reflection data from P- and C-wave data might lead to difficulties in resolution as the enhanced offset is very small.

Analysis of error propagation suggests that estimating χ from data has a lower magnification factor than η when the parameter is used for model building and thus calculating σ. Also, I find that an error in η as large as 0.04 leads to a non-negligible distortion in traveltimes. This means that η has to be estimated as exactly as possible. As I have shown, it is possible to decrease the error in η when it is calculated from χ.

Due to error propagation, the estimates of anisotropic parameters may not be sufficiently accurate to get an exact VTI model even when both P- and C-wave data are available and η is estimated from P-wave moveout. However, using joint inversion from P- and C-wave moveout data can provide a better constraint on the VTI model and allows us to obtain η more accurately from C-wave moveout. This is essential for model building. This result is based on a single VTI layer study. I will investigate in the next chapter how layering influences parameter estimation.

Chapter 5

Moveout inversion in multilayered VTI media

In the previous chapter I discussed the feasibility of parameter estimation for a single VTI layer. Here, I will show how moveout inversion is affected by layering. In a multilayered media the anisotropy parameters η and χ become effective parameters, but can still be estimated by means of a double scanning semblance analysis over non-hyperbolic reflection moveout. It is very important for the purpose of processing to know how accurately these parameters can be estimated and how they are affected by the layering and the geological setting.

To investigate the accuracy of resolving the P-wave anisotropic parameter η_{eff} using semblance double scanning from vertical components (P-wave) and the C-wave anisotropy parameter χ_{eff} from the inline horizontal components (C-wave), I have undertaken a full-wavefield modelling study on a range of models from equally thick layers to varying layer thickness, and to low velocity layers. The model properties are roughly based on information from the Alba data set (well logs and VSP data). Typical values for the P-wave anisotropy parameter η_{eff} from this theoretical study are between 0.07 and 0.08 and cannot be resolved by P-wave non-hyperbolic moveout analysis. In contrast typical values of the C-wave anisotropy parameter χ_{eff} are about an order of magnitude larger and within the range 0.18 and 0.40, which can be estimated accurately by C-wave non-hyperbolic moveout analysis.

The second part of this chapter focuses on the occurrence of phase reversals

together with diminishing amplitudes and suggests possible mechanisms. This chapter will focus on the use of P- and PS-converted waves. S-waves are not a particularly good choice for moveout inversion as shown in the previous chapter.

5.1 Parameters in layered media

In Chapter 4 I have discussed parameter estimation and its feasibility for the case of a single layer. Of course this situation is far from the reality that usually consists of many layers. Therefore, I want to start this chapter by giving a short overview of the parameters found in a layered media.

1. **Interval quantities** These are the parameters characterising a certain subsurface layer, for example V_{pi},V_{si}, χ_i, η_i. For the ith layer of thickness z_i, if the one-way traveltime of a vertical ray through it is t_i, then the interval velocity is given by $v_i = z_i/t_i$.

2. **Average parameters** The interval velocities of several layers can be used to yield the time-average velocity $\bar{V}$. In a medium with n layers the average velocity on top of these layers is

$$\bar{V} = \frac{\sum_{i=1}^{n} z_i}{\sum_{i=1}^{n} t_i} = \frac{\sum_{i=1}^{n} t_i v_i}{\sum_{i=1}^{n} t_i}.$$

   The average parameters are often used to refer to a ray reflected at normal incidence and the corresponding parameters are for instance V_{p0},V_{s0} and γ_0.

3. **Root-mean-square (RMS) parameters** *The square root of the average of the square of a series of measurements* (Sheriff, 1997). In a single layer medium, the raypath is a straight line. In a multilayered medium, the raypath is usually a bending curve consisting of segments of straight lines. For small offsets, the bending raypath may be replaced by a straight raypath and the corresponding velocity is then replaced by the $root - mean - square$ velocity V_{RMS} of the layers above the reflector.

$$V_{\mathrm{RMS}} = \sqrt{\frac{\sum_{i=1}^{n} t_i v_i^2}{\sum_{i=1}^{n} t_i}}.$$

The RMS velocities are strictly speaking not identical to the stacking velocities which are obtained from normal-moveout measurements. However, for small offsets and importantly, horizontal layers, the NMO value for each reflection can be used to extract the RMS velocity for the layers overlying the reflector (Kearey and Brooks, 1991), e.g. V_{p2}, V_{c2} and V_{s2}.

4. **Effective anisotropy parameters** Effective anisotropy parameters are the defined for a stack of layers. The effective anisotropy parameters also describe the departure from hyperbolic moveout and include the effect of layering, for example χ_{eff}, η_{eff}. The definition of the effective anisotropic parameters are introduced in Equations (2.34), (2.35) and (2.36).

5.2 Aspects of parameter estimation

For P-waves in layered VTI media the moveout can be approximated using Equation (2.57) (see Chapter 2) which shows that the moveout is governed by the parameters V_{p2} and η_{eff}. Thus, only η_{eff} and V_{p2} can be estimated from P-wave moveout by a double semblance scanning technique. Whilst for C-waves, the moveout signature can be described by Equation (2.62) in Chapter 2. This equation shows that the C-wave traveltime in layered VTI media is controlled by four parameters: $V_{c2}, \gamma_0, \gamma_{\text{eff}}$ and χ_{eff}. Similar to the single VTI case, only V_{c2} and χ_{eff} may be recoverable from the C-wave moveout. γ_0 and γ_{eff} have to be determined by joint P- and C-wave analysis.

Time processing such as NMO correction and stack can be accomplished with the estimated anisotropy parameter and stacking velocity for each wave type. However, ultimately the goal is to obtain a depth image. For this purpose the Thomsen anisotropy parameters have to be known. Equations (2.32) and (2.29) can be used to obtain χ and η. Alternatively, the relationship between χ and η, Equation (2.33), can be used to calculate η from the picked values of χ.

In practice, γ_0 and γ_{eff} have to be estimated before V_{c2} and χ_{eff} can be esti-

mated. Since this is a modelling study of the accuracy of moveout inversion I assume γ_0 and γ_{eff} are known. Details of the inversion procedure and examples of how γ_0 and γ_{eff} are estimated from real data can be found in Chapter 7. Here I will only give a brief discussion of this matter.
Also, parameter estimation in layered media may often require the building of the interval model as discussed in Section 5.1. This may be achieved through Dix or Dix-type inversion. Again I will not discuss this here. Application to real data can be found in Chapter 8. Accuracy and error propagation of Dix-inversion is well discussed in the literature (e.g. Yilmaz, 2001) and will not be repeated here.

Estimation of γ_0: The vertical velocity ratio γ_0 is usually determined by event correlation between P- and C-wave data. After event correlation Equation (2.25) can be used to calculate γ_0. Note, that if γ_0 is estimated in such a way it is an average quantity. In the synthetic study in this chapter γ_0 is assumed to be known.

Estimation of γ_{eff}: γ_{eff} is often estimated from V_{p2}, V_{c2} and γ_0 using Equation (2.27). γ_{eff} can also be estimated using the moveout and more details can be found in Chapter 7.

Conversion from RMS to interval quantities: Assuming small offsets and parallel, horizontal layers, the RMS velocities can be used to extract the interval velocities using the Dix formula (Sheriff, 1997)

$$V_i = \sqrt{\frac{V^2_{\text{RMS}_i} t_i - V^2_{\text{RMS}_{i-1}} t_{i-1}}{t_i t_{i-1}}}$$

where V_{RMS_i} and $V_{\text{RMS}_{i-1}}$ are the RMS velocities from the datum to the reflectors above and below the layer and t_i and t_{i-1} are the respective travel times. Interval anisotropy parameters can be obtained from effective parameters in a similar manner.

In the following sections, I will perform a detailed analysis of the accuracy of moveout inversion for varying layer parameters.

5.3 Multilayered models for synthetic studies

For the synthetic study of accuracy of parameter estimation in multilayered VTI media, I have chosen a four-layer model roughly based on the Alba field parameters. I define the background properties of the base model using well log data from wells 16/26-28 and 16/26-28z. The location of wells 28 and 28 z are indicated in Figure 3.3(a) in Chapter 3. The well logs are displayed in Figure 3.13 for sonic, porosity, gamma ray and caliper log for the depth interval from 1000 to 2200 metres. Figure 3.14 highlights the depth segment of 1800-2100 metres which includes the reservoir layer. Figure 3.15 shows the curves for the total water saturation (SWT) and the volume of shale (VSH). Table 5.1 gives the contents and thickness of the layering of the basic model and the four variations 1b, 2, 3 and 4. Table 5.2 gives the properties of materials of the multilayered models. These are taken from both well logs and literature as seen in Leaney et al. (2001b) and MacLeod et al. (1999). The anisotropic properties of the model, δ and ϵ, are according to the mismatch analysis from Mikhailov et al. (2001b) and Mikhailov et al. (2001a). These values agree with values derived from walkaway VSP data.

To gain insight into the influence of the layer thickness on parameter estimation

model	lvs	sand	shale	lvs	sshale	reserv.	Lime.	η_{eff}	χ_{eff}
1	0	0.5	0.5	0.0	0.5	0.5	HS	0.075-0.0757	0.18-0.22
1b	0	0.5	0.5	0.0	0.5	0.5	HS	0.100-0.170	0.17-0.11
2	0	1.4	0.23	0.0	0.27	0.075	HS	0.076-0.077	0.18-0.20
3	0	0.5	0.5	0.05	0.5	0.5	HS	0.075-0.076	0.18-0.24
4	0.25	1.15	0.23	0.0	0.27	0.075	HS	0.069-0.0755	0.39-0.41

Table 5.1: Contents and layer thickness for multilayer VTI models. Note that model 3 includes a low velocity layer in the middle of the model while model 4 has a near-surface isotropic low velocity layer. (HS=halfspace, lvs=low velocity sand, sshale=sandyshale, all layer thicknesses are given in km.). A zero thickness denotes absence of the layer.

and the influence of near surface low velocity layers, I vary the layer thickness in Section 5.4.3 (model 2). Furthermore, the base model will be extended with a low velocity layer in the middle (Section 5.5.1, model 3) and finally combining both, leading to a model with varying layer thicknesses and a low velocity layer on top (Section 5.5.2, model 4). Table 5.1 also lists the range of the P- and C-wave anisotropy parameters η_{eff} and χ_{eff} which are calculated from the model properties.

layer	ρ [g/cm^3]	V_{p0i}	V_{s0i}	ϵ	δ	δ^*
low velocity sand (lvs)	1.9	1.6	0.2			
low velocity sand$*$	1.9	1.6	0.2	0.001	0.0004	
sand	2.3	2.13	0.9	0.11	0.03	0.0083
shale	2.19	2.2	0.9	0.11	0.03	-0.031
sandyshale (sshale)	2.19	2.5	0.975	0.11	0.04	-0.064
reservoir sand	2.2	2.56	1.372	0.13	0.06	-0.09
limestone	2.01	2.43	0.731			

Table 5.2: Properties of the materials for the multilayered VTI modelling study. δ^* indicates the changed values for Model 1b. The low velocity layer within model 3 is very lightly anisotropic and the layer is marked $*$. All velocities are in [km/s].

Synthetic seismograms are calculated using the modelling package ANISEIS (Taylor, 2001), utilising the reflectivity method (Kennet, 1983). Each model scenario produces three components: vertical, inline and crossline components. However, the crossline component is zero in this case. The vertical component represents mainly the P-wave and the horizontal component the C-wave events.

5.4 Effects of layering

In this section I want to investigate the influence of varying layer thickness on parameter estimation. Therefore, as a first step I use an isotropic version of model 1 (the base model) to see the effect of layering without overlying anisotropy. In a second step I use the anisotropic model 1 as introduced above. Finally, in the third study I vary the layer thickness and compare the result with the equally thick layers. For the first model I use the double semblance scanning technique to estimate the P-wave stacking velocity V_{p2} and anisotropy parameter η_{eff} of the P-wave. Likewise I estimate the C-wave stacking velocity V_{c2} and anisotropy parameter χ_{eff} with a similar routine for all models.

5.4.1 Isotropic media

Before considering the effects of VTI media I want to investigate if there is an effect of layering when the layers themselves are purely isotropic estimating η_{eff} and

χ_{eff}. From Equations (2.37) and Equation (2.38) I expect to find small effective anisotropic parameters even in an isotropic medium due to layering. Therefore, I set the anisotropy parameters δ and ϵ in model 1 to zero and apply the double scanning routines to the synthetic seismograms of horizontal and vertical components. The synthetic seismograms are displayed in Figure 5.1. Arrows indicate the events corresponding to the 4 layers and circles mark diminishing amplitudes and phase reversals, which will be discussed in Section 5.7.

Figure 5.2 shows the output from the double scanning analysis search-

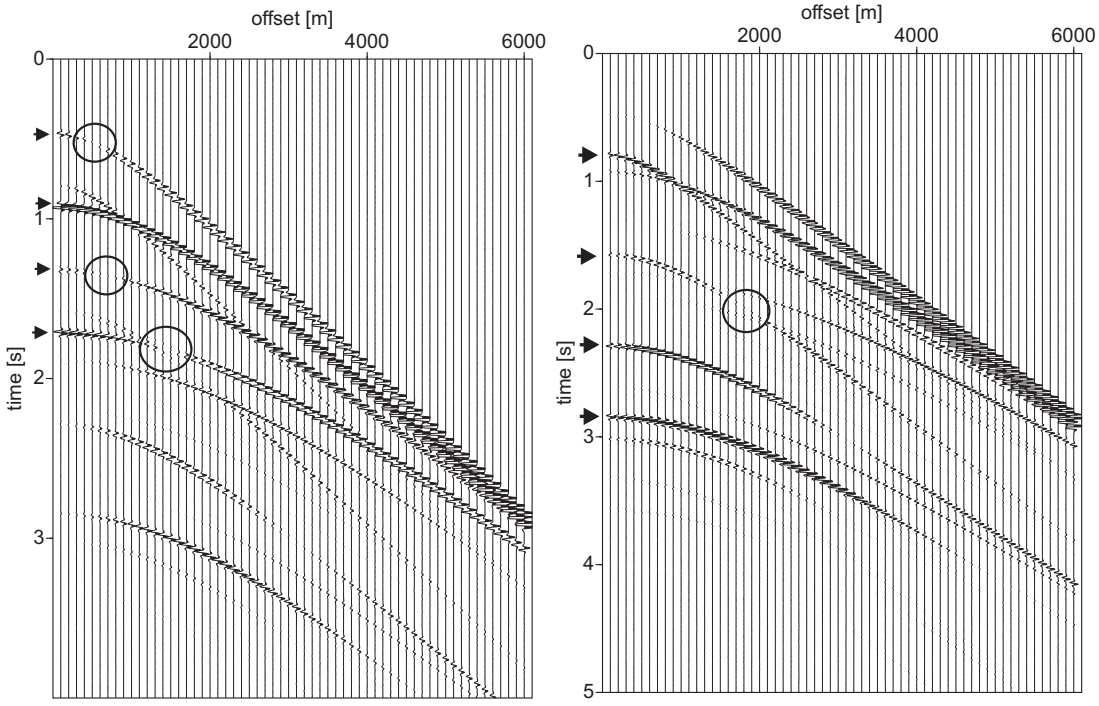

(a) Z-component (b) X-component

Figure 5.1: Synthetic seismograms for isotropic model 1. (a) Vertical (Z) component and (b) horizontal (X) component. Arrows indicate the events corresponding to the 4 layers and circles mark diminishing amplitudes and phase reversals.

ing for χ_{eff} and V_{c2}. From left to right the events corresponding to $t_{c0} = 0.79, 1.573, 2.286, 2.846$ seconds are shown. The black dots indicate the model values. An offset-to-depth ratio of $x/z = 2$ has been used for the parameter estimation. The results for layer 1, 3 and 4 are very good with errors around $\Delta\chi_{\text{eff}} = 0.02$ and thus the model values almost coincide with the maxima in

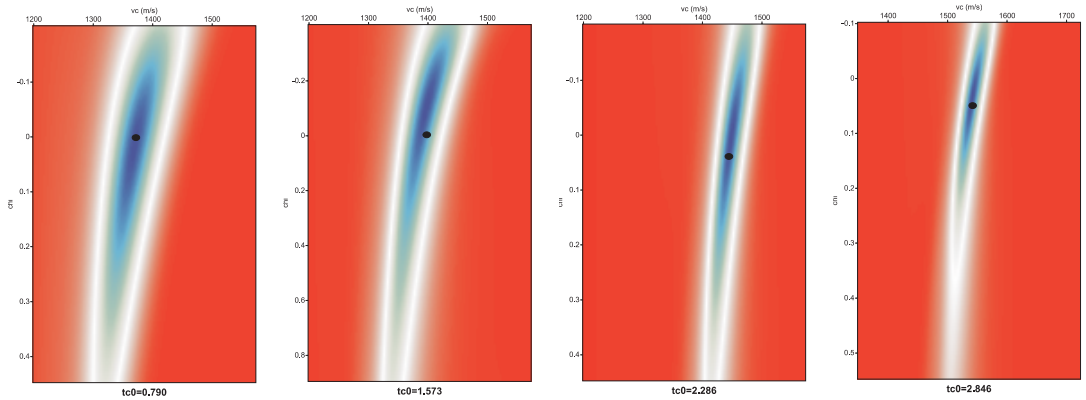

Figure 5.2: Results for double scanning of χ_{eff} and V_{c2} in Model 1, with isotropic layers, for the events corresponding to $t_{c0} = 0.79, 1.573, 2.286, 2.846$ seconds. The effective parameters, found with double scanning, are purely effects of layering. The black points indicate the model values. An offset-to-depth ratio of $x/z = 2$ was used except for layer 2, were a reduced $x/z = 1.8$ was applied.

Figure 5.2. However, layer 2 gave a very high error of $\Delta\chi_{\text{eff}} = 0.3$. A closer examination of the synthetic seismogram (Figure 5.1(b)) shows, that at the maximum of the included offset of 2000 metres the amplitude becomes very weak and when it reappears shows a reversed phase. Therefore, I repeated the parameter estimation for that layer with a reduced $x/z = 1.8$ to avoid this region and the improved result is shown in see Figure 5.2. It still features the largest error with $\chi_{\text{eff}} = 0.002 \pm 0.08$.

The ellipses of maxima from the parameter estimation are located almost vertically in the $\chi_{\text{eff}} - V_{c2}$ parameter space. As found in Chapter 4, this suggest decoupled parameters. This means, that the estimation of one parameter has not a big influence on the other. The stacking velocity V_{c2} is very well confined with a maximum error of $\Delta V_{c2} = 0.026$ km/s for a range of possible χ_{eff} within the maximum ellipse, further supporting this suggestion.

For comparison, Figure 5.3 shows the result for the P-wave $\eta_{\text{eff}} - V_{p2}$ double scanning using a $x/z = 3$. If I pick the values without knowing the actual model values, I would obtain picks with a maximum error for the first layer of $\eta_{\text{eff}} = 0.0 \pm 0.114$ and otherwise $\eta_{\text{eff}} = 0.0031 \pm 0.055$. Again, the synthetic seismogram reveal that the first layer shows a diminished amplitude with a phase reversal within the included offset for the analysis. As this amplitude phenomenon appears not at the

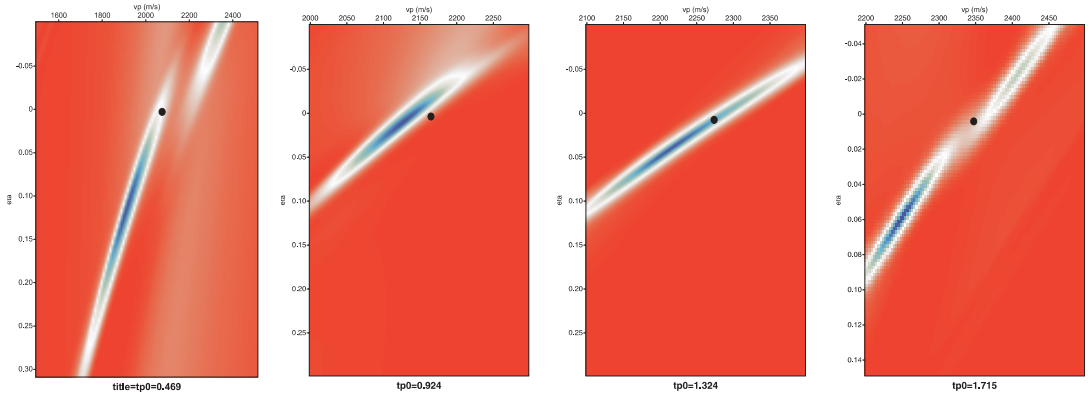

Figure 5.3: Results for double scanning of η_{eff} and V_{p2} in model 1, with isotropic layers, for the events corresponding to $t_{p0} = 0.469, 0.924, 1.324, 1.715$ seconds. The effective parameters, found with double scanning, are purely effects of layering. The black dots indicate the model values. For the parameter estimation a $x/z = 3$ was used.

edge of the offset range, I use this result.

Furthermore, for the P-waves the resulting maxima for parameter estimation lies at an angle in the $\eta_{\text{eff}} - V_{p2}$ parameter space. I have found the same behaviour in Chapter 4 and concluded that the stacking velocity V_{p2} is not decoupled from the anisotropy parameter η_{eff}. The results here confirm these findings as for both parameters large picking errors occur ($\Delta V_{p2} = \pm 0.22$ km/s for layer one and the next largest error is $\Delta V_{p2} = \pm 0.09$ km/s). Also, the model value coincides with the model maximum only for layer 3. For layers one and four, the actual model values are between two local maximum, i.e. cannot be resolved uniquely. The stacking velocity V_{p2}, in particular, is not well defined and not located within the maxima. This confirms that picking one parameter with an error leads to a big error for the other parameter, i.e. they are not decoupled.

All picking results for both P- and C-waves are listed in Table 5.3. The errors for each pick are illustrated in Figure 5.4 in relation to the model value. At a first glance the errors for both P- and C-waves appear to be large in comparison to the very small model values. However, in Chapter 4, I found that the picked value always has an inherited error, i.e. even for a single isotropic layer the anisotropy value could not be estimated without any error. Also, although there is an order of magnitude difference between the size of the anisotropy parameters of P- and C-wave, the picking errors for both have the same magnitude. This means, that

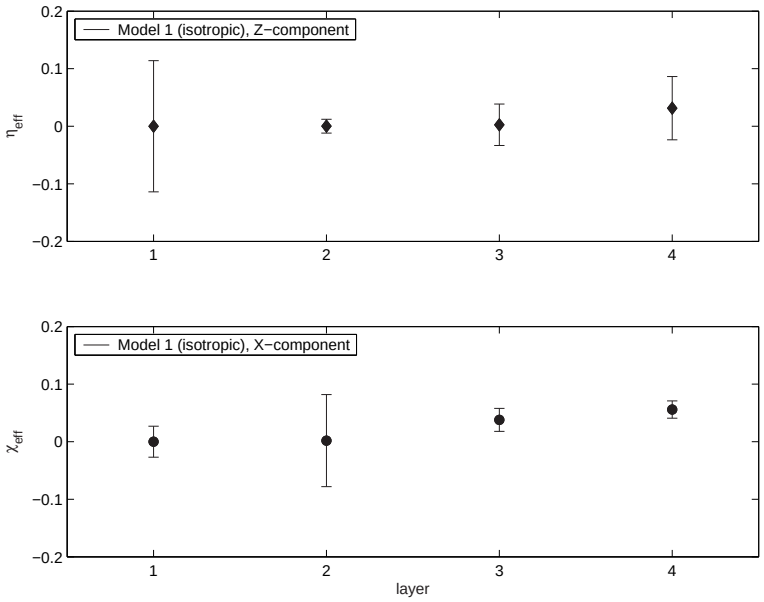

Figure 5.4: Model values for the isotropic version of the base model (model 1) for η_{eff} and χ_{eff} and its picking errors. Results are also listed in Table 5.3.

the C-wave parameter the smaller relative errors.
In summary this study shows that P-wave parameters are less well resolved (no unique pick possible for two layers) and the relative errors are larger than for the C-wave. Furthermore, the stacking velocity and anisotropy parameter are not decoupled and thus less suitable for parameter estimation. On the contrary, C-waves do not show these problems. We must ask if the more reliable results from C-waves can be used to obtain the P-wave parameters, i.e. is it is possible to calculate η from χ reliably?

5.4.2 VTI media

The anisotropic model 1 is the simplest model version featuring equally thick layers. Figure 5.5 shows the resulting seismograms for this model: (a) the vertical and (b) the horizontal components. The solid lines which are plotted on top of the seismograms are traveltimes of reflected events for each layer. They are calculated with Equation (2.62) for the C-wave and Equation (2.57) for the P-waves respectively. Both seismogram and traveltime curves are muted according to the limits of validity of the traveltime equations, i.e. $x/z = 3$ for the P-wave and $x/z = 2$ for the C-wave. The agreement shows that in their limits the traveltime

	model	sand	shale	sandyshale	res. sand
η_{eff}	iso	0.000	0.0001	0.0025	0.0031
	iso (pick)	0.114	0.012	0.038	0.058
V_{p2}	iso	2.130	2.165	2.271	2.340
	iso (pick)	1.910	2.120	2.220	2.250
χ_{eff}	iso	0.000	0.002	0.038	0.056
	iso (pick)	0.027	-0.070*	0.020	0.041
V_{c2}	iso	1.385	1.396	1.449	1.542
	iso (pick)	1.370	1.390*	1.450	1.540

Table 5.3: Comparison of theoretical and picked χ_{eff} and V_{c2} and η_{eff} and V_{p2} values for isotropic version of model 1. 'pick'stands for picked values from double scanning. All velocities are in km/sec. * indicates the values which were gained with a slightly reduced $x/z = 1.8$ for that layer.

approximations match very well with the seismograms.

Figure 5.6 shows the results from the double scanning for the P-wave, and Figure 5.7 for the C-wave. I first have a closer look at the results for the P-waves. The model values for $\eta_{\text{eff}} - V_{p2}$ are indicated by a black dot for each of the four events which correspond to the four layers in the model. Obviously, it is not possible to pick a unique value for the first ($t_{p0} = 0.469$ sec) and fourth ($t_{p0} = 1.715$ sec.) event. Only the second event ($t_{p0} = 0.924$ sec) allows an easy pick of the values. In comparison the double scanning results searching for $\chi_{\text{eff}} - V_{c2}$ show a good resolution for the picks. For all four reflected events, parameters can be picked which coincide well with the model values. Both theoretical and picked values are listed in Table 5.7. The maximum error for these four events is $\chi_{\text{eff}} = 1.194 \pm 0.034$. The model values and the errors are also illustrated in Figure 5.16. Considering the good fit of the calculated traveltime curves with the seismograms the poor resolution for the vertical components is a surprise. I expect that one reason for this poor resolution is the small size of the parameter η_{eff} (see Table 5.1). In contrast, the C-wave parameter χ_{eff} is an order of magnitude larger than η_{eff} and can be resolved. For a deeper understanding, I next investigate the resolution of the double scanning when the values of the parameter η_{eff} are increased to the same size as the ones of χ_{eff}.

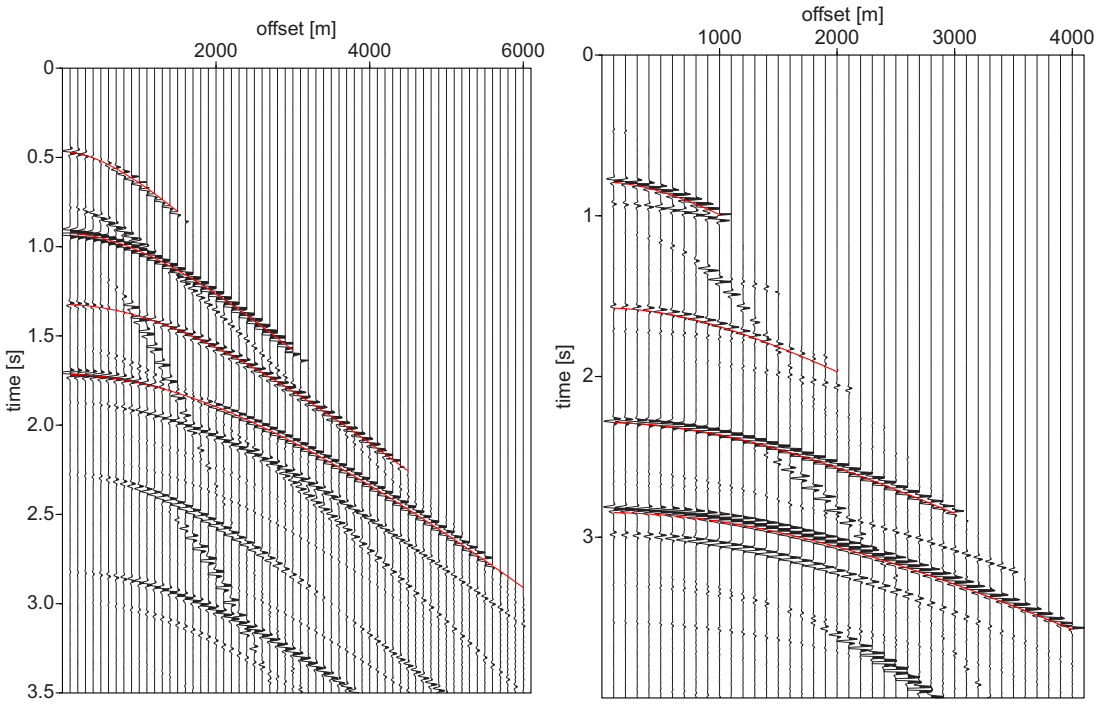

(a) Z-component (b) X-component

Figure 5.5: Synthetic seismograms for VTI model 1 featuring equally thick layers. For the 4 layers traveltime curves are printed on top of the seismograms. (a) Vertical component and (b) horizontal component.

Model 1b: Increased η_{eff}-values

Model 1b is essentially the same as model 1 with the exception that the values of η_{eff} are increased by an order of magnitude (see Table 5.2). The seismograms for this slightly altered model are displayed in Figure 5.8 (a) for the vertical and (b) horizontal components, respectively. Again the approximated traveltime curves are superimposed on the seismograms. For the vertical component I also calculate and plot the traveltimes for slightly changed η_{eff} values, i.e. $\eta_{\text{eff}} \pm 0.05$. The traveltimes of the seismograms agree with the approximated traveltimes. The approximated traveltimes for $\eta_{\text{eff}} \pm 0.05$ show that an error in η_{eff} of 0.05 has effects on the mid- to far-offsets. I only repeat the double semblance scan for $\eta_{\text{eff}} - V_{p2}$ on this CDP-gather as the $\chi_{\text{eff}} - V_{c2}$ were well resolved by the original model. The results of the double semblance scan are illustrated in Figure 5.9 and the model values are indicated by black dots. The results have improved although the model

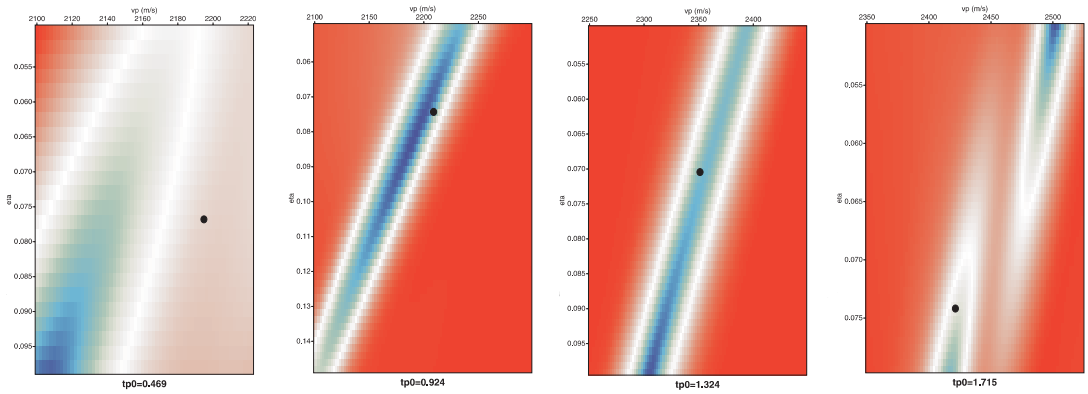

Figure 5.6: Double semblance scanning results for the P-wave parameters $\eta_{\text{eff}} - V_{p2}$ for the 4 events of model 1. Model values are indicated by a black dot.

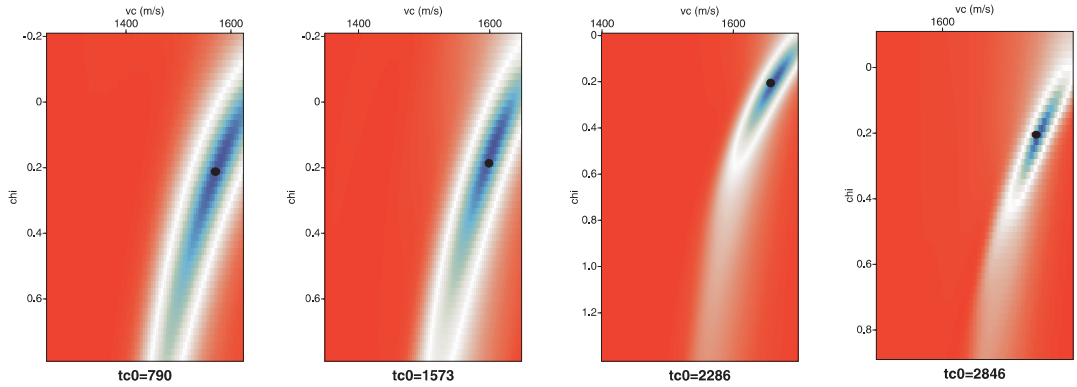

Figure 5.7: Double semblance scanning results for the C-wave parameters $\chi_{\text{eff}} - V_{c2}$ for the 4 events of model 1. Model values are indicated by a black point.

values for the first and fourth layers are not within the maximum contour. The actual values are listed in Table 5.7. The maximum error is $\eta_{\text{eff}} = 0.17 \pm 0.06$. The values for all four layers and the error bars are displayed in Figure 5.10. The size of the parameter seems to have a great impact on the parameter estimation. Small values for η_{eff} for model 1 could not be resolved, whereas values an order of magnitude larger can be resolved. Yet, the maximum error in estimating η_{eff} is double the error as for estimating χ_{eff} in model 1.

Summarising the results, model 1, featuring equal thickness anisotropic layers, I have obtained parameter estimations for both P- and C-waves using the vertical and horizontal CDP/ACP gathers, respectively. I find that the C-wave parameter χ_{eff} and the corresponding velocity V_{c2} are very well defined and can be easily picked. The P-wave parameter η_{eff} and velocity V_{p2} cannot be resolved. There are

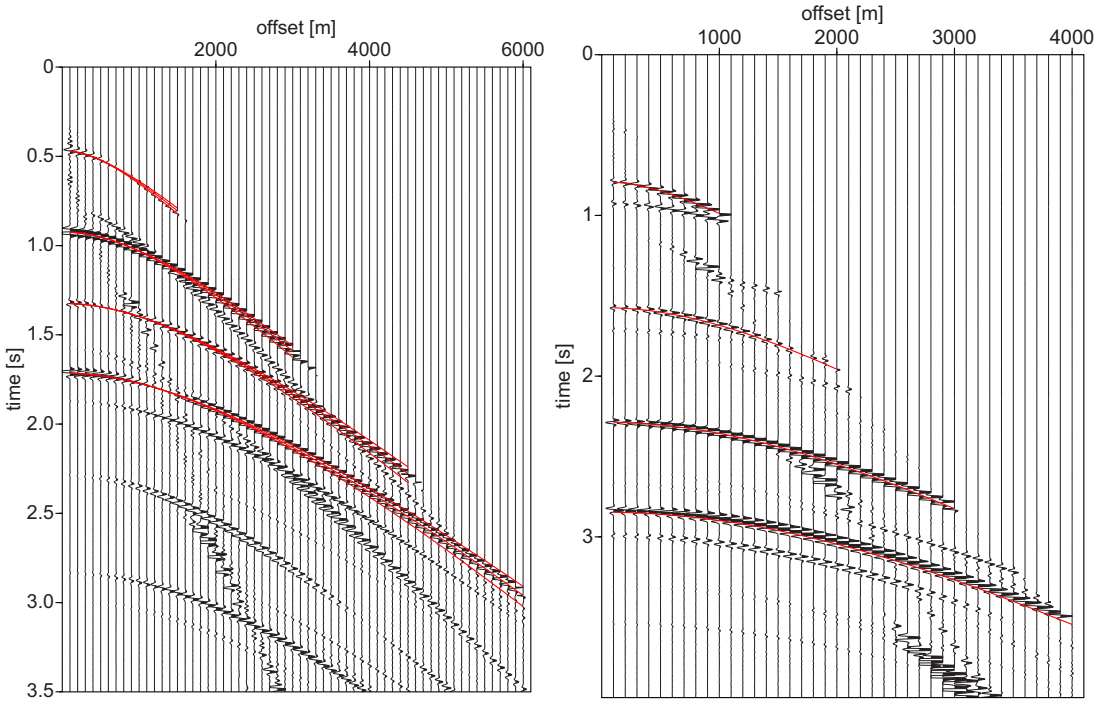

(a) Z-component (b) X-component

Figure 5.8: Seismograms for model 1b with equally thick layers but increased η_{eff}-values. Traveltime curves for the 4 layers are printed on top of the seismograms of (a) vertical component and (b) horizontal component. The solid traveltime curve has been calculated using the correct η_{eff} values and the dashed curves are calculated using $\eta_{\text{eff}} \pm 0.05$.

two possible reasons: Firstly, the magnitude of the P-wave non-hyperbolic moveout is much smaller than the magnitude of the C-wave non-hyperbolic moveout in the same range. Secondly, η_{eff} values for this model are very small (less than 0.1) whereas the χ_{eff} values are larger in a range of 0.18-0.22. These arguments are supported by a test where I increase the values of η_{eff} to the same range of the χ_{eff} values. These values could then be resolved. Secondly, I investigated an effect of layering without polar anisotropy. I find that the effect of the layering leads to an effective anisotropy parameter, which is much smaller than the one in the VTI case. η_{eff} and stacking velocity V_{p2} are not decoupled and often do not yield a unique pick. χ_{eff} and C-wave stacking velocity V_{c2} show a better decoupling and also smaller picking errors than the P-wave parameters.

Considering these findings I performed the semblance double scanning only for

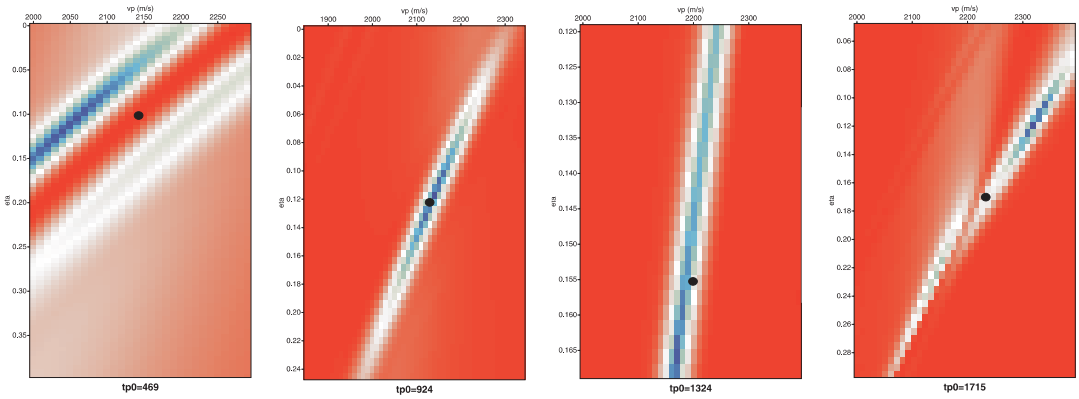

Figure 5.9: η_{eff} values for model 1b have been increased to 0.1-0.17 by changing δ to 0.083-(-0.09). $\eta_{\text{eff}} - v_p$-scanning result for the 4 events of Model 1b. The black dots indicate model values for the layers.

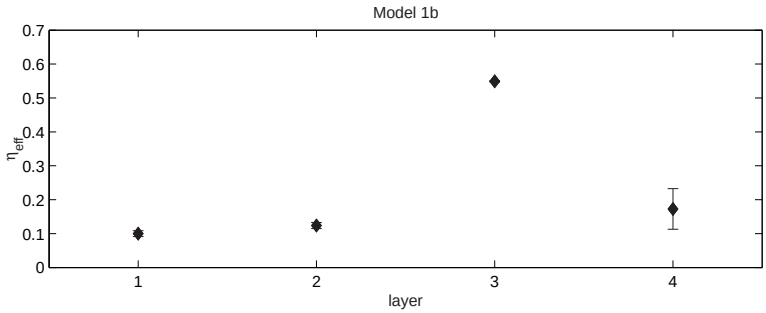

Figure 5.10: Model values of η_{eff} for model 1b and the corresponding picking errors. Values are also listed in Table 5.7.

χ_{eff} and V_{c2} for the models 2-4. The η_{eff} values are in the same small range as for model 1 and thus cannot be resolved.

5.4.3 Varying layer thicknesses in VTI media

The influence of different layer thicknesses was studied with model 2. The model parameters are as for the model 1 except for the layer thicknesses given in Table 5.1. Focusing on the parameter estimation for the C-wave only, Figure 5.11 shows only the seismogram of the horizontal component for model 2. The solid lines illustrate the traveltimes for reflected events for each layer calculated using Equation (2.62). The result of the double semblance scanning for χ_{eff} and V_{c2} are shown in Figure 5.12. All maximum contours show a good match with the model values (black dots). The corresponding picked values are listed in Table 5.8. Note that the plot for the third layer shows the re-estimated values after

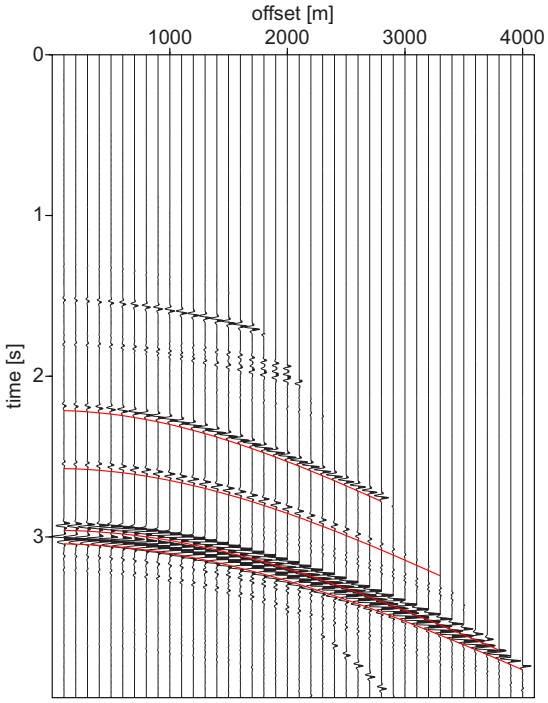

Figure 5.11: Seismogram of horizontal component of model 2. The solid lines represents the calculated traveltime using the traveltime approximation by 2.62 in their region of validity $x/z = 2$.

muting the interfering events due to thin layers. Hence, a thick top layer and thinner layers underneath lead to interfering events. Only after muting of these events can the model values be resolved with a maximum error of $\chi_{\text{eff}} = 0.2 \pm 0.02$. This implies that careful processing to isolate the target horizon is required in real data analysis.

5.5 Effects of velocity contrasts

After studying the effect of variation in layer thickness on parameter estimation, I focus in this section on the effect of velocity contrasts. Model 1, whose parameters are unchanged in model 2, shows smoothly varying velocities without large jumps. To explain this in some more detail, I list different vertical velocity ratios γ_0 for model 1 as well as model 3 and 4 which both feature a low velocity layer in Table 5.4. The γ_0 values show that the first model varies smoothly between 2.319 and 2.45 while the low velocity layer in model 3 shows a moderate jump from 2.405 to 2.76 and the low velocity layer on top (model 4) has a strong contrast of 8.0

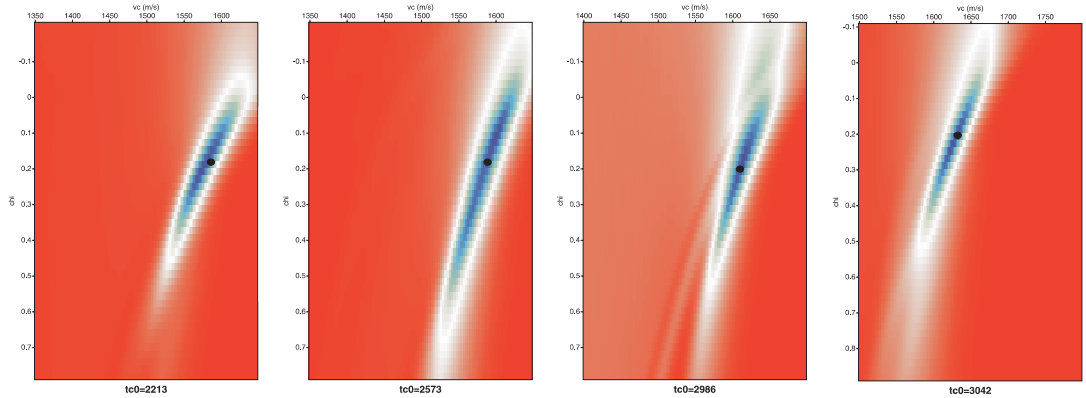

Figure 5.12: $V_{c2} - \chi_{\text{eff}}$ double semblance scanning result for the 4 events of model 2.

to 3.631. These γ_0 values are calculated from the total traveltime for each layer and thus are not interval velocity ratios. Model 3 is used to investigate on the impact of this jump in velocities occurring within a sequence of equally thick layers with smooth varying velocities. Here the averaging of the overlying layers smooth the strong velocity contrast between the individual layers. Finally, model 4 describes a setting with varying layer thicknesses and a low velocity layer on top which could be for instance a near-surface layer with low cementation. The velocity contrast here is not smoothed by overlying layers and a stronger impact on parameter estimation is expected in this setting. A more detailed study on near surface problems can be found in Chapter 6.

model	layer 1	layer 2	layer 3	layer 4	layer 5
1	2.367	2.405	2.453	2.319	-
3	2.367	2.405	2.760	2.703	2.519
4	8.000	3.631	3.476	3.368	3.321

Table 5.4: Vertical velocity ratios γ_0 of the base model and its extensions featuring a low velocity layer.

5.5.1 Influence of low velocity layer

With model 3, I used the equally thick layers from model 1 but included in the middle a thin low velocity and low anisotropic layer (for parameter values see Table 5.2 and Table 5.1 using the low velocity layer $*$). Table 5.5 lists the model values for the P- and C-wave parameter estimation. In line with the results of my previous studies I use only the C-wave data. The fullwave seismograms for the

depth [km]	t_{p0} [s]	V_{p2} [km/s]	η_{eff}	t_{c0} [s]	V_{c2} [km/s]	χ_{eff}
0.5	0.469	2.193	0.0755	0.790	1.58	0.181
1.0	0.924	2.229	0.0757	1.573	1.6	0.187
1.05	0.986	2.194	0.0773	1.854	1.49	0.262
1.55	1.387	2.318	0.0770	2.567	1.58	0.267
2.05	1.777	2.409	0.0759	3.127	1.68	0.241

Table 5.5: P- and C-wave model values for velocity and anisotropic parameter estimation for model 3 with low velocity layer in the middle.

horizontal component is displayed in Figure 5.13(a), and the calculated traveltime curves are superimposed for the 5 layers. Applying the double semblance scanning technique to this seismogram I obtain the five picks displayed in Figure 5.14, from the left to the right, for vertical traveltimes $t_{c0} = 0.791, 1.573, 1.854, 2.567, 3.127$ seconds. The black dots indicate the model values. Looking at the semblance plots and the model values it is clear that the first two layers can be estimated fairly well as can the third, low velocity, layer. However, underneath the low velocity zone, the semblance plots for layer 4 and 5 indicate a larger error. Table 5.8 lists the actual picked values with very small errors for the C-wave velocities (max. 0.023 km/s) and a range from 0.017 to 0.059 for the anisotropy parameter. The result from parameter estimation on the C-wave data of model 3 suggests, that the low velocity layer itself is not problematic but the layers underneath it show a lower resolution. Nevertheless, the largest total error for the anisotropy parameter is found for the layer underneath the low velocity zone with $\chi_{\text{eff}} = 0.267 \pm 0.067$. The low velocity layer occurs in the middle of the model and its velocity ratios are therefore smoothed by the overlying events. Hence, the parameter estimation is not severely affected by it.

5.5.2 Influence of low velocity layer and varying layer thickness

In model 4 the isotropic low velocity layer is set on top of the other layers in order to simulate a near surface surrounding. The strong velocity contrast is not smoothed by overlying layers and thus has stronger impact on the parameter estimation. Furthermore, the layering is similar to model 2, i.e. it is varying in thickness (see Table 5.1). Figure 5.13 (b) shows the seismograms of the horizontal

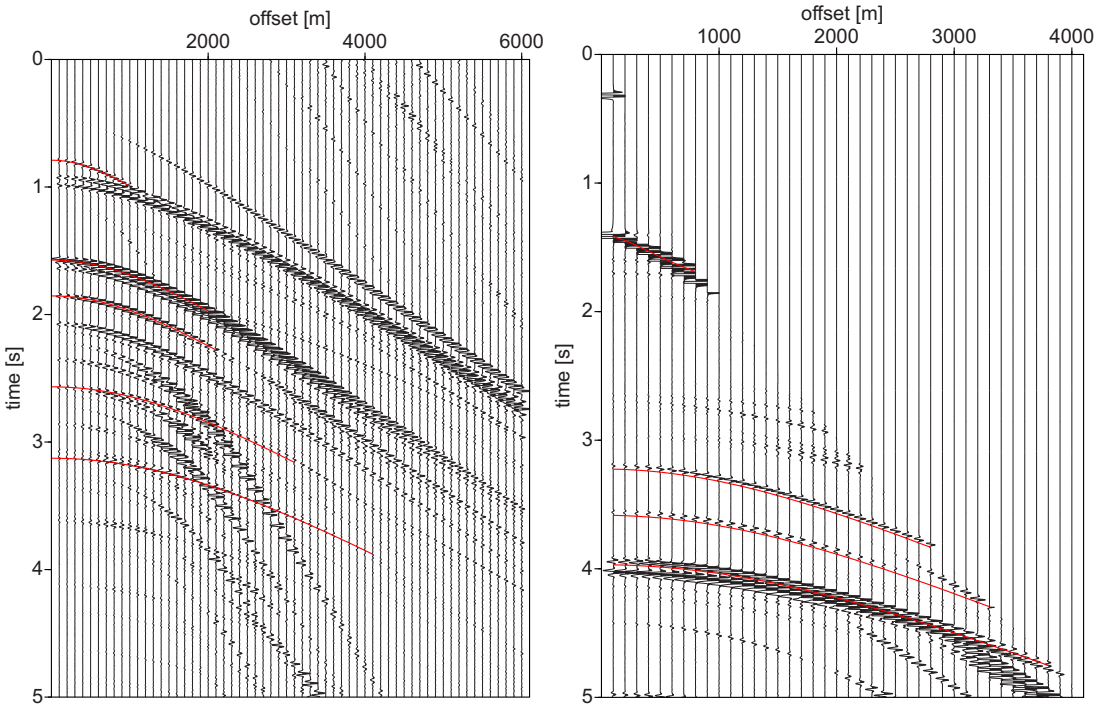

(a) model 3 (b) model 4

Figure 5.13: Synthetic seismograms of horizontal component for (a) model 3 (see Table 5.5) and (b) model 4 (see Table 5.6). Superimposed are the calculated traveltime curves for the 5 layers using the traveltime approximations in Chapter 2 Equation (2.62) for C-wave traveltimes. The curves are muted according to the restriction of the traveltime equations.

components and the traveltime curves plotted on top of it while Table 5.6 gives the model values for parameter estimation. However, I focus again on the C-wave component only as the values for η_{eff} are very small and could not be recovered in model 1. The double semblance scanning results for the four anisotropic layers are displayed in Figure 5.15. Comparing these results with the ones from model 2, it can be seen that it is not possible to pick a unique event for layer 2. The other 3 layers show a larger mismatch between the model values and the maximum contours than for model 2. The actual values are listed in Table 5.8. Again, from the double scanning analysis I find that muting of interfering events helps to identify and resolve the correct values for the third layer. The parameter estimation is now more difficult and the maximum error is $\chi_{\text{eff}} = 0.4 \pm 0.05$ and the exceptional upper shale event has an error bar of 0.39 ± 0.17. The presence

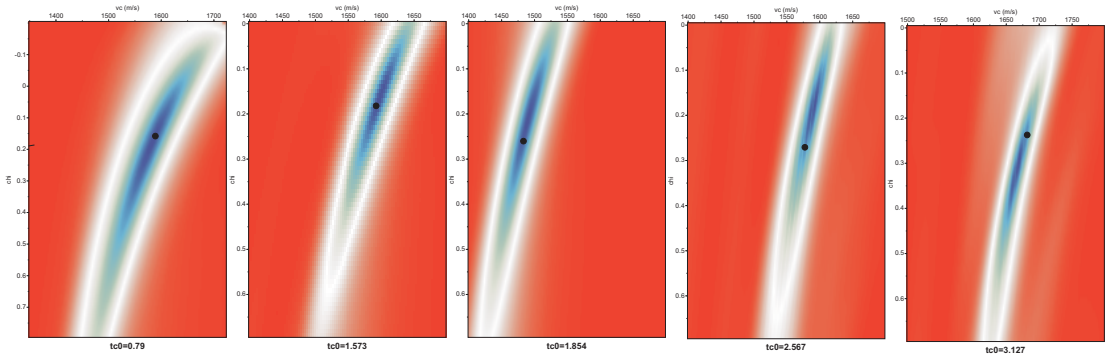

Figure 5.14: $V_{c2} - \chi_{\text{eff}}$ double semblance scanning result for the 5 events of model 3 (for C-wave time $t_{c0} = 0.791, 1.573, 1.854, 2.567, 3.127$ seconds). A black dot indicates the model value for each layer.

depth [km]	t_{p0} [s]	V_{p2} [km/s]	η_{eff}	t_{c0} [s]	V_{c2} [km/s]	χ_{eff}
0.25	0.313	1.600	0.000	1.406	0.566	0.000
1.40	1.392	2.075	0.069	3.224	1.246	0.418
1.63	1.601	2.101	0.071	3.584	1.288	0.394
1.9	1.817	2.166	0.075	3.969	1.345	0.406
1.975	1.876	2.185	0.075	4.053	1.365	0.404

Table 5.6: C- and P-wave model parameters for parameter estimation on model 4 with low velocity layer on top and varying layer thickness.

of the low velocity layer increased the difficulty in parameter estimation. Careful processing is required to isolate the events. The accuracy and resolution is also reduced. However, the errors are within the error margins.

5.6 Results of modelling studies

5.6.1 Isotropic model

My first modelling study looked at an isotropic model to see the effect of layering. The effective anisotropy parameters are purely due to layering and are very small. Thus parameter estimation shows for the C-wave a maximum error of $\chi_{\text{eff}} = 0.002 \pm 0.08$. In comparison, the maximum error for the P-wave parameter is $\eta_{\text{eff}} = 0.0314 \pm 0.06$, which is in relation to the size of the parameter an error of almost 200%. Note, that for the first layer the error is larger due to a diminishing amplitude and phase reversal ($\eta_{\text{eff}} = 0.0 \pm 0.114$). In relation to the magnitude of the model values the errors seem large. However, η_{eff} is an order of magnitude

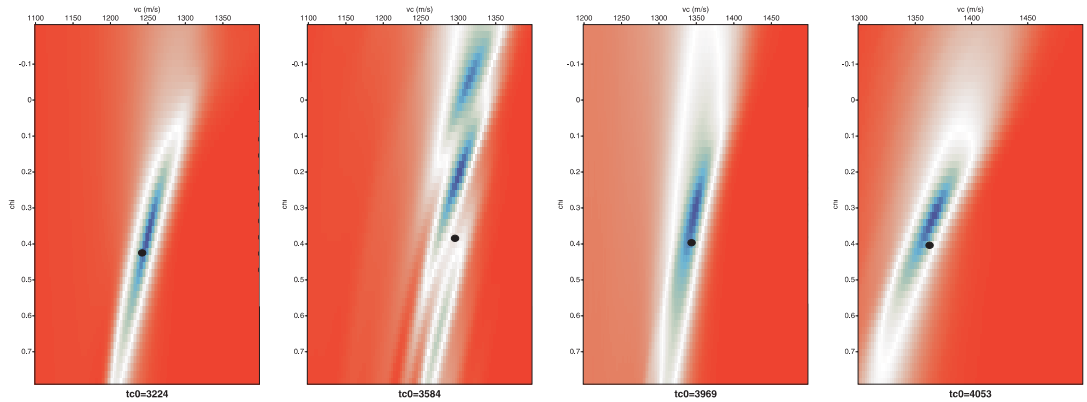

Figure 5.15: Double semblance scanning results for $\chi_{\text{eff}} - V_{c2}$ of the horizontal component of model 4. Displayed are the results for the four anisotropic layers underneath the low velocity layer. The black dots indicate the model values.

smaller than χ_{eff} but the errors are of the same magnitude, i.e. the χ values are better resolved and all of them are within the error margin. Further, the stacking velocities are very well resolved for the C-wave with a maximum error of $V_{c2} = 1.360 \pm 0.026$ km/s. The largest error of the P-wave stacking velocity is $V_{p2} = 2.340 \pm 0.09$ km/s. The parameter estimation results also suggest from the form and location of the maxima ellipses, that the parameters are not decoupled for P-waves but mostly decoupled for C-waves. This explains the well resolved C-wave velocities in contrast to the P-wave parameters.

5.6.2 Equal thickness model

VTI model 1 features C-wave anisotropy parameters an order of magnitude larger than the P-wave parameter. Parameter estimation of P-wave anisotropy parameter η_{eff} from the vertical component confirms the findings from the isotropic case, i.e. that small values are not very well resolved or not at all (layer 1 and 4). If the η_{eff} values are increased to the same size as the C-wave parameters the parameter estimation improves and the maximum absolute picking error is as small as $\eta_{\text{eff}} = 0.17 \pm 0.06$.

5.6.3 Comparison of all models

Summarising the results for parameter estimation of C-wave parameters of all anisotropic models, Figure 5.16 shows the model values and the corresponding

error bars from picking. As expected, model 1 shows the smallest errors and the parameter estimation is straight forward. With varying layer thicknesses, the parameter estimation becomes difficult for model 2. Thin layers are interfering and these events have to be muted to obtain a unique and accurate picking result. Yet, the final results show mostly small errors.

5.6.4 Influence of low velocity model

The influence of a low velocity layer in the model, i.e. a strong velocity contrast, is investigated in model 3 and 4. Model 3 is similar to model 1 but has a thin low velocity layer in its middle. Due to the surrounding layering the velocity contrast of the stacking velocities is not extreme ($\gamma_0 = 2.405$ to $\gamma_0 = 2.76$). However, the absolute picking error for the layer underneath the low velocity zone is $\chi_{\text{eff}} = 0.267 \pm 0.067$, which is still fairly good.
Finally, model 4 is affected by the influence of a low velocity layer as a first layer on top of model 2, i.e. varying layer thicknesses. Parameter estimation can be improved by muting interfering events so the event is clearer to pick but the errors are larger than for the other models. Thus I conclude that variable layer thicknesses, especially thin layers, and the occurrence of near surface low velocity layers complicate parameter estimation and make the estimated parameter values less reliable. The largest error is $\chi_{\text{eff}} = 0.41 \pm 0.087$ which is still acceptable.

	model	sand	shale	sandyshale	res. sand
χ_{eff}	1	0.180	0.194	0.220	0.203
	1 (pick)	0.18	0.16	0.20	0.201
V_{c2}	1	1.584	1.600	1.662	1.755
	1 (pick)	1.573	1.593	1.659	1.745
η_{eff}	1b	0.100	0.124	0.155	0.173
	1b (pick)	0.109	0.115	0.157	0.113
V_{p2}	1b	2.148	2.139	2.200	2.228
	1b (pick)	2.050	2.141	2.181	2.319

Table 5.7: Comparison of theoretical and picked χ_{eff} and V_{c2} values for model 1 and η_{eff} and V_{p2} values for Model 1b. 'pick' stands for picked values from double scanning. All velocities are in km/sec.

	model	sand	shale	sandyshale		low vel.	res. sand
χ_{eff}	2	0.181	0.185	0.202			0.202
	2 (pick)	0.18	0.188	0.303	0.202∗		0.22
V_{c2}	2	1.5837	1.5884	1.616			1.6312
	2 (pick)	1.5753	1.5807	1.608	1.6065∗		1.6254
χ_{eff}	3	0.181	0.187	0.262		0.267	0.241
	3 (pick)	0.20	0.17	0.234		0.2	0.3
V_{c2}	3	1.584	1.600	1.490		1.580	1.683
	3 (pick)	1.570	1.600	1.490		1.590	1.677
χ_{eff}	4	0.42	0.39	0.41			0.40
	(pick)	0.386	0.22	0.39	0.323∗		0.34
V_{c2}	4	1.2465	1.2885	1.3454			1.3651
	4 (pick)	1.249	1.296	1.3566	1.3469∗		1.3635

Table 5.8: Comparison of theoretical and picked χ_{eff} and V_{c2} values for model 2-4. The asterisk (∗) marks re-estimated values after muting the interfering events due to the thin reservoir. 'pick' stands for picked values from double scanning and all velocities are in km/s.

5.6.5 η estimation from χ values

As in Chapter 4, I use the picked χ_{eff} values to calculate η with Equation (2.33). Table 5.9 lists these calculated values and the absolute error when compared with the model values. Recalling that for model 1 the η_{eff}-values were hard to estimate and partly not resolvable from P-waves while the calculated values are very good with a maximum error of $\eta_{\text{eff}} = 0.0757 \pm 0.011$. The modified model 1b with increased η_{eff}-values had a maximum error of $\eta_{\text{eff}} = 0.124 \pm 0.019$. This means, for the original model 1, η_{eff} could not be resolved from P-waves but calculated from the C-wave parameter with no larger error than the picked η_{eff} from the modified model 1b.

Model 2 shows a maximum error of $\eta_{\text{eff}} = 0.0766 \pm 0.012$ where the best picked values were used for muted events. Model 3 shows larger errors for layer 4 and 5 underneath the low velocity zone. This is expected as the χ_{eff} values have a larger error there too. Nevertheless, the maximum error is only $\eta_{\text{eff}} = 0.0759 \pm 0.026$. Finally model 4 displays the largest errors with a maximum of $\eta_{\text{eff}} = 0.079 \pm 0.038$. Again, these large errors are probably due to the combined influence of layering and the strong velocity contrast from the low velocity layer on top of the model.

model	1		2		3		4	
layer	$\eta(\chi)$	$\lvert\Delta\eta\rvert$	$\eta(\chi)$	$\lvert\Delta\eta\rvert$	$\eta(\chi)$	$\lvert\Delta\eta\rvert$	$\eta(\chi)$	$\lvert\Delta\eta\rvert$
sand	0.075	0.003	0.075	0.003	0.084	0.008	0.066	0.013
shale	0.065	0.011	0.078	0.002	0.069	0.007	0.042	0.038
sandyshale	0.074	0.001	0.080	0.004	0.072	0.006	0.064	0.017
low vel.	-	-	-	-	0.061	0.016	-	-
res. sand	0.081	0.006	0.088	0.012	0.102	0.026	0.069	0.012

Table 5.9: Comparison of η_{eff} calculated from picked χ_{eff} values and the model values for η_{eff} for model 1-4.

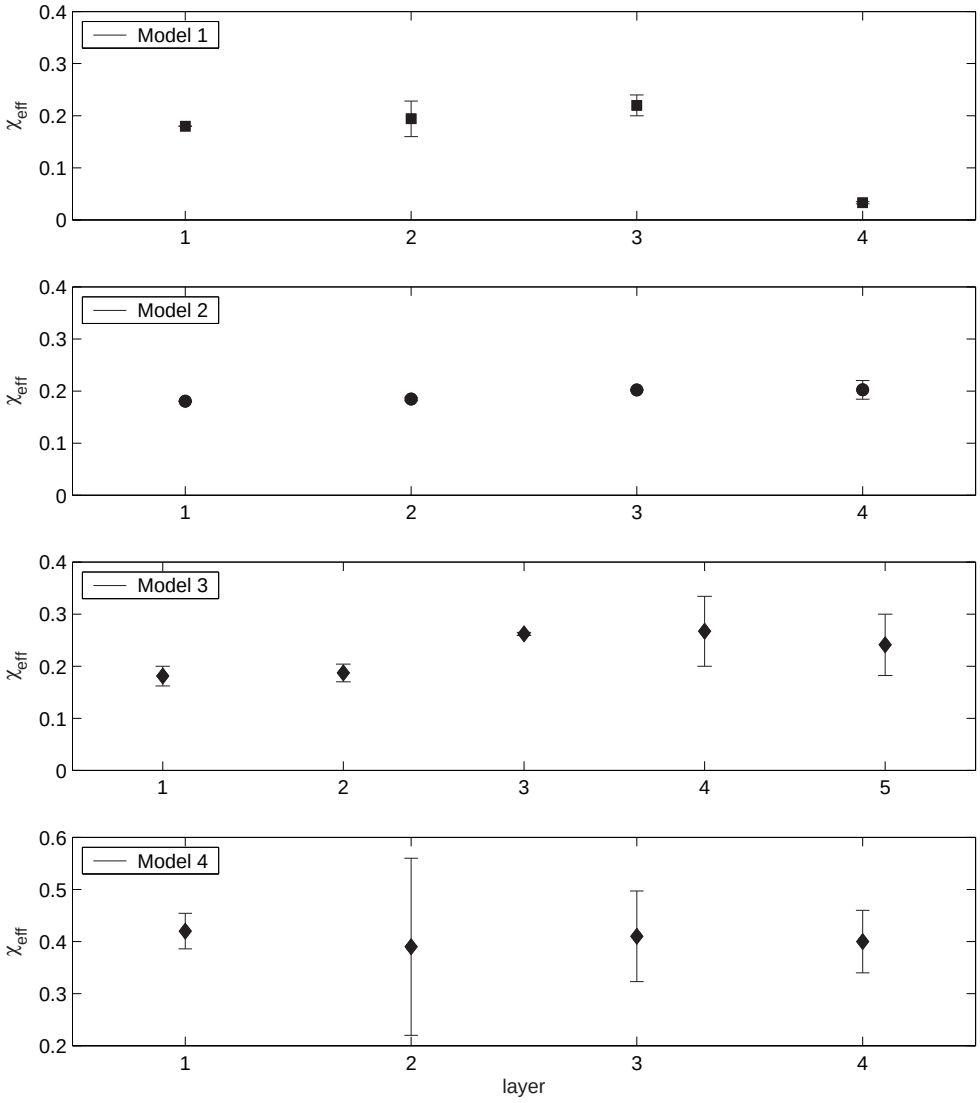

Figure 5.16: Anisotropic parameter χ_{eff} for all 4 models and corresponding picking errors. See also Tables 5.7 and 5.8 for more details.

5.7 Phase behaviour

In the first part of this chapter, I analysed the effect of multilayered media on moveout inversion. However, in the most simple case of an isotropic model with equally thick layers the synthetic seismograms (see Figure 5.1) show for some events a diminishing amplitude which occurs together with a phase reversal. The 3 events on the vertical component are marked by circles. They can also be found on the horizontal component. In this section, I want to explain why this phenomenon occurs and what influence it has on the moveout inversion.

5.7.1 Reflection and transmission coefficients in single and layered media

In order to explain the origin of this phenomenon the effective reflection coefficient for the reflection from the bottom of each layer in a single or multilayer media has to be calculated. The effective reflection coefficient of a specific layer in an isotropic medium is found by calculating the product of all transmission coefficients for the interfaces above for the down-going and up-going path and the reflection coefficient at the target interface. The transmission and reflection coefficient for each layer is calculated by using the exact formula for isotropic horizontal layered media by Aki and Richards (2002) for a plane wave. These effective coefficients for each wave type are normalised by source amplitude and do not accounting for spherical divergence. The reflection coefficients are complex values from which the amplitude and the phase can easily be obtained.
However, Wright (1987) points out that the reflection coefficient is influenced by anisotropy in a VTI media. Hence, focusing on the reflection on the bottom of the first layer, the anisotropic reflection coefficient can be calculated for a single layer with a code using the method of Schoenberg and Protazio (1992). In Figure 5.10 I compare the isotropic and anisotropic coefficients for the amplitudes over incidence angle for a single layer model (Table 5.10) which consists of the first 2 layers of the base model 1. The plot visualises how similar the reflection coefficients are for this amount of anisotropy. The angles for the PP reflected wave are slightly smaller than for the anisotropic case, which has to be kept in mind for further studies. As the single layer model is taken from the multilayered base

model the amount of anisotropy does not change for model 1 and its variations. Thus, I will continue this study using the isotropic multilayered code to calculate the reflection coefficients.

Dai (2003b) published a study about occurrence of phase changes at a water-

layer	ρ [g/cm^3]	V_{p0i} [km/s]	V_{s0i} [km/s]	ϵ	δ
sand	2.3	2.13	0.9	0.11	0.03
shale	2.19	2.2	0.9	0.11	0.03

Table 5.10: Single layer model for comparison of anisotropic and isotropic reflection coefficients similar to first two layers of VTI model 1. For the isotropic model the Thomsen parameters ϵ and δ are set to zero.

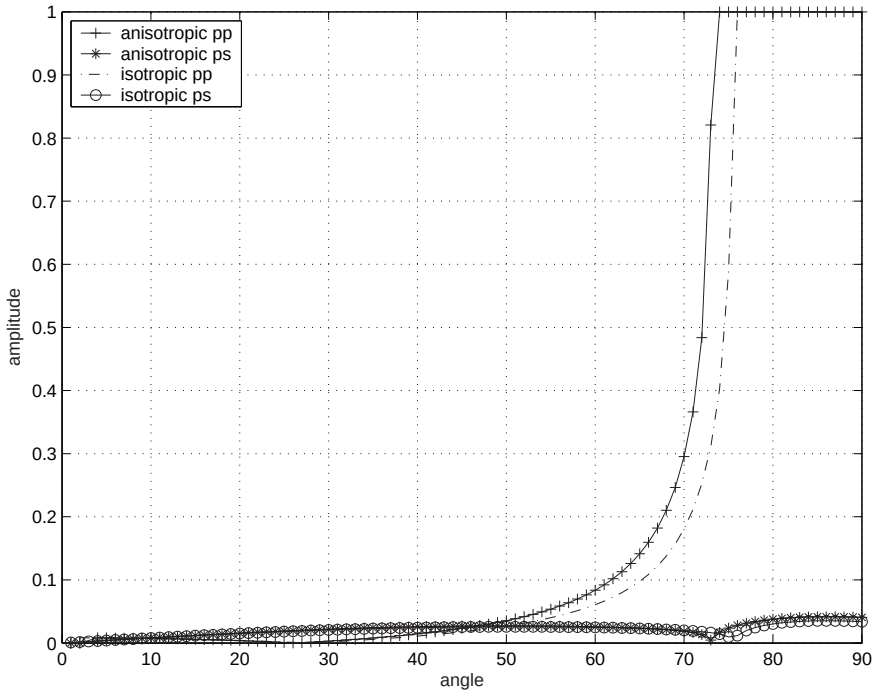

Figure 5.17: Comparison of reflection coefficient of isotropic and VTI single layer medium (see Table 5.10).

sediment interface, i.e. at or near the sea-bed where the S-wave leg of the C-wave is recorded. He found that in the case of horizontal sea-bed and reflector no phase change can occur. In case of a dipping reflector or dipping sea-bed and if they are not parallel to each other a phase change in the C-wave may be observed.

Furthermore, he states that VTI media do not cause a phase change.
As I showed before in Chapter 3 the geology of the Alba reservoir overburden is assumed to be horizontally layered. According to this prerequisite the models in this chapter are all horizontally layered. Thus, the observed phase change in the isotropic model 1 cannot be due to the interaction with the water-sediment interface at the receiver. Hence, I will concentrate on the reflection and conversion

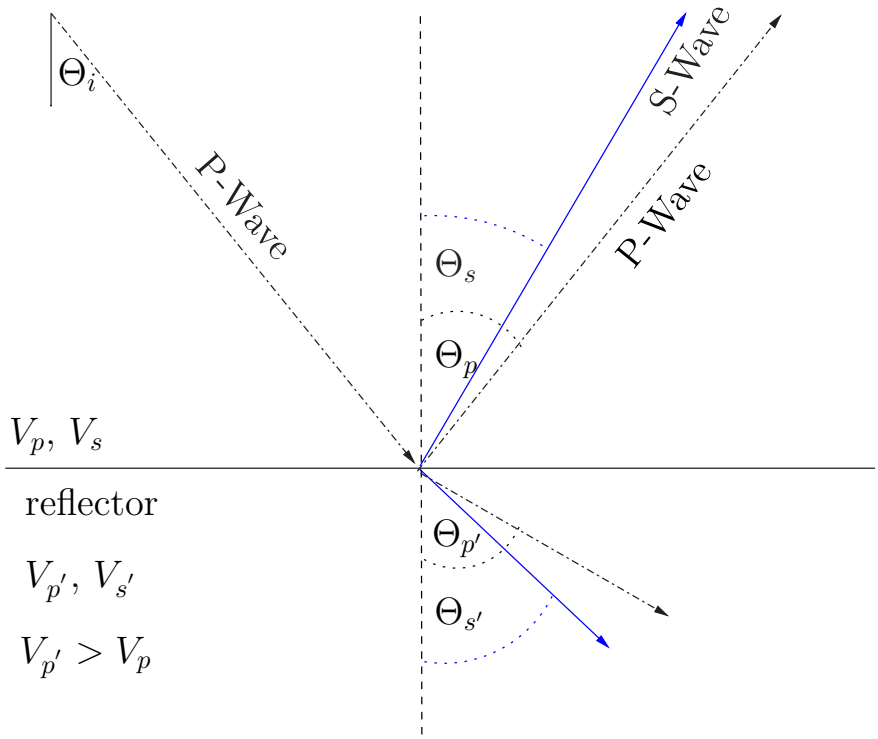

Figure 5.18: Plane body wave incident upon the deep reflector, a solid-solid interface.

angle at the deep reflectors. Figure 5.18 shows the raypath and angles, simplifying it to a single layer case. The relationship between the angles of incidence and refraction is given by Snell's law

$$\frac{\sin\Theta_i}{V_i} = \frac{\sin\Theta_p}{V_p} = \frac{\sin\Theta_{p'}}{V_{p'}} = \frac{\sin\Theta_s}{V_s} = \frac{\sin\Theta_{s'}}{V_{s'}}, \tag{5.1}$$

where Θ_i is the angle of the incident wave with a velocity V_i, which is in our case the P-wave velocity V_p. Θ_p and Θ_s are the angles of reflected P- and S-waves in the medium of the incident wave with the velocities V_p and V_s. $\Theta_{p'}$ and $\Theta_{s'}$ are the angles of refraction of P- and S-waves in the medium of the reflector. If the

velocity in the lower medium is larger than that above, total reflection occurs for $\frac{\sin\Theta_i}{V_p} = \frac{\sin 90°}{V_{p'}}$ so that $\Theta_c = \arcsin\frac{V_p}{V_{p'}}$. For angles equal to and larger than the critical angle the phase of the P-wave will change by 180°. Even in case of a critical angle for the P-wave there is still a small percentage of the energy transformed into a reflected S-wave, i.e. the later recorded C-wave. Its reflection angle can be computed with Snell's law $\Theta_s = \arcsin(\frac{V_s}{V_{p'}}\sin\Theta_c)$. Snell's law holds also for many layers and the angles can be calculated similarly taking the transmission angle of the layers above into account.

5.7.2 Amplitude and phase behaviour for multilayered model with layers of equal thickness

As mentioned before, the seismograms from the vertical components of the isotropic model 1 (Figure 5.1) show a diminishing amplitude together with a phase reversal for the following events: layer 1 at an offset of about 500 metres, layer 3 at about 700 metres and layer 4 at about 1500 metres. The anisotropic model 1 shows the same phenomenon in its seismograms, see Figure 5.5. Calculated effective reflection coefficients for the PP reflection on the bottom of each layer are displayed in Figure 5.19. The coefficients, normalised by source amplitude and their moduli, are plotted as a function of offset with the amplitude on top and the phase on bottom. The same coefficients as a function of incidence angle are shown in the Appendix C, Figure C.1. The diagram confirms the diminishing amplitudes (i.e. they almost become zero) for all 3 events at the observed offsets with corresponding abrupt phase reversals of 180°. Furthermore, the effective coefficient as a function of incidence angle indicates that the critical angle occurs for layer 1 at an incidence angle of 75° (which corresponds to an offset of 3890 metres) and for layer 2 at 59° (or 3490 metres offset). The amplitude at these angles are increasing rapidly and the phase is reversing slowly by −180°. Layer 3 and 4 show between the diminishing amplitude angle and higher incidence angles (56° and 59°) a strong increase in amplitude which rapidly drops to zero and then increases. Total reflection is not visible within the first 6000 metres of offset, which is our area of interest. Nevertheless, the parameter estimation on both, isotropic and anisotropic model 1 show large errors on η_{eff} for layer 1, 3 and 4. I believe this is due to the width of the included offsets. For the first layer, the offset range

of x/z includes an offset of only 1500 metres and thus the parameter estimation would be feeling the effect of the diminishing amplitude. The second layer is not affected by a weakened amplitude or phase reversal and the parameter estimation gives a reasonable result. The third and fourth layer have offsets included for the parameter estimation at which the amplitude and phase phenomenon appear.As a result estimated anisotropy parameters show large errors.

Turning to the C-wave data, the horizontal component of the isotropic model

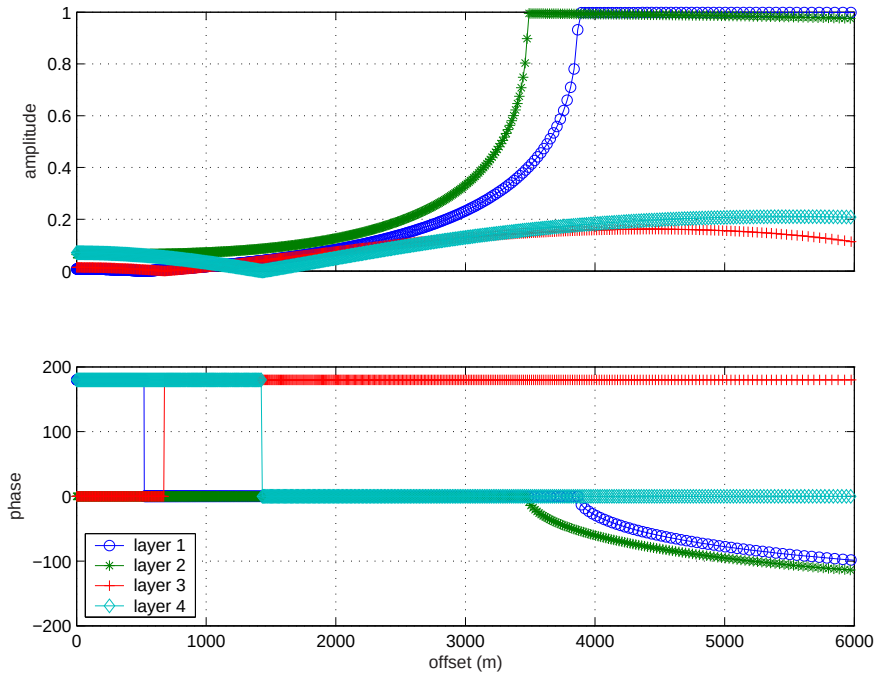

Figure 5.19: Effective reflection coefficients for the isotropic model 1 are calculated for PP reflection on the bottom of the model layers and displayed over offset. Top: Effective reflection coefficient over offset. Bottom: Corresponding phase behaviour.

1 also shows weakened amplitudes with corresponding phase reversals (layer 2 at about 1800 metres, layer 3 at about 3000 metres and layer 4 in the very far offset at about 5000 metres) which are again the same on the VTI media seismograms. However, the parameter estimation results are better, i.e. smaller errors, for χ_{eff} from the VTI model. Considering now the effective reflection coefficient for the C-wave, Figure 5.20, one can see that again, the amplitudes for these 3 layers drop to almost zero before they increase again and furthermore show a phase change of 180°. Again, Appendix C, Figure C.1 shows the coefficients as a function of

incidence angle. Comparing the amplitude against incidence angle diagrams for P- and C-wave there is a clear relationship. The critical angle for the P-wave of the first layer occurs at an incidence angle of 75°. At the same angle the C-wave shows a little peak in its amplitude plot. For both wave types the phase decreases from 0 to -180°. However, for C-waves this occurs only at an offset of about 2000 metres and is therefore at the edge of the included offset for parameter estimation. As I showed in Section 5.4.1 estimation of χ_{eff} gives seriously erroneous values if the included offset is 0-2000 metres. However, if this offset is a little reduced, i.e. to 1800 metres which corresponds to $x/z = 1.8$, parameter estimation is not affected. Layer 2 has its critical angle for the P-wave at an angle of incidence of 59° and shows again a little peak in the C-wave amplitude and decreasing phase for both wave types. However, just before this the C-wave amplitude decreases to almost zero at an angle of 52° which corresponds to 1780 metres and has a rapid 180° phase shift which fits with the observed effect in the synthetic seismograms. This angle marks for the P-wave amplitude the beginning of its strong and fast increase.
The third and fourth layer also show corresponding amplitude and phase behaviour between P- and C-wave: at the point when the P-wave amplitude starts to increase dramatically (for both about 56°) the C-wave amplitude becomes very weak and flips the phase. Speaking in terms of offsets this happens for layer 3 at an offset of 3080 metres and for layer 4 at about 5120 metres which are confirmed by the observed effects in the synthetic seismograms.

These observations suggest that the diminishing amplitudes on the C-wave are linked to extremely strong amplitudes on the P-wave for example as they occur just before the critical angle. However, for parameter estimation on the C-wave the phase reversal usually happens outside or at the very edge of the usable offsets. In the same time the amplitude and phase effects occur within the usable offset range for the P-wave. Therefore, the C-wave anisotropy parameter is better constrained since parameter estimation is not affected by diminishing amplitudes and reversed phases.
The horizontal seismograms for models 2, 3 and 4 do not show evidence of strong amplitude diminishing effects. As the layer thickness is varying for model 2 and 4 the thick top layer changes the positioning of these effects.

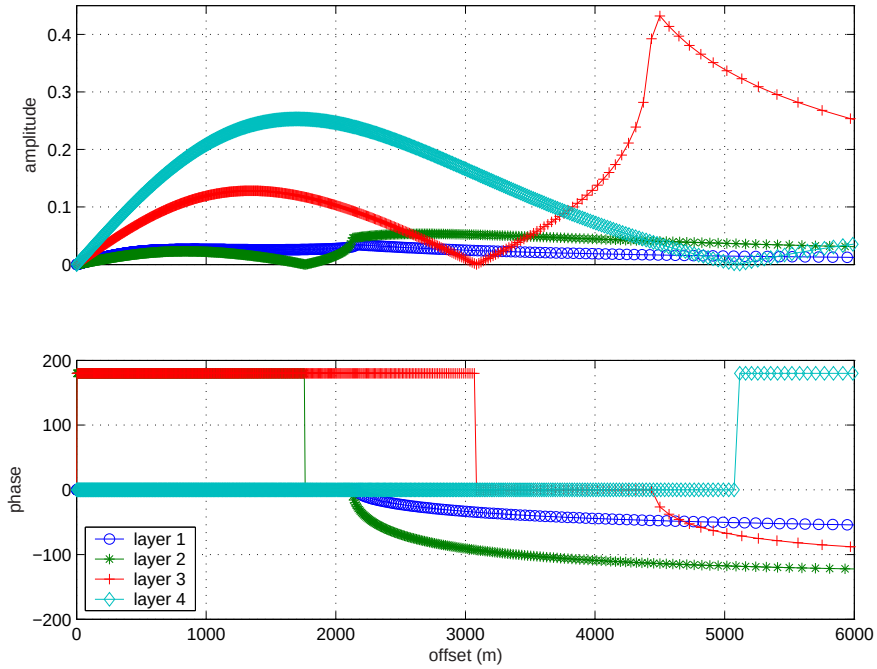

Figure 5.20: Effective reflection coefficients for the isotropic model 1 are calculated for PS conversion on the bottom of the model layers. Top: Effective reflection coefficient over offset. Bottom: Corresponding phase behaviour.

5.7.3 Influence of changes in γ_0 on amplitude and phase behaviour

In the first part of this chapter I found that a strong difference between P- and S-wave velocity, i.e. a low velocity layer, influences the moveout inversion. Now, I study how the size of γ_0 influences the amplitude and phase behaviour of the P- and C-wave. Table 5.11 lists the basic model used for this study consisting of a single layer over a reflector. In a first test, the S-wave velocity of the layer is kept constant while the P-wave velocity varies between $V_{p0} = 1.5, 1.6, 1.8, 2.0, 2.2, 2.3, 3.0$ km/s. I computed the corresponding effective reflection coefficients and displayed them against offset in Figure 5.21 for the P-wave, Figure 5.22 for the C-wave and in Figure C.3, Appendix C, against incidence angle. The amplitude behaviour of

	thickness [km]	V_{p0} [km/s]	V_{s0} [km/s]	ρ [g/cm^3]
layer	0.5	1.6	0.65	2.2
reflector	0.5	2.2	0.9	2.2

Table 5.11: Basic model for study on influence of γ_0 on amplitude and phase behaviour. In two tests are either V_{p0} or V_{s0} of the first layer varied to obtain a changing γ_0.

P-waves shows that with increasing V_{p0}, and thus also increasing γ_0, the critical angle of total reflection occurs at higher incidence angles. Also, with increasing V_{p0} the magnitude of the amplitude is decreasing at zero offset. However, with a $V_{p0} = 3.0$ km/s, corresponding to $\gamma_0 = 4.62$, the critical angle is not reached and the magnitude of the amplitude is again high at zero offset. The phases do not change until the critical angle. After the critical angle is reached they decrease by 180°. For the C-wave the amplitude has zero magnitude at zero incidence

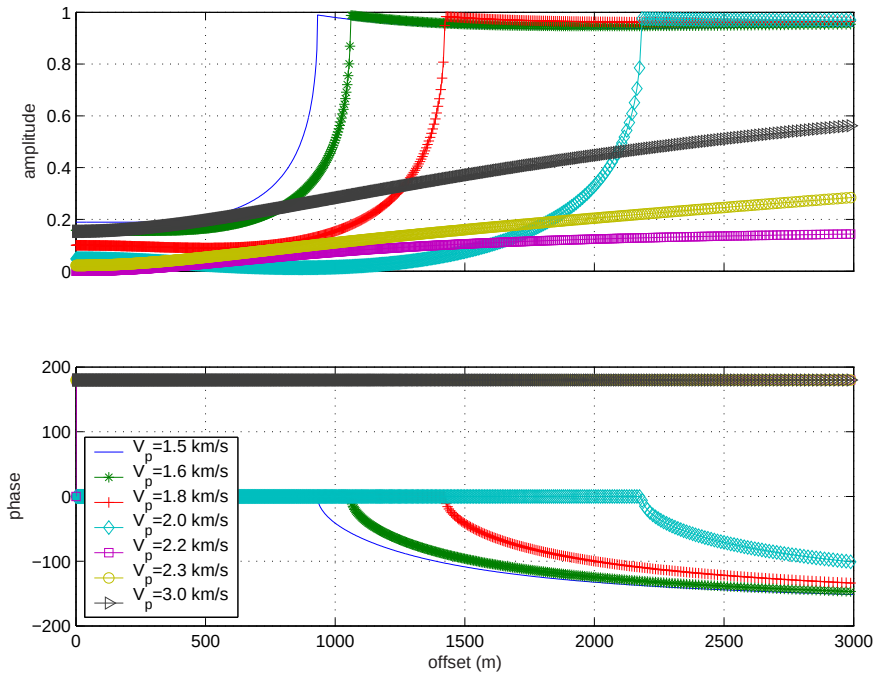

Figure 5.21: Coefficients for a PP reflection. Top: Reflection coefficient for $V_s = 0.65$ km/s and varying P-wave velocity over offset. Bottom: Corresponding phase behaviour.

and then increases for all γ_0. However, the amplitude drops to about zero again at incidence angles at which the corresponding P-waves rapidly increase in amplitude just before the critical angle is reached. After this angle is reached the C-wave amplitude increases strongly before it drops to zero at an incidence angle of 90°. For this particular model, I find that if $V_p > 2.2$ ($\gamma_0 = 3.4$) the diminished amplitude is occurring at an larger offset than 1250 metres which is the upper limit for C-wave moveout inversion if $x/z = 2.5$.

The C-wave phase shows an interesting phenomenon in that it changes by 180° when the amplitude is zero, just before the P-wave critical angle. The phase then stays on zero until the critical angle is reached after which it slowly decreases by

another 180°. However, the C-wave phase lag increases with increasing V_p and γ_0, before it reaches the P-wave critical angle and decreases again.
In the context of parameter estimation this experiment suggests that a larger offset is needed before the amplitude and phase effects appear so they lie outside the usable offset.

In my second test I keep the P-wave velocity of the layer constant at 1.6 km/s

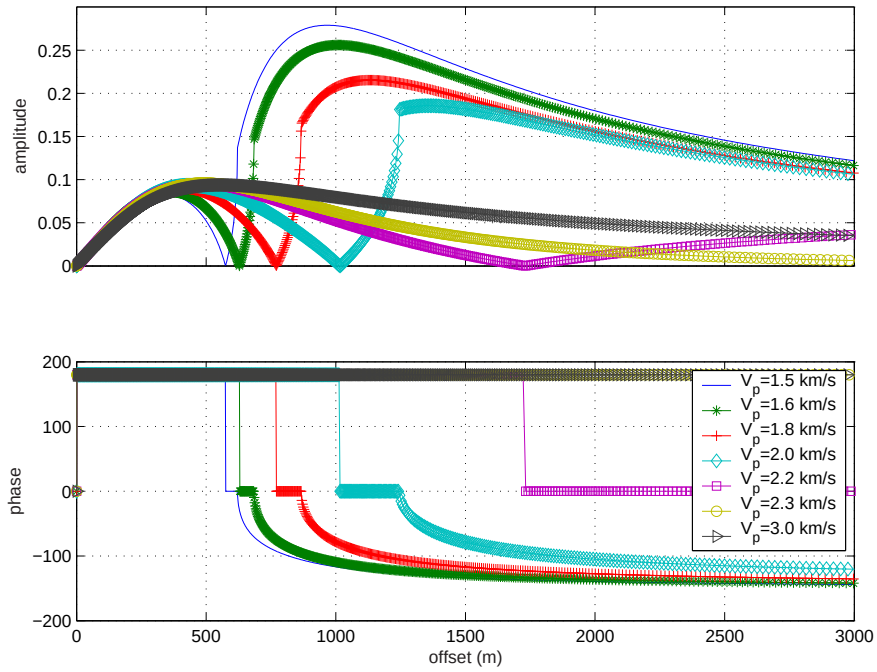

Figure 5.22: Coefficients for PS conversion. Top: Reflection coefficient for $V_s = 0.65$ km/s and varying P-wave velocity over offset. Bottom: Corresponding phase behaviour.

but vary the S-wave velocity. For $V_{s0} = 0.35, 0.45, 0.55, 0.65, 0.75, 0.85, 0.95, 1.05$ km/s I computed the effective reflection coefficients. The amplitude behaviour against offset is displayed for P-waves in Figure 5.23 and for C-waves in Figure 5.24 while Figure C.4 illustrates them against incidence angle. Due to the fixed P-wave the critical angle is the same for all variations at an incidence angle of 47° degrees. Also, all P-wave amplitudes start with the same magnitude and vary slightly in size and in the rate of increase before the critical angle.
The C-wave shows the expected zero crossing at the angle when the P-wave increases its amplitude rapidly. However, depending on how fast the P-wave increases, i.e. the steepness of the curve, the smaller the incidence angle of the zero

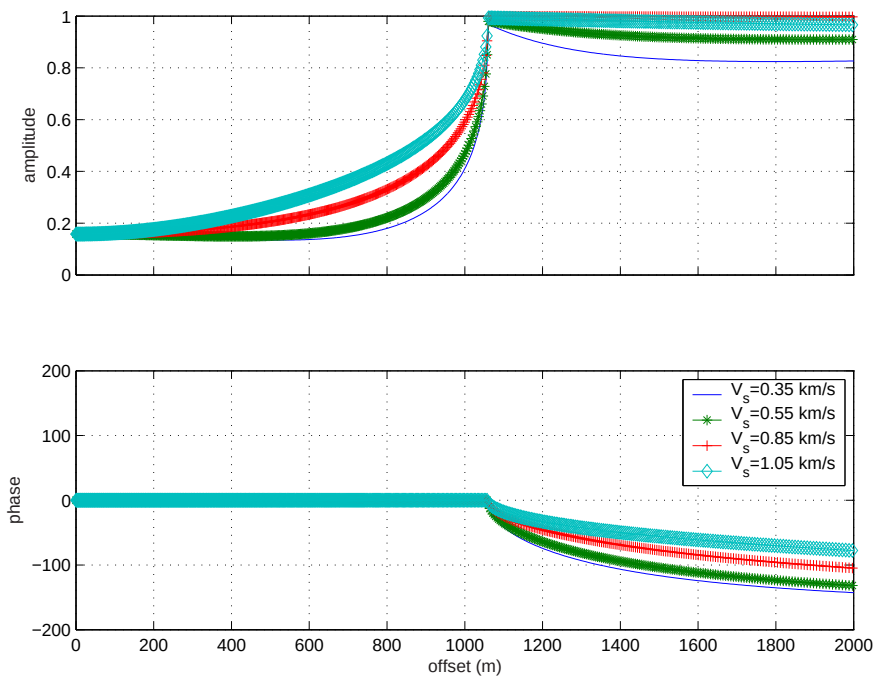

Figure 5.23: Coefficients for PP. Top: Reflection coefficient for varying S-wave velocity and constant $V_p = 1.6$ km/s over offset. Bottom: Corresponding phase behaviour.

amplitude and the larger the amplitude between zero incidence and this angle. I find, that for small S-wave velocities, i.e. the larger γ_0, the angles of incidence of the zero amplitude are also small. Nevertheless, for this example, there is always a diminished amplitude for C-waves within the range of offsets used for moveout inversion due to the fixed value of the P-wave velocity well below that of the reflector.

The C-wave phases show again the phase reversal of 180° and slower phase decrease at the critical angle of the corresponding P-wave. In contrast to the first study, I find that the phase reversal lag is small for the large γ_0, i.e. small V_s. Just looking at the velocity ratio these two studies seem to give contrary results. However, the critical angle is constant in the second study and thus only shows little variations on the location of diminishing amplitude due to variations in the S-wave velocity. Furthermore, the phase reversal lag when the amplitude is zero is only a minor problem in parameter estimation as the main point is when and where the amplitude diminishes. C- and P-wave amplitude behaviour are linked with each other and relate to the critical angle of the P-wave. Therefore the P-wave velocity ratio across the interface mainly determines where the ampli-

tude diminishes. Thus, large P-wave velocities ratios lead to the occurrence of diminishing C-wave amplitudes at larger angles of incidence and hence offsets.

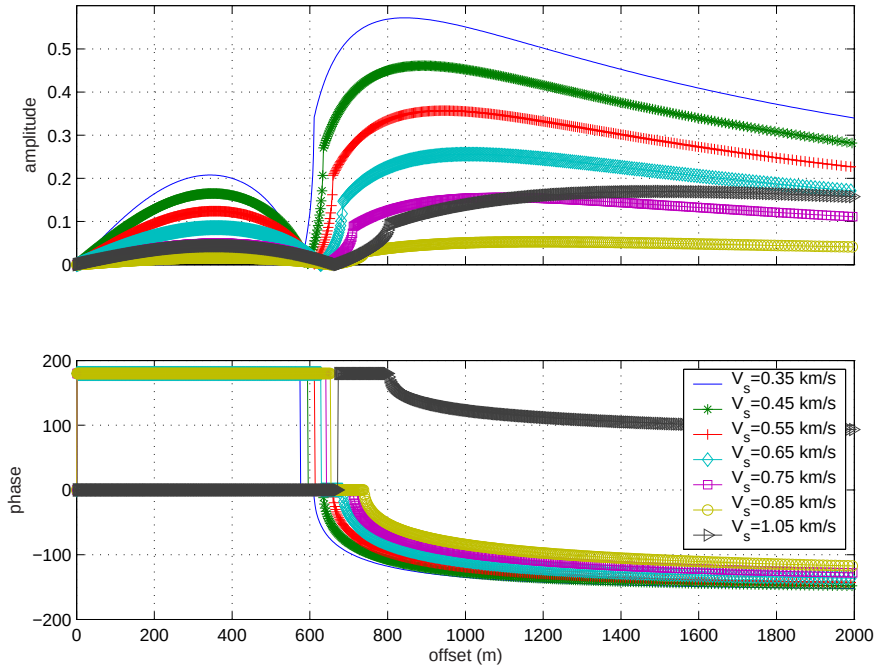

Figure 5.24: Coefficients for PS conversion. Top: Reflection coefficient for varying S-wave velocity and constant $V_p = 1.6$ km/s over offset. Bottom: Corresponding phase behaviour.

5.7.4 Influence of low velocity gradient as near-surface layer

My final test on phase changes is about the influence of a gradient layer overlying the isotropic model 1. In the original model the first layer has been changed so it consists now of a gradient layer of 200 metres and underneath a layer of 300 metres of the original material. The gradient is defined by a low density range of $\rho = 1.1 - 2$ g/cm^3 and the velocities $V_{p0} = 1.55$ to 1.85 km/s and $V_{s0} = 0.1$ to 0.47 km/s. These values are chosen to be very low in order to represent a near surface loose and still un-cemented sediment layer. I divided this gradients in 40 equal steps to simulate the gradient and facilitate computations. Table 5.12 summarises the model values for all layers. Synthetic seismograms from this model are displayed in Figure 5.25. The reflections from gradient and the 4 layers beneath are marked by arrows on both components. On the vertical component layer 1, 3

layer [km]	depth [km]	V_{p0} [km/s]	V_{s0} [km/s]	ρ [g/cm^3]
0.2	0.2	1.55-1.85	0.1-0.47	1.1 - 2
0.3	0.5	2.13	0.9	2.3
0.5	1.0	2.2	0.9	2.19
0.5	1.5	2.5	0.975	2.19
0.5	2.0	2.56	1.372	2.2
HS	2.5	2.43	0.731	2.01

Table 5.12: Summary of isotropic base model 1 with modified first layer. The first layer is divided into a layer with density and velocity gradients (realised by dividing it up into 40 layers for further computation) and the original model layer.

and 4 show the diminishing amplitude and on the horizontal component layer 2, 3 and, only lightly visible at an far offset layer 4. Recalling the seismograms in Figure 5.1 of the isotropic model the pattern of diminishing amplitude is similar. However, the gradient seems to weaken the energy on the near offset traces (e.g. layer 3 on the vertical components).

The effective reflection coefficients have been calculated for the reflection/conversion at the bottom of the gradient and for each subsequent layer. Figure 5.26 displays the amplitude and the phase against offset for the PP reflection (Figure C.4 in Appendix C show them over incidence angle). The amplitude of the P-wave reflection at the bottom of the gradient layer reaches its critical angle at an angle of incidence of about 48° which corresponds to the layer thickness of only 200 metres with a small offset of about 500 metres. The amplitude of this event has the most energy of all layers at zero offset. Similar to the phase behaviour in the other models, the corresponding phase slowly decreases by 180° after the critical angle has been reached. Interestingly, the amplitudes and phases of the layers underneath the gradient still show the characteristics that were seen in the isotropic model 1. However, the angle of incidence at which the amplitude and phase phenomena occur is reduced. Due to the constant total depth of the layers, this has only little influence on the offset where these phenomena happen.

The amplitude and phase for the PS conversion is shown in Figure 5.27 against offset and Figure C.4 (in Appendix C) against incidence angle. Again, layer 1-4 fit with the findings from the isotropic model 1 except that the angles of incidence are smaller. The gradient layer itself further diminishes the amplitude.

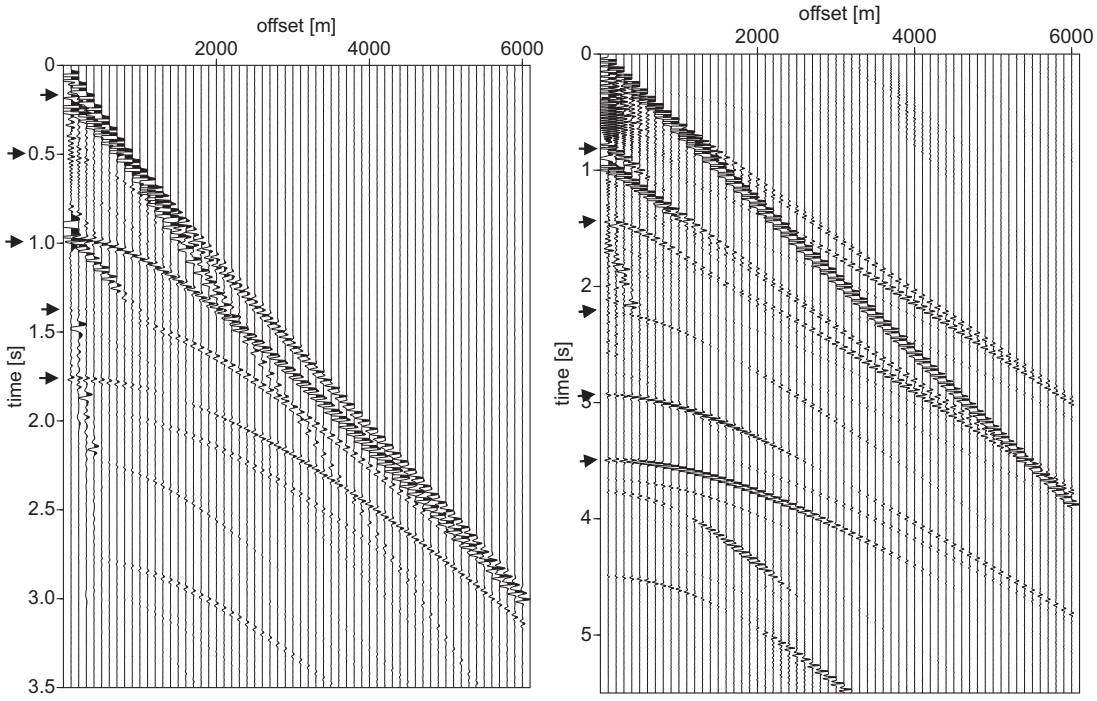

(a) Z-component (b) X-component

Figure 5.25: Synthetic seismograms for model with gradient represented by 40 thin layers (see Table 5.12). (a) Vertical (Z) component and (b) horizontal (X) component. Arrows indicate the events due to the gradient and the layers underneath.

Furthermore, the C-wave amplitude is stronger than that of the model without the gradient.

Both, P- and C-wave amplitude against offset diagrams confirm the finding of diminishing amplitudes and phase reversals at certain offsets, as already shown for the isotropic model 1. Thus, the gradient layer in the near surface does influence the energy transmitted to the lower layers but will not change the offset strongly at which the amplitude and phase phenomena occur.

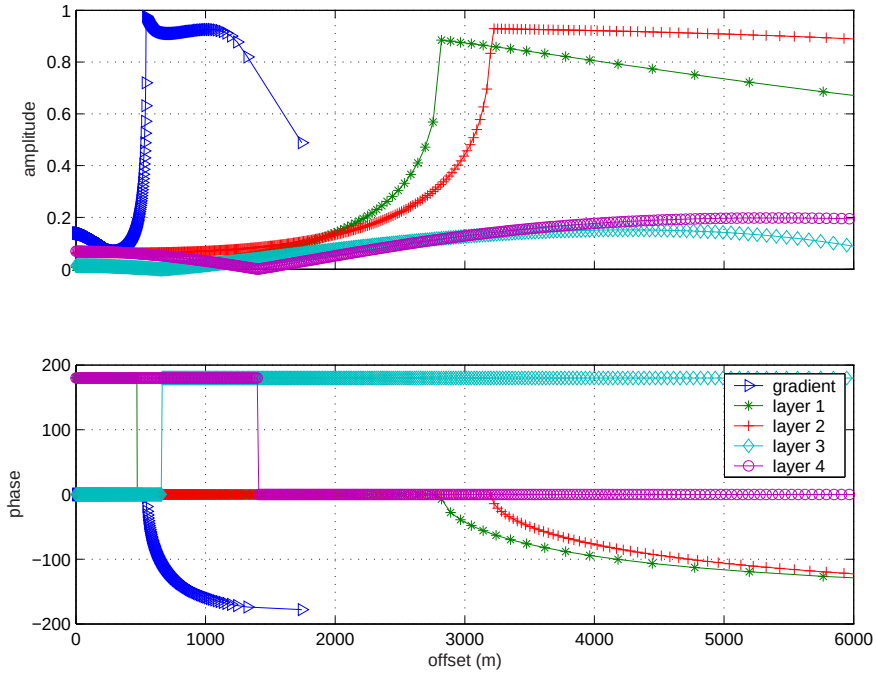

Figure 5.26: Coefficients for PP reflection on the bottom of each model layer underneath the gradient. Top: Effective reflection coefficient over offset. Bottom: Corresponding phase behaviour.

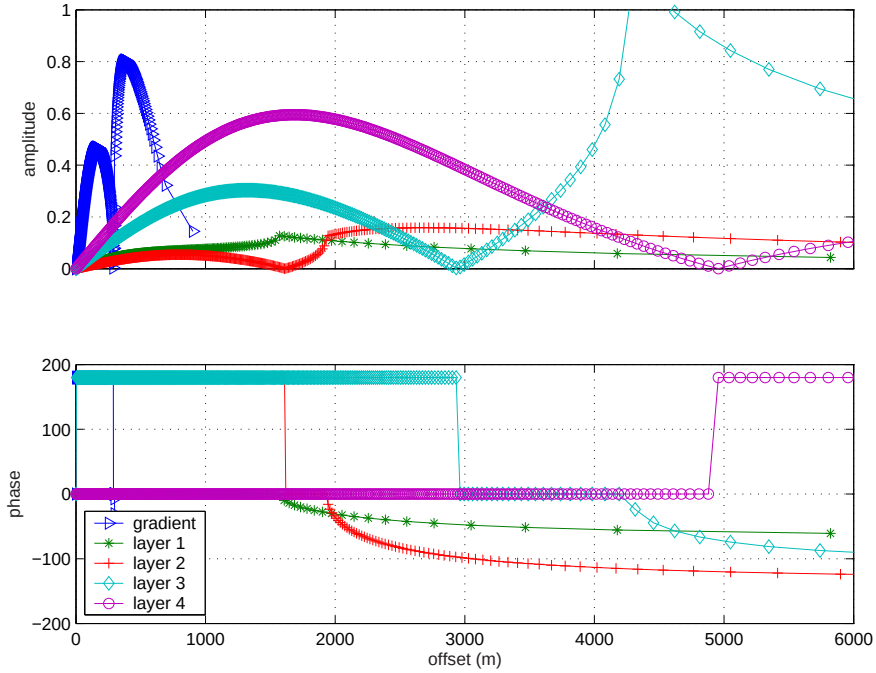

Figure 5.27: Coefficients for PS conversion on the bottom of each model layer starting underneath the gradient. Top: Effective reflection coefficient over offset. Bottom: Corresponding phase behaviour.

5.8 Discussion and Conclusion

Synthetic modelling studies show that the resolution and accuracy of χ_{eff} from C-wave reflection moveouts are higher than those of η_{eff} from P-wave reflection moveouts. Firstly, the magnitude of P-wave non-hyperbolic moveout is much smaller than the magnitude of the C-wave non-hyperbolic moveout in the same range. Secondly, η_{eff} values in the chosen models are often smaller than 0.1, whereas the χ_{eff} values are within a much larger range between 0.2 and 0.4. When η_{eff} is increased to 0.1-0.2, the resolution improves.

A low velocity layer influences moveout inversion in that the parameters of the layer underneath have a worse resolution than if estimated without the strong velocity contrast. A low velocity layer as found near to the surface, with varying layer thicknesses underneath leads to the largest errors of this study. Moveout inversion is based on a straight ray approximation. However, in the vicinity of strong velocity contrasts the rays cannot be assumed to be straight rays anymore. Thus, if the velocity contrast is very strong, the moveout inversion based on Taylor series expansion breaks down and leads to erroneous results.

I conclude that small η_{eff} cannot be resolved reliably using double-scanning semblance analysis of P-wave reflection moveout. However, I have found that the estimation of χ_{eff} from the C-wave is very robust and calculations of η from the C-wave parameters are well resolved.

The low resolution and low accuracy when estimating η_{eff} directly from P-wave data from the model 1 can also be explained by the occurrence of diminishing amplitudes and phase reversals on three layers. These effects are confirmed by computing the effective reflection coefficients. Although they can be found in C-wave data too, they only occur at larger offsets and thus do not affect the usable offset for moveout inversion.

Generally, P- and C-wave amplitude and phase behaviour are coupled. For instance if the P-wave reaches its critical angle the C-wave amplitude drops to zero while the P-wave amplitude reaches almost 1. At the same time the C-wave phase

flips by 180°. Although influenced by a gradient layer such as the sea-bed the phase shifts and amplitude weakening of the subsequent layers is still found at only slightly smaller offsets.

Finally, changes in γ_0 have an influence on the incidence angle/offset when the diminishing amplitude appears. As for moveout inversion an offset as large as possible is desired. The amplitude behaviour of the C-wave relates to the point when the P-wave reaches the critical angle. Therefore, the P-wave velocity contrasts at interfaces mainly determine where the amplitude diminishes.

Chapter 6

Characterisation of near surface anisotropy

Following from the theoretical and modelling studies in the previous chapters, I investigate in this chapter how reliably one can extract η from P- or C-wave data using near surface layer multicomponent data from the Alba Field, North Sea.

Complications in seismic processing can occur, firstly, due to variations in sea-bed properties because they significantly influence the amplitudes, phases and travel times of seismic waves. Secondly, near surface layers induce complications in seismic data processing due to strong gradients especially for shear velocities and density due to compaction processes (Theilen et al., 1997). These gradients can lead to estimation of an apparent anisotropy in an isotropic media (Jones et al., 2002)

As explained in earlier chapters parameter estimation for 4-component data is either performed on P-wave data, searching for $\eta - V_{p2}$, or on C-wave data, estimating $\chi - V_{c2}$. Alternatively, I calculate the parameter η from χ extracted from C-wave data. A problem may arise when using this technique in the presence of phase reversals which lead to energy cancellations. Phase reversals have been observed in multicomponent data (e.g. Brandsberg-Dahl and Barkved, 2002) and its effects are discussed in Chapter 5.

Using only near surface events, I assume VTI structure and recall Equation (2.33):

$$\eta = \frac{\chi}{\gamma_{\text{eff}}^2(\gamma_0 - 1)}$$

Equation (2.33) is only strictly valid for a single layer but experience shows that it is a good approximation for multilayered media in time processing.

6.1 Near surface events in the Alba 4C data set

I use the vertical and horizontal component of the Alba 4C data set to extract the anisotropy parameters η and χ from near surface events. In this study I will investigate the influence of near surface effects such as strong velocity contrast on parameter estimation. This data set is suitable for the study as the field is mainly flat layered, especially in the overburden. Furthermore, it displays weak S-wave velocities at the seabed, i.e. a strong S-wave velocity contrast below, while the P-wave velocities are varying smoothly in the near surface layers. I will discuss the results for the vertical and horizontal component, respectively. Figure 6.1(a) illustrates one example of CDP gather of the vertical component. Arrows indicate the three selected events for the study. Figure 6.1(b) shows the corresponding ACP (asymptotic-conversion point) gather and the arrows indicate corresponding events to Figure 6.1(a).

6.1.1 Estimating η from P-wave data

I applied the double scanning semblance analysis after Alkhalifah (1997) to the vertical component of the 4C Alba data. Parameter estimation has been performed on three selected events on the P-wave at $t_{p0} = 0.347, 0.631, 0.66$s (see seismogram in Figure 6.1(a)) to obtain η and V_{p2}. No parameter could be resolved for the event at $t_{p0} = 0.347$ s. The double scanning results for the other 2 events are well defined and shown in Figure 6.2 with picked values indicated by an "x". The results are also summarised in Table 6.1. The picked parameters η and V_{p2} were used for NMO correction. The result for the used CDP gather 500 is displayed in Figure 6.5(a). The arrows mark the picked events for $t_{p0} = 0.631, 0.66$ s.

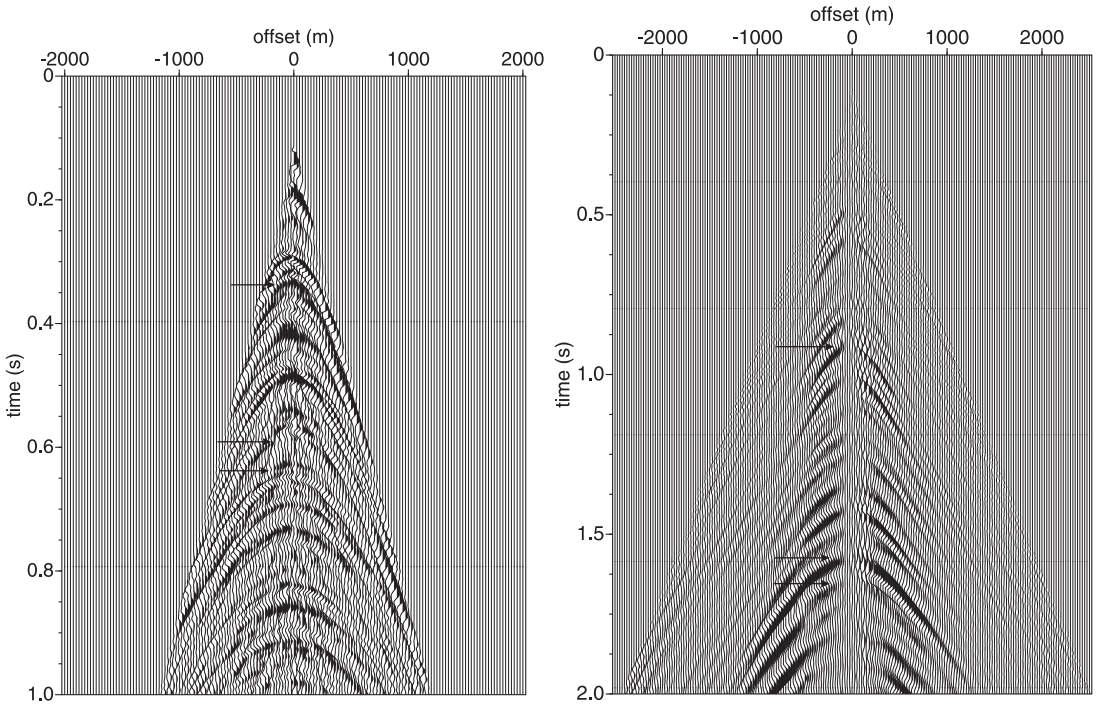

(a) z-component (b) x-component

Figure 6.1: (a) CDP gather of P-wave (vertical component) from Alba 4C data. Arrows indicate the three events used for the parameter estimation at $t_{p0} = 0.347, 0.631, 0.66$ seconds. (b) Corresponding ACP gather of C-wave (horizontal component). Arrows indicate the events at $t_{c0} = 0.913, 1.578, 1.64$ seconds which correspond to the events of the P-wave.

t_{p0} [s]	η	V_{p2} [km/s]
0.347	-	-
0.631	0.163	1.545
0.66	0.35	1.61

Table 6.1: Picked η parameters from near surface events of one CDP gather in the vertical component of the 4C Alba data. The corresponding gather is displayed in Figure 6.1.

The events from 0.5 seconds are flattened. From 0 to 0.5 seconds the gather still shows under-corrected events due to too small offsets. The results of the other CDP gathers are similar and CDP gathers 600, 700 and 800 are displayed in Appendix D (Figures D.2 - D.4). Applying the NMO correction to the whole data set and stacking give a brute stack which is displayed in Figure 6.3. Well and surface data from the Alba Field provided us with information about V_p,γ_0,ϵ

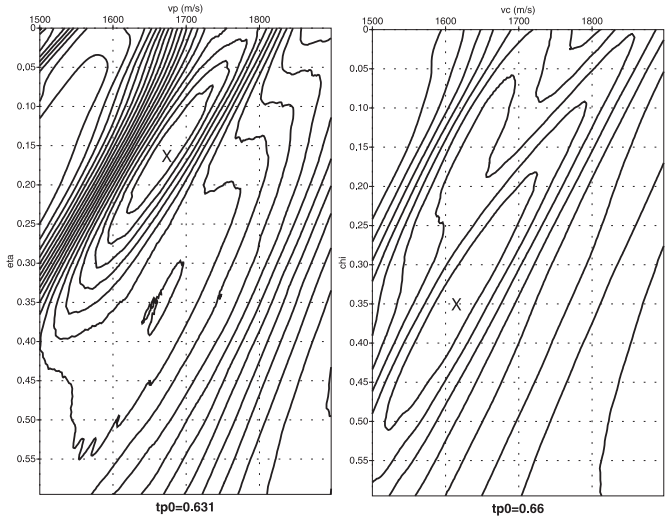

Figure 6.2: CDP 500 pick from vertical component for $t_{p0} = 0.631, 0.66$ s events. For the event at $t_{p0} = 0.347$ s. no parameters were resolved. Picked values are indicated by a "x" and results are shown in Table 6.1.

and δ for various depths (Leaney et al. (2001a) and Chapter 3). From these data I calculated η, χ and the corresponding traveltimes t_{p0} and t_{c0} (see Table 6.2) in order to get an idea about the size and behaviour of the parameters. It can be seen that the range of η in the near surface layer estimated from surface P-wave data is much larger than the model data, but values for V_{p2} show agreement. The near surface layers of a marine environment feature very strong P- and S-wave differences, i.e. large γ_0, and also velocity gradients due to compaction of sand and mud. These effects can contribute to the erroneous values in parameter estimation. Hence, this could be the same effect I observed on the synthetic data, where η estimated from the vertical component is too large.

$t_{p0}[s]$	$V_{p2}[km/s]$	η	t_{c0} [s]	χ	V_{c2} [km/s]
0.301	1.590	0.005	0.858	0.39	0.744
0.545	1.701	0.017	1.467	0.65	0.845
0.650	1.746	0.023	1.726	0.71	0.885

Table 6.2: Parameters η, V_{p2}, χ and V_{c2} calculated for near surface events using model data derived from well and surface data.

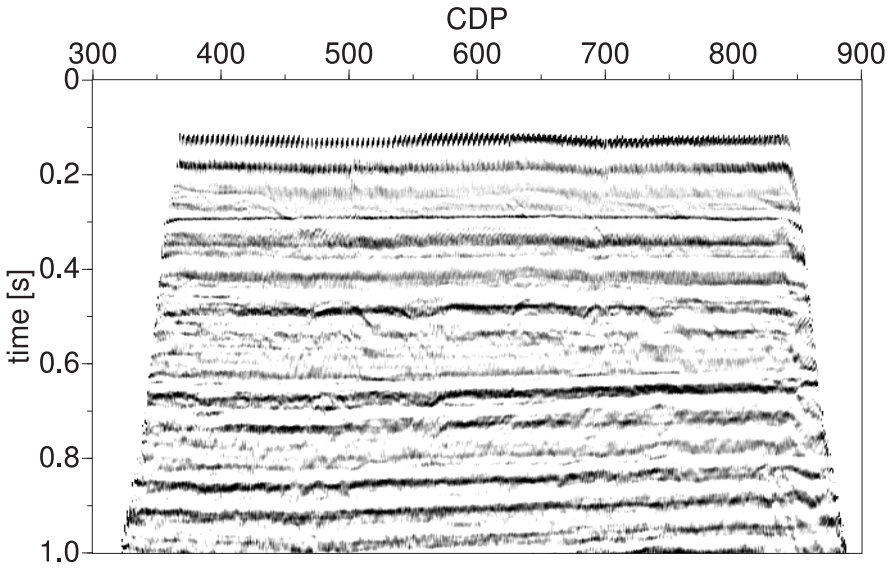

Figure 6.3: Anisotropic NMO and stack for vertical component using picked values for η and V_{p2}.

6.1.2 Estimating η using converted waves

In the next step I calculate η from picked χ values. Parameter estimation for χ and V_{c2} was performed on two events on the horizontal component (Figure 6.1) corresponding to the ones used on the vertical component. Then, I used Equation (2.33) to calculate η. The results from the double scanning analysis are illustrated in Figure 6.4, where picked values are indicated by an "x". The picked parameters

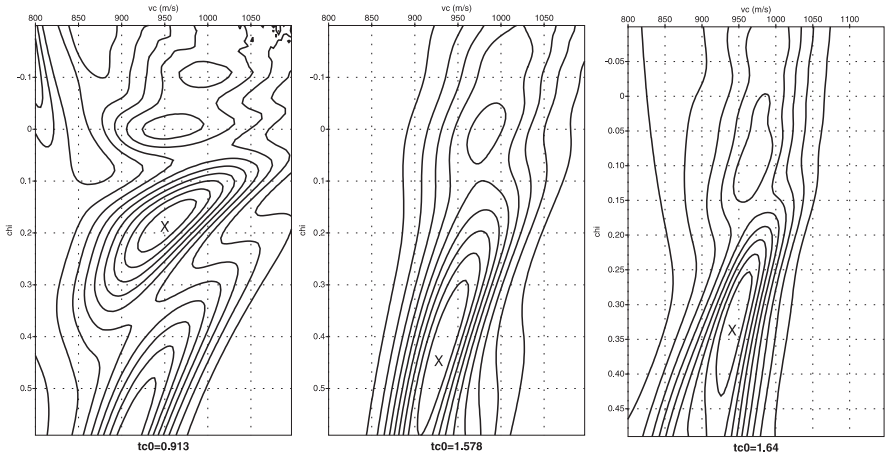

Figure 6.4: Parameter estimation results for events on the horizontal component at $t_{c0} = 0.913, 1.578, 1.64$ seconds which correspond to the events used in the vertical component. Picked values are indicated by an "x' and results are shown in Table 6.3.

χ and V_{c2} and the calculated η for the CDP gather 500 are listed in Table 6.3. Comparing these values with the model values in Table 6.2 it can be seen that the estimated values of η from the C-wave are much smaller than the ones estimated from the P-wave and, therefore, correspond better to the expected values derived from the model data. The values are now of the same order of magnitude as the model values. A reason for the difference might be that the first near surface layer shows a stronger P- to S-wave contrast, i.e. larger γ_0, than I used for the analysis. The χ values are only slightly smaller than the expected ones from the model data. Note that the converted wave analysis also shows an induced anisotropy in the presence of a compaction velocity gradient and, therefore, χ values are affected. However, both, η and χ estimated from the C-wave have the order of magnitude expected from the model values. Figure 6.5(b) shows the NMO

t_{c0} $[s]$	χ	V_{c2} $[km/s]$	$\eta(calculated)$
1.578	0.45	0.927	0.01
1.64	0.34	0.941	0.0086

Table 6.3: Picked anisotropy parameter χ and velocity V_{c2} from near surface events of ACP gather 500 in the horizontal component of the 4C Alba data (Figure 6.1). η is calculated from χ using Equation (2.33).

correction for the same CDP gather of the vertical component using the calculated η values. Remember for comparison that Figure 6.5(a) shows the NMO correction using the picked η values. Both gathers were muted. Comparing the two NMO corrections for the same gather I find only small differences between them. This is unexpected as the calculated values are in the range of the estimated anisotropy values of the model data and thus differ in size by an order of magnitude.
Next, applying the NMO correction to the whole data set and stacking gives the corresponding brute stack, illustrated in Figure 6.6. For comparison refer to the stack after using the picked $\eta - V_{p2}$ values shown in Figure 6.3. These stacks display only the first second as this study concentrates on near surface events. However, the stacks show almost no difference and the question arises about how sensitive NMO correction in the near surface is to the anisotropy parameter η. This further confirms that P-wave data alone cannot resolve anisotropy parameters and C-wave data is needed. Figure 6.7 shows the near surface brute stack of the horizontal

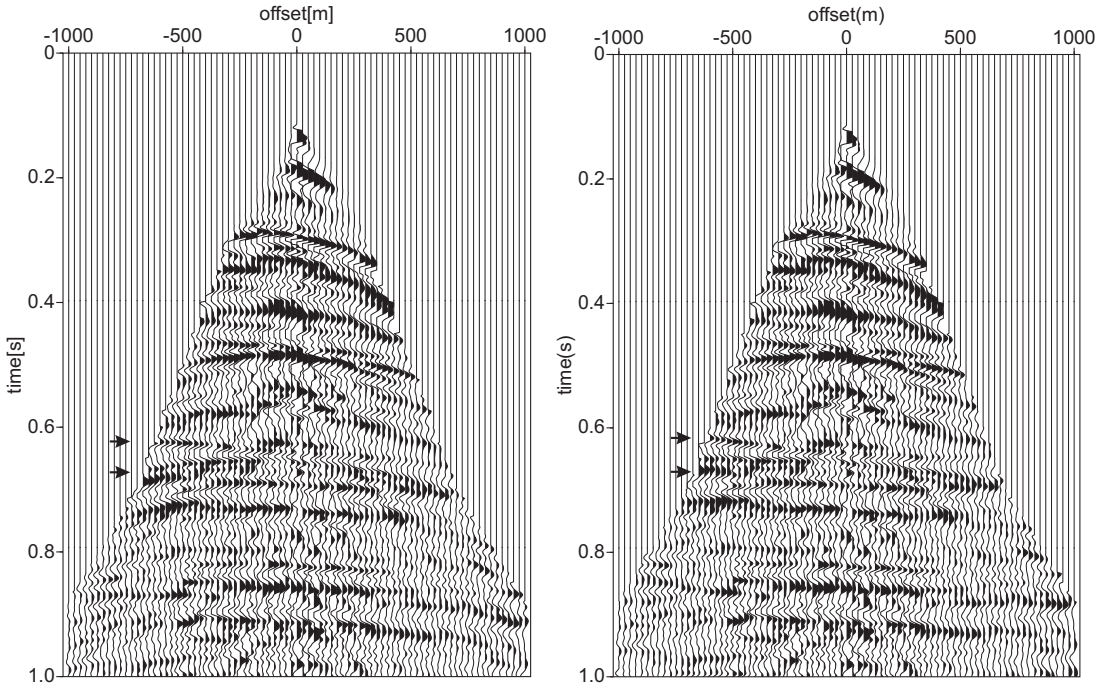

Figure 6.5: (a) Anisotropic NMO using picked values (see Table 6.1) for CDP gather 500. (b) Anisotropic NMO using η calculated from picked χ-values (see Table 6.3) for CDP gather 500 shown in Figure 6.1. The arrows indicate the events used for the parameter estimation.

component when the anisotropic NMO correction was applied to C-wave events using χ and V_{c2}.

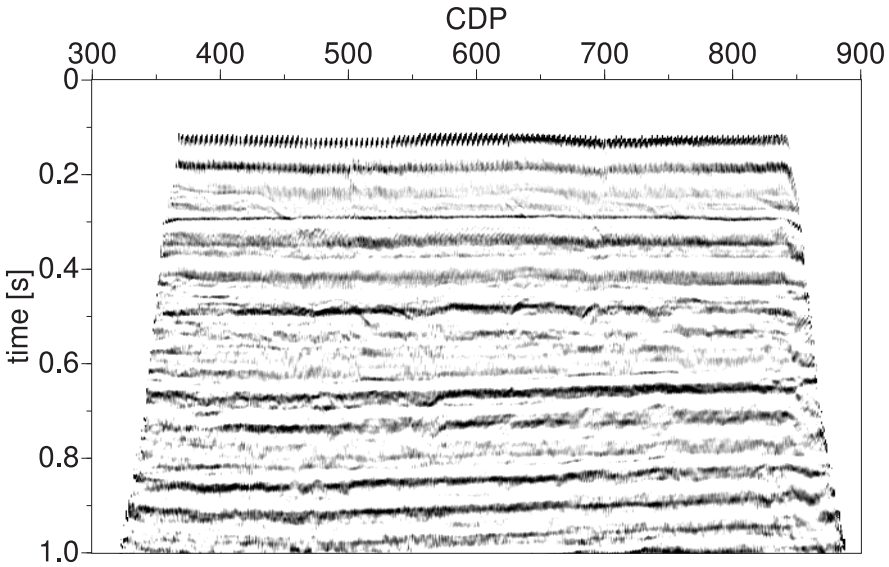

Figure 6.6: Brute stack of P-wave using η calculated from picked χ-values.

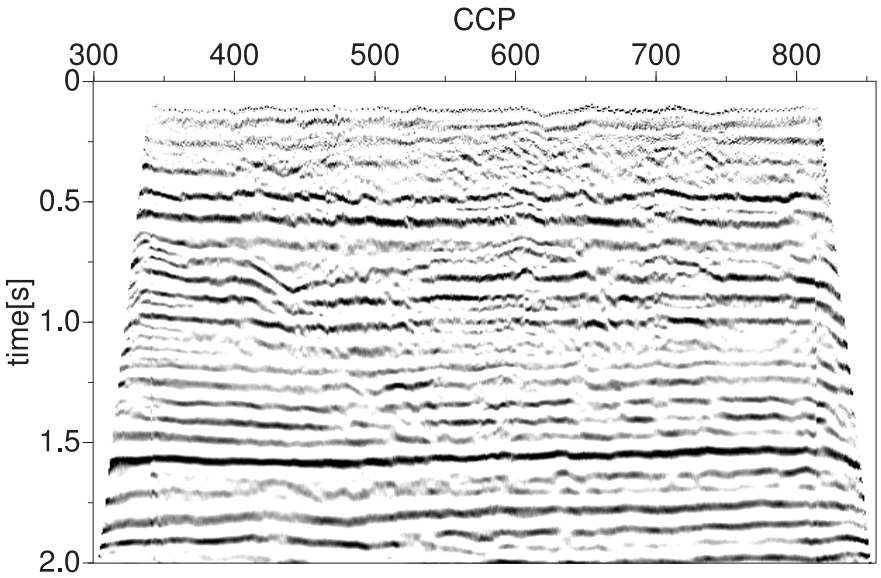

Figure 6.7: Anisotropic brute stack for horizontal component using picked χ and V_{c2} values.

6.1.3 Phase behaviour

Close observation of Figure 6.1(a) shows phase reversals for the selected horizons 2 and 3. In comparison, the horizontal component displayed in Figure 6.1(b) does not show a signal in the near offset traces, as expected from C-wave data. Otherwise, the three events show no phase reversal. Dai (2003b) suggests that phase changes do not occur if a C-wave is incident at the water-solid interface. A phase change in P-wave data may originate from a phase change after reflection on a subsurface layer boundary. Therefore, I use trace analysis to calculate the instantaneous phase function for both, P- and C-wave data. For this analysis the data is sorted in CDP and ACP gathers, in order to learn about the phase behaviour due to reflection and conversion on a certain subsurface point. After preprocessing the three events indicated by arrows in CDP gather 500 (Figure 6.1(a)) and its corresponding ACP gather (Figure 6.1(b)) have been used.
To calculate the instantaneous phase function each signal from one horizon was picked separately. Then, a time window of 40 ms has been chosen for each event to firstly, compute the Hilbert transform and secondly, the instantaneous phase function from the signal and the Hilbert transform.
Figure 6.8(a) shows the instantaneous phase function for all 3 events of the vertical component. Figure 6.8(b) shows the results for the corresponding events on the horizontal component. The analysis shows evenly scattered data points for the instantaneous phase function against offset for the horizontal component, suggesting that no phase reversal occurs. In contrast, the vertical component shows a trend of phase reversal for the 2^{nd} and 3^{rd} horizon indicated by a line plotted over the data results. This supports that phase reversals occur in the near surface layers and thus might lead to bad parameter estimation on these events.

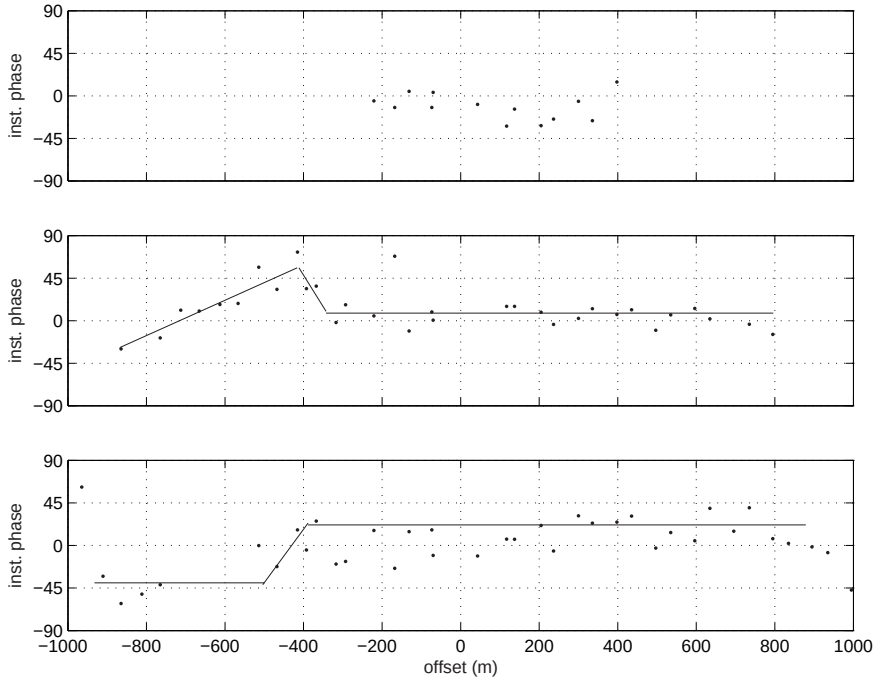

(a)

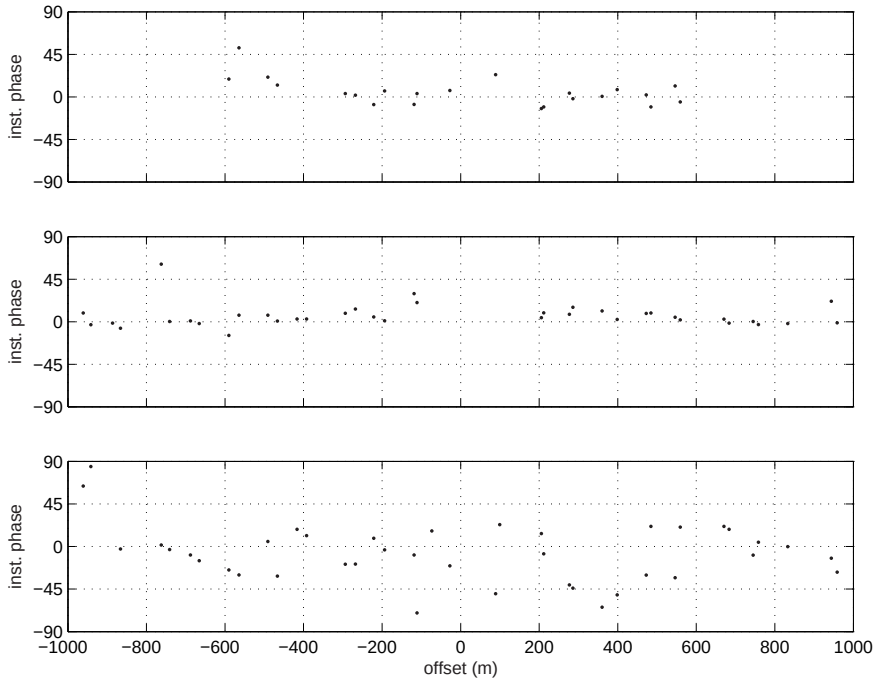

(b)

Figure 6.8: Instantaneous phase function for (a) the three events indicated in the CDP gather in Figure 6.1(a). Event 2 and 3 indicate a phase change in the real data. The lines plotted over the data indicate a possible phase change. (b) the corresponding events in the ACP gather in Figure 6.1(b). No clear phase change can be seen.

6.2 Apparent anisotropy due to compaction

In the second part of this chapter, I will explain the near surface effects, such as low shear-wave velocities and phase reversals, found in the real data with modelling studies.

Parameter estimation for the near surface layers may be erroneous due to vertical velocity compaction gradients Jones et al. (2002). A model was used to investigate the effect of apparent anisotropy on parameter estimation in an isotropic medium due to compaction. Synthetic seismograms were generated using a Pseudo-Spectral Finite-Difference code. Theilen et al. (1997) showed a typical occurrence of strong S-wave velocity gradient below the sea surface. Beside the S-wave gradient, I also included a smaller gradient for the P-wave velocity and a density gradient. These parameters are listed in Table 6.4. The model is illustrated in Figure 6.9. It shows the 660 metres thick layer featuring a velocity and density gradient (displayed are the values for the s-wave velocity) over a halfspace. Figure 6.10(a) and (b) show the vertical and horizontal components and

	V_{p0} [km/s]	V_{s0} [km/s]	ρ [g/cm^3]	t_{p0} [s]	V_{p2} [km/s]	t_{s0} [s]	V_{s2} [km/s]
A	1.6	0.4	1.5	0.825	1.6	2.063	0.8
B	1.8	0.9	2.3	0.733	1.8	1.1	1.273

Table 6.4: Model values for the gradient model with minimum values indicated as model A and maximum values as B.

an arrow indicates the P-wave or C-wave event, respectively. The PP reflection of the P-wave has a zero offset time of $t_{p0} = 0.86$ s and the C-wave reflection on the horizontal component of $t_{c0} = 1.43$ s. In order to enhance the understanding of the effect of the velocity gradient on the traveltimes, the P- and C-wave traveltimes from the minimum (model A) and maximum (model B) of the gradient model were calculated after Equation (2.57) and (2.62) and printed on top of the seismograms (A in blue, B in green). Figure 6.10(a) shows, that t_{p0} for the P-wave of the gradient model is very close to the times of the homogeneous models. The traveltime follows closer to the traveltime curve of model B whose properties represent the maximum values of the gradient model. Thus, the higher velocity values have the larger influence on the P-wave progressing through the

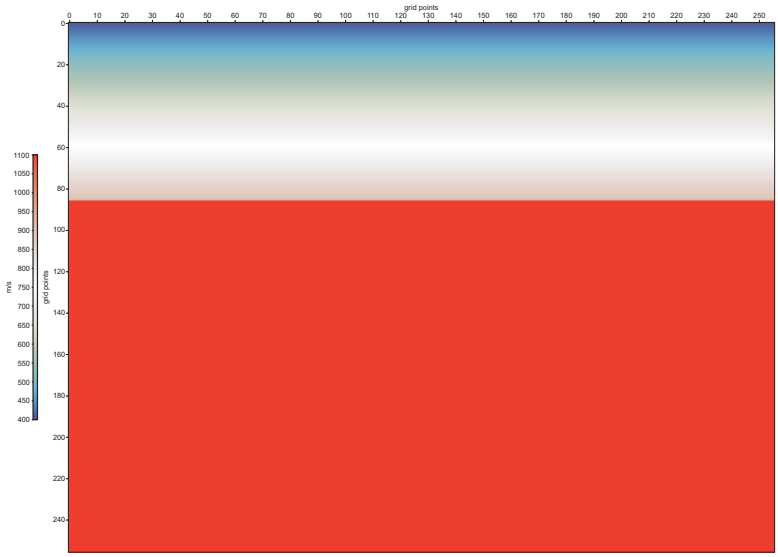

Figure 6.9: Gradient model showing the S-wave gradient in the first 660 metres.

gradient model. The behaviour of the C-wave on the horizontal component shows a larger difference between the individual t_{c0} times. Again, the traveltime curve of the gradient model follows more closely the traveltime curve of model B. Figure 6.11 shows the results of applying the semblance double scanning technique. The picked values are indicated by an "x". The parameters picked from the P-wave (vertical component) are $\eta = 0.1$ and $V_p = 1.6$ km/s from the higher of the two semblance maxima. For the parameter estimation on the C-wave (horizontal component) I used a $\gamma_0 = 2.3$ calculated from picked $t_{p0} = 0.86$ and $t_{c0} = 1.435$ using the relation $\gamma_0 = 2t_{c0}/t_{p0} - 1$. The picked values are $\chi = -0.076$ and $V_{c2} = 1.06$ km/s.

The estimated parameters were then used to perform an NMO correction focusing on the events at the chosen t_{p0} and t_{c0} times. Figure 6.12(a) shows the NMO correction of the C-wave (horizontal component) using a hyperbolic traveltime approximation. The corrected event is not straight and only flat up to approximately 1000 m offset. Figure 6.12(b) shows the non-hyperbolic NMO correction using the anisotropy parameter χ. Here, the event is flatter for a wider offset. In the next step, I approximated η by calculating it from χ with Equation (2.33) as discussed above. From $\chi = -0.076$ I obtain $\eta = -0.01$. This parameter is negative and an order of magnitude smaller than the one estimated directly from the P-wave data. Remembering that the medium is isotropic but with a velocity

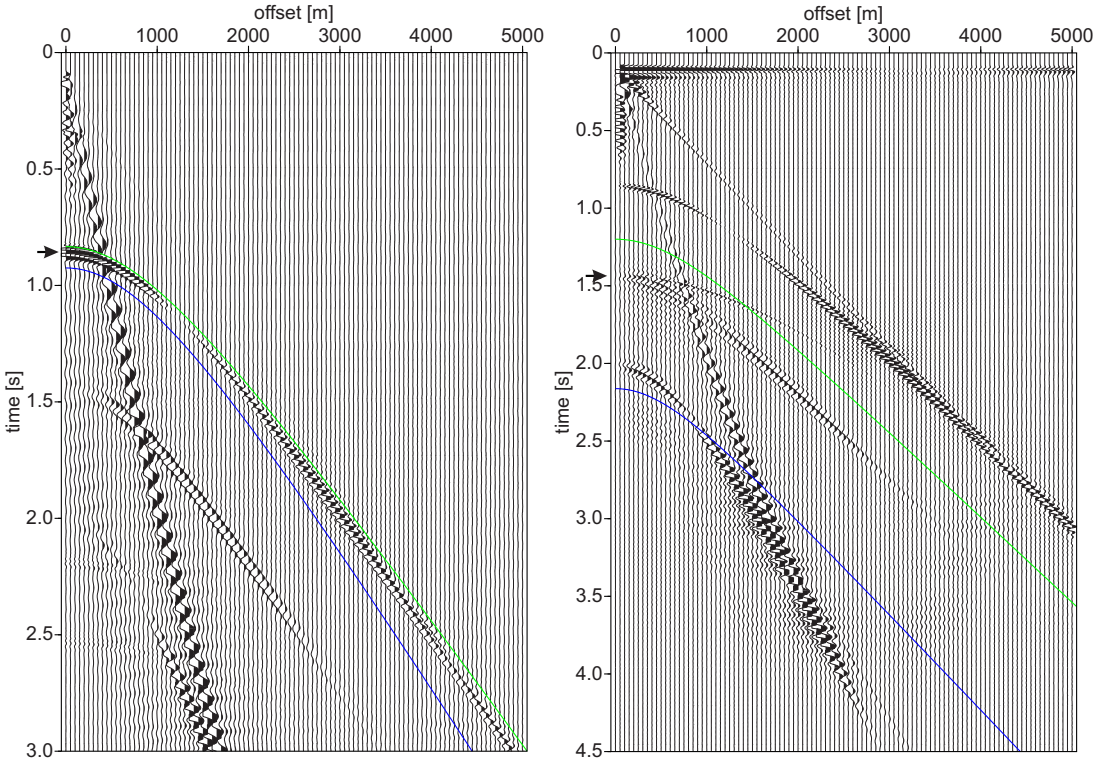

(a) z-component (b) x-component

Figure 6.10: Seismogram of (a) vertical and (b) horizontal component of isotropic model with velocity and density gradient. The PP- and PS-reflections are indicated by an arrow, respectively. For comparison the PP- and PS-reflections from the homogeneous models A and B are printed in blue and green on top of the seismograms.

gradient, the picked $\eta = 0.1$ overestimates the anisotropy while $\eta = -0.01$ seems more realistic. Figure 6.13(a) shows the P-wave gather when corrected with the picked data and Figure 6.13(b) when using the η calculated from χ. I find that the picked and larger η corrects the reflection event marginally better than the calculated one. This is believed to be due to the effect of the velocity gradient. This result suggests that the calculated η represents the effect of anisotropy better. In contrast the directly picked η from P-wave includes the effect of gradients and/or structure and, therefore, corrects all those effects.

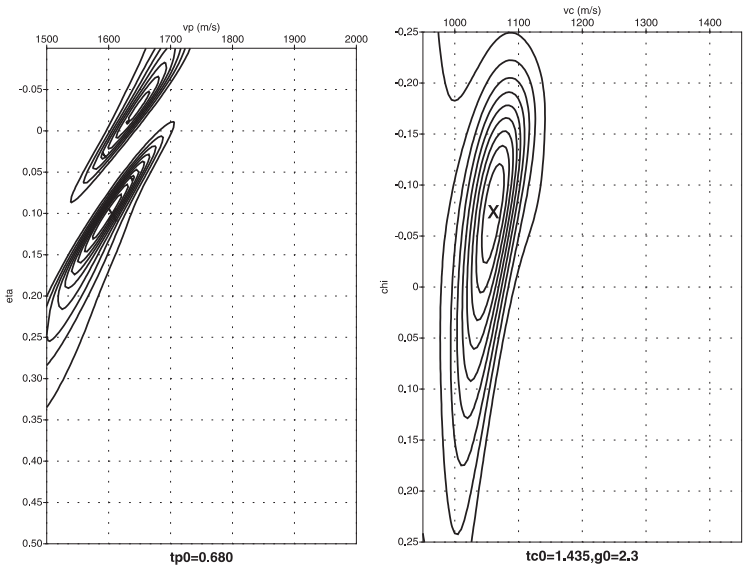

(a) z-component (b) x-component

Figure 6.11: Results of double scanning semblance analysis from the gradient model. (a) Using the vertical component (i.e. P-wave) scanning for η and V_{p2}. The result is not unique. (b) Using the horizontal component (i.e. C-wave) to estimate χ and V_{c2}. The picked values are indicated by an "x".

6.3 Influence of γ_0 on parameter estimation

Next I want to investigate if errors are introduced in parameter estimation due to strong velocity contrast, i.e. large γ_0 value in the near surface layer. Therefore, a ray tracing study of one layer models with varying γ_0 values was carried out. The physical properties of these models are listed in Table 6.5. The layer thickness is

	V_p [km/s]	V_s [km/s]	γ_0	V_c [km/s]	ϵ	δ	χ	η	t_{c0} [s]	$t_{p0}[s]$
1	1.6	0.35	4.6	0.916	0.09	0.03	0.39	0.057	0.557	0.2
2	1.6	0.5	3.2	1.034	0.09	0.03	0.288	0.057	0.42	0.2
3	1.6	0.8	2.0	1.239	0.09	0.03	0.116	0.057	0.3	0.2
4	1.6	1.0	1.6	1.360	0.09	0.03	0.057	0.057	0.26	0.2

Table 6.5: Physical properties of models for study of the influence of γ_0 on parameter estimation.

160 metres to reflect a thin near surface layer which might display a strong velocity contrast between P- and S-wave velocities due to unconsolidated sediments

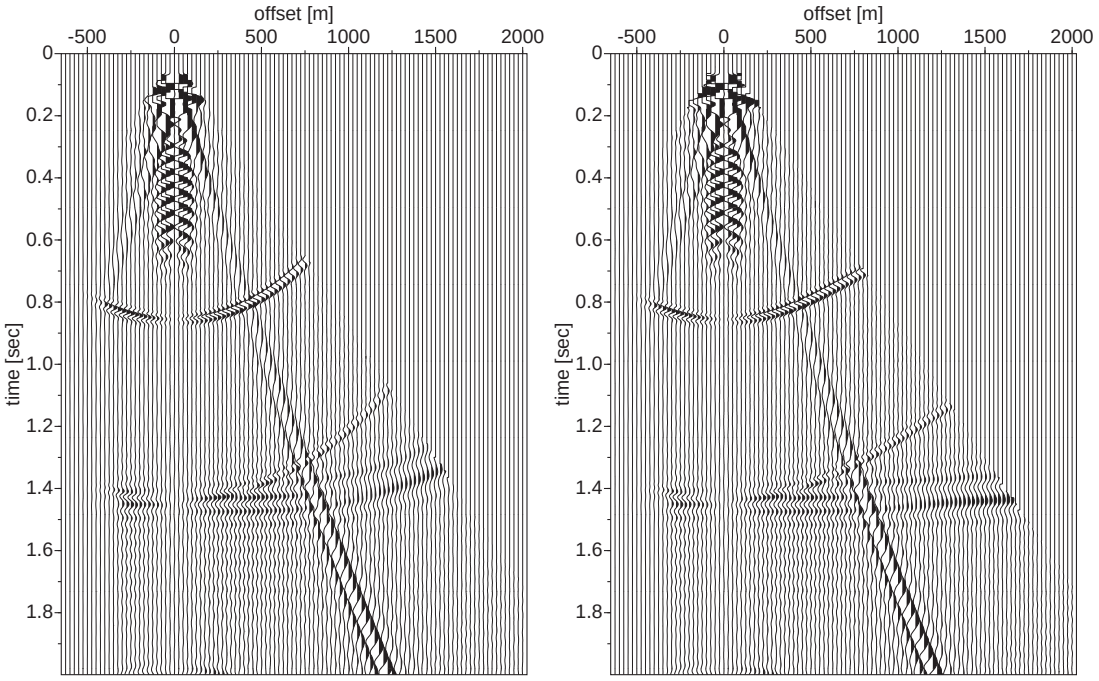

Figure 6.12: NMO corrected C-wave gather of gradient model using (a) conventional hyperbolic NMO. (b) anisotropic non-hyperbolic NMO.

and mud (e.g. the model with $\gamma_0 = 4.6$). The C-wave traveltime approximation is valid up to $x/z = 2.5$ which means only 400 metres of offset can be used for the double semblance routine. Estimating $\eta - v_{p2}$ allows an offset-depth ratio up to $x/z = 3.$, i.e. an offset up to 480 metres. Because the only difference between the various models is a change in S-wave interval velocity, t_{p0} and η stay the same. The P-wave rms-velocity for all models is $V_{p2} = 1.647$. Figure 6.14 illustrates the result of the semblance double scanning analysis. The model values are indicated by an "x". The pick of the maximum semblance coincides with the model values. All four models show the same result as this analysis is independent of γ_0 and thus not affected by its changes.

The parameter estimation for $\chi - V_{c2}$ is strongly influenced by changes in γ_0. Figure 6.15(a) shows the result for the model with $\gamma_0 = 4.6$ and Figure 6.15(b) for $\gamma_0 = 3.2$. Both models represent the situation of very low S-wave velocities as one would expect in muddy layers. Unfortunately, the double scanning technique cannot resolve those values exactly, as the model values are in both cases on the edge of the maximum semblance. Smaller γ_0 values, i.e. smaller velocity

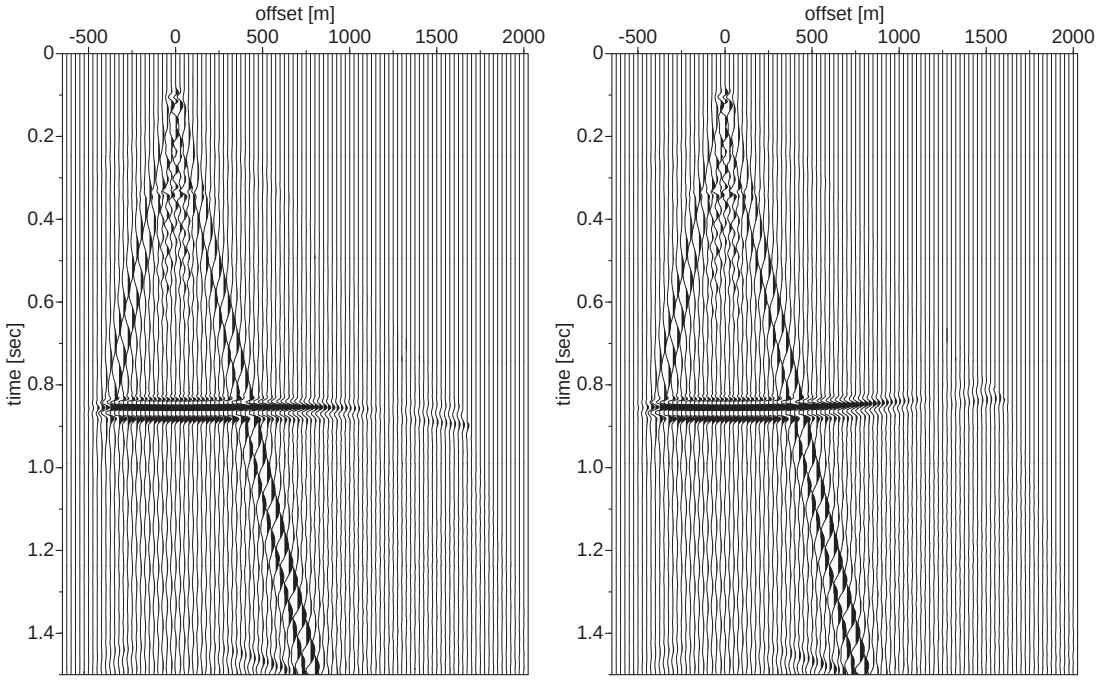

Figure 6.13: Anisotropic NMO corrected P-wave gather using (a) picked η-values and (b) calculated η-values from χ.

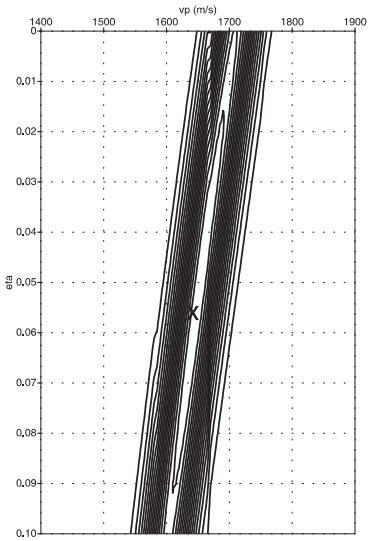

Figure 6.14: Double scanning semblance analysis for $\eta - v_{p2}$ on the vertical component (P-wave) of the γ_0 study model. Note, that the P-wave is independent of γ_0. Theoretical values are indicated by an "x". Note that $V_{p2} = 1.647$ km/s.

differences between P- and S-wave, show a better resolution as shown in Figure 6.15(c) for $\gamma_0 = 2.$ and Figure 6.15(d) for $\gamma_0 = 1.6$. The model values coincide

almost perfectly with the maximum semblance and thus the picked value, and the largest picking error occurs for the largest $\gamma_0 = 4.6$, i.e. $\chi = 0.39 \pm 0.178$. The

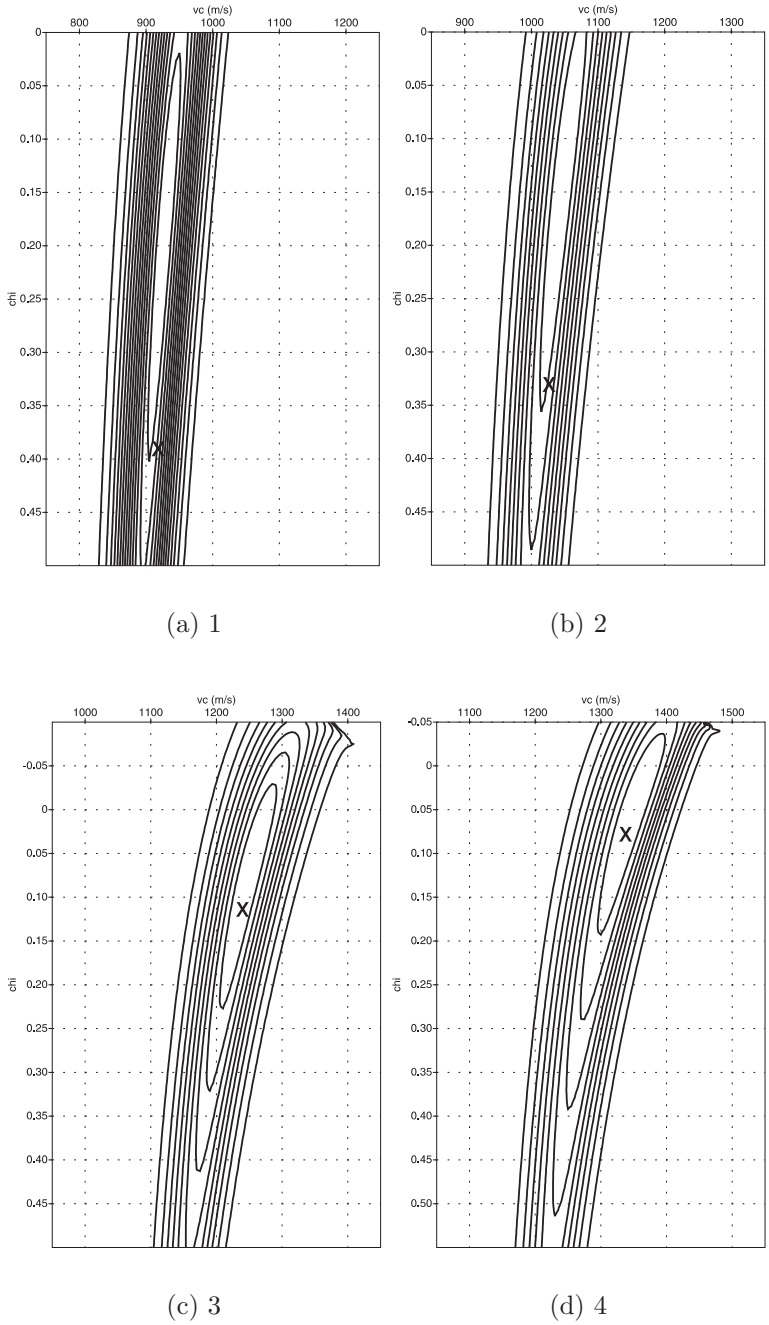

Figure 6.15: Parameter estimation of χ and V_{c2} from the C-wave of the 4 models with decreasing γ_0 ratios in the single layer. (a) $\gamma_0 = 4.57$, (b) $\gamma_0 = 3.2$, (c) $\gamma_0 = 2.$ and (d) $\gamma_0 = 1.6$. Model values are indicated by an "x".

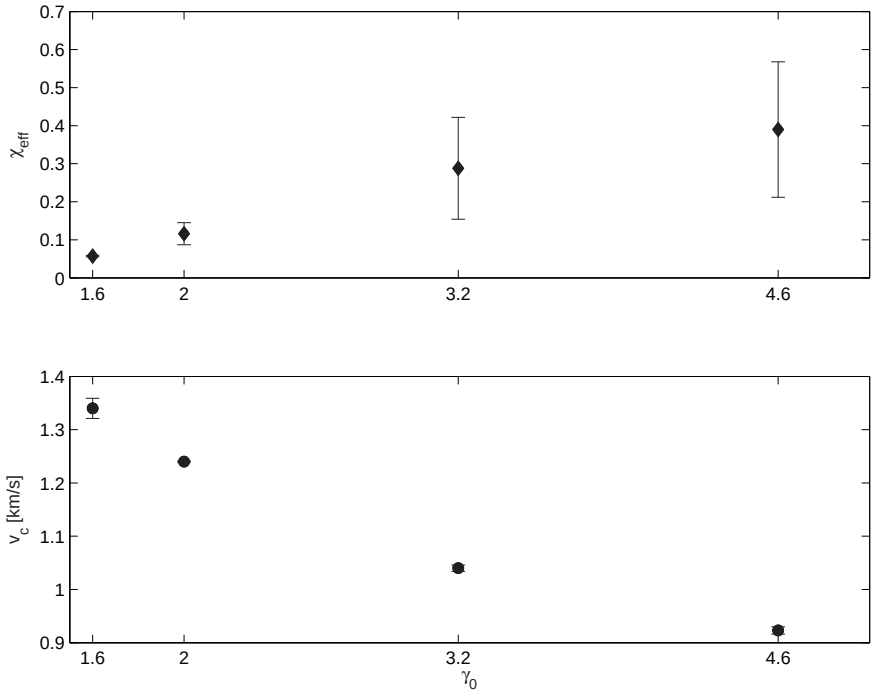

Figure 6.16: Top: Error in picked χ is decreasing with decreasing γ_0. Bottom: The maximum error of estimating velocity V_{c2} is 20 m/s.

decreasing error in estimating χ with decreasing γ_0 is shown in Figure 6.16 (top). The second part of this figure shows that the quality of the estimated velocity V_{c2} is good for all values of γ_0 with maximum error of 20 m/s.

In summary it can be observed that a strong contrast between P- and S-wave velocity in a near surface layer leads to errors in anisotropic parameter estimation using the semblance double scanning technique for the C-wave. A velocity ratio of $\gamma_0 = 2$ and less gives exact results while velocity estimation is not affected. Note though that the anisotropy value decreases with decreasing γ_0 which might lead to problems in parameter estimation. Estimation of anisotropy parameter η from the P-wave is not affected by the velocity ratio.

6.4 Near-surface Alba model

In a second study I investigate the accuracy of estimating anisotropy parameters in a flat layered medium without structure or velocity gradients. I estimate η in

two ways, firstly directly from P-waves, and secondly, by calculating it from the C-wave parameter χ. A variation of the base Alba model, introduced in Traub and Li (2002) was used for the study. The model consists of 3 layers of VTI over an isotropic halfspace. Table 6.6 summarises the background model properties for density, P- and S-wave velocity and the anisotropy parameters ϵ and δ and the thickness of each layer. The model properties are based on VSP and well log data from the Alba Field. A low S-wave velocity has been observed in the data and consequently displayed in the near-surface model. Seismograms were computed

Layer	ρ $[g/cm^3]$	V_{p0i} [km/s]	V_{s0i} [km/s]	ϵ	δ	depth [m]
Sand	2.2	2.2	0.4	0.11	0.03	300
Shale	2.2	2.5	0.7	0.11	0.04	250
Sandyshale	2.2	2.55	1.372	0.13	0.06	250
Limestone	2.01	2.43	0.731	0.0	0.0	halfspace

Table 6.6: Properties of the near-surface base model.

with the modelling package ANISEIS (Taylor, 2001). Figure 6.17(a) illustrates the vertical and 6.17(b) the horizontal component. Traveltime curves for the P- and C-wave have been calculated and printed on top of the corresponding seismogram. They were muted according to the range of validity of the traveltime equations (x/z=3 for P-wave and x/z=2.5 for C-wave). To illustrate the need of anisotropic moveout correction both seismograms have been NMO corrected with a conventional hyperbolic moveout correction using model values for the velocities. The results are again muted to the x/z ratio of the anisotropic traveltime equations to make comparison easier. Figure 6.18(a+b) shows these results, respectively. It is clear that even within this restricted area the events are not flat but still show a moveout curvature.

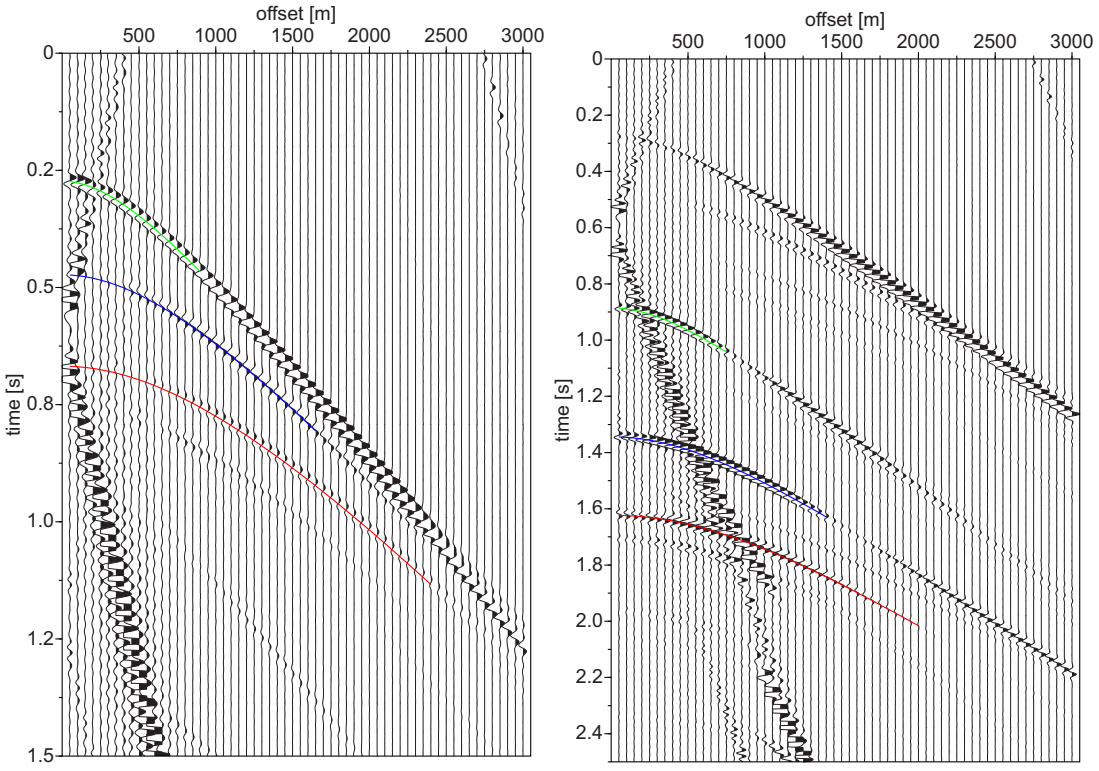

(a) z-component (b) x-component

Figure 6.17: Seismograms of the near-surface model with traveltime curves for the P- and C-wave printed on top. Traveltime curves are muted according to the restricted range of the traveltime equation. (a) Z-component with x/z=3. Arrows indicate phase reversal and weakened amplitude. (b) Horizontal component with x/z=2.5.

	$t_{p0} = 0.273s$	$t_{p0} = 0.473$ s	$t_{p0} = 0.668$ s
model value η	0.075	0.073	0.071
picked η	0.064	0.17	0.108
η calculated from χ	0.073	0.072	0.07
model value V_{p2} [km/s]	2.265	2.412	2.502
picked V_{p2} [km/s]	2.29	2.24	2.44
	$t_{c0} = 0.886s$	$t_{c0} = 1.344$ s	$t_{c0} = 1.623$ s
model value χ	0.338	0.360	0.308
picked χ	0.328	0.352	0.303
model value V_{c2} [km/s]	1.257	1.381	1.528
picked V_{c2} [km/s]	1.230	1.360	1.520

Table 6.7: Anisotropy parameters for 3-layer near-surface Alba model.

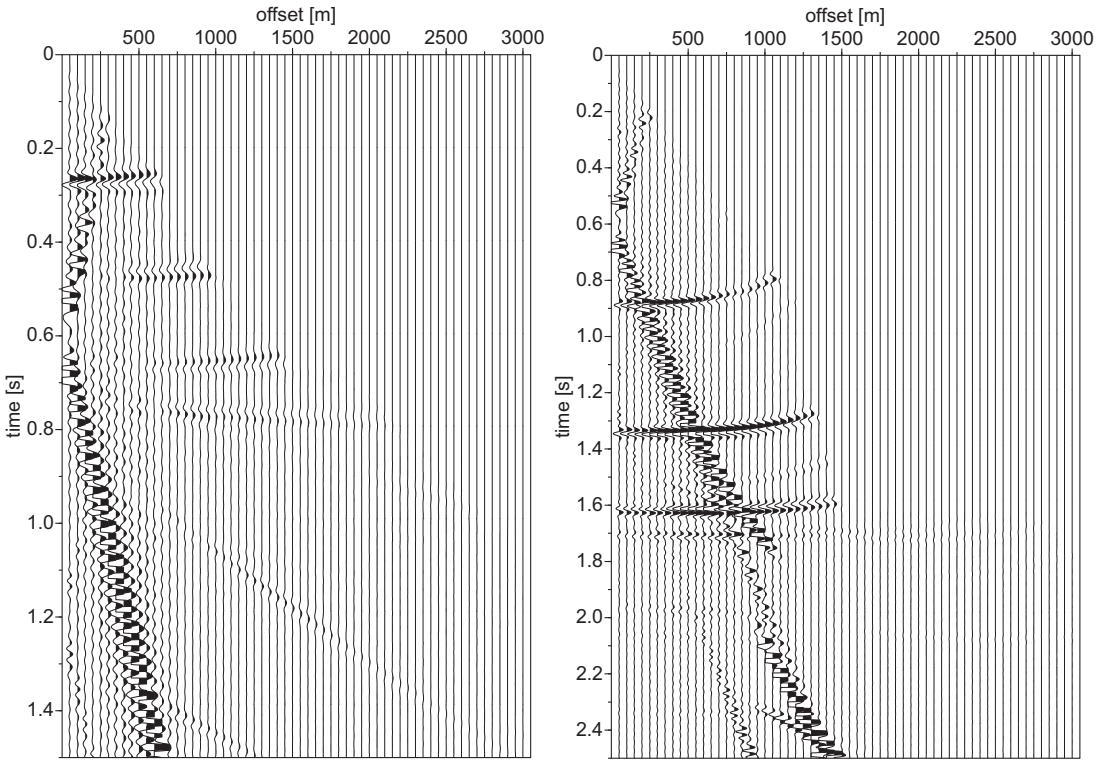

(a) z-component (b) x-component

Figure 6.18: Hyperbolic NMO correction for (a) vertical component and (b) horizontal component. Model values haven been used for the corrections.

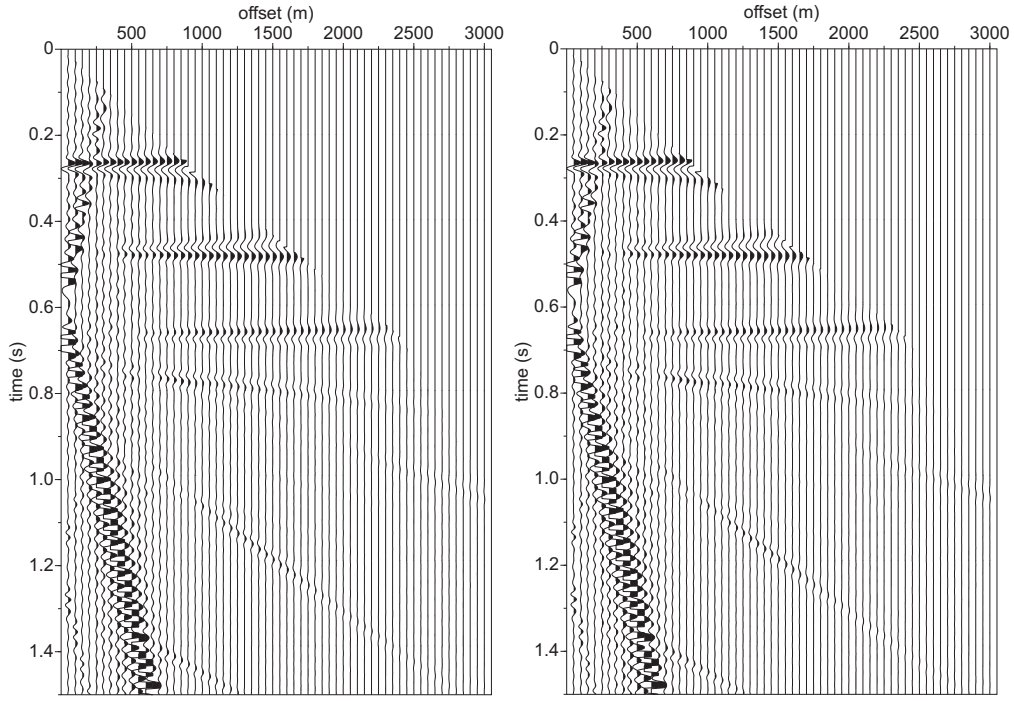

(a) (b)

Figure 6.19: Anisotropic NMO corrected P-wave gather using (a) model values. (b) using η-values calculated from picked χ and model values for V_{p2}.

Firstly, I estimated the anisotropy parameters of this model using the double semblance scanning technique utilising Equation (2.57) searching for $\eta - V_{p2}$ on the P-wave or $\chi - V_{c2}$ on the C-wave using Equation (2.62). Secondly, I use these picked χ values from the horizontal component to calculate η after Equation (2.33). Both values and the model values are listed in Table 6.7. Note especially that the picked η-values for the 2$^{\text{nd}}$ and 3$^{\text{rd}}$ layer differ by considerable from the model values. Next, I carried out an NMO correction of the P-wave gather for each set of anisotropy parameters. Mute was applied according to the offset-depth restriction of the traveltime approximation. Figure 6.19(a) shows the NMO correction using the model values for η and V_{p2}. Figure 6.19(b) shows the same gather when the η-values were used, calculated from the picked χ and model V_{p2}. Both gathers show flat events.

Figure 6.20(a) shows the NMO corrected gather when the picked $\eta - V_{p2}$ values were used. The 1$^{\text{st}}$ events is flat, but the layer 2 event describes a bow and the 3$^{\text{rd}}$ layer event is slightly curved. For better comparison Figure 6.20(b) shows the NMO correction using the model V_{p2} and the picked η values. The 1$^{\text{st}}$ event is flat but the 2$^{\text{nd}}$ layer still describes a bow while the 3$^{\text{rd}}$ layer is straight and flat. These results confirm the observed results where the η values calculated from χ values are closer to the model anisotropy values. In other words, they describe the anisotropy of a medium better. The η-values estimated from P-wave data double semblance scanning differ from the model values by up to an order of magnitude. The resulting NMO correction shows the expected unsatisfactory results in a medium which is not influenced by structure or velocity gradients.

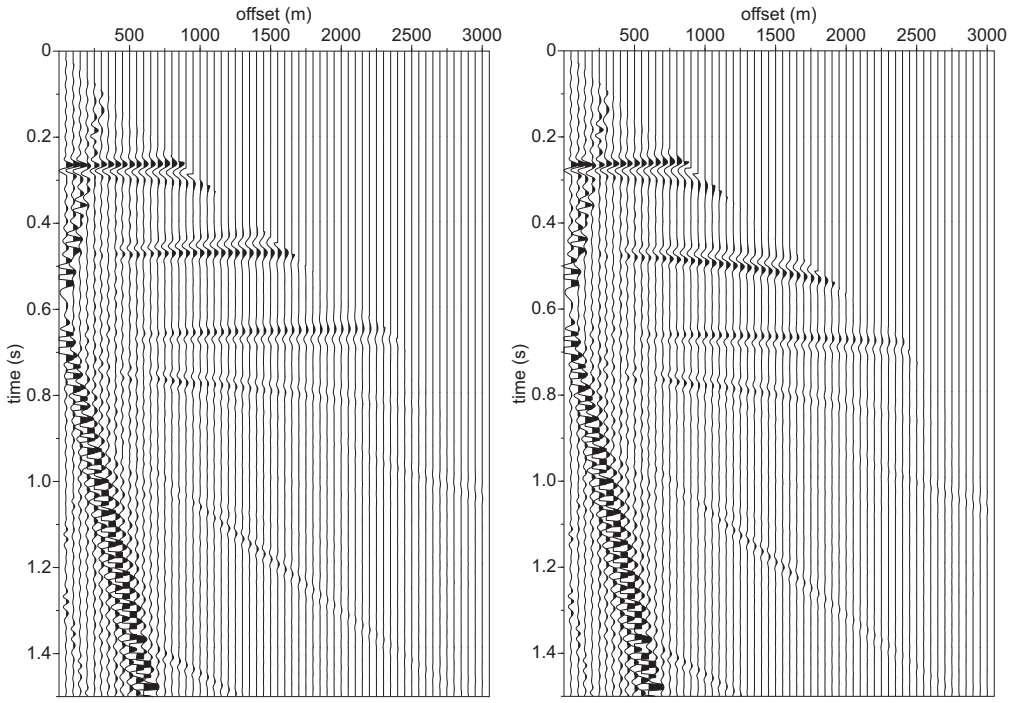

(a) (b)

Figure 6.20: Anisotropic NMO corrected P-wave gather using (a) picked $\eta - V_{p2}$-values. (b) picked η-values and model values for V_{p2}.

6.4.1 Instantaneous phase function

In the vertical component of the synthetic seismogram from the near-surface model phase reversals can be observed in the 2nd and 3rd layer as indicated in Figure 6.17(a) by arrows. The phase reversals coincide with diminishing of the amplitudes. The horizontal component does not show such a feature within the range of validity of the C-wave traveltime equation. For further confirmation the complex trace analysis Taner et al. (1979) has been applied to calculate the instantaneous phase function for each reflection response of the 3 subsurface interfaces of the model. Calculation of the instantaneous phase function gives a measure of the continuity of events on a seismic section with the same reflection or conversion point. To calculate the instantaneous phase function each signal from one horizon was picked separately. The results are displayed in Figure 6.21(a) for the vertical and Figure 6.21(b) for the horizontal component. The vertical component shows for the first layer a generally continuous trend without changes of the phase. The phase for the second layer shows scattering for an offset up to ca. 500 metres and no changes thereafter. The scattering in the beginning is taken as an indication for phase reversal in the near offset. Finally, the third layer shows scattering for an offset up to about 700 metres and after that a continuous flat line. Again, this is taken as a confirmation of phase changes in the near offset. The lines plotted over the data from layer 2 and 3 highlight the overall behaviour of the phase function indicating a phase change. However, the instantaneous phase for the horizontal component of the model shows no indication for phase reversals for the corresponding events.

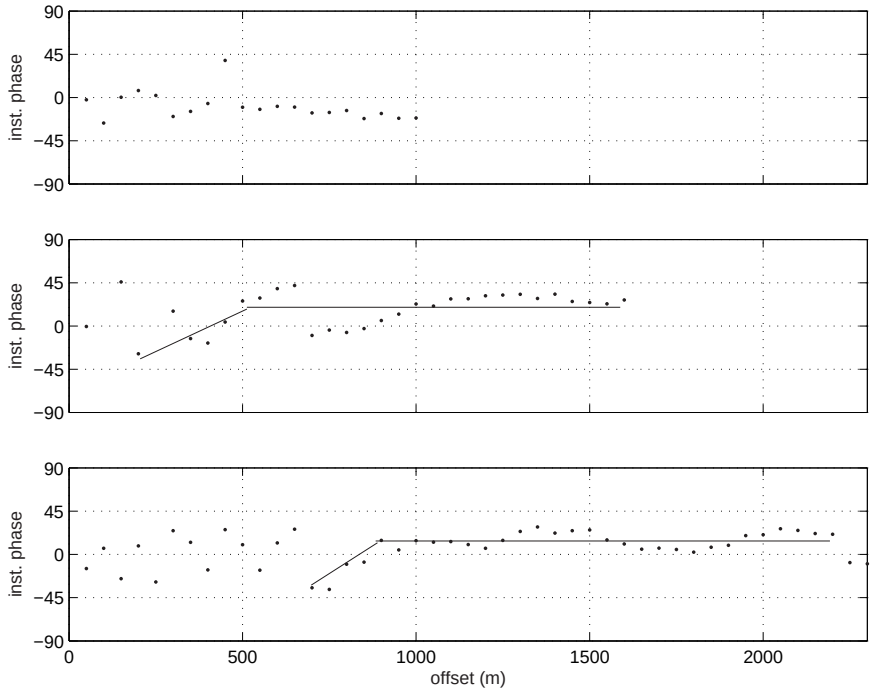

(a)

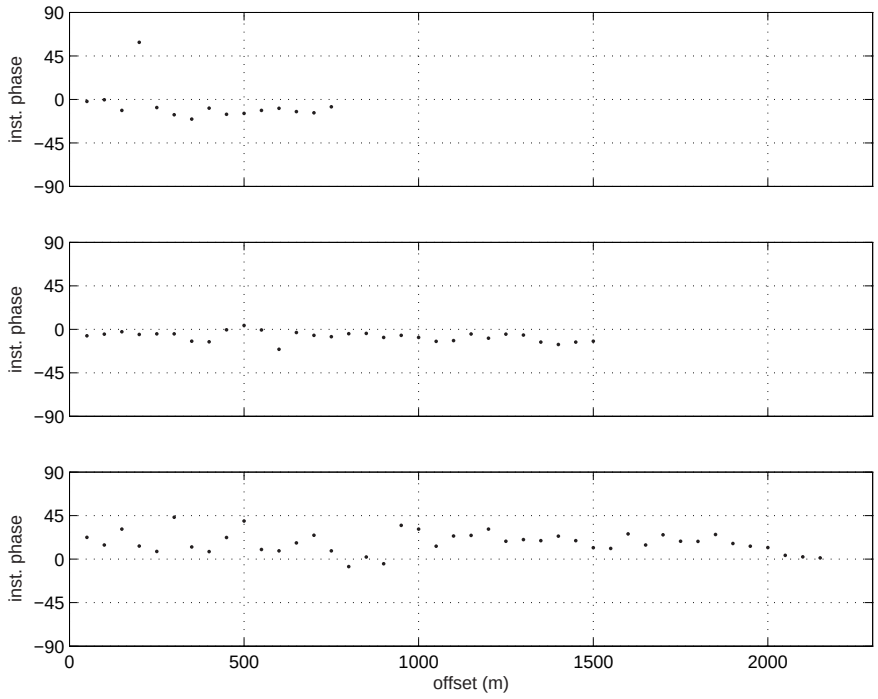

(b)

Figure 6.21: Instantaneous phase function calculated for the three interfaces of the near-surface model. (a) Vertical component. Lines indicate the trend of the instantaneous phase function. (b) Horizontal component. There is no clear indication of a phase change.

6.4.2 Phase and amplitude behaviour of reflections on layer boundaries

It has been shown that synthetic data show phase reversals in the vertical component. In order to explain the origin of this phenomenon the effective reflection coefficient for the reflection from the bottom of each layer in the near-surface model has been calculated using the code introduced in Chapter 5, Section 5.7. The reflection coefficients are normalised by source amplitude and their moduli are plotted as a function of offset or incidence angle. For this study the model was first isotropic. The coefficients are normalised by source amplitude and their moduli are plotted as a function of offset. In Figure 6.22 the amplitude (top) and phase (bottom) of the PP-reflection has been displayed for an offset up to 3000 metres. The reflection coefficient as a function of incidence angle is displayed in the Appendix D, Figures D.13 and D.14. The diagram shows, that for the first layer the amplitude increases rapidly just before the critical angle is reached. The critical angle for a PP-reflection at this layer boundary occurs at an incidence angle of 62° or 1110 metres offset. The phase changes after this exponentially. The 2nd and 3rd layer show first an decrease of the amplitude to almost zero and then it increases again. This coincides with a phase change of 180°. The amplitude vanishes for the second layer at an offset of 202 metres and for the third layer at 590 metres. These offsets correspond to the observed vanishing amplitude and following phase reversal in the seismogram of the vertical component. Furthermore, these offsets are in the range which is included in the parameter estimation and thus lead to energy cancellation and possible erroneous parameters.

The horizontal component shows a similar behaviour of the effective reflection coefficient as shown in Figure 6.23. Note, that here, the first layer shows a decrease of the amplitude to almost zero at about 550 metres. This corresponds to a phase reversal and is followed by an exponentially change of phase up to 180°. The offset of 550 metres corresponds to an angle 59° and the start of the exponential change of phase with 62°. This indicates, that the C-wave is influenced by the total reflection of the PP wave. The second and third layer have amplitudes of almost zero at 1280 and 2133 metres with a corresponding phase reversal, respectively. A close observation of these offsets in the synthetic seismogram confirms these

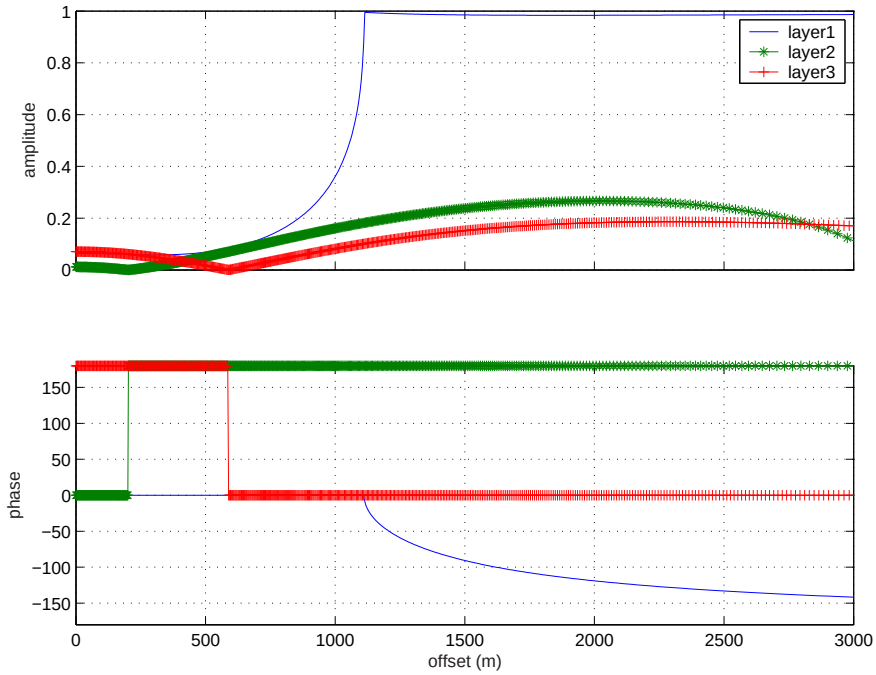

Figure 6.22: Top: Effective reflection coefficient for the 3 interfaces in the Alba near-surface model for PP reflections over offset. Bottom: Corresponding phase behaviour.

phenomenon. But in contrast to the vertical component they occur out of the range of validity of the traveltime equations used for the semblance double scanning analysis and, therefore, do not affect the parameter estimation. These findings help to explain the erroneous high values for the anisotropy parameters for the second and third layer of the vertical component.

In order to find out if there is a large difference between isotropic and anisotropic reflection coefficients regarding the reflection on the bottom of the first layer, I calculated the anisotropic reflection coefficient again using the method described by Schoenberg and Protazio (1992) . Figure 6.24 shows the amplitude behaviour over incidence angle for both, P- and C-wave. It can be seen that there is a very good agreement between anisotropic and isotropic results. Only for high incidence angles near to the angle of total reflection does the anisotropic amplitude for the P-wave start to increase earlier than the isotropic amplitude. The amplitudes of the C-wave show good agreement. The anisotropic amplitude diminishes smaller angles to zero as does the isotropic amplitude. In conclusion, the near-surface model is only weakly anisotropic and therefore the differences in the reflection

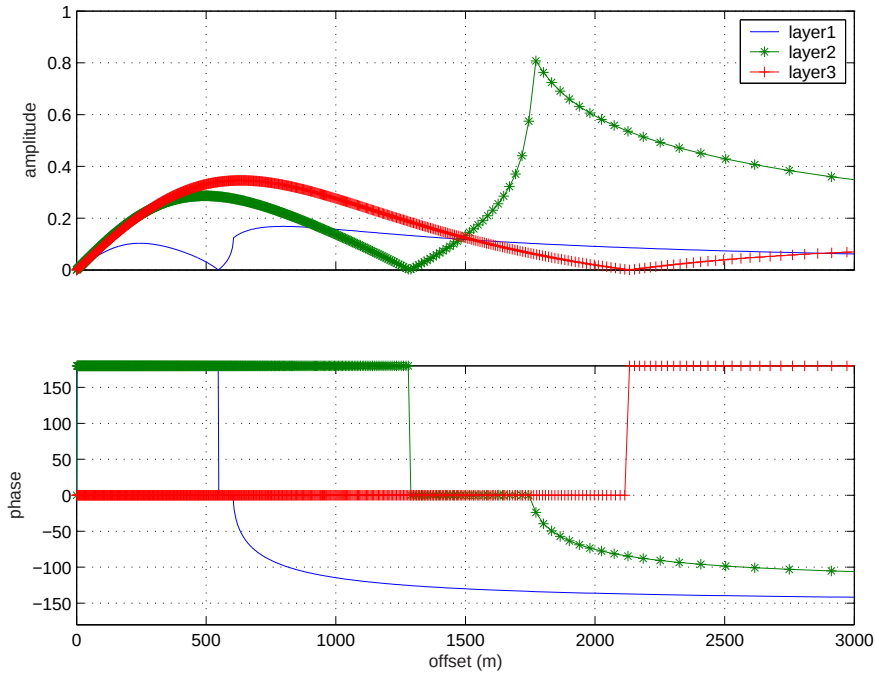

Figure 6.23: Effective reflection coefficient for the 3 interfaces in the Alba near-surface model for P-S reflections over offset. Bottom: Corresponding phase behaviour.

coefficients can be neglected. Therefore, the effective reflection coefficient of the isotropic version of the model can be used to explain the phase reversals and amplitude diminishing seen in the anisotropic model.

6.5 Conclusion

In this study I have investigated the problems in anisotropy parameter estimation of near-surface events. Parameter estimation has then been applied to real data from the Alba field. P-wave anisotropy parameter η has been estimated from the vertical component and also been calculated from χ, obtained from the horizontal component. I also used χ from C-wave moveout to calculate η. However, the calculated η is about an order of magnitude smaller than the picked value. In order to understand the difference I also carried out a full-waveform modelling study. From well, VSP and surface data I generated a model which allowed the calculation of reference parameter values. Full-waveform synthetics were calculated for this model. The same estimation procedure were applied to these synthetics. I find that 2 out of 3 values of η from P-wave of the near-surface model are an order

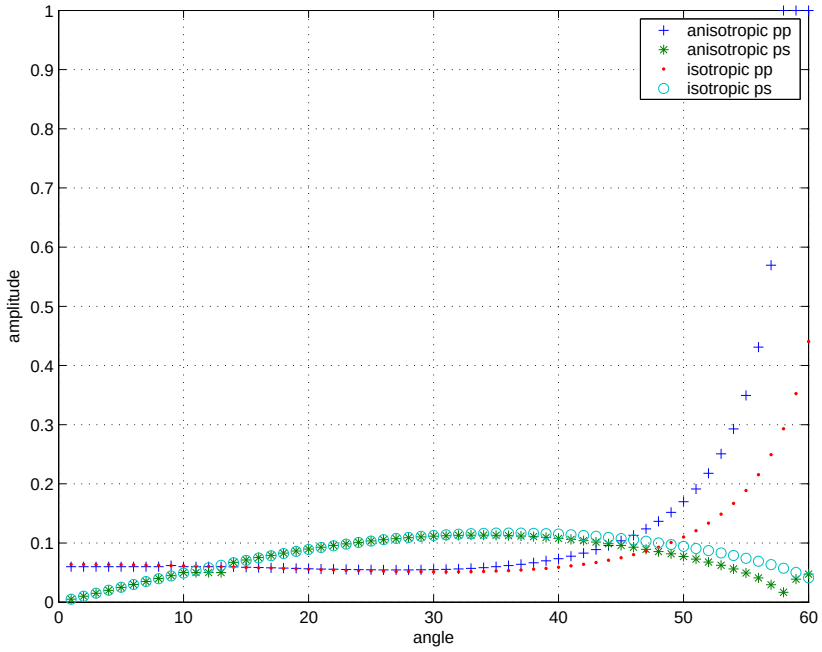

Figure 6.24: Comparison of reflection coefficient of isotropic and VTI version of near-surface model.

of magnitude larger than the model values. Estimating the anisotropy parameter χ from C-waves and calculating η from it gives a more accurate result. However, anisotropic NMO corrected CDP gathers show slightly better results when the picked η values are used. Therefore the modelling study confirms that η from C-wave data represents the anisotropy of the medium better then η estimated from P-wave data. In contrast η from P-wave data may also represent the effect of layering and compaction and not just anisotropy.

In order to explain the erroneous value of the P-wave parameter estimation I find phase reversals and coinciding weakened amplitudes occurring in the range of offsets used for parameter estimation. Phase reversals interfere with the double semblance technique due to energy cancellations. These phase reversals are confirmed by computation of the instantaneous phase function for each event on the P-wave component. In contrast, the C-wave does not show this effect in the range of offsets used for parameter estimation. This phenomenon of phase reversals and diminishing amplitude can be explained by means of effective reflection coefficients. I find that phase reversal only occurs for the given model in the offsets of interest on the vertical component. This explains why the parameter estimation

gives erroneous results when encountering phase reversals. Furthermore, I find that near surface effects, like compaction gradients, induce apparent anisotropy, which leads to erroneous parameter values influencing the imaging of the target in deeper layers.

I conclude from the above that both real and modelling studies show that η can be better estimated from converted waves than P-waves. This agrees with the theoretical studies in Chapter 4 and Chapter 5.

Chapter 7

Analysis of the Alba 4C data for anisotropy: Part I - Nonhyperbolic processing and parameter estimation

In this chapter, I apply the findings of previous chapters to the Alba data and perform an integrated study on imaging and model building. The main aim of seismic processing and parameterisations is to obtain a good image of the subsurface. In many cases the hyperbolic assumption for traveltime calculations and thus velocity analysis, NMO correction and stacking gives a good image. However, in the presence of anisotropy these assumptions break down and the more complicated non-hyperbolic traveltime approximations which incorporate anisotropy must be used.

Over recent years, reprocessing of the Alba 4C data revealed the presence of strong polar anisotropy, vertical transverse isotropy (VTI), in the data. In order to obtain further improvements in C-wave imaging (Dai et al., 2001; Mikhailov et al., 2001b) this anisotropy has to be taken into account. However, how to estimate anisotropy parameters and how to utilise them for imaging are still subjects of intensive research. There are several approaches to the problem of converted-wave imaging in anisotropic media. At one end of the spectrum, there is the

traditional CCP binning, NMO, DMO and post-stack migration approach (e.g. Rommel, 1996; Tsvankin and Grechka, 2000) and at the other end, there is the total-depth solution approach (e.g. Mikhailov et al., 2001b). Since 1999, the Edinburgh Anisotropy Project (EAP) has been promoting the approach of using prestack time migration (PSTM) to replace the CCP binning, DMO and post-stack migration approach, and has developed the basic theories and a range of tools for this purpose (e.g. Li et al., 2001b; Dai, 2003a; Li and Yuan, 2003).

Following this approach, the converted-wave kinematic response is separated into a zero-dip response for horizontally layered media (moveout signature), and an all-dip response from a point scatter (diffraction signature). The former controls the stacking process, and the latter controls the process of prestack time migration (PSTM). The moveout signature is determined by four parameters: the C-wave stacking velocity V_{c2}, the vertical and effective velocity ratios γ_0 and γ_{eff}, and the anisotropic coefficient χ_{eff}, collectively referred to as the stacking velocity model. The diffraction curve is determined by five parameters: the vertical velocity ratio γ_0, the P- and S-wave stacking velocities V_{p2} and V_{s2}, and their corresponding anisotropic coefficients η_{eff} and ζ_{eff}. Parameters V_{p2}, V_{s2}, η_{eff} and ζ_{eff} are referred to as the PSTM velocity model.

There is a one-to-one link between the stacking and PSTM velocity models. Therefore, anisotropic imaging can proceed first with moveout analysis to build the stacking velocity model. This model can then be used as an initial model for PSTM for constructing common-imaging-point (CIP) gathers. These CIP gathers can be used to update the PSTM model for final imaging. We will use the Alba 4C data to test this approach and to demonstrate how anisotropic parameters can be estimated and utilised for improved imaging. Bench marks of the anisotropic parameters are obtained from the Alba VSP data for calibration and verification.

Some prior knowledge of the subsurface (for instance the velocity ratios) are often needed before anisotropy can be estimated. These ratios are assumed to be known for the synthetic studies in the previous chapters. Here, I will present a work flow aiming at obtaining all necessary parameters from the 4C data. I will then apply the this approach to the Alba 4C data set.

The results of this work will be presented in two parts. In the first part, I focus on moveout analysis to estimate the four stacking parameters. In the second part, I focus on model updating and validation as well as final imaging.

7.1 Work flow for parameter estimation from 4C data

As discussed in Chapter 2 and Chapter 4 only two parameters, V_{p2} and η_{eff}, are involved in controlling the P-wave moveout. In contrast, the C-wave moveout is controlled by four parameters, i.e. $V_{c2}, \chi_{\text{eff}}, \gamma_0$ and γ_{eff}. Knowledge of γ_0 and γ_{eff} are required before V_{c2} and χ_{eff} can be estimated. In the previous chapters, γ_0 and γ_{eff} were assumed to be known for the theoretical studies. In real data applications, they need to be estimated from the data itself.
Next, I will briefly discuss how γ_0 and γ_{eff} can be estimated from the 4C data and then introduce the work flow.

7.1.1 Estimation of γ_0 and γ_{eff}

The vertical velocity ratio γ_0 is usually determined by event correlation between P- and C-wave data. This involves processing the P- and C-wave data using only standard hyperbolic methods to obtain two stacked sections. For convenience, this initial processing may be carried out in the ACP or CDP gather domain. γ_0 is then obtained by correlating the P- and C-wave stacked sections.
An interactive tool developed in the EAP (Dai, 2003a) simplifies this task by displaying the P- and C-wave sections next to each other. The γ_0 value can then be interactively selected to match events from both sections. Compression of C-wave to P-wave arrival time is also a helpful tool for event correlation. A screen shot is displayed in Figure 7.14.
Once γ_0 is obtained, γ_{eff} is calculated using Equation 2.51,

$$\gamma_{\text{eff}}^2 = \frac{V_{p2}^2}{(V_{c2}^2(1+\gamma_0) - V_{p2}^2)}, \tag{7.1}$$

which originates from knowing

$$V_{s2}^2 = V_{c2}^2 \left(1 + \frac{1}{\gamma_0}\right) - \frac{V_{p2}^2}{\gamma_0}.$$

and rearranging it using the definition $\gamma_2 = V_{p2}/V_{s2}$ and Equation 2.27. Error propagation may be an issue when using this equation. However, it will still give a good initial estimate.

7.1.2 Work flow

For 4C data, which includes vertical and inline data, I summarise a "typical" work flow as follows:

1. Produce brute stacks of the vertical (P-wave) and the inline (C-wave) component and build an initial velocity model for V_{p2} and V_{c2}.
2. Estimate γ_0 by joint correlation of the stacked sections.
3. Calculate initial γ_{eff} from V_{p2}, V_{c2} and γ_0 by using the Equation 7.1
4. Use non-hyperbolic anisotropic processing to update and finalise the velocity model for V_{c2} by applying a semblance double scanning technique to obtain both, χ_{eff} and V_{c2}.
5. Calculate V_{s2} using γ_0 and γ_{eff}.
6. Calculate σ from χ in order to estimate V_{s0} from $V_{s2} = V_{s0}\sqrt{1+2\sigma}$.

The above scheme shows that one can determine from the data only the parameters V_{p2}, V_{c2} and χ_{eff} directly. Not mentioned above, the P-wave anisotropy parameter η_{eff} can be determined from single mode far-offset PP-reflection data.

7.1.3 A GUI (Graphic User Interface) for model building

The above work flow involves extensive parameter picking. Effective picking can be an issue. In addition, double-scanning is not very efficient and tends to be a time-consuming method because its application to real data involves several iterations to obtain the best value. Quality control has to be performed with different

tools and involves paper work for handling the picked parameters. Furthermore, the interchange of parameter and error propagation has also to be taken into account. In order to simplify these procedures a GUI (Graphic User Interface) has been developed to perform these tasks (Dai, 2003a). The GUI tools use the Taylor series equation of C-wave moveout (Equation (2.62)) which requires γ_0 as prior knowledge. The data input to the tool are ACP gathers. The successful application of GUI lies in the offset dependent behaviour of the moveout. In a recent study Li (2003) found that the three moveout parameters (V_{c2}, χ_{eff} and γ_{eff}) control different offset ranges of primary influence: V_{c2} controls the hyperbolic moveout in the near-offset (offset-to-depth $x/z \leq 1.0$), γ_{eff} controls the non-hyperbolic moveout in intermediate offset ($x/z \leq 1.5$) due to the asymmetric raypath and χ_{eff} controls the non-hyperbolic moveout in the far offset due to anisotropy. Thus, these parameters may be estimated from the corresponding data aperture. These understandings underline the GUI tools for parameter estimation. Last but not least, the GUI tool is very efficient. The calculated traveltime curve is displayed on top of the real data as an instant check of quality. The velocity can be updated from a semblance spectrum and the parameters γ_{eff} and χ_{eff} are selected according to the fit of the calculated curve on the real data event based on the corresponding data aperture. Figure 7.22 shows a snapshot of the interactive GUI tool.

In the following section I will apply the work flow to the data and present and discuss results at each step. The GUI tools will also be used in model building whenever appropriate. Based on the work flow, I first use conventional processing methods (ProMAX processing package) to get an initial stack of the vertical and the two horizontal components. A post-stack Kirchhoff migration is then applied to the inline component. In order to show the effects of the non-hyperbolic moveout I obtain an initial stack for the inline component using non-hyperbolic processing tools developed within the Edinburgh Anisotropy Project (EAP). During this process I estimate the anisotropy parameter χ_{eff} from C-wave and η_{eff} from P-wave data together with the corresponding stacking velocities. I build a model for the Alba data by obtaining interval quantities from the estimated RMS-values. I verify the result for the overburden with a synthetic modelling study. Finally I show the result from the pre-stack Kirchhoff time-migration of the C-wave data.

7.2 Conventional processing

7.2.1 P-wave processing (vertical component)

From the two components which record P-waves (vertical geophone and hydrophone) I will only discuss the vertical geophone data. In Chapter 3, Section 3.2, I have shown the good data quality of the vertical component and thus summation of this data with the hydrophone data may not be necessary. Figure 7.1 shows a typical processing flow for conventional processing of P-wave data with ProMAX. The geometry had to be inserted into the headers and checked, which

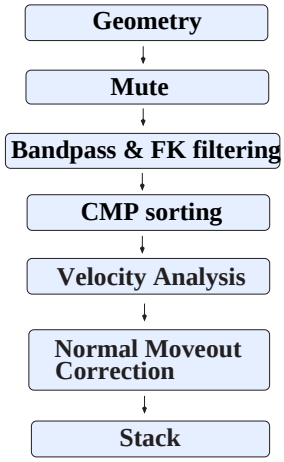

Figure 7.1: Initial processing flow for the P-wave data (vertical component).

turned out to be time consuming. After the geometry settings were finished, I applied a mute to remove the direct wave, and amplitude recovery, to make the reflection events more visible. Bandpass- and fk-filtering were used to remove linear events and generally to improve the signal-to-noise ratio. Next, I performed CMP sorting and then carried out the velocity analysis to get an initial velocity model (see Figure 7.2) which was used for the NMO correction as well as for further non-hyperbolic processing steps. Finally, Figure 7.3 shows the initial vertical stack. It shows events up to about 6 seconds two-way traveltime, although a closer look reveals that between 1.7 and 2.2 seconds the reflectors are less continuous. This is coincident with the approximate location of the Alba reservoir. The second reservoir, the main Britannia field, is recognisable at about 3 seconds two-way traveltime. The aim of this processing is to generate a P-wave stacked section for event correlation.

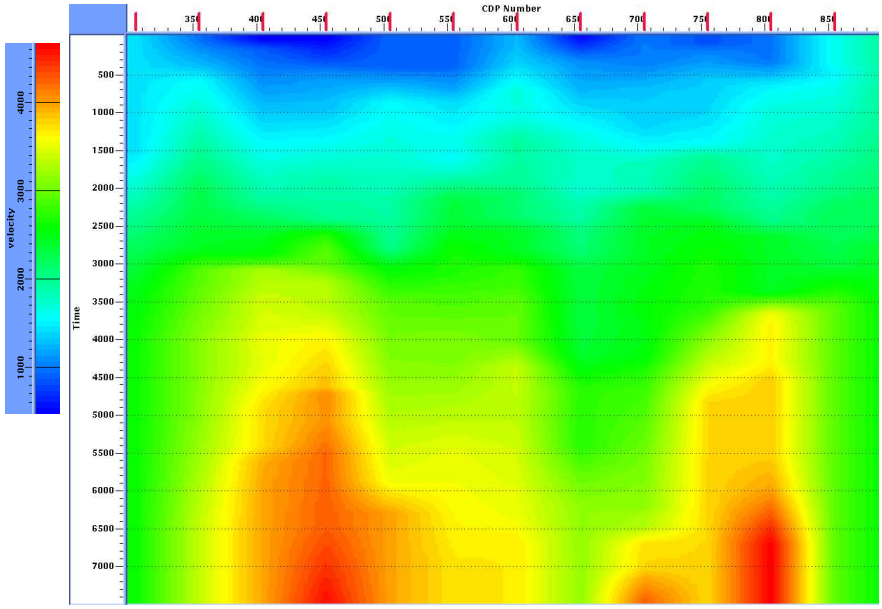

Figure 7.2: Initial P-wave stacking (RMS) velocity profile estimated from the vertical component data.

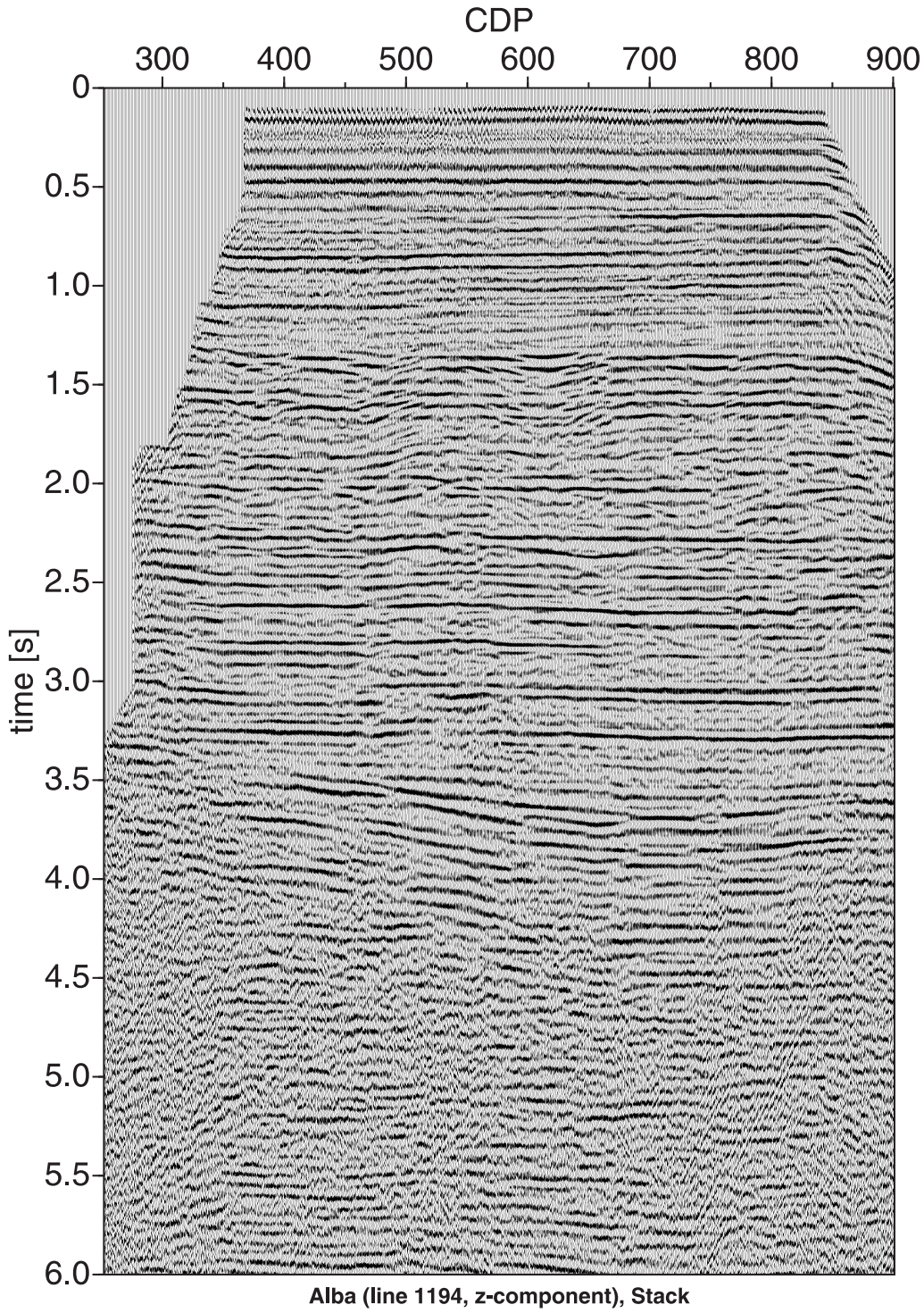

Figure 7.3: Initial vertical brute stack.

7.2.2 Initial images of the C-wave data (horizontal components)

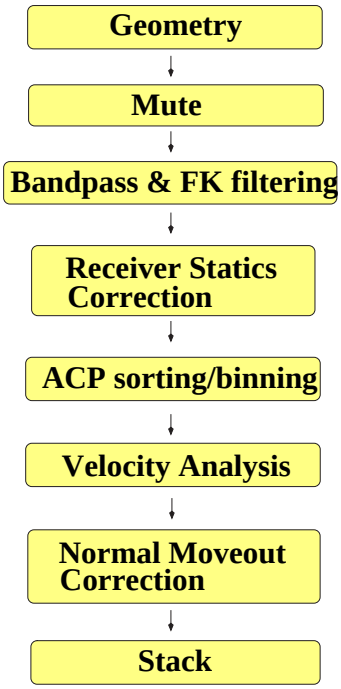

Figure 7.4: Conventional processing flow for the horizontal components.

Converted waves are recorded on the horizontal components, inline (X) and crossline (Y), in a multicomponent survey. For the Alba data the main energy is in the inline component due to the acquisition geometry, where the shotlines were parallel to the receiver cables. The crossline component shows mainly noise indicating no converted wave energy. Hence, no rotation of the components is necessary (see Chapter 3). Figure 7.4 illustrates the isotropic processing sequence applied to both horizontal components finishing with initial stacked sections for each component. Similar to the P-wave flow, mute, amplitude recovery and filtering is applied to the data. The first significant difference in the processing flow of the vertical component is an asymptotic conversion point (ACP) binning instead of the "normal" CDP or CMP binning. I used the conversion point approximation after Tessmer and Behle (1988), Equation (2.6). For the initial processing γ_{bin} was fixed to a depth-independent initial guess of $\gamma_{\text{bin}} = 2.8$ for the ACP binning. Recalling that the geology of Alba consists of flat, horizontal layers it is intuitive that in a horizontal layer there is little velocity variation and thus a lateral shift

in the ACP position will not produce a large effect on the velocity value. Dai and Li (2002a) confirm in their study that in such a structure the C-wave velocity is not very sensitive to errors in γ_{eff}. However, in a different geological setting with dips, e.g. the Lomond field, the estimation of stacking C-wave velocity is influenced by the binning velocity ratio (Mancini et al., 2003). The second difference

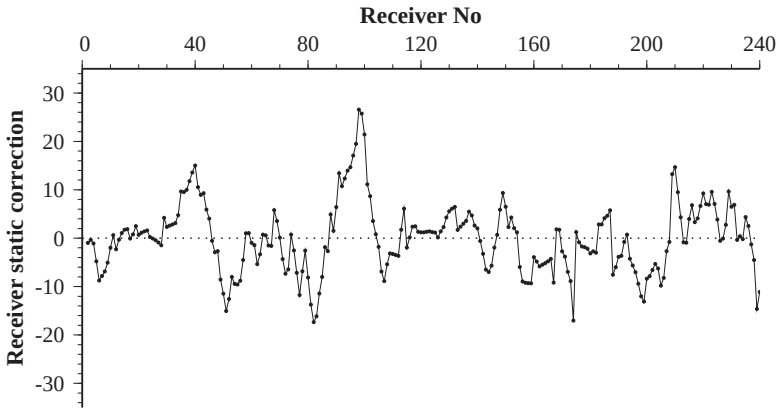

Figure 7.5: Values for the receiver static correction of the x-component.

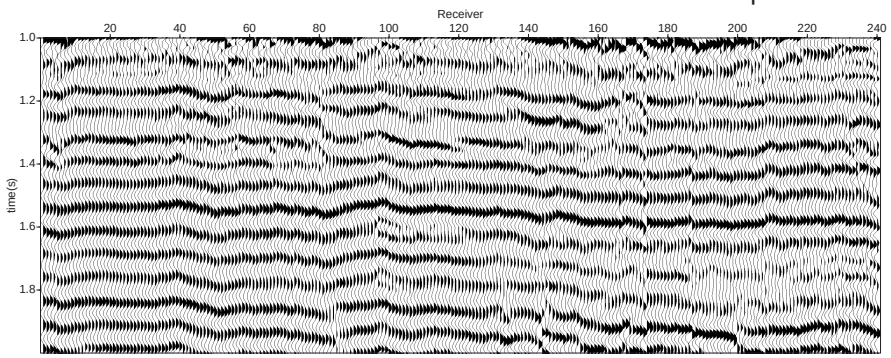

Figure 7.6: Common receiver stack before shear (receiver) static correction.

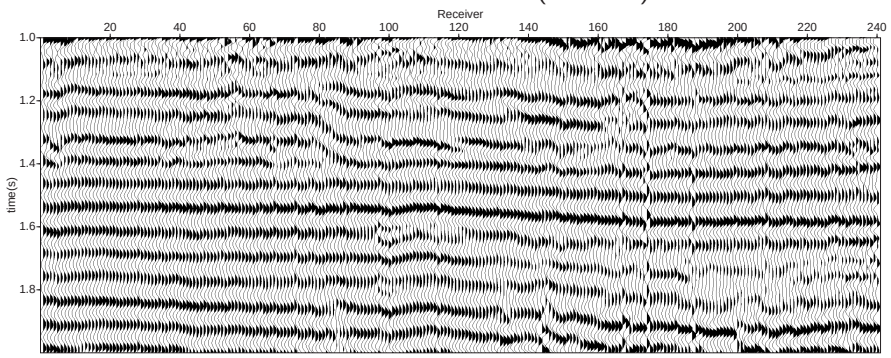

Figure 7.7: Common receiver stack after shear (receiver) static correction.

between the processing procedures is the shear (receiver) static correction. It has

been shown that the low shear velocity of the uppermost layer under the sea bed influences the reflected arrival time from one receiver group to the next (Underwood and Tilling, 1999). A small variation in the thickness or velocity within this layer gives rise to such a significant static expressed as a receiver static. The values for the shear static correction I applied are plotted in Figure 7.5. The effect is illustrated on a common receiver stack before and after the correction in Figure 7.6 and Figure 7.7, respectively. The event at 1.55 seconds in particular is flattened and continuous after the correction.

Figure 7.8 illustrates how velocities have been picked in the case of the ACP (700) gather. The left hand side shows the picked value from the velocity semblance and the right panel the corresponding NMO-correction of the gather. The complete C-wave stacking velocity (V_{c2}) profile is shown in Figure 7.9 and has been used for the NMO correction of both horizontal components. Finally, Figure 7.10

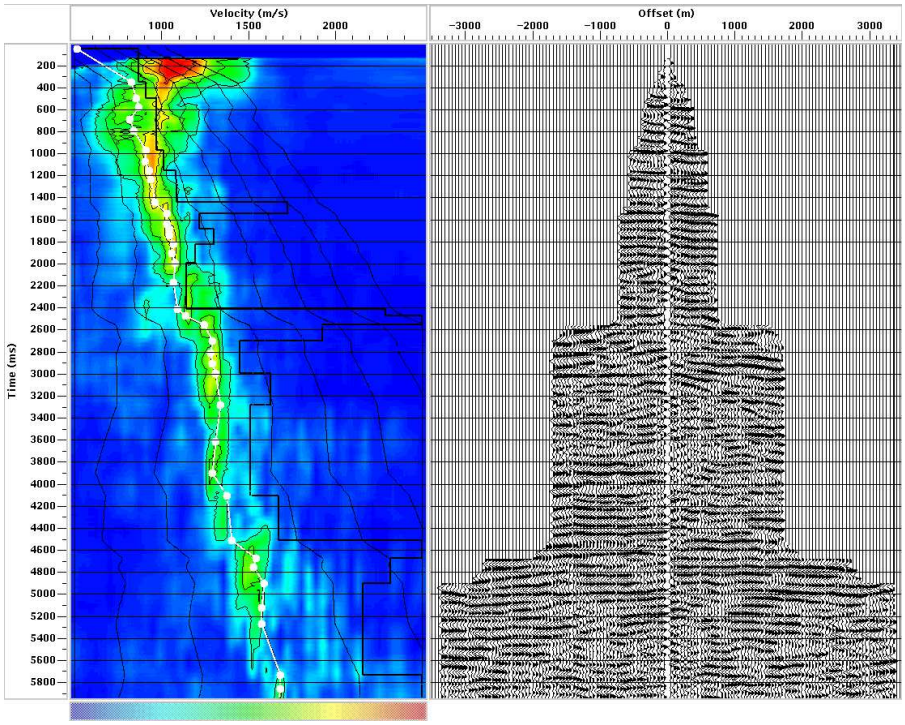

Figure 7.8: An example to illustrate the velocity picking for the converted waves. The right panel shows the NMO-corrected ACP (700) gather and the left panel the corresponding velocity semblance.

shows the stacked section of the inline component. The events at about 3.7-4 seconds correspond to the events at 2.0 seconds in the vertical stack indicating the

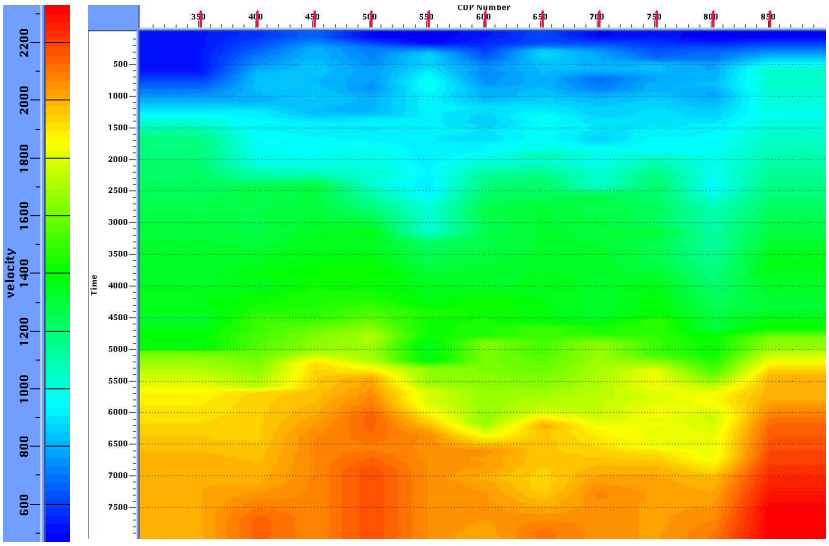

Figure 7.9: Initial C-wave stacking (RMS) velocity profile estimated from the horizontal x-component data.

location of the Alba field. Another indicator for the existence of the reservoir is an anticline visible at these traveltimes. Although the overall quality is relatively good for an initial stack this area is blurred and not well resolved. The Britannia field, which is found in the vertical stack at about 3 seconds two-way traveltime, has corresponding reflections at about 5.5 seconds in the inline component stack. Unconventional non-hyperbolic processing is required for further improvement of the image quality.

The initial stack of the crossline component, Figure 7.11, is very noisy and shows only indistinctly an anticline feature at about 4 seconds. Reflectors illuminated at 0.5, 1. and 1.5 seconds are slightly clearer. These events have corresponding events at the same time in the inline component. In theory, only the SH-wave is recorded on the crossline component, which does not exist in an isotropic medium with an airgun source. Thus, the signals could have originated from the C-wave on the inline component due to azimuthal anisotropy (Dai et al., 2001) and energy leakage from the inline component even though, azimuthal anisotropy, if any, is very weak.

As a final step I applied the ProMAX post-stack Kirchhoff time migration, on the inline stack. For the result see Figure 7.12. The image has not improved

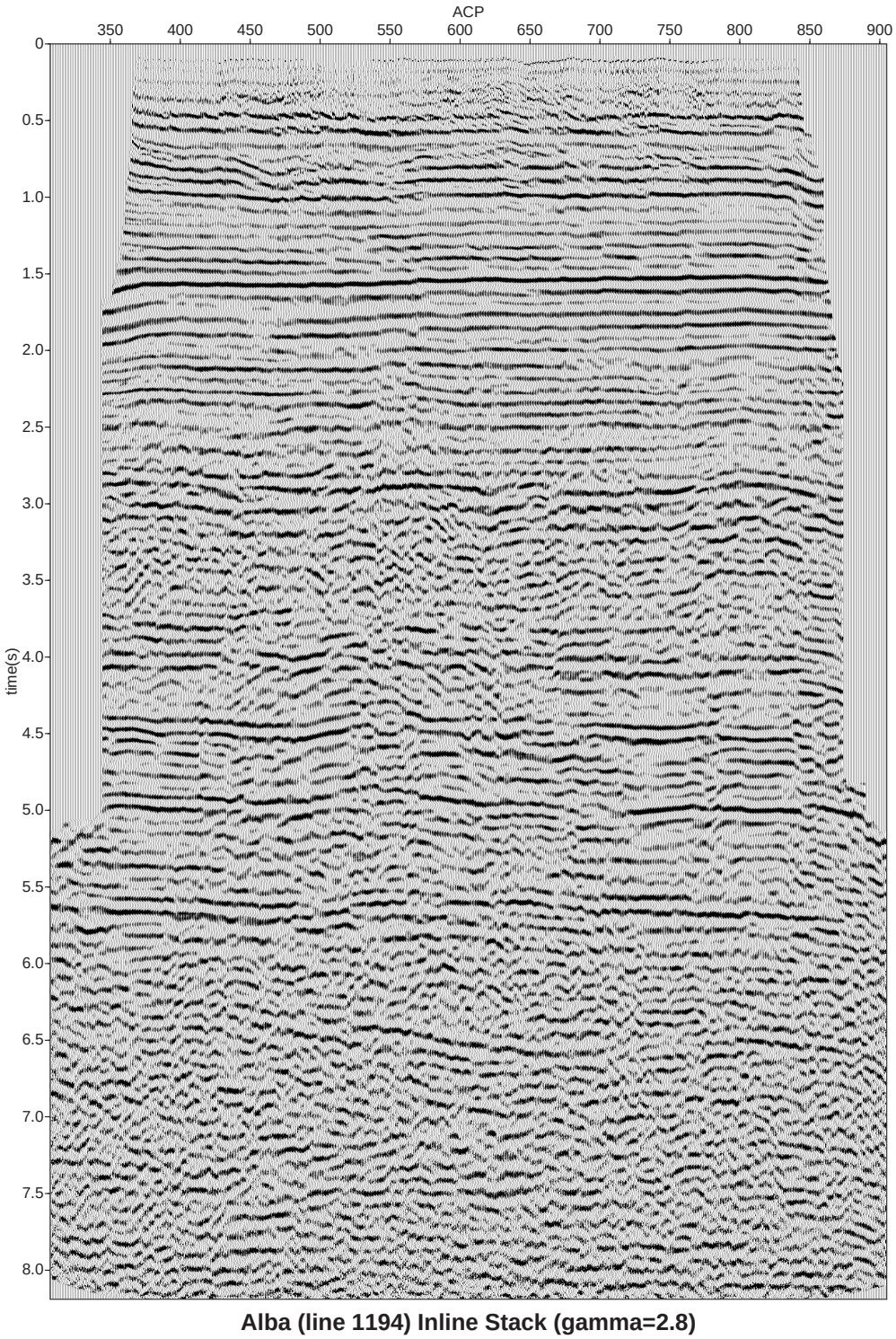

Figure 7.10: Initial C-wave stack section of the inline component, using $\gamma_{\text{bin}} = 2.8$ for the ACP binning. (ProMAX)

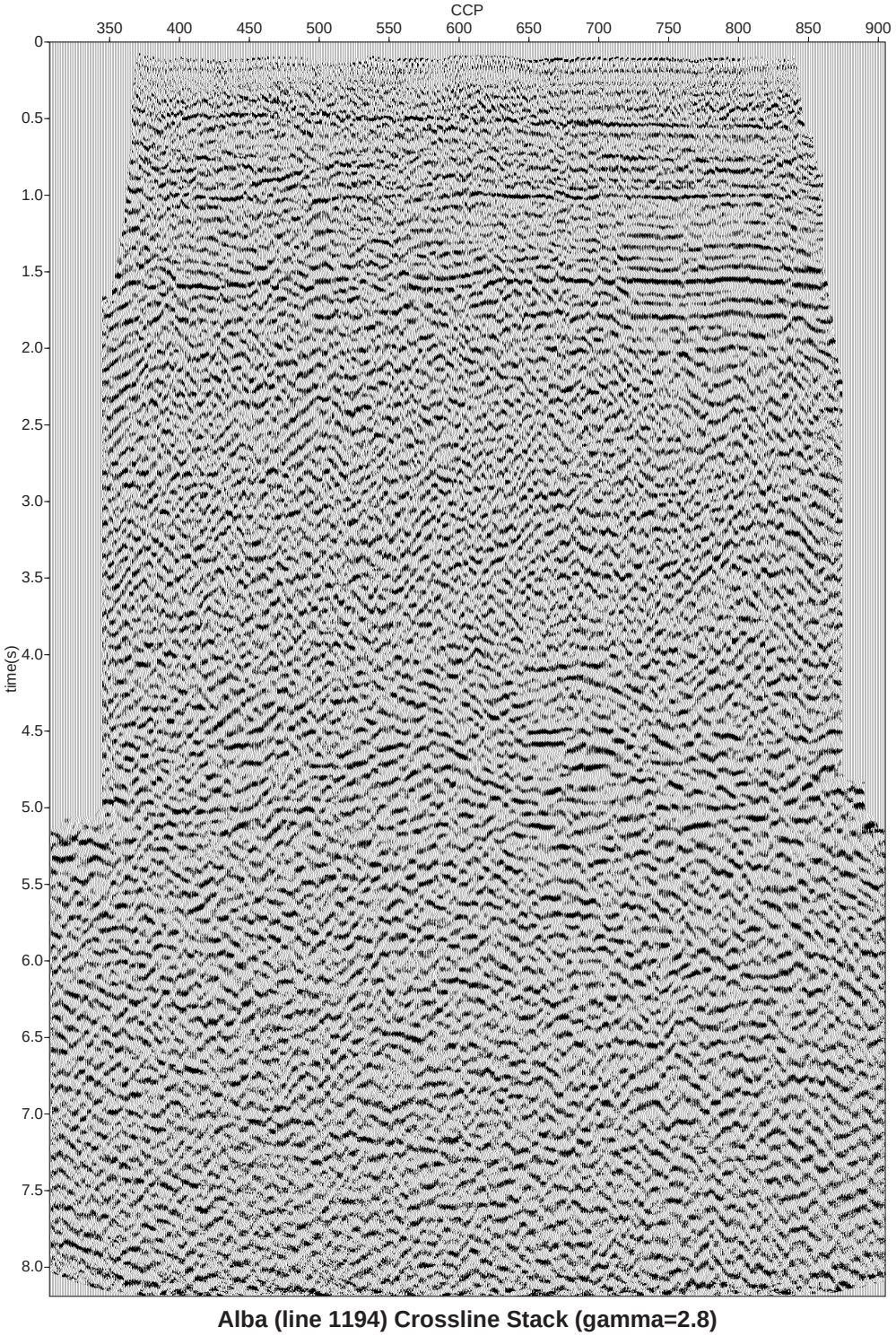

Figure 7.11: Initial C-wave stack section of the crossline component, using $\gamma_{\text{bin}} = 2.8$ for the ACP binning. (ProMAX)

much and the section between 3 and 4.5 seconds especially shows 'smiles' which are indicators of wrong migration velocities.

7.2.3 Event correlation and velocity ratios

Next, γ_0 is extracted from event correlation between P- and C-wave data. As initial guess I have chosen γ_0 according to Underwood and Tilling (1999) and to the results from Dai et al. (2001). Figure 7.13 displays the brute stacks for P- (left hand side) and C-wave (right hand side). For event correlation five events are marked by arrows with the corresponding event on the other section using the initial values of γ_0. These events are later used for anisotropic parameter estimation (see Figure 7.16 and Figure 7.20). Using an interactive tool, the GUI described in section 7.1.3, displaying both, P- and C-wave data, the γ_0 values were updated. Figure 7.14 shows this tool with P- and C-wave sections where the C-wave data is compressed to P-wave time to allow a better event correlation. C-wave traveltimes, and thus velocity analysis, and ACP locations are not very sensitive to changes in the vertical velocity ratio or, in other words, a raw event correlation does not affect the accuracy of the entire processing flow. Li and Yuan (2001b) found that an error of 10-15% in γ_0 has no crucial impact on double-scanning semblance analysis for V_{c2} and χ_{eff}. With known V_{p2}, V_{c2}, and γ_0, γ_{eff} can be calculated using Equation (7.1). Figure 7.15 displays the γ_0 and γ_{eff} obtained in this way. These values will not be changed for subsequent anisotropic processing.

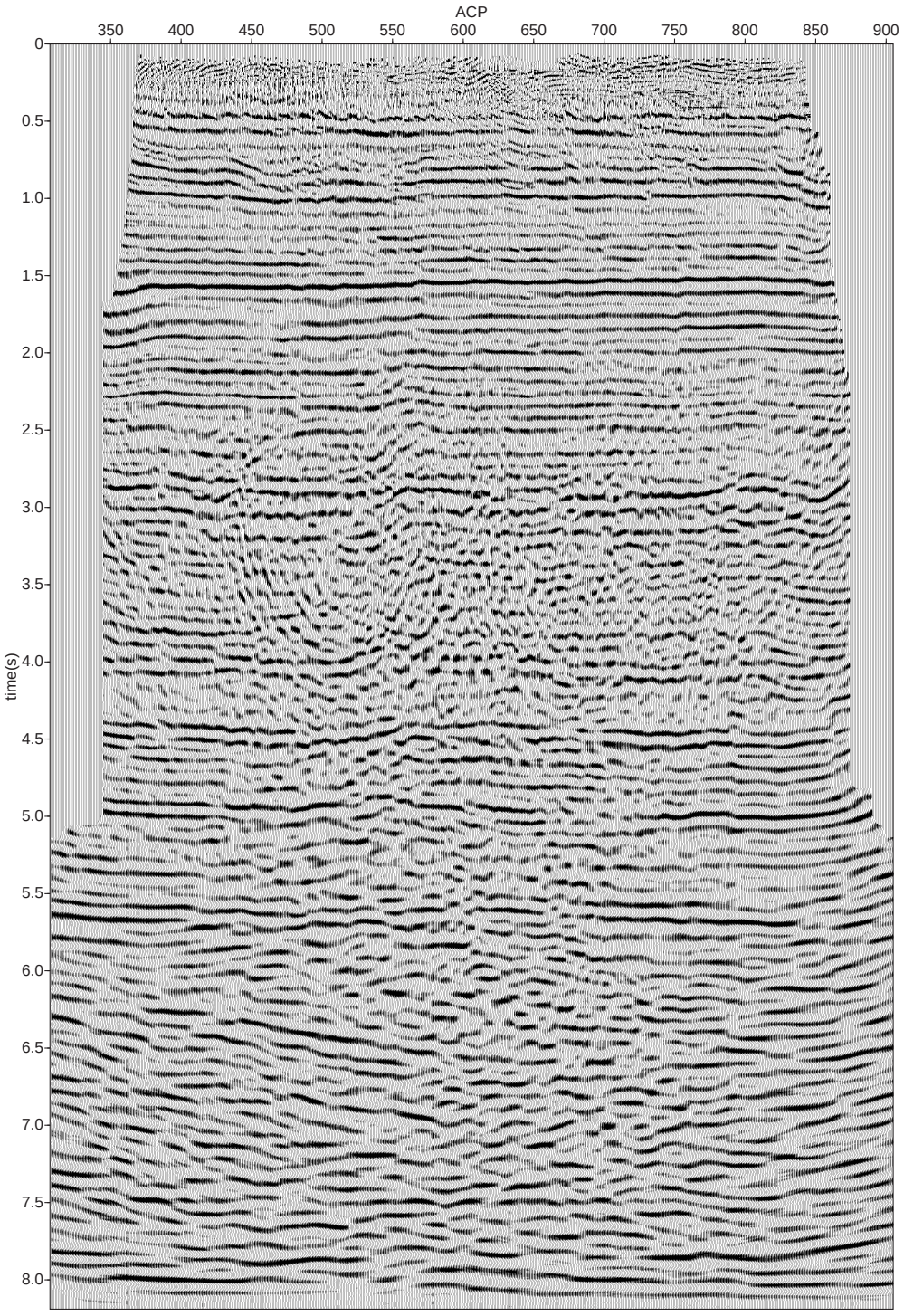

Figure 7.12: ProMAX post-stack Kirchhoff migration of the horizontal (inline) component.

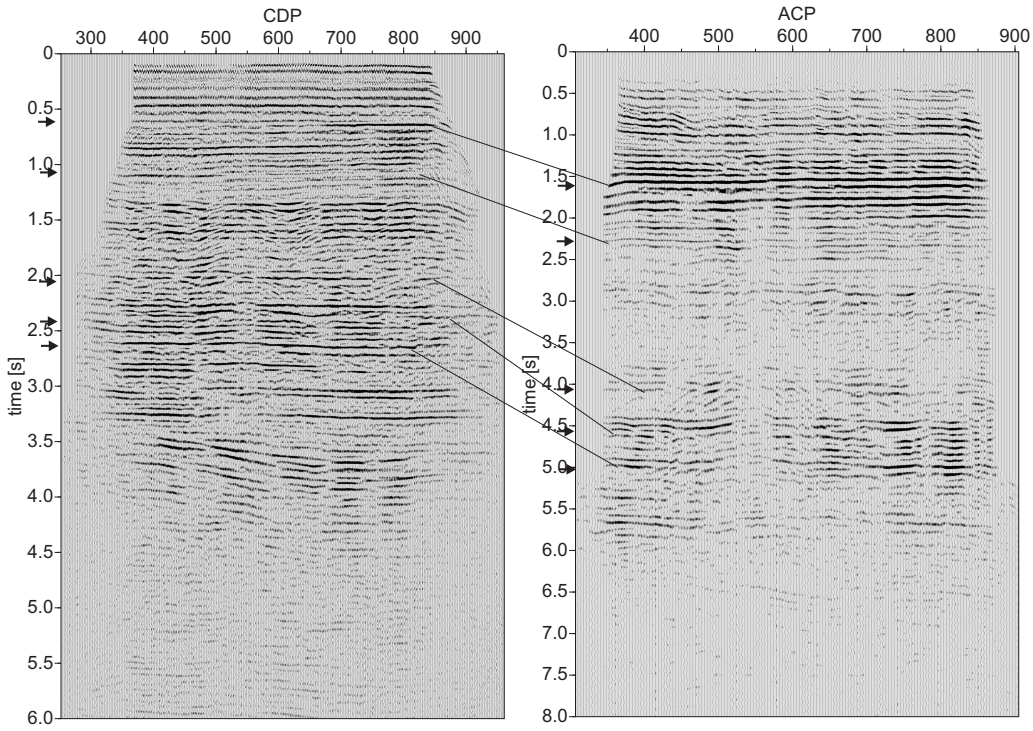

Figure 7.13: Event correlation between P- (left) and C-wave (right) stacked sections. The arrows indicate the events which are used for further anisotropic processing.

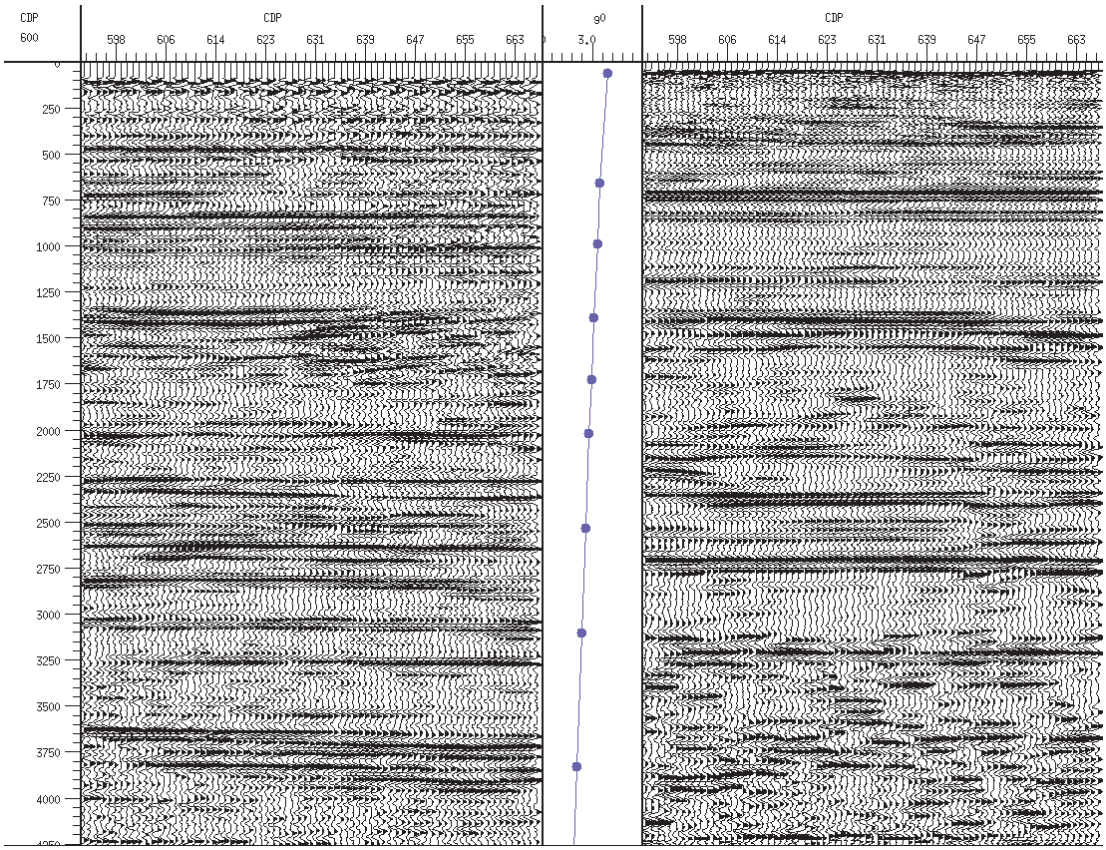

Figure 7.14: Event correlation between P-wave (left) and C-wave (right) sections. Events are displayed in P-wave arrival time.

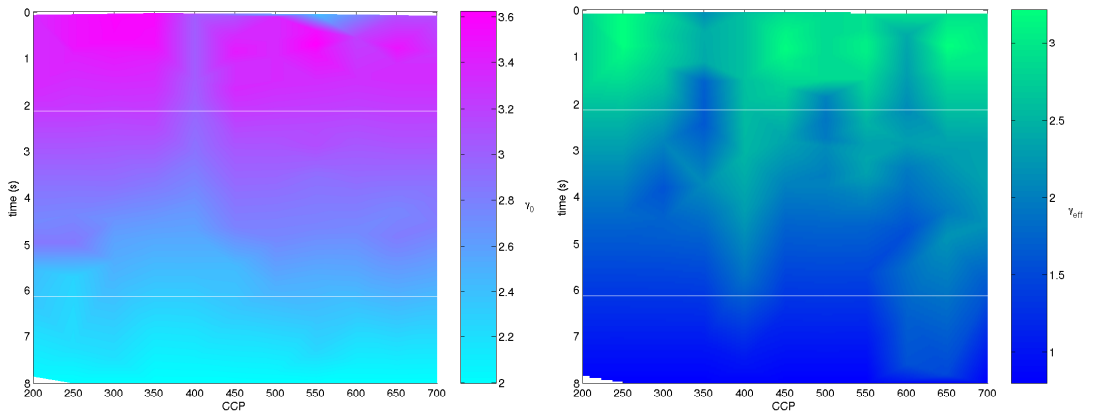

(a) γ_0 (b) γ_{eff}

Figure 7.15: (a) γ_0 and (b) γ_{eff} estimated from initial processing.

7.3 Non-hyperbolic anisotropic processing - vertical component

The anisotropic non-hyperbolic analysis has been applied to the 4C Alba data for both, C- and P-wave data. Yuan et al. (2001) and Li and Yuan (2001b) introduced these routines and also showed their applications on the Guillemot data. Using the vertical component, P-wave, I have chosen CDP gather 500 as an example to illustrate the processing steps and results. The location of the CDP gather corresponds with the same number in the ACP gather. For a better signal-to-noise ratio the data has been sorted into supergathers for parameter estimation. In Figure 7.16 I show 5 events for which I picked η_{eff} and V_{p2} using the double semblance analysis technique on CDP gather 500. The events correspond to the C-wave events chosen for the non-hyperbolic parameter estimation analysis on the horizontal component and will be shown in the next section . To quantify the quality of the picked values I apply a non-hyperbolic NMO correction to the CDP gather (see Figure 7.17(b)). For comparison, Figure 7.17(a) shows the conventional hyperbolic NMO correction from ProMAX, where the velocity values from the hyperbolic velocity analysis are used. Note, that an automatic mute is applied. Although the C-wave events at $t_p = 1.6, 2.3$ and 2.6 seconds are flattened, there are still hyperbolic events of other wavetypes (surface waves) visible in the near offset region. I applied the double scanning technique on every 50^{th} CDP gather. Interpolating between these values gives the parameter fields displayed in Figure 7.18, where (a) shows η_{eff} and (b) the corresponding velocity field V_{p2}.

Furthermore, the picked values are used for a NMO correction of the whole data set in order to obtain a stacked section. Figure 7.19 shows the final stack of the vertical components (P-waves) after anisotropic non-hyperbolic processing. The resolution of the stack is good and shows strong events between 1.3 and 1.6 seconds. These events are continuous but not always flat. More strong signals can be seen at 2.0 seconds and between 2.2 and 3.2 seconds. The location of the Alba reservoir is between 1.9 and 2.2 seconds with the Oil-Water-Boundary (OWB) at about 2.0 seconds. This corresponds with the strong signal observed at 2.0

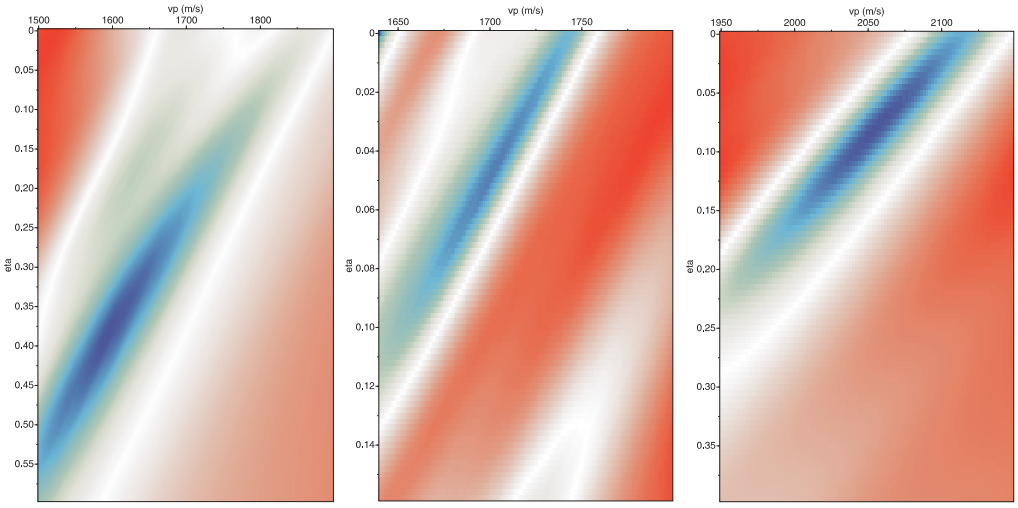

(a) 0.66 s (b) 1.03 s (c) 2.04 s

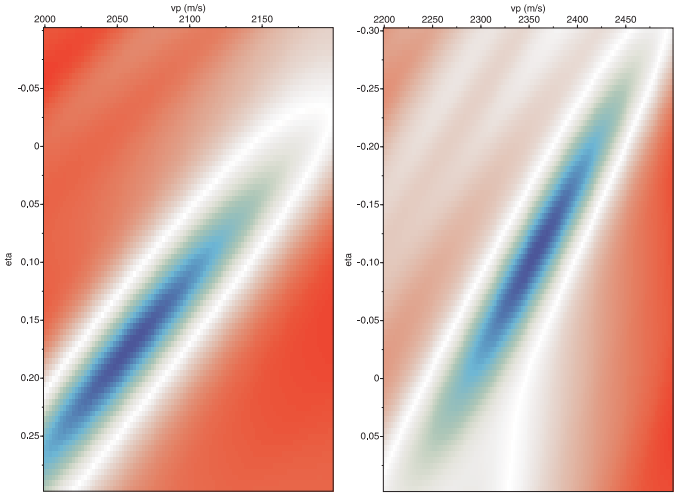

(d) 2.40 s (e) 2.65 s

Figure 7.16: $\eta_{\text{eff}} - V_{p2}$ scanning semblance result for 5 selected events of CDP gather 500. From left to right $t_{p0} = 0.66, 1.027, 2.042, 2.39, 2.65$ seconds.

seconds. Furthermore, between 1.8 and 2.2 seconds a dome shaped feature can be seen quite similar to the shape observed in the isotropic inline stack of the C-wave (Figure 7.10). However, the stack does not reveal anything about the actual dimensions of the reservoir which is expected due to the low impedance contrast. Comparing the isotropic stack (Figure 7.3) with the anisotropic stack (Figure 7.19) an improvement is found especially at the deeper events after 3 sec-

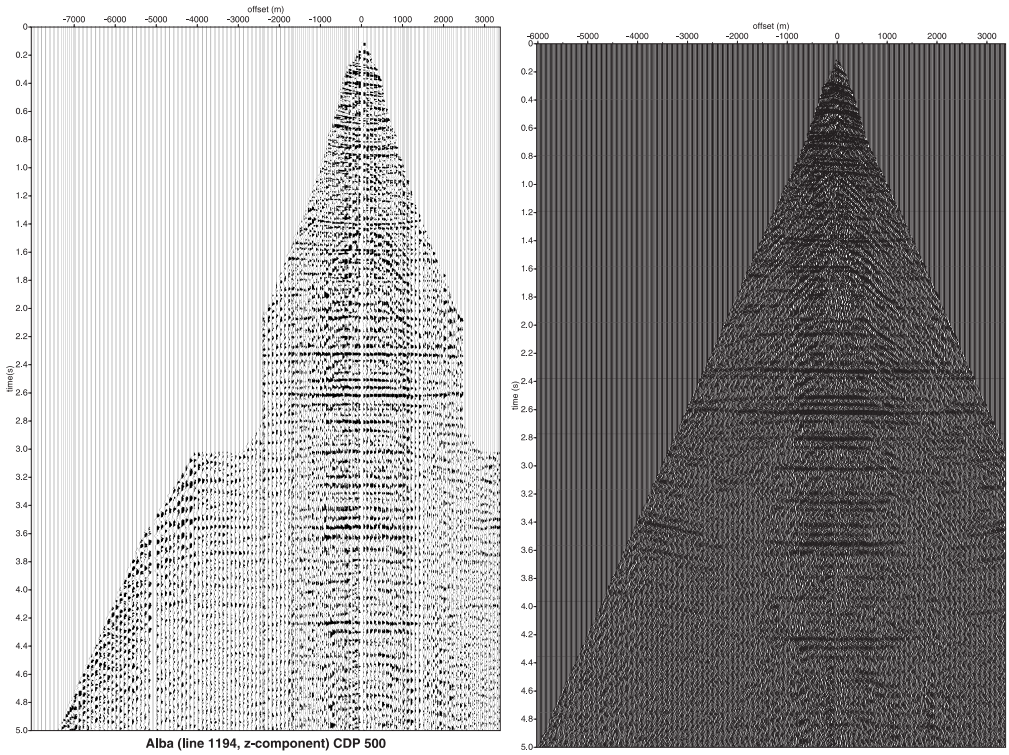

(a) hyperbolic NMO (b) non-hyperbolic NMO

Figure 7.17: Comparison of (a) hyperbolic NMO correction of CDP 500 (ProMAX with automatic mute) and (b) non-hyperbolic NMO correction of CDP 500.

onds traveltime. It also enhanced the response from the events about 2.0 seconds, i.e. the reservoir area.

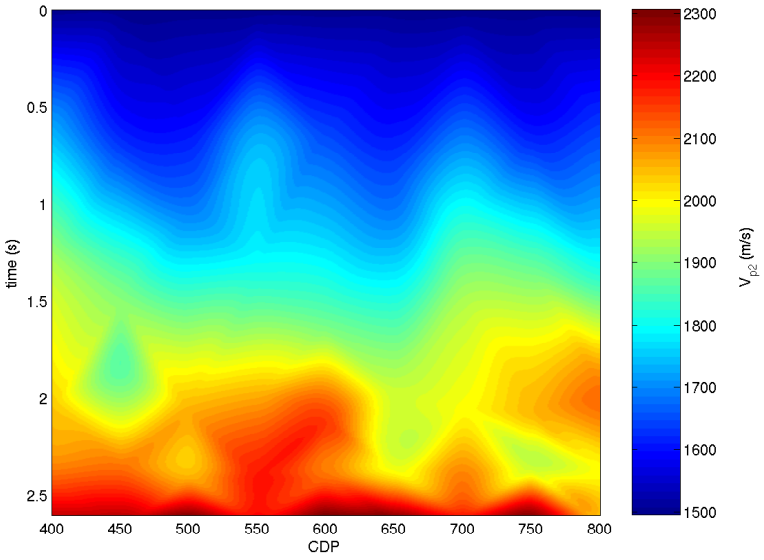

(a) V_{p2}

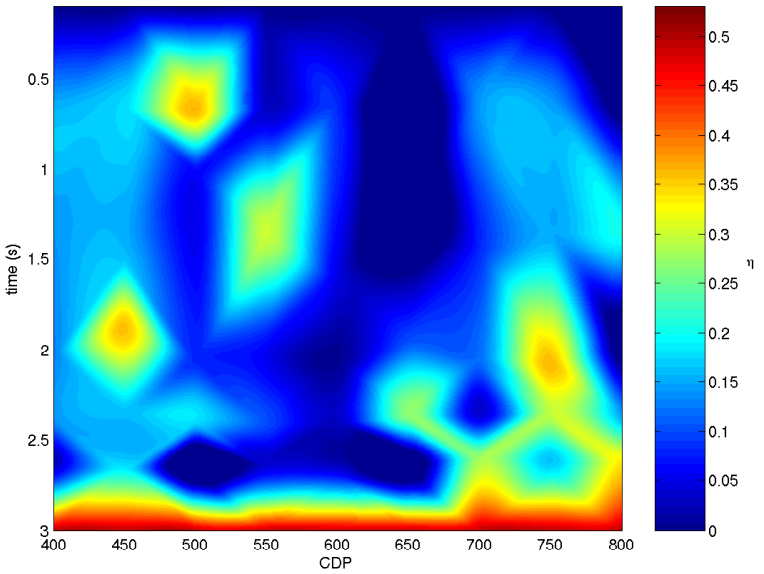

(b) η_{eff}

Figure 7.18: Parameter fields from (a) velocity field V_{p2} and (b) η_{eff} (stacking quantities) from P-wave data. Both parameters have been determined on every 50$^{\text{th}}$ CDP gather and interpolated.

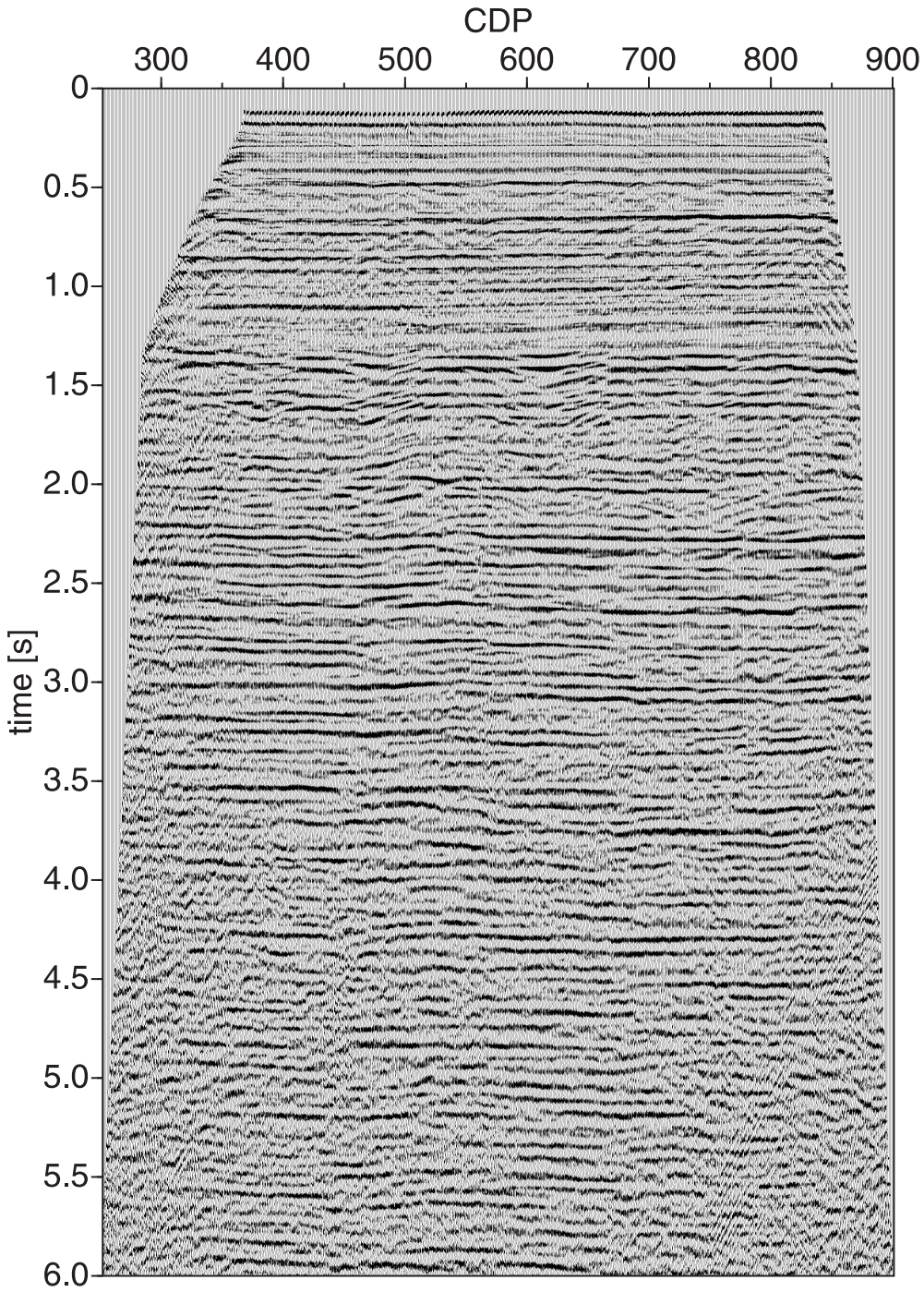

Figure 7.19: Final brute stacks for the vertical component (P-wave) using the parameter fields for η_{eff} and V_{p2} as shown in Figure 7.18.

7.4 Non-hyperbolic anisotropic processing - horizontal component

Similar to the analysis for the P-wave component in Section 7.3 the anisotropic non-hyperbolic analysis has been applied to the horizontal component using the double semblance scanning technique to determine χ_{eff} and V_{c2}. The included offset-to-ratio for the horizontal component is chosen to be $x/z = 2.5$. Double scanning has been applied to events corresponding to those used for the P-wave. An example of the scanning results are displayed in Figure 7.20 using ACP gather 500, which is the same location as CDP gather 500. I used supergathers of 5 gathers every 50 ACP gather for the determination of the parameters. The values obtained using this method were used for an anisotropic non-hyperbolic NMO correction. Figure 7.21(a) shows the NMO corrected ACP (500) gather using a hyperbolic moveout correction. The anisotropic non-hyperbolic moveout correction applied to ACP (500) is shown in Figure 7.21(b). The latter shows a broader offset where the events are flattened. It is clear that the heavy mute from the hyperbolic NMO correction is no longer needed due to the correction of the non-hyperbolic effect. All results from the double scanning on every 50^{th} ACP supergather were interpolated to obtain the parameter fields for V_{c2} and χ_{eff} for the whole shot line.
Note, that the double scanning analysis can be implemented through a GUI tool as discussed in Section 7.1.3 in an interactive fashion. Figure 7.22 illustrates the interactive velocity and parameter estimation for supergather 500. Initial values of γ_0 and γ_{eff} are shown in Figure 7.15. Then, for each supergather the velocities and parameters are adjusted so that the gather is as flat as possible. All parameters are saved automatically to a file, which can then be used for subsequent processing.

These two fields are used as the initial input for the migration but will be updated. However, these parameter fields are also used for an anisotropic non-hyperbolic NMO correction and stacking of the whole data set. Figure 7.23 displays the resulting stacked section. In comparison with the hyperbolic brute stack, Figure 7.10, I find less energy in the shallow events and between 2 and 2.5 seconds. However, the anisotropic non-hyperbolic stack shows more continuous

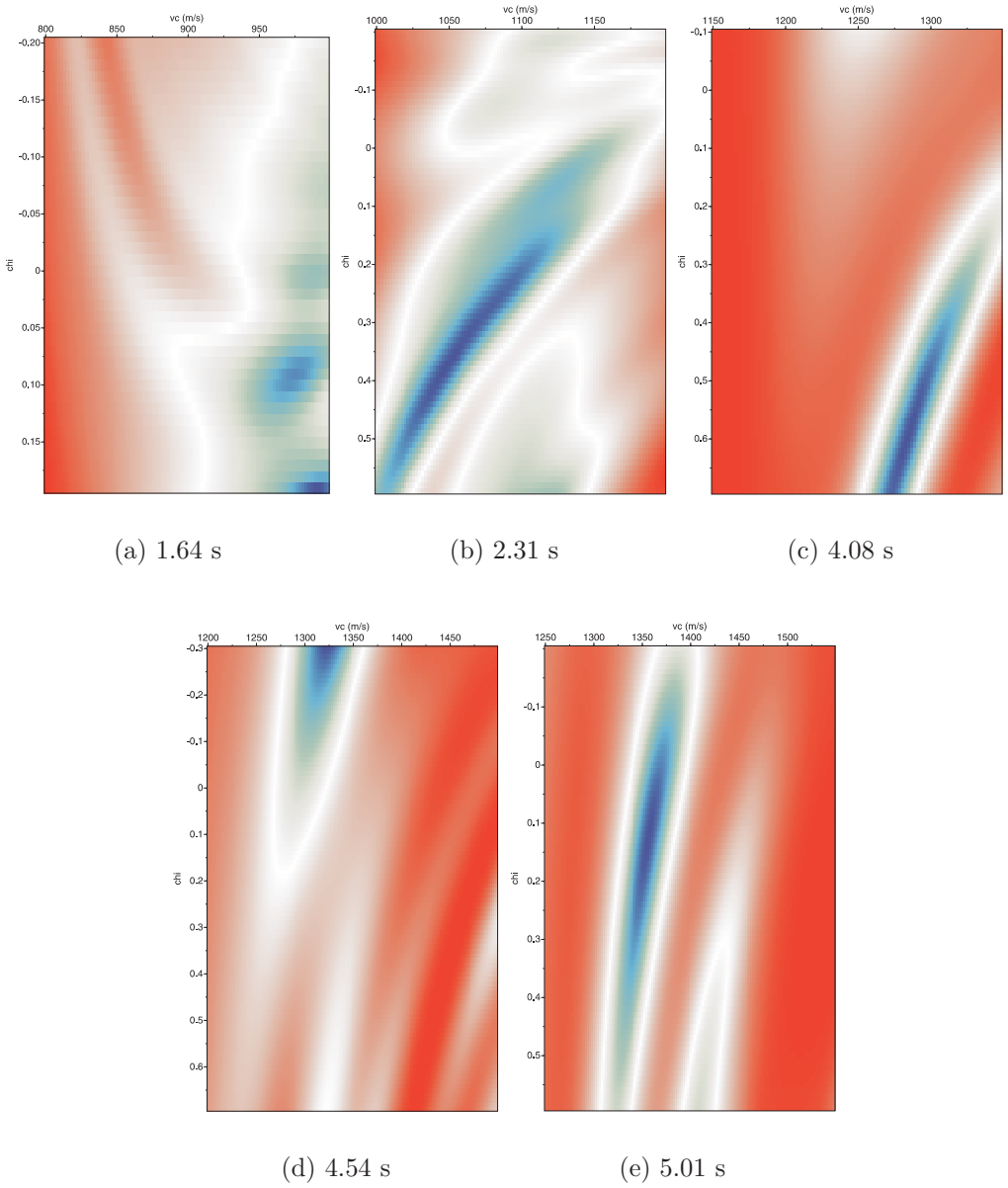

(a) 1.64 s (b) 2.31 s (c) 4.08 s

(d) 4.54 s (e) 5.01 s

Figure 7.20: $\chi_{\text{eff}} - V_{c2}$ scan semblance result for 6 selected events of ACP gather 500. From left to right $t_{c0} = 1.643, 2.311, 4.083, 4.54, 5.01$ seconds.

events at 2.9-3.1 seconds and beneath the reservoir at about 4.5 seconds. At about 4 seconds the events are interrupted by a bent feature which might be originated by the Alba reservoir, which is expected at about 3.8 seconds. Deeper events at about 5-5.5 seconds are quite continuous again and only interrupted by zones of weaker energy. In summary, the anisotropic non-hyperbolic stack shows more

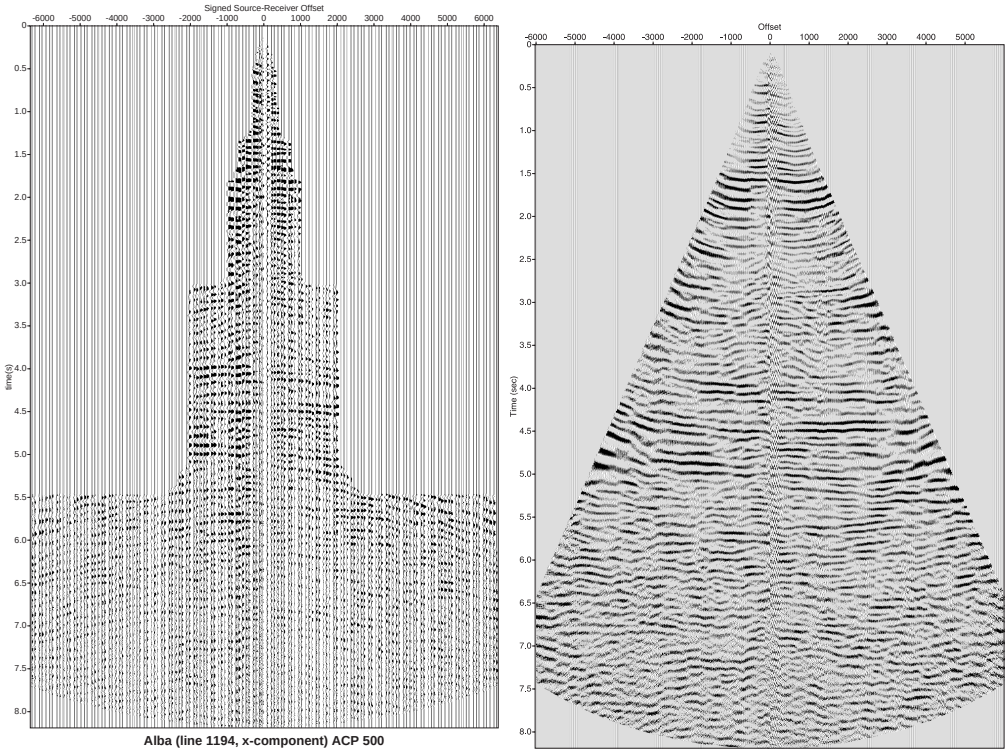

(a) (b)

Figure 7.21: a) Hyperbolic NMO correction of ACP 500. b) Anisotropic non-hyperbolic NMO correction of ACP 500 (ProMAX with automatic mute).

continuous events than the hyperbolic stack but does not resolve the target zone optimal. Bent events still exist.

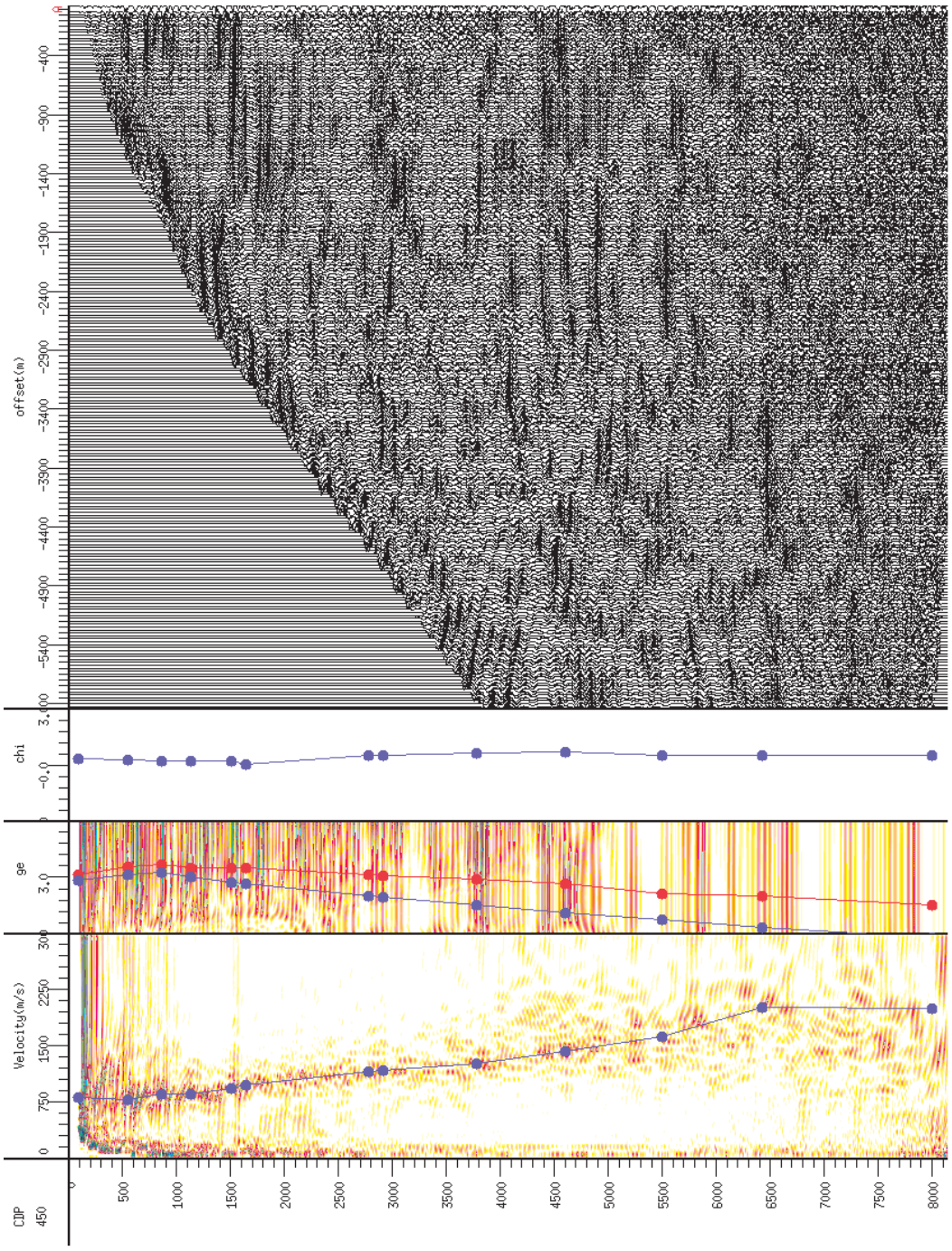

Figure 7.22: Interactive determination of velocity and anisotropy parameter of supergather ACP 450.

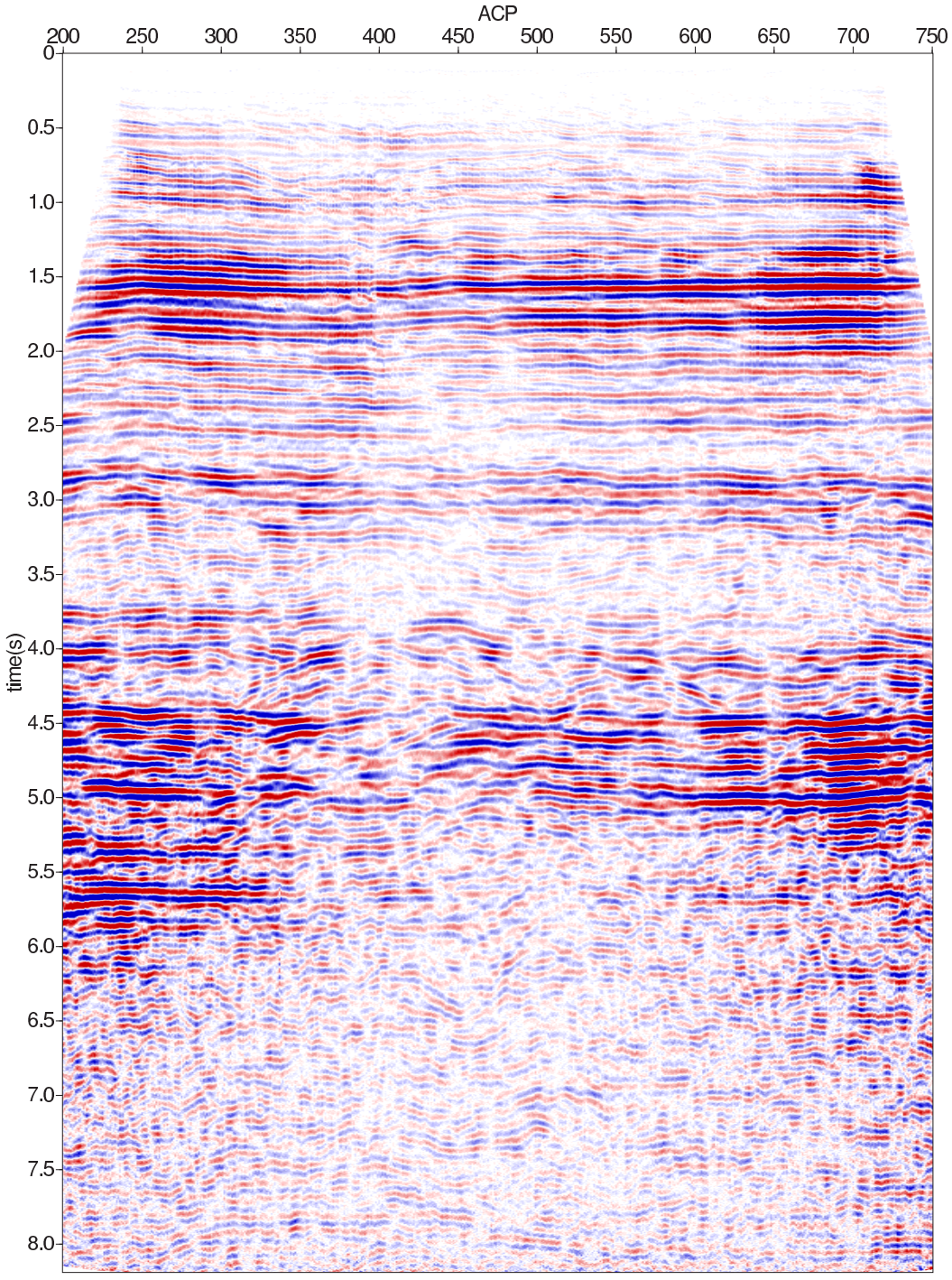

Figure 7.23: Final stack for the C-wave after anisotropic non-hyperbolic processing.

7.5 Discussion and Conclusions

I have presented a work flow to obtain the anisotropic stacking velocity model using 4C seismic data and applied it to the Alba 4C data. The P-wave anisotropy parameter η_{eff} estimated directly from the P-wave data varies between the values of -0.1 and 0.4 with most values centred around 0.1-0.2. This parameter was estimated together with the stacking velocity V_{p2} using a double semblance scanning routine. The resulting stack from the anisotropic NMO correction and stacking shows a better quality and more flat continuous events.

The C-wave moveout is controlled by four parameters: V_{c2}, γ_0, γ_{eff}, γ_0 and χ_{eff}. Several iterations are required to estimate these parameters and perform anisotropic stacking. Therefore, instead of the double semblance analysis an interactive GUI tool was used to determine anisotropy parameter, adjust velocity ratios and estimate velocity in one step. The resulting stack is an improvement compared to the isotropic stack but still shows bent and blurred events especially at the two-way traveltime where the reservoir is expected to be.

In conclusion, I have successfully estimated the stacking velocity model including four parameters from non-hyperbolic processing. These parameters have lead to improved stacked sections for PP and converted-waves. However, further improvement is still possible through prestack time migration. In Chapter 8 these estimated parameters will then be used as initial PSTM model for migration and further processing.

Chapter 8

Analysis of the Alba data for anisotropy: Part II - Migration model building and final imaging

In Chapter 7, I have presented the results of non-hyperbolic moveout analysis, and built a stacking velocity model that contains four parameters, V_{c2}, γ_0, γ_{eff} and χ_{eff}. I then applied this model to perform anisotropic moveout correction and stacking, which led to improved stacked sections. However, apart from non-hyperbolic moveout, another major effect of VTI anisotropy is mis-positioning of horizons, including both lateral and vertical mis-positioning (Larner and Cohen, 1993). The only effective way to correct mis-positioning is by anisotropic migration. However this requires a more accurate anisotropic model to be built.

Based on the Kirchhoff approach, prestack time migration (PSTM) can be implemented as weighted summation along the diffraction curve from a point scatter. This converted-wave (C-wave) diffraction curve contains five parameters: the vertical velocity ratio γ_0, the P- and S-wave stacking velocities V_{p2} and V_{s2}, and their corresponding anisotropic coefficients η_{eff} and ζ_{eff}. These parameters are referred to as the PSTM velocity model.

There is a unique one-to-one link between the PSTM model and the four-parameter stacking velocity model. Therefore, I can use the stacking velocity

model as an initial input for PSTM. Common imaging point (CIP) gathers are then generated from this initial model for updating the parameters. The Alba 4C data will be used for testing the approach.

After a brief discussion of migration algorithms, I present the procedure for updating the velocity model, and I apply this procedure to the Alba data. The updated model is then validated through comparison with full-wave modelling and borehole data, and is used to generate the final image.

8.1 Anisotropic model building and Kirchhoff prestack time migration (PSTM)

Generally speaking, migration model building often involves initial model building, model updating, model evaluation and final migration. Initial model building is still based on moveout analysis and previous results can be used. However, model updating is very much dependent on the chosen migration algorithm. Next, I will discuss the migration algorithm and illustrate model updating using the GUI tools.

8.1.1 Migration algorithm and the migration model

In this study, I will use Kirchhoff pre-stack time migration (PSTM). PSTM is an efficient imaging method for processing 2D and 3D seismic data because of its potential for I/O and it is target oriented (Bevc, 1997). Another advantage of this method is that it avoids ACP binning for C-waves and thus overcomes the problem of smeared stacked images due to wrongly calculated conversion points. Furthermore, time migration is fast and only requires RMS velocities which can be obtained by moveout velocity analysis. Therefore, the initial model obtained from moveout inversion can be directly used for PSTM and be updated for migration properties. The version of PSTM used for this data analysis is developed by Dr. Hengchang Dai in the Edinburgh Anisotropy Project (EAP) and has been successfully tested on other data sets, e.g. the Valhall field (Dai et al., 2000). In this work, I will only use it for the migration of C-waves in a VTI media.

In PSTM energy is summed along a diffraction curve and relocating it to the scatter point. The position of a scatter point is defined by the position of source and receiver of a trace. The energy is spread to all possible scattering points according to the traveltimes which are calculated using the RMS velocities along a straight path. The traveltime is calculated using the Double-Square-Root (DSR) equation for a scatter point located beneath a stack of VTI layers, see Equation (2.66). The DSR equation depends on the P-wave velocity and anisotropy parameter η_{eff}, the S-wave velocity and anisotropy parameter ζ_{eff}, the vertical travel times and the vertical velocity ratios γ_0. I will refer to these values of $V_{p2}, V_{s2}, \eta_{\text{eff}}$ and ζ_{eff} as the migration velocity model. They are directly linked to the moveout parameters $V_{p2}, V_{s2}, \eta_{\text{eff}}$ and χ_{eff}:

1. Calculate V_{p2} and V_{s2} from V_{c2}, γ_0 (or γ_{eff}) using

$$V_{p2}^2 = V_{c2}^2 \frac{\gamma_{\text{eff}}(1+\gamma_0)}{1+\gamma_{\text{eff}}}$$
$$V_{s2}^2 = V_{c2}^2 \frac{\gamma_{\text{eff}}(1+\gamma_0)}{\gamma_0(1+\gamma_{\text{eff}})}.$$

2. Convert V_{p2}, V_{s2} and γ_0 into interval quantities $V_{p2i}, V_{s2i}, \gamma_{0i}$ using layer-stripping method.

3. Convert χ_{eff} to the interval quantity $\chi_{\text{eff}i}$ and calculate η_{eff} and ζ_{eff} or directly calculate η_{eff} and ζ_{eff} from Equation (2.33) and (2.31).

8.1.2 Work flow and model updating

Figure 8.1(a) describes the work flow of the PSTM. Prior to the migration, the velocity ratios, anisotropy parameter χ_{eff} and the RMS velocity V_{c2} needs to be determined (see initial model, Chapter 7). In Dai and Li (2002b) it has been shown that velocity ratios are not very sensitive to the migration image. These parameters allow an error of 10% while the C-wave velocity error must not exceed 2% for an optimal C-wave image. The velocities obtained from ACP binning and stacking velocity analysis are not equal to the migration velocities. Thus the stacking velocities are only used as an initial value and needs to be updated. Because of this only the velocity and the anisotropy parameter are updated during

the migration velocity analysis.

Dai and Li (2003) and Dai (2003a) explained the interactive update of velocity

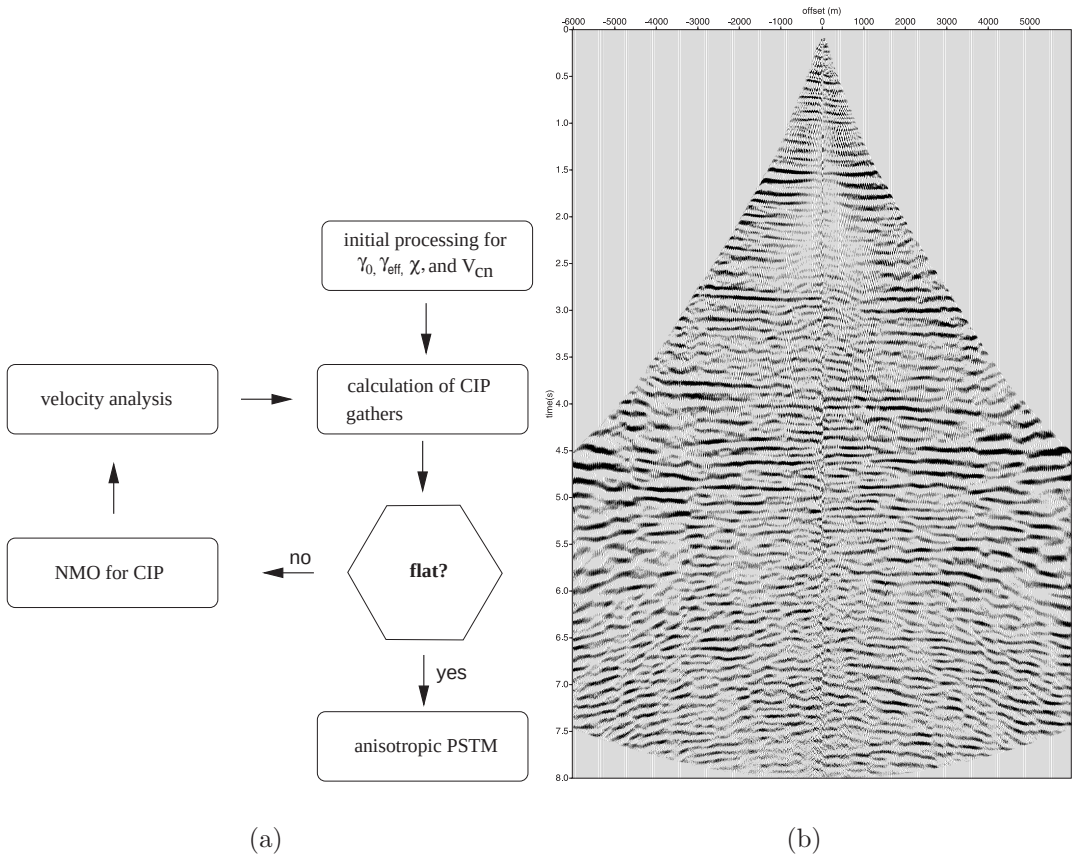

(a) (b)

Figure 8.1: (a) PSTM processing flow for C-wave data using initial parameter values obtained from moveout inversion analysis. (b) An example of a whole flattened CIP gather after migration velocity analysis (CIP gather 500).

and anisotropy parameter using inverse NMO (INMO)-CIP gathers obtained from PSTM. An event in a CIP gather after pre-stack migration is similar to an event in a CDP gather after NMO correction. The event in the CDP gather can be inverted back to its original position. A hyperbolic moveout semblance analysis can then be applied to improve the velocity estimate. The determined velocity converges to the correct value of the migration velocity after a few iterations. Often even one update is adequate. Figure 8.2 shows the GUI interface for the migration velocity and anisotropy parameter update for the CIP gather 500. On the left is the semblance panel for the velocity, followed by the velocity ratio and

the anisotropy parameter χ_{eff}. On the right hand side the CIP gather is shown with flat events after one iteration. It can be seen, that all 4 parameters could be changed in the update process. However, in practise only the velocity and χ_{eff} are updated. In the following section, I present and evaluate the anisotropy model.

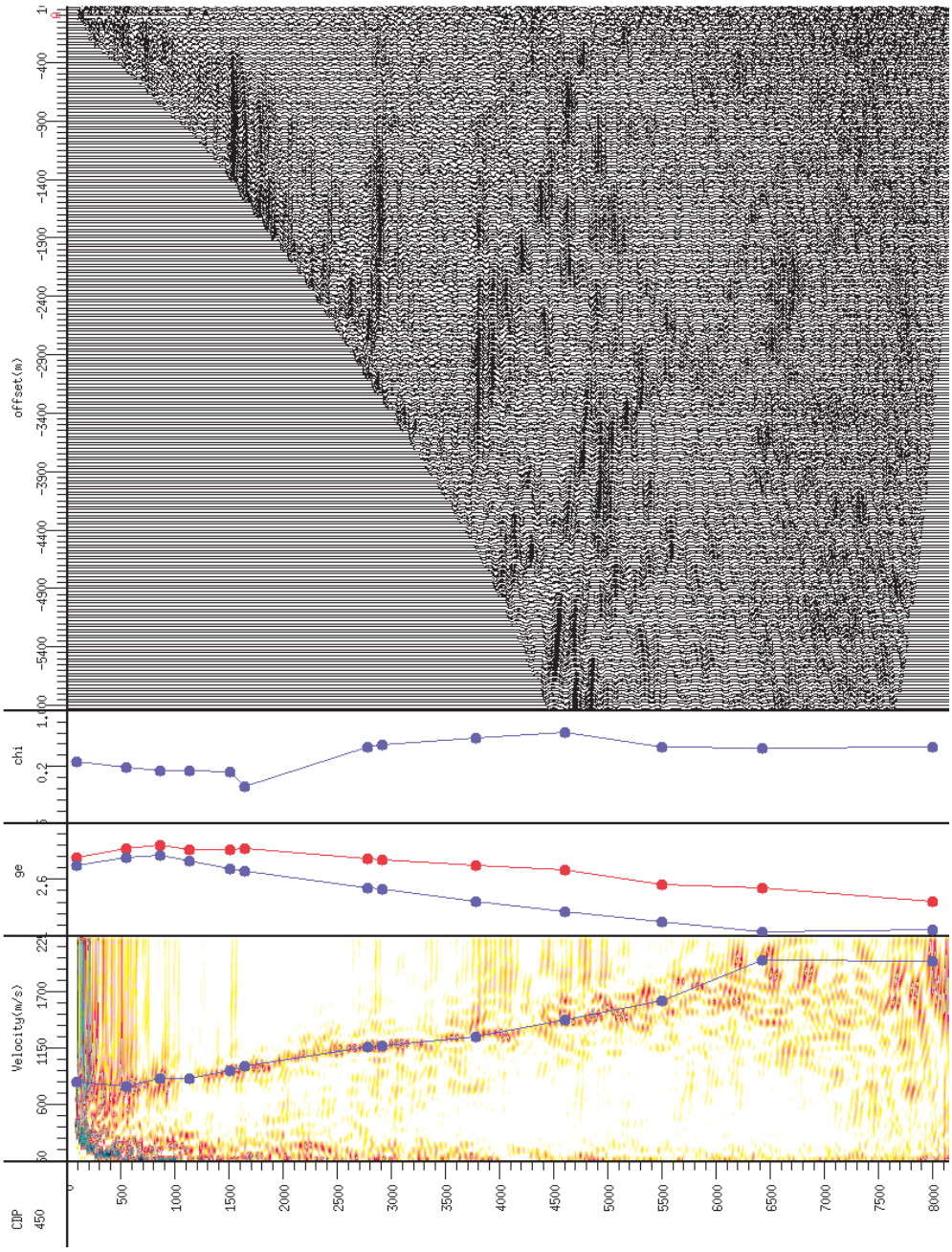

Figure 8.2: Interactive velocity analysis and updating of velocity ratios and anisotropy parameter χ_{eff} for PSTM. The example shows the CIP gather 450.

8.2 The Alba subsurface model

Anisotropic processing produces not only an image of the subsurface but also supplies information for a subsurface velocity and anisotropy model which, possibly, can also give information about the geometry. From both, moveout inversion analysis and stacking and PSTM, RMS-quantities are obtained. Using a Dix-layer stripping approach interval quantities are extracted to represent the subsurface model. In the following sections I will give an overview of the estimated RMS- and interval subsurface model from the Alba data and verify it by full wavefield modelling and by comparison with well log data. Ultimately, the interval quantities are used to gain a final migrated image which I will show in the next section.

8.2.1 RMS model from moveout inversion and PSTM

From both NMO analysis and migration, RMS velocities V_{p2} and V_{c2} can be estimated as well as the effective anisotropy parameter χ_{eff} which then can be used to obtain η_{eff}. However, the migration velocity is not equal to the NMO obtained RMS-velocity. The difference between the stacking and migration velocities can be found by comparing the corresponding velocity fields, see Figure 8.3(a) and (b), respectively. I find, that the velocities increase slightly faster up to 4 seconds two-way traveltime for the migration. The overburden shows a C-wave velocity of 1.1-1.2 km/s when estimated from NMO analysis and 1.0-1.1 km/s from migration. The reservoir area at about 3.8 seconds traveltimes is represented by $V_{c2} = 1.4$ km/s and $V_{c2} = 1.5$ km/s, respectively. Below 4 seconds the migration velocity shows a greater diversity until it reaches the maximum velocity of 2.2 km/s. The events for two-way traveltimes larger than 6 seconds are noisy and not clear to pick.

In theory, the effective anisotropy parameter fields can also differ between NMO and migration quantities. Figure 8.4 shows the fields for χ_{eff} estimated from (a) NMO and (b) migration. The difference in this case is very small with slightly lower values obtained by migration. Comparing the parameter fields I find most values range between 0.1 and 0.6 and increase with depth. Similar to the C-wave velocity, in general the values are smaller when estimated from migration than

NMO analysis. The velocity ratios needed only minor adjustments for the PSTM and thus are not displayed again.

As I explained in the last section one step in the model building process for PSTM is estimating the P-wave anisotropy parameter η_{eff} from χ_{eff}. η_{eff} from χ_{eff} values for the overburden are in the range of 0.05-0.1 and increasing in average only up to 0.18. However, from the modelling studies in Chapter 5 I know that the η_{eff} values are expected to be very small. In comparison the η_{eff}-field obtained directly from P-waves (Figure 7.18) show a more patchy field with generally higher values reaching as high as 0.3.

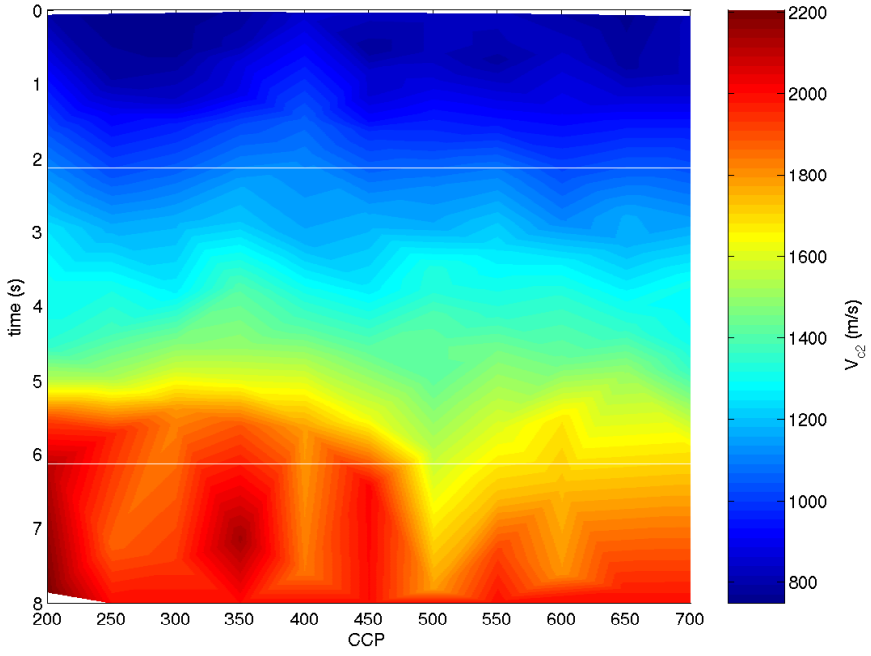

(a) stacking V_{c2}

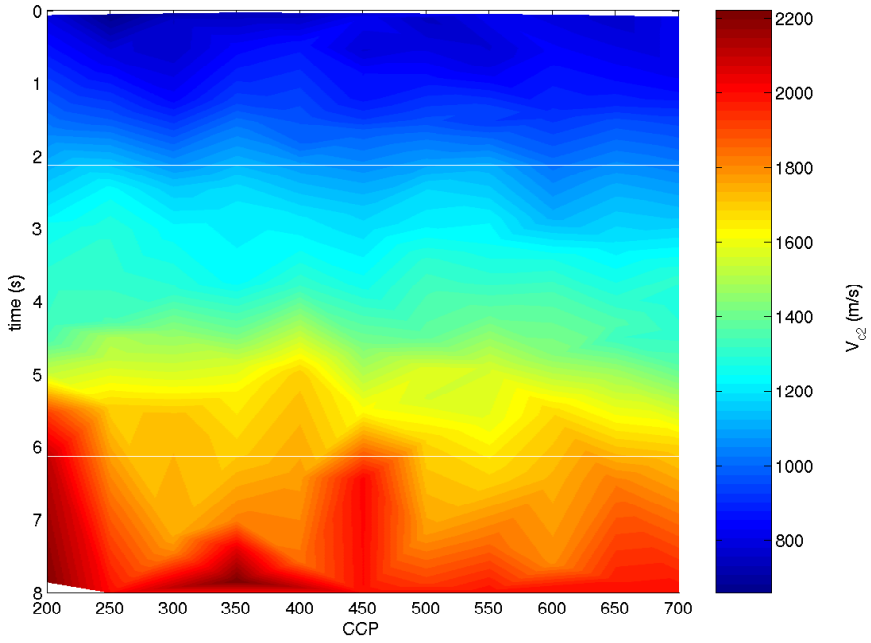

(b) migration V_{c2}

Figure 8.3: Velocity fields for (a) stacking (b) migration.

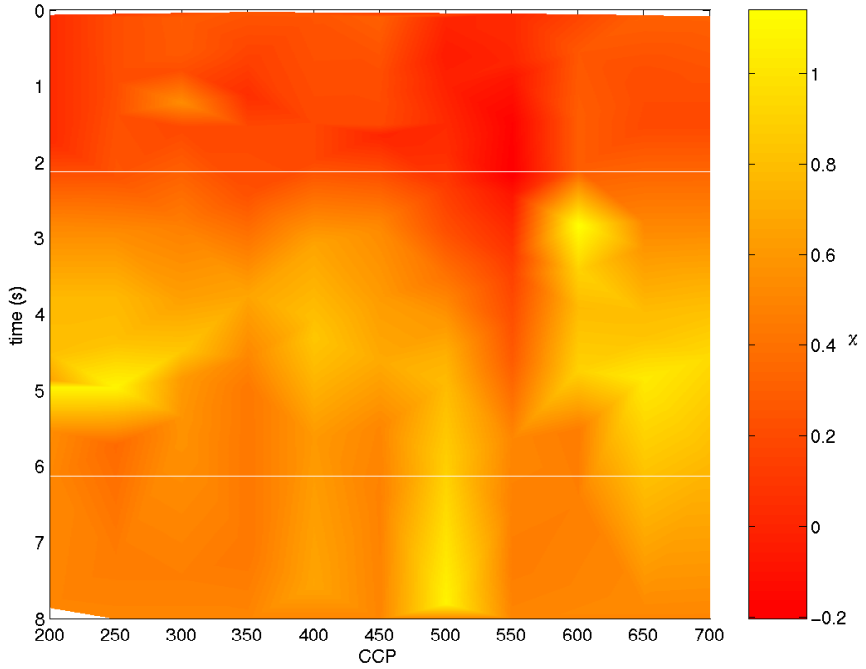

(a) stacking χ_{eff}

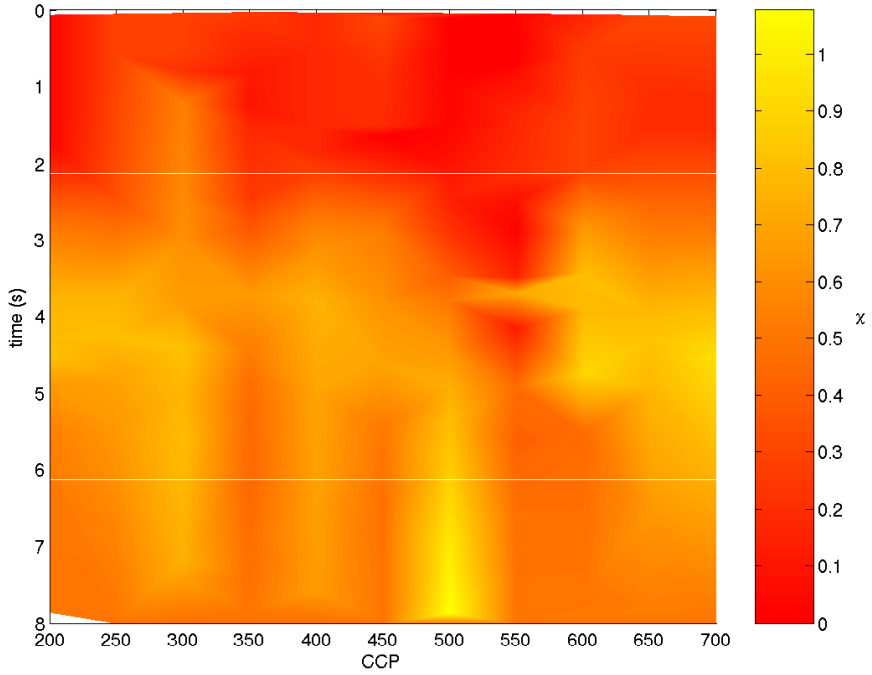

(b) migration χ_{eff}

Figure 8.4: Parameter fields for χ_{eff} obtained from (a) NMO or (b) migration analysis.

8.2.2 Interval model

So far, the estimated velocities and anisotropy parameters are RMS and effective parameters. Hence, in order to gain an idea what the individual layers of the subsurface are made of interval quantities are calculated by a Dix-type layer-stripping approach (software developed in the EAP). In this way, V_{c2}, γ_0 and γ_{eff} are converted to P- and S-wave interval velocities. From the effective C-wave anisotropy parameter χ_{eff} the interval quantity $\chi_i (i = 0, \ldots N)$ can be determined. Establishing the interval velocities for P- and S-waves rather than C-waves will allow, together with other subsurface properties, to fit lithology to the parameter properties found. The interval velocities for P- and S-wave are shown in Figures 8.5 and 8.6 respectively. V_{p2i} shows values from just over 1.5 km/s in the near-surface up to 3.0 km/s. Faster velocities are observed especially after 2.5 s P-wave arrival time which corresponds to layers underneath the reservoir. The S-wave interval velocities are in the range from 0.4 to 1.7 km/s. The velocity field shows a rough layering.

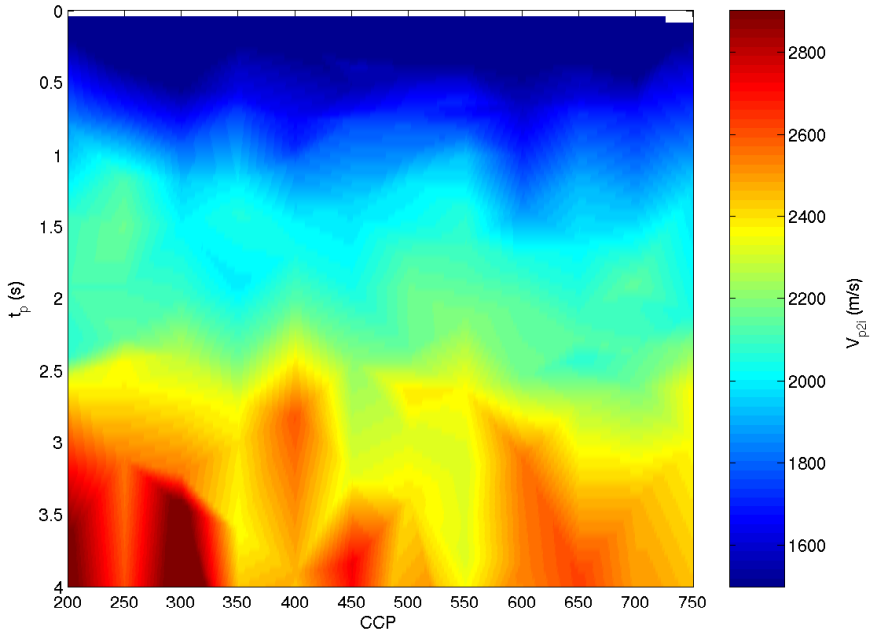

Figure 8.5: Parameter field for interval V_{p2i} over P-wave arrival time from C-wave data.

Using a similar Dix-type layer-stripping approach the effective anisotropy param-

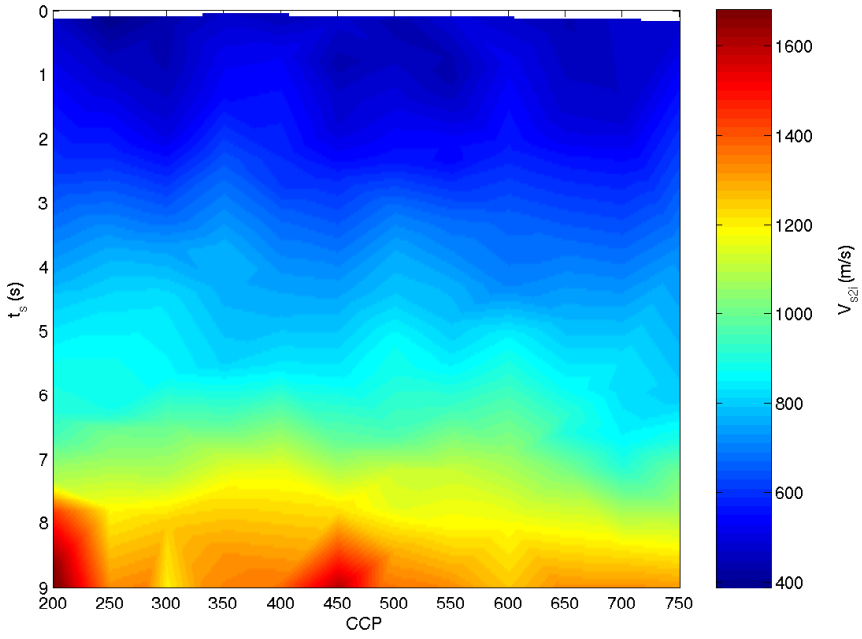

Figure 8.6: Parameter field for interval V_{s2i} over S-wave arrival time from C-wave data.

eters can be converted into interval quantities. Again, from C-wave properties the corresponding P- and S-wave anisotropy parameters are obtained. Firstly, in Figure 8.7 I have plotted different values of the P-wave anisotropy parameter η for one CDP gather. In this figure I compare the effective η_{eff} calculated from VSP, with data calculated from C-wave data and with that directly gained from P-wave data. The values from P-wave data are distinctly larger than the other values. VSP and C-wave effective parameters correspond very well for the first 2 seconds C-wave arrival time and only start to differ after that. The interval η_i calculated from VSP and C-wave data are also included in this plot. As expected from the effective parameters the interval parameters agree especially well in the first 2 seconds. However, comparing effective with interval parameters, it is clear that the differences are only small for this data in the overburden.

Secondly, Figure 8.8 and 8.9 illustrate the parameter fields obtained for interval P-wave parameter η_i and S-wave parameter ζ_i, respectively. In order to simplify the comparison of the effective and interval values I have plotted both of them over C-wave arrival time. The interval η_i field compared to the RMS quantities shows the same small values as in the overburden. However, after 3 seconds ar-

rival time the interval model shows sharp variations with higher values at about CCP gather 600.

In the case of the S-wave anisotropy parameter ζ_i, no effective parameter is

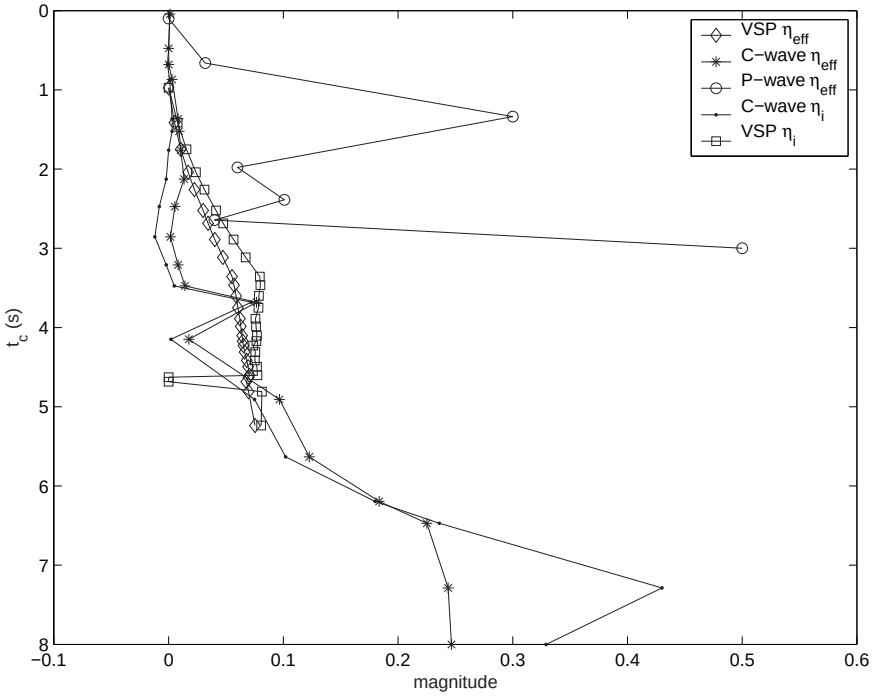

Figure 8.7: Comparison of η_{eff} over C-wave time calculated from VSP, surface C-wave and surface P-wave data as stacking quantities and interval η_i from C-wave surface and VSP data.

available for comparison. The interval parameter field shows values mainly in the range of 0.1-0.3 with patches of higher and lower values which can even be negative. However, higher values are observed after 3 seconds C-wave arrival time and might be related to the reservoir. The parameter field shows considerable variation compared with the other parameter fields. I think this may be due to problems with the algorithm estimating the S-wave parameter and it may need to be revised.

8.2.3 Full wave modelling results

In the previous sections I have introduced the RMS and interval models obtained from the 4C Alba data. In order to verify them I carried out a modelling study. The model for this study focus on three events in the overburden of the Alba field.

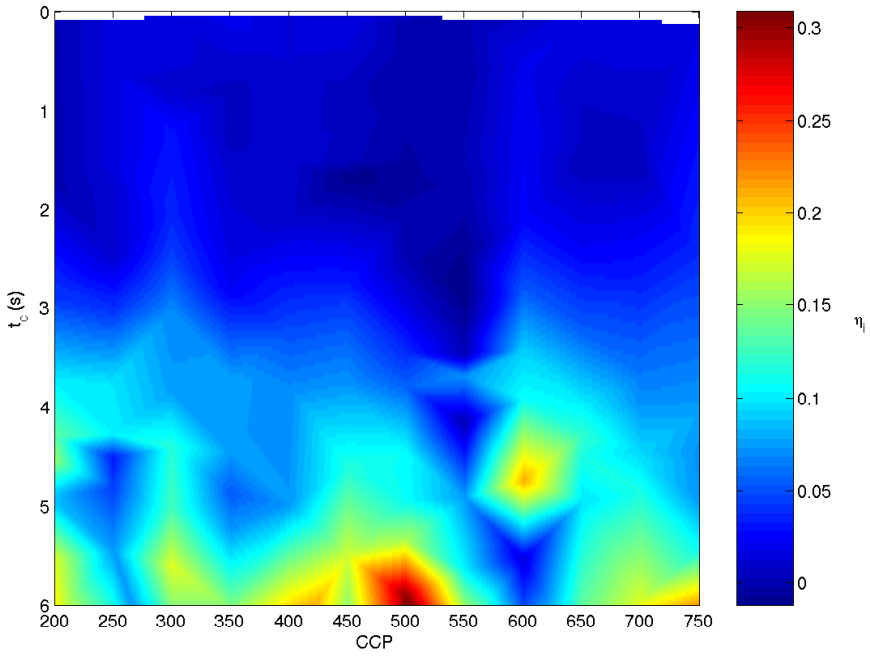

Figure 8.8: Parameter field for interval η_i over arrival C-wave time from C-wave data

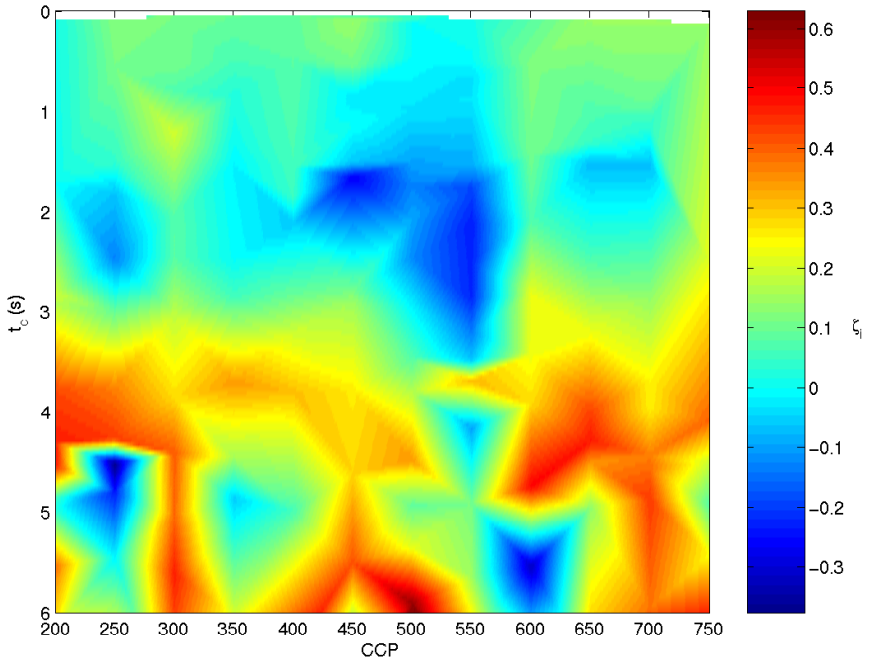

Figure 8.9: Parameter field for interval ζ_i over arrival C-wave time from C-wave data.

The model values are based on the processing results from VSP and surface data and is listed in Table 8.1. In order to show the similarities with the real data I have extracted velocity and anisotropy parameters from one CDP/ACP gather and plotted them together with the VSP data and the model values. Figure 8.10 (a) shows the resulting diagrams for the C-wave (top) and P-wave (bottom). Note, that the model itself consists of only three layers corresponding to the overburden. The P-wave velocities are quite consistent while the C-wave velocity from the model corresponds well with the subsurface values but less well with the VSP data. In Figure 8.10 (b) I have plotted the anisotropy parameters η_{eff} (top), χ_{eff} (middle) and the velocity ratio γ_0 (bottom) against the C-wave traveltime. Only the model P-wave parameter η_{eff} shows good agreement with both, VSP and surface data values. The C-wave parameter χ_{eff} from VSP and C-wave are very different for the near-surface area. However, the model values for the second and third event agree well with the result from the C-wave data while the first event shows the same tendency as the VSP data. Finally, the model values for the vertical velocity ratio γ_0 lie between those from VSP and C-wave data but follow the trend of the VSP data.

Before the actual generation of synthetic data I computed the traveltimes cal-

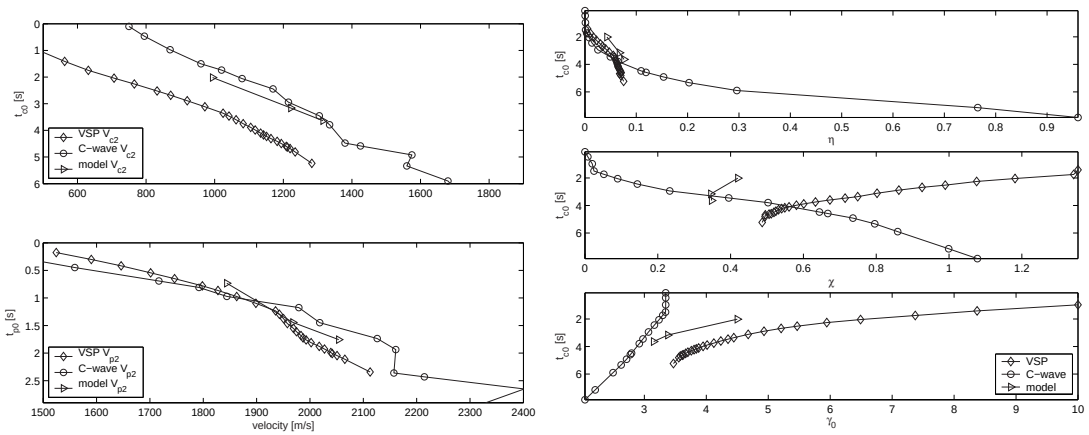

(a) RMS velocities (b) anisotropy parameters

Figure 8.10: Model building from the real data for 3 overburden events. In (a) the C-wave (top) and P-wave (bottom) velocities from VSP and surface data are compared with the model values. (b)displays the comparison of anisotropy parameter η (top), χ (middle) and vertical velocity ratio γ_0 (bottom) estimated and/or calculated from VSP and surface data with the model values.

culated from the model with the real data. Figure 8.15(b) and (d) displays one CDP or ACP gather from the P- and C-wave data set, respectively. The three chosen events are indicated by the red line plotted over the seismograms. The red traveltime curves are calculated from the model parameters and muted according to the range of validity of the traveltime approximations. Both, P- and C-wave show a fairly good agreement between calculated traveltimes and real data for the first and second event. The third one is hardly visible on the C-wave data. However, it can be seen on the P-wave. For all three events the calculated traveltimes fit the events very well for small offsets.

Next, using the modelling package ANISEIS I generate synthetic seismograms

total depth	V_{p0i}	V_{s0i}	t_{p0}	V_{p2}	t_{c0}	V_{c2}	η_{eff}	χ_{eff}
[km]	[km/s]	[km/s]	[s]	[km/s]	[s]	[km/s]		
0.66	1.8	0.4	0.733	1.844	2.017	0.994	0.043	0.421
1.37	2.0	0.9	1.443	1.968	3.161	1.222	0.067	0.346
1.73	2.3	1.1	1.756	2.054	3.644	1.316	0.076	0.348

Table 8.1: Parameters for the 3-layer Alba model aiming to describe 3 anisotropic overburden events from the real data.

from the model values. In Figure 8.15(a) and (c) I display the P- and C-wave component opposite to the real data gathers. Again, the three events are superimposed with the calculated traveltime curves. On the synthetic data I find the third event to be weaker than the first two which agrees with the real data findings.

I have focused on parameter estimation from the C-wave data and show the result from both, the interactive tool (Figure 8.11) and semblance double scanning (Figure 8.13). However, I have also performed the semblance double scan to estimate η_{eff} and V_{p2} on the P-wave synthetic data. Figure 8.14 displays these results.

Firstly, using the interactive tool for parameter estimation I set up all the model parameters and carried out the NMO correction on the seismogram (see Figure 8.11). Because the layer thickness is known the offset for which the NMO correction is valid ($x/z = 2.5$) can be calculated for each layer. For the first layer the allowed offset is $x = 1.65$ km. Unfortunately even within this offset the event is not flat after NMO correction. For the second event the valid offset range is $x = 3.43$ km and again, the event is not flat after an offset of about 3 km. Only

the last event is flat for the whole offset. However, changing the vertical velocity

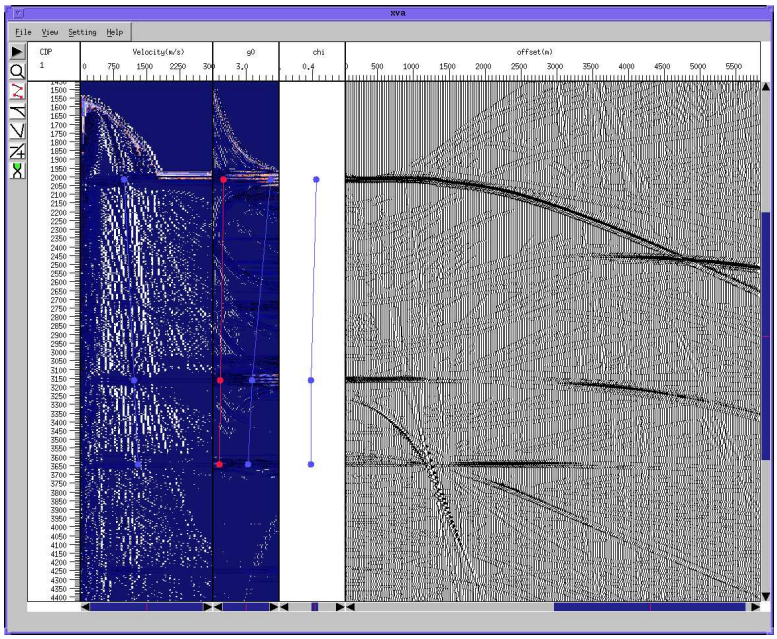

Figure 8.11: Parameter estimation from synthetic C-wave data using interactive tool and model values. The display shows the semblance panel for the C-wave velocity, velocity ratio, anisotropy parameter χ_{eff} and the corresponding NMO correction of the synthetic data.

ratio for the first layer to $\gamma_0 = 2.84$ gives a flat event up to an offset of $x = 2.5$ km (see corresponding Figure 8.12). Furthermore, the second layer improves with a change from $\chi_{\text{eff}} = 0.346$ to $\chi_{\text{eff}} = 0.24$ and shows now a flat event up to an offset of 4 km.

As a second approach I estimated χ_{eff} and V_{c2} using the semblance double scanning technique. The result is displayed in Figure 8.13 and the picks are listed in Table 8.2. Confirming the result from the interactive tool, the first layer has the largest error for the anisotropy parameter while the third layer gives the most accurate results. The velocity estimates have small errors (~ 0.006 km/s) for all layers.

Both parameter estimation methods are based on the same traveltime approximation (Equation (2.62)) and therefore the large errors in the estimated results from the first layer could indicate a problem in the theory of coping with high γ_0 values.

On the P-wave or vertical component I have only applied the semblance double scanning technique to obtain V_{p2} and η_{eff} for the 3 events. Figure 8.14 shows

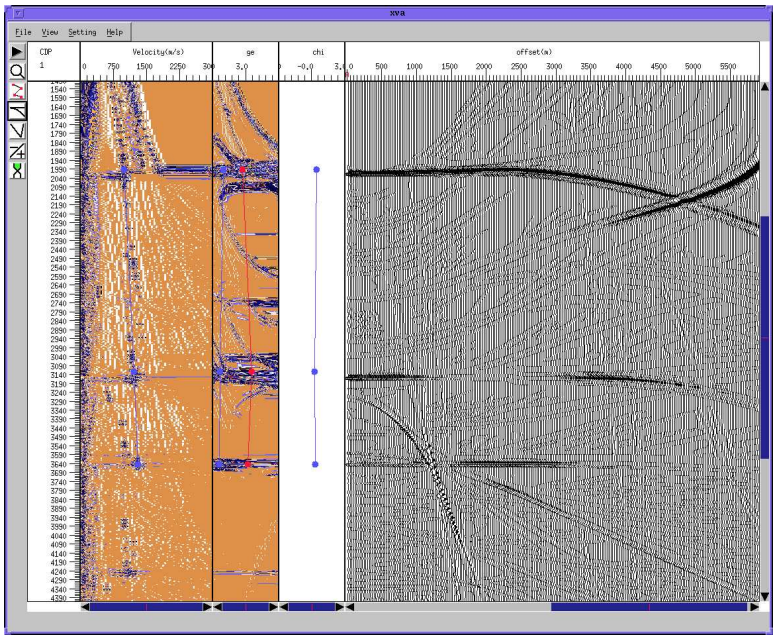

Figure 8.12: Parameter estimation from synthetic C-wave data using interactive tool and changed model values. The display shows the semblance panel for the C-wave velocity, velocity ratio, anisotropy parameter χ_{eff} and the corresponding NMO correction of the synthetic data.

the results and Table 8.2 summarises the picks and its errors. The maximum semblance picks for layer 1 and 3 are not unique. I have chosen in each case the stronger semblance point. In agreement with the results from the C-wave data I find again the largest errors occurring for the parameters from the first layer. Here, even the velocity has an error of 0.156 km/s. However, the second and third event give more accurate results. The absolute error of the anisotropy parameter is even smaller than the one obtained on the C-wave. But bearing in mind, that also the parameter itself is an order of magnitude smaller than the C-wave parameter, the error in relation to the parameter size is only small for the third event. Again, this might be caused by the large γ_0 in the first layer.

Comparing the double scanning results for C-waves (Figure 8.13) and P-waves (Figure 8.14) I find once more that the C-wave ellipses are more vertical in the $\chi_{\text{eff}} - V_{c2}$ coordinate system than the P-wave ones. This agrees with the findings in Chapter 4 that the C-wave parameters are de-coupled while the P-wave ones are not. Furthermore, the C-wave results are, except of the layer 2 event, unique while the P-wave only show a unique pick for layer 2. For both wave types the

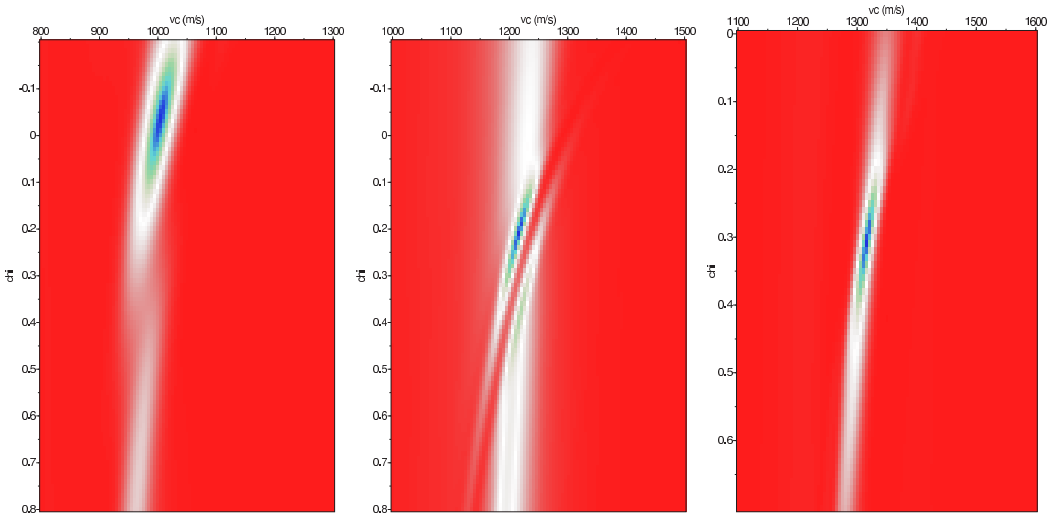

(a) $t_{c0} = 2.017$ s (b) $t_{c0} = 3.161$ s (c) $t_{c0} = 3.644$ s

Figure 8.13: Double scanning result estimating V_{c2} and χ for the 3 events from the horizontal component of the synthetic data from the Alba model.

stronger peak has been picked if the result was not unique. For the P-wave, this give a reasonable pick for layer 3 but not layer 1. In order to explain the larger errors for layer 1 in both wave types and the non-unique double scanning results I examine the synthetic seismograms for diminishing amplitude and phase reversal effects. The C-wave seismogram shows for the event of layer 1 a weakening signal about an offset of 1400 metres which also changes the shape of the wavelet. Layer 2 displays a diminishing amplitude with a phase reversal at an offset of 2400 metres and layer 3 is very weak in the near offset. For parameter estimation this implies, that the change in waveform of layer one may be another reason for the large error in parameter estimation in layer one. Certainly, the amplitude and phase effects do explain the error in the layer 2 results while parameter estimation on layer 3 is not affected.

I find that the P-wave seismogram shows these phenomena for the 1^{st} layer at an offset of about 800 metres and none for the 2^{nd}. For the 3^{rd} layer there is a zone between 1500-2100 metres offset which displays a slightly weakened signal. For arrivals with an $x/z = 3$ this means that the amplitude/phase effects are in the middle of this range of weakened signal for layer 1 and thus affect the double scanning severely. The weakened signal on layer 3 does not appear to have a large

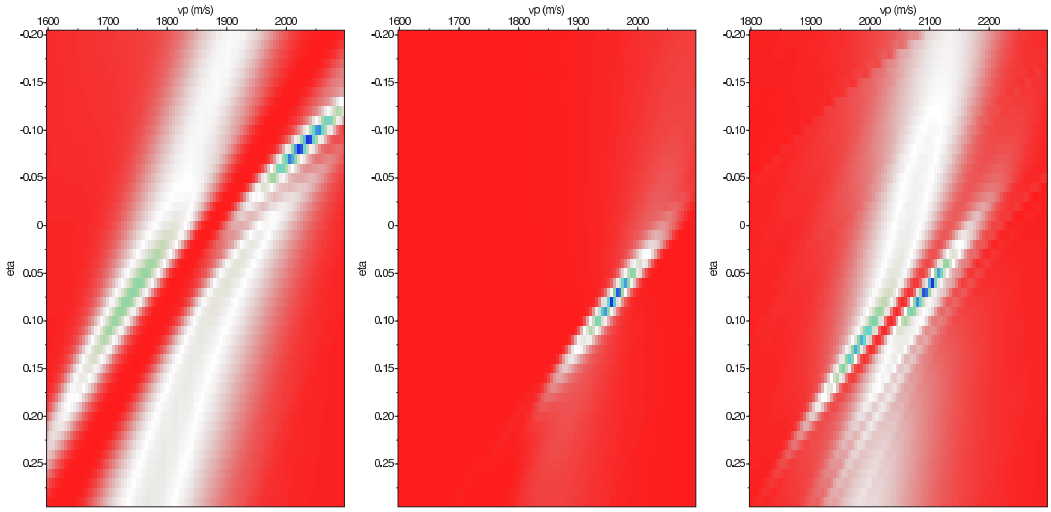

(a) $t_{p0} = 0.733$ s (b) $t_{p0} = 1.443$ s (c) $t_{p0} = 1.756$ s

Figure 8.14: Double scanning result estimating V_{p2} and η_{eff} for the 3 events from the vertical component of the synthetic data from the Alba model.

influence.

In summary, the synthetic modelling study of three events of the overburden from Alba confirms the findings from the real data. The traveltimes can be modelled with the model and the parameters estimated from the synthetic data are in the same range as I find for the real data.

layer	V_{p2} [km/s]	$\lvert\Delta V_{p2}\rvert$	η_{eff}	$\lvert\Delta\eta_{\text{eff}}\rvert$	V_{c2} [km/s]	ΔV_{c2}	χ_{eff}	$\lvert\Delta\chi_{\text{eff}}\rvert$
1	2.0	0.156	-0.0691	0.112	1.0	0.006	-0.0331	0.387
2	1.954	0.014	0.08	0.013	1.215	0.007	0.212	0.134
3	2.092	0.038	0.0695	0.007	1.31	0.006	0.313	0.035

Table 8.2: Table of picking results from synthetic data using the interactive tool and double scanning techniques.

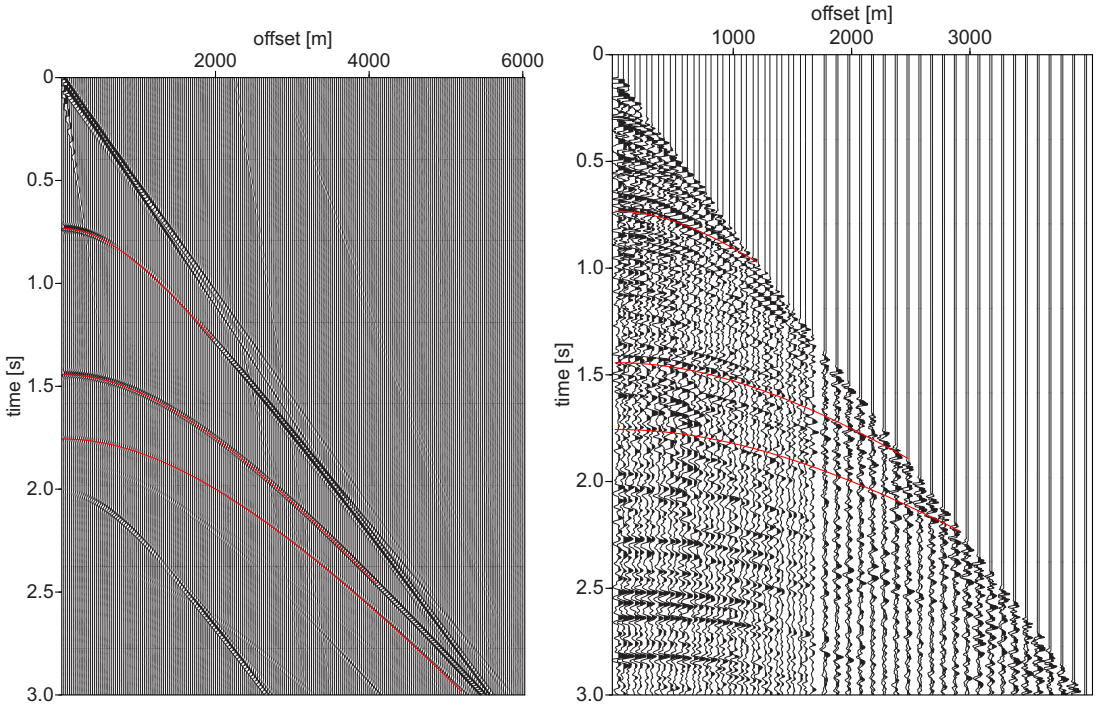

(a) Z

(b) Z

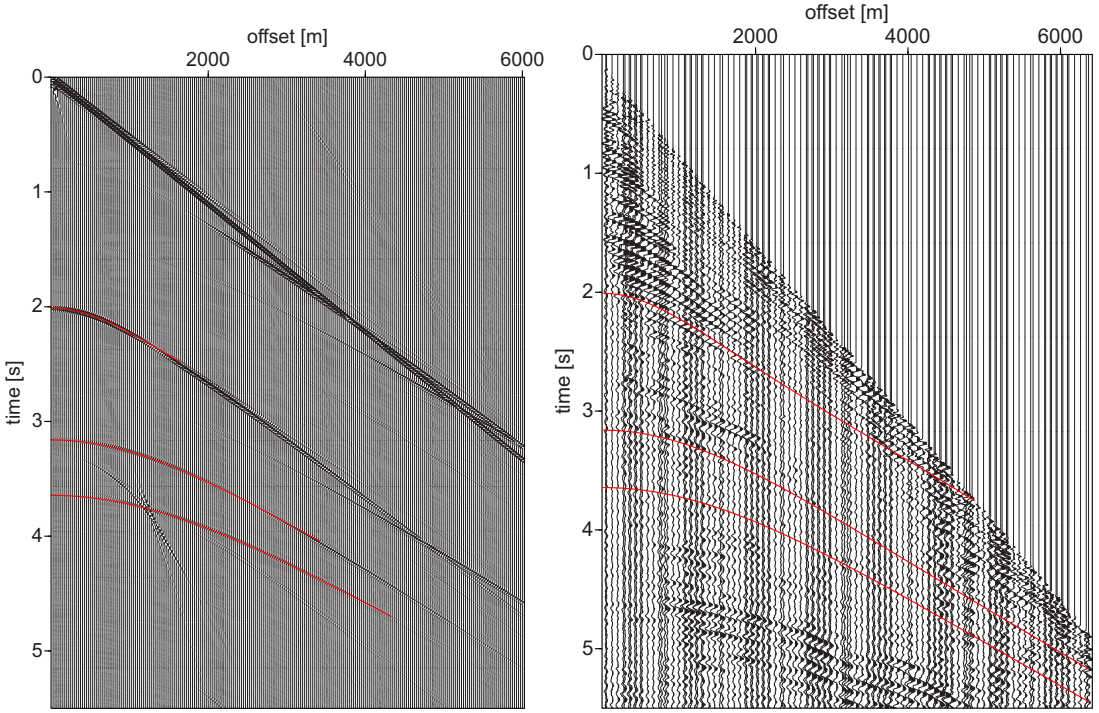

(c) X

(d) X

Figure 8.15: Comparison of real data and synthetic seismograms for 3 overburden events from Alba and the 3-layer Alba model (see Table 8.1). All seismograms have the calculated traveltime curves from the 3 events of the alba model printed on top to give feel for the fit. (a) Z-component from model, (b) Z-component, i.e. one CDP gather from the real data, (c) synthetic X-component and (d) one ACP gather (X-component) from real data.

8.2.4 Comparison with borehole data

In Chapter 3, I introduced the results from VSP data analysis with the interval velocities V_{p0i}, V_{s0i}, and corresponding depth and anisotropy parameters ϵ and δ (Figure 3.12(b)). From these values the RMS and effective parameters can be calculated. I use these VSP quantities to evaluate the results from the surface data processing. Figure 8.16 shows comparison of RMS-velocities for (a) C-waves, (b) P-waves (estimated from VSP, C-wave and directly from P-wave data) and (c) S-waves. The P-wave RMS-velocities show the best fit with each other. C-

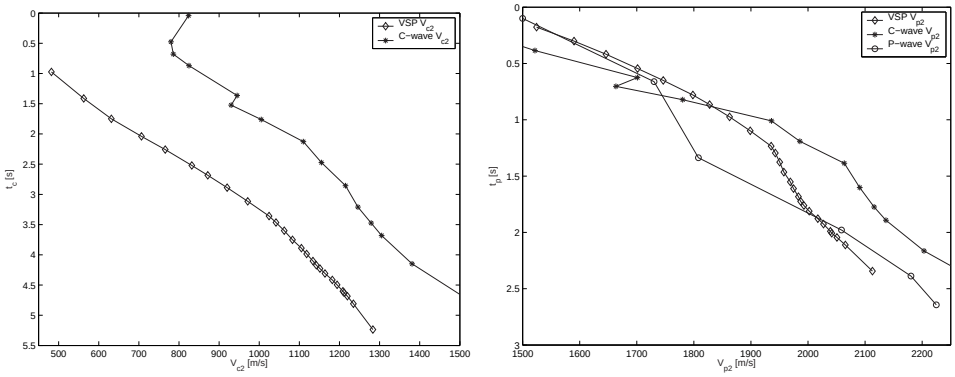

(a) V_{c2} (b) V_{p2}

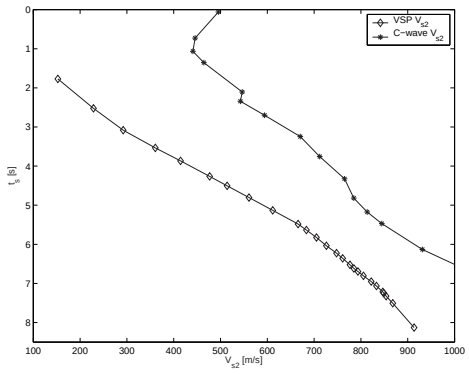

(c) V_{s2}

Figure 8.16: Comparison between RMS velocities from VSP data and extracted from one ACP gather for (a) V_{c2}, (b) V_{p2} and (c) V_{s2}.

and S-waves show similar differences which is expected as the S-wave velocities are calculated values not obtained directly from real data. The difference between

the C-wave velocities from VSP and from C-wave data is about 0.4 km/s at an arrival time of 2 seconds and 0.25 km/s for an arrival time of 3.5 seconds. The difference between the S-wave velocities vary in the same range (t_s = 4 s: 0.4 km/s and t_s = 6 s: 0.25 km/s).

Taking the obtained velocity and depth information from the VSP data into account I can obtain η_{eff} values in the C-wave time domain. Figure 8.17 compares η_{eff} obtained from VSP results with η_{eff} calculated from the C-wave parameter χ_{eff} and directly estimated from P-wave data. The VSP curve shows the smoothest course. However, η_{eff} from C-wave data shows values in the same range as the VSP data while the P-wave η_{eff} values are generally larger. This result confirms our finding from the modelling studies, that calculated η_{eff} values from C-wave parameter χ_{eff} fit the anisotropy in the medium better than η_{eff} from P-wave data.

Finally, I will show the fit between interval velocities obtained from surface data

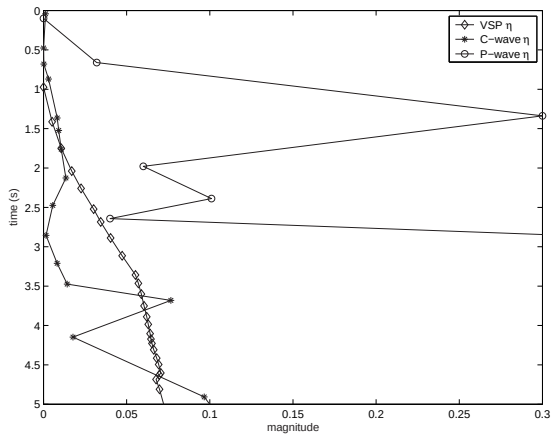

Figure 8.17: Comparison of η_{eff} calculated from C-wave surface data, estimated from P-wave data and obtained from VSP data.

processing with the results from the VSP data. Firstly, in Figure 8.18 I have plotted the interval velocities for P-waves in Figure 8.18(a) and for S-waves in Figure 8.18(b). As for the RMS-velocities I find a better consensus between the P-wave velocities than between the S-wave velocities. For instance, the difference at t_p = 1.0 seconds is about 190 m/s between the P-wave interval velocities. However, the S-wave interval velocities show a similar difference to the RMS-velocities of 360 m/s for a arrival time of t_s = 4 seconds.

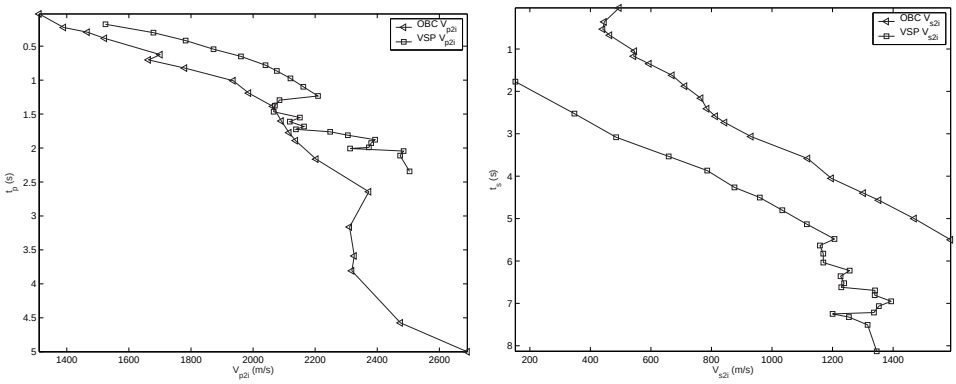

(a) V_{p2i} (b) V_{s2i}

Figure 8.18: Comparison of interval velocity (a) V_{p2i} and (b) V_{s2i} from VSP and extracted from surface C-wave data.

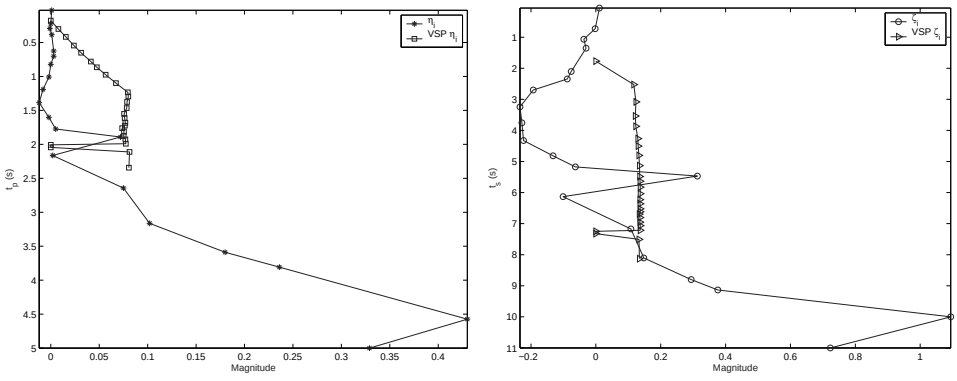

(a) η_i (b) ζ_i

Figure 8.19: Comparison of interval anisotropy parameters (a) η_i and (b) ζ_i from VSP and extracted from OBC C-wave data.

Secondly, in Figure 8.19 I compare the interval anisotropy parameters for the P-wave parameter η_i in (a) and for the S-wave parameter ζ_i in (b). The P-wave quantities show differences between well log and surface data as large as 0.097 at a $t_p = 1.45$ seconds. For the S-waves the largest difference occurs at about $t_s = 3.8$ seconds with a value of 0.36. Although the S-wave difference is much larger it has to be kept in mind that the parameter values itself are larger too.
In summary, comparing results from well log data (i.e. VSP) and surface data (C-wave) I find that the P-wave velocities match fairly well with each other while there are differences for the C-wave and S-wave velocities (computed from C-wave results). An explanation could be an error in event correlation. Furthermore, Leaney et al. (2001b) found the values of V_s in deviated wells significantly elevated and in need of some form of calibration. They also explain the high values with the presence of polar anisotropy. Mancini et al. (2002) found large differences between the velocity ratios extracted from seismic data and well logs.

8.3 Final image results

After a detailed evaluation of the anisotropy model, I use it to perform a final PSTM. The final result after PSTM on the C-wave data is displayed in Figure 8.20. It is interesting to compare this result with the anisotropic non-hyperbolic stack in Figure 7.23. The migration shows a clearer signal in the first 2 seconds. Both images indicate a dip at ACP 350 and 1 second two-way traveltime. The events are continuous and especially between 1.5 and 2 seconds traveltime very clear in the migrated section. However, the events at about 2.8 seconds are stronger in the migrated section but less continuous than in the stacked one. The reservoir area does not show the bent events anymore in the migrated section (at 3.8 seconds). The events beneath the reservoir layer have improved considerably in the migrated image. Here, events are visible very clearly up to at least 6 seconds.

Focusing on the reservoir area at about 3.8 seconds two-way traveltime Figure 8.21 shows the direct comparison between the stacked and migrated section. The stacked image shows an event with one interruption at about 4.4 seconds traveltime and a not continuous bent event above it at about 3.8 seconds. This is, where the Alba reservoir should be visible according to literature and the processing report (MacLeod et al. (1999), Underwood and Tilling (1999)). The area between ACP 350 and 450 is also very blurry and not continuous at all times. By contrast, the migrated image shows two clear continuous events at 4.0 and 4.4 seconds. The dome shape feature from the stacked image at 3.8 seconds is not visible anymore. However, between ACP 350 and 450 the broken events indicate the possible location of the reservoir.

Finally, Dai and Li (2001) show migration results from a neighbouring sailing line to the one I have worked on. Their results confirm that the events in the target area are more continuous after PSTM than isotropic migration or stacking only. Furthermore, they show similar interrupted events between CIP 500 and 600. The difference in the CIP numbering is possibly due to different calculation of these numbers.

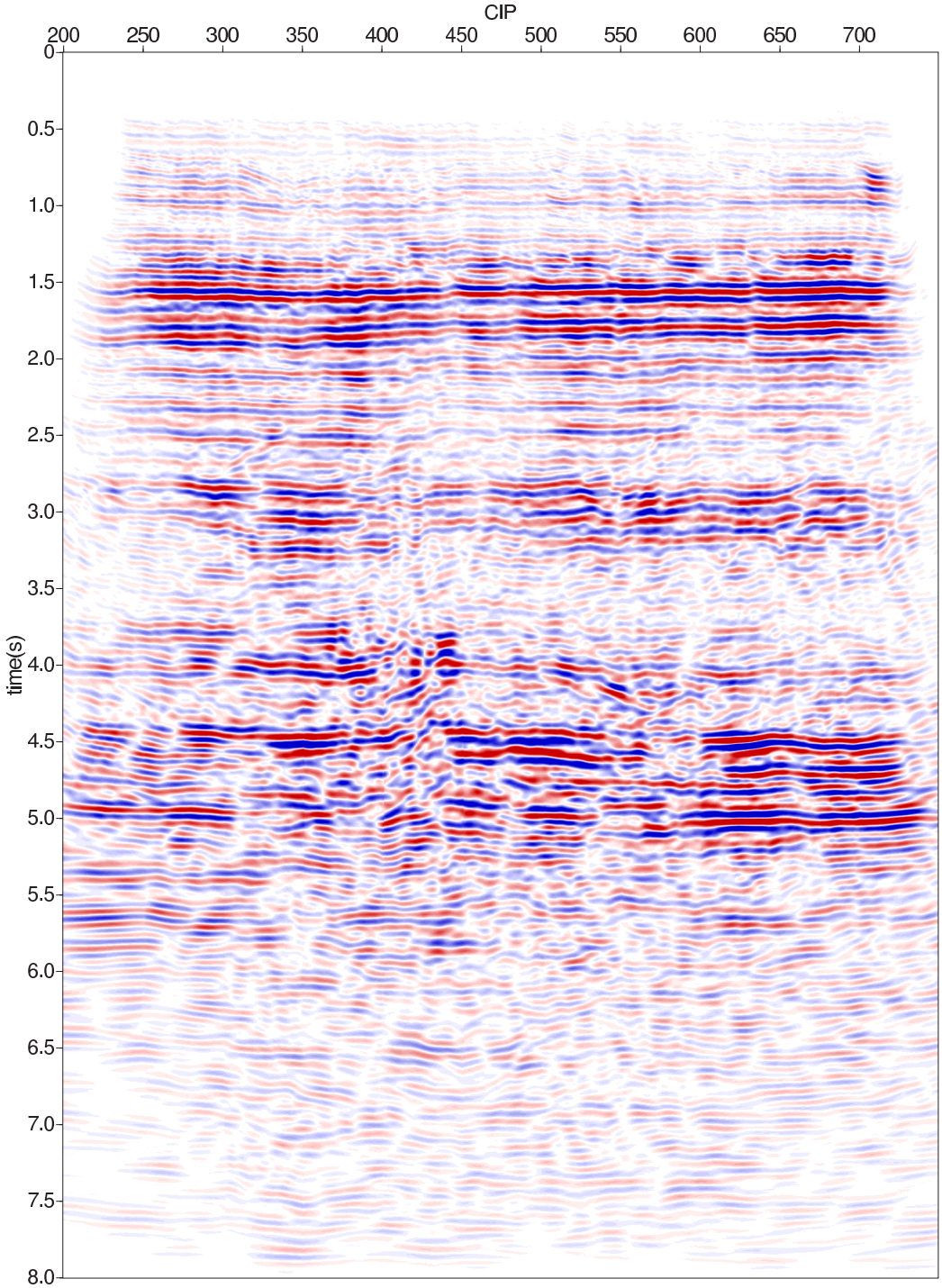

Figure 8.20: Final anisotropic PSTM result.

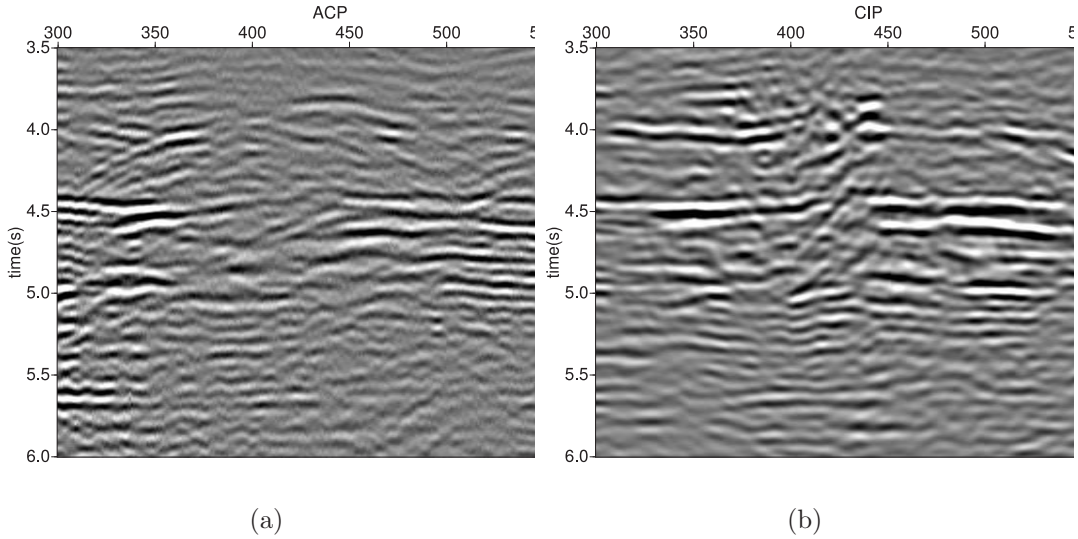

Figure 8.21: C-wave stack and migration result focusing on the target depth of the Alba reservoir. (a) anisotropic non-hyperbolic stack. (b) PSTM.

8.4 Discussion and Conclusions

I have presented an integrated study on imaging and model building of the Alba data. In this study, I demonstrated how anisotropic parameters can be estimated from 4C seismic data, and how such information can be used for improving subsurface imaging. Both isotropic and anisotropic processing flows have been introduced and applied to the data set. I found that the isotropic results for both P- and C-wave give unsatisfactory images. Determination of the anisotropy in the data showed that the C-wave anisotropy is stronger than the P-wave anisotropy and confirms the findings of Dai et al. (2001) and MacLeod et al. (1999).

Using the stacking velocity model estimated in Chapter 7 as an input for an anisotropic prestack Kirchhoff time migration, I generated CIP gathers for updating the velocity and the anisotropy parameter χ_{eff}. The final migrated image represents the best results among all the results I obtained. The former bending events are now flat. Strong reflectors are visible in the overburden (1.5 and 2.8 seconds), the assumed location of the reservoir (4 seconds) and underneath it at 4.5-5.5 seconds, where the Britannia field is assumed to be at about 5.5 seconds two-way traveltime.

I also carried out a detailed evaluation of the subsurface anisotropy models built from the 4C Alba data. This includes comparing results with VSP borehole data and synthetic modelling. Comparing results from well log data (i.e. VSP) and surface data (OBC C-wave) I find that the P-wave quantities match well while there are distinct difference for the C-wave and S-wave quantities (computed from C-wave results).

Furthermore, focusing on the comparison between η from VSP results as model value with η determined from P-wave data or calculated from C-wave χ, I found the synthetic studies confirmed that η calculated from χ is closer to the "model" η values from VSP data than the values determined directly from P-wave data.

Finally, I have verified the processing results from the surface data by a modelling study for 3 chosen events from the overburden. I built a model based on

well log and surface data to fit these 3 events and performed parameter estimation on the synthetic data. The traveltime curves from the model match the real data reasonably well. However the parameter estimation shows problems in the first layer with a large velocity ratio γ_0. In summary:

- Standard processing tools have been used to obtain a first isotropic image for both P- and C-wave data.
- A typical anisotropic work flow was carried out for model building and imaging.
- It has been shown that the non-hyperbolic moveout analysis can be used to help constrain a VTI model for better imaging.
- PSTM was used for C-wave data to get an improved image and both RMS and interval models were derived.
- The processing results were verified with a synthetic modelling study for 3 events from the overburden.
- The η calculated from C-wave anisotropy parameter is closer to observed VSP anisotropy values than that directly obtained from P-wave data.
- Hence, I could confirm that the results from the integrated study were consistent with my findings in the previous chapters.

Chapter 9

Conclusions

9.1 Thesis conclusions

The advantages of using converted-wave seismic data in hydrocarbon exploration have become widely accepted in recent years. Such data can be used for lithology and fluid prediction and fractured reservoir characterisation as well as improved imaging in complex areas. Due to their asymmetric raypath and sensitivity to anisotropy, C-wave data processing is more complicated than P-wave data processing. Various methods have been proposed to estimate anisotropy in order to use it for processing purposes and subsequent model building. P-wave moveout in anisotropic media has been described by Alkhalifah and Tsvankin (1995) using the anisotropy parameter η, a combination of Thomsen parameters. Yuan et al. (2001) introduced the anisotropy coefficient χ which describes the effect of anisotropy on C-waves. Moveout for P- and C-waves can be described as a Taylor series expansion including higher order terms. Based on these, a double-scanning semblance analysis routine can be used to determine stacking velocity V_{p2} and anisotropic parameter η for P-waves and V_{c2} and χ for C-waves. These parameter pairs can then be used for time processing of each wave type. In this thesis the main emphasis was on anisotropic parameter estimation, how accurately it describes the anisotropy of the studied medium and how sensitive the parameter estimation reacts to influences of geology such as multilayering and velocity gradients, as well as how it can be used for improved imaging.

From the study of a single VTI layer, I found that the resolution of the moveout approximations for P- and C-waves can be specified by the newly introduced inherited error Δ_{inh}. I find that, regardless of the magnitude of the anisotropic parameter, the inherited error has the same order of magnitude for each wave type, i.e. $\Delta_{\text{inh}}\eta = 0.02$ and $\Delta_{\text{inh}}\chi = 0.04$. Thus, it can be suggested that if the difference (Δ) between anisotropic parameters of different models is smaller than the inherited error ($\Delta < \Delta_{\text{inh}}$), one cannot differentiate between these models. Inversion and the error bars from a set of models confirm this finding. Furthermore, I find that in general the stacking velocity is better constrained than the anisotropy parameter. However, the approximations are good enough to be used for moveout inversion. The power to resolve the anisotropic parameters between two different models using these moveout approximations is in the same range for P- and C-waves.
In most cases the picking errors from the actual inversion are smaller for C-wave parameters than P-wave parameters, i.e. the C-wave parameters are estimated more accurately. Furthermore, the anisotropic parameter η can be estimated from the C-wave moveout data, by calculating it from χ, more accurately than from P-wave data. In most cases the error of η, calculated from χ, is half the picking error of χ. Considering that the picking error of χ tends to be smaller than the one from η, this means that the error of the calculated η from C-wave χ is often half the error of estimating directly from P-wave data.

Extending the analysis to multilayered media, I find, as for the single layer case, that the resolution and accuracy of χ_{eff} from C-waves are higher than those of η_{eff} from P-waves. There are two reasons for this. Firstly, the magnitude of the P-wave non-hyperbolic moveout is much smaller than the magnitude of the C-wave non-hyperbolic moveout in the same offset range. Secondly, η_{eff} values in the chosen models are often smaller than 0.1, whereas the χ_{eff} values are within a much larger range between 0.2 and 0.4. When η_{eff} is increased to 0.1-0.2, the resolution improves. However, calculating η_{eff} from the C-wave parameter χ_{eff} is more accurate than estimating it directly from P-waves. The influence of a low velocity layer (i.e. a high γ_0) on moveout inversion leads to a poorer resolution of the parameters extracted from the layers beneath.

For this part of my synthetic study, I used true amplitude modelling and found from this that the low resolution and poor accuracy when estimating η_{eff} directly from P-wave data can also be explained by the occurrence of diminishing amplitudes and phase reversals. These effects are confirmed by computing the effective reflection coefficients. Although they can be found for C-waves too, they mostly occur at larger offsets and so do not affect the usable large offset for moveout inversion as strongly as for P-waves.

Applying the parameter estimation to the 4C data set of the Alba field I first concentrated on near-surface effects.The P-wave anisotropic parameter η_{eff} was estimated from the vertical component and also calculated from χ_{eff}, obtained from the horizontal component. However, the calculated η_{eff} is roughly an order of magnitude smaller than the picked value. In order to understand this difference in the size of η_{eff}, I generated a model from well, VSP and surface data to calculate reference parameter values. I find that 2 out of 3 values of η_{eff} derived from P-wave inversion of the near-surface model are an order of magnitude larger than the model values. The χ_{eff} values extracted from C-wave events are in the same order of magnitude as the model values and calculating η_{eff} from these χ_{eff} values gives a more accurate result. In order to explain the unusually high values of the P-wave parameter estimation, I carried out a full-waveform modelling study and also calculated the effective reflection coefficients. I found that compaction effects in the near-surface influence the estimation process and thus may lead to erroneously high values for η_{eff}. Furthermore, phase reversals and weakened amplitudes occur in the range of offsets used for parameter estimation of the vertical component. These phase reversals interfere with the double semblance technique due to stacking of incoherent energy.

Finally, I presented and applied a full work flow for anisotropic model building and imaging (including PSTM) using 4C seismic data and applied it to the Alba 4C data. Parameter estimation using double semblance analysis gives an initial velocity and anisotropy field but the procedure is very time consuming for a full data set. In order to simplify the process I used an interactive GUI (graphical user interface) tool for model updating. Use of the anisotropic work flow gives improved stacked sections. Further improvements are still possible by applying

prestack time migration using the parameters $\eta_{\text{eff}}, \chi_{\text{eff}}, V_{p2}$ and V_{s2}. The stacking model was used as an initial model for PSTM and was updated by an interactive GUI tool for migration properties. The final migrated image represents the best results among all the results I obtained.

I also carried out a detailed evaluations of the subsurface anisotropic models built from the 4C Alba data. This included comparing results with VSP borehole data and synthetic modelling. Comparing results from well log data (i.e. VSP) and surface data (OBC C-wave) I found that the P-wave velocities estimated from P- and C-wave data match well with the VSP velocities while there are distinct differences for the C-wave and S-wave quantities (computed from C-wave results). An explanation could be an error in event correlation. I also compare η_{eff} from VSP data with η_{eff} determined from P-wave data or calculated from C-wave data χ_{eff}. The synthetic studies confirmed that η_{eff} calculated from χ_{eff} is closer to the η_{eff} values from VSP data than the values determined directly from P-wave data. Furthermore, I calculated interval quantities and compared η_i from VSP and C-wave data together with RMS values. I found that the difference between interval and RMS quantities were only small. Also, I have verified the processing results from the surface data by a modelling study for 3 chosen events from the overburden.

In summary, I find that anisotropic parameter estimation is often more accurate for C-waves than P-waves. Moreover, the P-wave anisotropy parameter η, which is necessary for model building and migration, can be obtained more accurately when calculated from the C-wave parameter χ. Hence, the calculated parameter η (from C-wave properties) gives a better description of the actual anisotropy in the medium. The proposed time processing flow and model building using C-wave data leads to improved subsurface images which correspond well with well log data in the time domain.

9.2 Future work

Research has progressed in large steps in the field of 4C seismic data processing. In my thesis I studied the accuracy of the parameter estimation on 4C data. I found that considerably better images can be obtained by applying these parameters in PSTM. However, there is more work left to be done. Intuitively, the desire to tie P- and C-wave events of 4C data in the depth domain is the next step forward. The difficulty here lies especially in correct velocity and anisotropy model building. One approach is to assume a correct P-wave velocity model and estimate the S-wave velocity by scanning the C-wave data and estimating anisotropy from mismatches between reflector depth in surface and well data. The anisotropy estimation is strictly only valid at the well location. Another approach is to build an anisotropic model by estimating the Thomson parameters ϵ and δ from the data then perturbing the parameters to find the best fit. This method is time consuming and needs fast computers if a raytracer is used for the scanning procedure. Following the EAP approach, which uses traveltime approximation for scanning stacking velocity and anisotropy parameters, I have shown that the necessary P-wave parameter η is more accurately determined when calculated from C-wave data. However, parameter estimation using double semblance analysis is very time consuming. Using an interactive GUI tool is more user friendly and gives very good results for time processing. However, stacking velocities and anisotropy parameters estimated this way will describe a good fit to the traveltime curve but may not reflect the actual anisotropy value of the medium. Certainly, more work needs to be done to investigate this.

Interpretation of multicomponent data has a high potential to be a powerful tool for reservoir characterisation and lithology identification, for instance differentiation between sand and shale in the reservoir body or fluid flow observation. Tatham (1982) started to correlate V_p/V_s ratio from laboratory values with lithology. Nowadays, V_p/V_s ratios can be obtained from multicomponent seafloor data. However, it is not clear how to link the V_p/V_s ratios and other parameters such as anisotropy from the multicomponent data to lithology and fluid flow. It is necessary to correlate the P- and C-wave data with a high degree of accuracy. Chuandong and Stewart (2004) used VSP (wide angle and zero-offset) to help

identify events in the C-wave domain, correlate them with events in the P-wave domain and subsequently derive a V_p/V_s curve. This ratio is then linked to lithology. This procedure depends on well control and good reflectors to correlate. Özdemir and Flanagan (2004) inverted stacked sections of 4C data to acoustic and shear impedance and density for interpretation. They found good correlation between inverted rock properties and well data but no great confidence about identification of pore fill (i.e. fluid).

One of the main remaining issues when working towards reliable interpretation is how to get an accurate correlation as this process is easily affected by errors in horizon interpretation, different frequency content of P- and C-wave sections and mis-match with well data.

It has also been suggested that the anisotropic parameters should be linked directly to lithology. Using P-wave data, Alkahalifah et al. (2001) showed a correlation between η, estimated from surface data, and lithology as interpreted from well log data for a field offshore Trinidad. Arnaud (2004) showed another attempt to use η, extracted from P-wave data, as lithology indicator. This study also highlights a problem. The effective anisotropic parameter has to be estimated very accurately and then converted into interval quantities. This can work in good conditions, i.e. good data quality, no structural effect on velocities, validity of anisotropy description and usable offset-to-depth ratio. However, as I have shown in this thesis, the accuracy of anisotropic parameters is still an issue. Furthermore, inverting the effective parameters into interval quantities using a Dix layer-stripping approach is unstable and so may not give the accuracy necessary for this type of analysis. More work need to be done to ensure a reliable inversion for interpretation. One possible approach is to use the C-wave data. As demonstrated here, anisotropy parameters can be estimated more accurately from C-wave data than from P-wave data.

References

K. Aki and P. G. Richards. *Quantitative Seismology*. University Science Books, Sausalito, California, 2nd edition edition, 2002.

T. Alkahalifah, A. King, and D. Rampton. Seismic anisotropy in Trinidad: A new tool for lithology prediction. *The Leading Edge*, 20(4):420–424, April 2001.

T. Alkhalifah. Velocity analysis using nonhyperbolic moveout in transversly isotropic media. *Geophysics*, 62(6):1839–1854, 1997.

T. Alkhalifah and K. Larner. Migration error in transversely isotropic media. *Geophysics*, 59(9):1405–1418, September 1994.

T. Alkhalifah and I. Tsvankin. Velocity analysis for transversely isotropic media. *Geophysics*, 60(05):1550–1566, 1995.

J. Arnaud. Seismic anisotropy as a lithology indicator. *EAGE 66th Conference and Exhibition, Paris, France*, page B026, 2004.

E. Ata and R.J. Michelena. Mapping distribution of fractures in a reservoir with P-S converted waves. *The Leading Edge*, 14(6):664–676, June 1995.

G. E. Backus. Long-wave elastic anisotropy produced by horizontal layering. *Journ. Geophys. Res.*, 67:4427–4440, 1962.

N.C. Banik. Velocity anisotropy of shales and depth estimation in the North Sea basin. *Geophysics*, 49(9):1411–1419, 1984.

F. J. Barr and J. I. Sanders. Attenuation of water-column reverberation using pressure and velocity detectors in a water-bottom cable. *59th Int. Mtg. Soc. Expl. Geophys., Expanded Abstracts*, pages 653–656, 1989.

D. Bevc. Imaging complex structures with semirecursive Kirchhoff migration. *Geophysics*, 62(2):577–588, 1997.

S. Brandsberg-Dahl and O.I. Barkved. Anisotropic P-wave velocity derived from deviated wells at the Valhall field. *EAGE 64th Conference and Exhibition, Florence, Italy*, page P135, 2002.

T. Cheret, R. Bale, and S. Leaney. Parameterization of polar anisotropic moveout for converted waves. *70th Ann. Intern. Mtg.: Soc. of Expl. Geophys.*, 2000.

X. Chuandong and R. R. Stewart. Using 3D multi-component seismic data, logs and VSP to interpret a sand-shale oil reservoir. *EAGE 66th Conference and Exhibition, Paris, France*, page P253, 2004.

S. Crampin. Evaluation of anisotropy by shear-wave splitting. *Geophysics*, pages 142–152, 1985.

H. Dai. Interactive estimation of anisotropic parameters and velocities from PS converted waves. *73rd SEG Annual Meeting, Conference and Technical Exhibition, Dallas, USA*, 2003a.

H. Dai. Phase behaviour of P-SV converted waves recorded at the sea-bed. *Geophysical Prospecting*, 51:347–364, 2003b.

H. Dai and X.-Y. Li. Anisotropic migration and model building for 4C seismic data: a case study from Alba. *SEG Annual Meeting, Conference and Technical Exhibition, San Antonio, USA*, 2001.

H. Dai and X.-Y. Li. A practical approach to update the migration velocity model for PS converted waves. *SEG Annual Meeting, Conference and Technical Exhibition, Salt Lake City, USA*, 2002a.

H. Dai and X.-Y. Li. Sensitivity analysis of migration velocities for P-S converted wave imaging. *EAGE 64th Conference and Exhibition, Florence, Italy*, 2002b.

H. Dai and X.-Y. Li. Migration velocity analysis of C-wave using INNMO-CIP gathers of PKTM: a case study from the Gulf of Mexico. *EAGE 65th Conference and Exhibition, Stavanger, Norway*, 2003.

H. Dai, X.-Y. Li, and M. MacLeod. Anisotropic analysis and processing of Alba 4C OBC data. *63rd EAGE Conference and Technical Exhibition, Amsterdam, Netherlands*, 2001.

H. Dai, X.-Y. Li, and M. Mueller. Compensating for the effects of gas clouds by prestack migration: a case study from Valhall. *SEG Annual Meeting, Conference and Technical Exhibition, Calgary, Canada*, 2000.

J. Dellinger, R. Clarke, and P. Gutowski. Horizontal vector fidelity correction by general linear transform. *SEG, Annual Meeting, Conference and Technical Exhibition, San Antonio, Texas*, 2001.

D. Duranti, A. Hurst, C. Bell, S. Groves, and R. Hanson. Injected and remobilized Eocene sandstones from the Alba Field, UKCS: core and wireline log characteristics. *Petroleum Geoscience*, 8(2):99–107, May 2002.

D. Duranti, A. Hurst, R. Hanson, C. Bell, and M. McLeod. Reservoir characterisation of remobilised sand-rich turbidite reservoir - The Alba field. *EAGE 62nd Conference and Technical Exhibition, Glasgow, Scotland*, 2000.

G. Fromm, T. Krey, and B. Wiest. *Static and dynamic corrections*, volume 15a, chapter Handbook of Geophysical Exploration, pages 191–225. Geophysical Press, 1985.

R. Garotta, P.-Y. Granger, and H. Dariu. Combined interpretation of PP and PS data provides direct access to elastic rock properties. *The Leading Edge*, 21(6), June 2002.

J.R. Granli, B. Arntsen, A. Sollid, and E. Hilde. Imaging through gas-filled sediments using marine shear-wave data. *Geophysics*, 64(3):668–677, 1999.

V. Grechka and P. Dewangan. Generation and processing of pseudo shear-wave data: Theory and case study. *Society of Exploration Geophysisists*, 2003.

V. Grechka and I. Tsvankin. Feasibility of nonhyperbolic moveout inversion in transversely isotropic media. *Geophysics*, 63(3):957–969, May-June 1998.

V. Grechka and I. Tsvankin. The joint non-hyperbolic moveout inversion of PP and PS data in VTI media. *Geophysics*, 67(6):1929–1932, Nov-Dec 2002a.

V. Grechka and I. Tsvankin. PP+PS=SS. *Geohpysics*, 67(6):1961–1971, November-December 2002b.

H. Hake, K. Helbig, and C.S. Mesdag. Three-term Taylor series for $t^2 - x^2$-curves of P- and S-waves over layered transversely isotropic ground. *Geophysical Prospecting*, 32:32,828–32,850, 1984.

R. Hanson, P. Condon, R. Behrens, S. Groves, and M. MacLeod. Analysis of time-lapse data from Alba Field 4C/4D seismic survey. *Petroleum Geoscience*, 9(1):103–111, 2003.

R. Hanson, M. MacLeod, C. Bell, C. Thompson, and J. Somod. Multicomponent seismic interpretation - data integration issues, Alba Field, North Sea. *61rd Mtg. Eur. Assoc. Expl Geophys., Extended Abstracts, Helsinki, Finland*, page Session:6027, 1999.

K. Helbig. A graphical method for the construction of rays and traveltimes in spherically layered media, part 2: Anisotropic case, theoretical considerations. *Bull. Seis. Soc. Am.*, (56):527–559, 1966.

M. Huuse, D. Duranti, C. G. Guargena, P. Prat, K. Holm, N. Steinsland, B. T. Cronin, A. Hurst, and J. Cartwright. Sandstone intrusions: detection and significance for exploration and production. *First Break*, 21:33–42, September 2003.

I. F. Jones, N. Bernitsas, P. Farmer, J. Leslie, and M. Bridson. Anisotropic ambiguities. *64th Mtg. Eur. Assn. of Expl. Geophys.*, 2002.

P. Kearey and M. Brooks. *An Introduction to Geophysical Exploration*. Blackwell Science Ltd, 2nd edition edition, 1991.

R.R. Kendall, S.H. Gray, and G.E. Murphy. Subsalt imaging using prestack depth migration of converted waves: Mahogany field, Gulf of Mexico. *Ann. Int. Conf. of Soc. of Expl. Geoph., New Orleans, USA*, 1998.

B.L.N. Kennet. *Seismic wave propagation in stratified media*. Cambridge University Press, 1983.

K. Larner and I. Tsvankin. P-wave anisotropy: its practical estimation and importance in processing and interpretation of seismic data. *65th Ann. Internat. Mtg.: Soc. of Expl. Geophys.*, pages 1502–1505, 1995.

K.L. Larner and J.K. Cohen. Migration error in transversely isotropic media with linear velocity variation in depth. *Geophysics*, 58(10):1454–1467, October 1993.

Don C. Lawton and J. Helen Isaac. Slip-slidin' away - some practical implications of seismic velocity anisotropy on depth imaging. *The Leading Edge*, January 2001.

S. Leaney, M. Wheeler, and S. Tcherkashnev. Walkaway VSP, Logs and 2D line 2295 Processing report. Alba, Block OPL-246, north Sea. *Chevron Petroleum Technology Company*, 2001a.

W. S. Leaney. Look-ahead walkaways using effective VTI models. *70th Ann. Intern. Mtg.: Soc. of Expl. Geophys.*, 2000.

W.S. Leaney, R. Bale, M. Wheeler, and S. Tcherkashnev. Borehole-integrated anisotropic processing of converted modes. *The Leading Edge*, 20(9):996–1007, 2001b.

X.-Y. Li. Fractured reservoir delineation using multicomponent seismic data. *Geophysical Prospecting*, 45:39–64, 1997.

X.-Y. Li. Converted-wave moveout analysis revisited: The search for a standard approach. *73rd Ann. Intern. Mtg.: Soc. of Expl. Geophys., Expanded Abstracts*, pages 805–808, 2003.

X.-Y. Li, H. Dai, M. C. Mueller, and O.Il Barkved. Compensating for the effect of gas clouds on c-wave imaging: A case study from Valhall. *The Leading Edge*, 20(9):1022–1028, September 2001a.

X.-Y. Li, H. Dai, and J. Yuan. Converted-wave imaging in inhomogeneous, anisotropic media - part II - prestack migration. *63rd Mtg. Eur. Assn. of Expl. Geophys., Expanded Abstracts*, page Session: P114, 2001b.

X.-Y. Li and J. Yuan. An accurate P-SV moveout equation for transverse isotropy. *Edinburgh Anisotropy Project, Annual Report*, 6, 1999a.

X.-Y. Li and J. Yuan. Geophone orientation and coupling in three-component sea-floor data: a case study. *Geophysical Prospecting*, (47):995–1013, 1999b.

X.-Y. Li and J. Yuan. Accuracy and sensitivity analysis for estimating anisotropic parameters from 4C seismic data. *71st Ann. Int. SEG Meeting, San Antonio, Texas, USA*, 2001a.

X.-Y. Li and J. Yuan. Converted-wave imaging in inhomogeneous, anisotropic media - part I - parameter estimation. *63rd Mtg. Eur. Assn. of Expl. Geophys.*, page Session: P109, 2001b.

X.-Y. Li and J. Yuan. Converted-wave moveout and conversion-point equations in layered vti media: theory and applications. *Journal of Applied Geophysics*, 54:297–318, 2003.

X.Y. Li. Processing PP and PS waves in multicomponent sea-floor data for azimuthal anisotropy: Theory and overview. *Revue de l'institut française du pétrol*, 53(5):607–620, Septembre-October 1998.

M. K. MacLeod, R. A. Hanson, C. R. Bell, and S. McHugo. The Alba field ocean bottom cable seismic survey: Impact on development. *The Leading Edge*, 18 (11):1306–1312, 1999.

F. Mancini. *Converted wave imaging in anisotropic media using sea-floor seismic data*. PhD thesis, School of GeoScienes, University of Edinburgh, 2004.

F. Mancini, X.-Y. Li, A. Ziolkowski, and T. Pointer. Interpreting velocity ratios from 4C data and well logs in the presence of gas and anisotropy. *72nd Annual International SEG Meeting, Salt Lake City, Utah, USA*, 2002.

F. Mancini, X.-Y. Li, A. Ziolkowski, and T. Pointer. Effects of binning velocity ratios on c-wave imaging in the presence of dips. *EAGE 65th Conference and Exhibition, Stavanger, Norway*, 2003.

G. F. Margrave, D. C. Lawton, and R. R. Stewart. Interpretating channel sands with 3C-3D seismic data. *The Leading Edge*, April 1998.

S. McHugo, A. Probert, M. Hodge, P. Kristiansen, D. Painter, and M. E. A. Hadley. Acquisition and processing of a 3D multicomponent seabed data from alba field - a case stury from the North Sea. *61st Mtg. European Association Of Geophysical Exploration*, page Session:6026, 1999.

O. Mikhailov, G.J. Ball, J. Johnson, and E. Shoshitaishvili. Imaging of 4C data in depth - residual velocity analysis and anisotropy parameter estimation. *63th*

Mtg. Eur. Assn. of Expl. Geophys., Amsterdam, The Netherlands, pages N–05, 2001a.

O. V. Mikhailov, J. Johnson, E. Shoshitaishvili, and C. Frasier. Practical approach to joint imaging of multicomponent data. *The Leading Edge*, 20(9):1016–1021, 2001b.

D. Miller, S. Leaney, and W. H. Borland. An in situ estimation of anisotropy elastic moduli for a submarine shale. *Journal of Geopysical Research*, 99(B11): 21,659–21,665, November 1994.

D. E. Miller and C. Spencer. An exact inversion of anisotropic moduli from phase slowness data. *Journ. Geophys. Res.*, 99(B11):21,651–21,657, 1994.

T. Mukerji, I. Takahashi, E. F. Gonzalez, and G. Mavko. Rock physics diagnostics and modeling of P-P and P-S seismic attributes in the Alba Field. *70th Ann. Internat. Mtg.: Soc. of Expl. Geophys.*, 2000.

K.S. Newton and K.P. Flanagan. The Alba Field: evolution of the depositional model. *Petroleum Geology of Northwest Europe, Proceedings of the 4th conference, The Geological Society London*, pages 161–171, 1993.

H. Özdemir and K. Flanagan. Lithology and hydrocarbon mapping from multicomponent seismic data - A North Sea case study. *EAGE 66th Conference and Exhibition, Paris, France*, page P163, 2004.

D.A. Pope, J.H. Kommedal, and J.O. Hansen. Using 3D 4C seismic to drill beneath the Lomond gas cloud. *62nd EAGE conference and technical exhibition, Glasgow, Scotland*, 2000.

R. Reid and C. MacBeth. Test of vector fidelity in permanently installed multicomponent sensors. *70th Ann. Internat. Mtg. of Soc. of Expl. Geophys., Calgary, Canada*, 2000.

B.E. Rommel. Dip move out processing DMO for converted waves in transversely isotropic media. *58th EAGE conference and technical exhibition, Amsterdam, Netherlands*, page P136, 1996.

S. Ronen, M. Jarvis, and A. Probert. Azimuthal anisotropy - more than just theory. *63rd EAGE conference and technical exhibition, Amsterdam, Netherlands*, 2001.

C.M. Sayers, M. J. Woodward, and R. C. Bartman. Predrill pore-pressure prediction using 4-C seismic data. *The Leading Edge*, 20(9):1056–1059, September 2001.

M. Schoenberg and T. M. Daley. qSV wavefront triplication in a transversely isotropic material. *73rd Ann. Internat. Mtg.: Soc. of Expl. Geophys.*, pages 137–140, 2003.

M. Schoenberg and P. Protazio. 'zoeppritz' rationalized and generalized to anisotropy. *Journal of seismic exploration*, pages 125–144, 1992.

A. J. Seriff and K. P. Sriram. P-sv reflection moveouts for transversely isotropic media with a vertical symmetry axis. *Geophysics*, pages 1271–1274, 1991.

R. Sheriff and L. Geldart. *Exploration Seismology*. Cambridge University Press, 1995.

R. E. Sheriff. *Encyclopedic Dictionary of Exploration Geophysics*. SEG, third edition edition, 1997.

R. R. Stewart, J. E. Gaiser, J. R. Brown, and D. C. Lawton. Tutorial - Converted wave seismic exploration: Methods. *Geophysics*, 67(5):1348–1363, 2002.

R.R. Stewart, J.E. Gaiser, R.J. Brown, and D.C. Lawton. Tutorial - Converted wave seismic exploration: Applications. *Geophysics*, 68(1):40–57, January-February 2003.

M. T. Taner, F. Koehler, and R. E. Sheriff. Complex seismic trace analysis. *Geophysics*, 44(6):1041–1063, June 1979.

M.T. Taner and F. Koehler. Velocity spectra - digital computer derivation and applications of velocity functions. *Geophysics*, 34(6):859–881, December 1969.

R. H. Tatham. Vp/Vs and lithology. *Geophysics*, pages 336–344, 1982.

D. Taylor. *ANISEIS 5.2 Manual*. Applied Geophysical Software Inc., Houston, 2001.

G. Tessmer and A. Behle. Common reflection point data-stacking technique for converted waves. *Geophysical Prospecting*, 36:671–688, 1988.

F. Theilen, A. Ayres, and G. Lange. Physical properties of near surface marine sediments. *EAGE 59th Conference and Technical Exhibition, Geneva, Switzerland*, page P064, 1997.

L. Thomsen. Weak elastic anisotropy. *Geophysics*, 51(10):1954–1966, 1986.

L. Thomsen. Converted-wave reflection seismology over inhomogeneous, anisotropic media. *Geophysics*, 64(3):678–690, 1999.

L.A. Thomsen, O.I. Barkved, B. Haggard, J.H. Kommedal, and B. Rosland. Converted-wave imaging of Valhall reservoir. *59th EAGE conference and technical exhibition, Geneva, Switzerland*, 1997.

B. Traub and X.-Y. Li. Sensitivity of anisotropic parameter estimation for 4c data. *EAP Report*, 9:A63–A96, 2002.

E. L. Tree. The vector infidelity of the ocean bottom multicomponent seismic acquisition system. *61st Eur. Assn. of Expl. Geophys. Conference, Helsinki, Finland*, 1999.

I. Tsvankin. P-wave signatures and notation for transversely isotropic media: an overview. *Geophysics*, 61(2):467–483, 1996.

I. Tsvankin and V. Grechka. Dip moveout of converted waves and parameter estimation in transversely isotropic media. *Geophyical Prospecting*, 48:257–292, 2000.

I. Tsvankin and H.B. Lynn. Special section on azimuthal dependence of p-wave seismic signatures - Introduction. *Geophysics*, 64(4):1139–1142, July-August 1999.

I. Tsvankin and L. Thomsen. Nonhyperbolic reflection moveout in anisotropic media. *Geophysics*, 59(08):1290–1304, 1994.

I. Tsvankin and L. Thomsen. Inversion of reflection traveltimes for transverse isotropy. *Geophysics*, 60(4):1059–1107, 1995.

D. Underwood and D. Tilling. Alba 4C OBC 3D survey - processing report. *performed by Geco-Prakla (UK) Ltd. for Chevron UK Limited*, 1999.

L. Vernik and X. Liu. Velocity anisotropy in shales: A petrophysical study. *Geophysics*, 62(02):521–532, 1997.

L. Vetri, E. Angerer, J. Gaier, A. Grandi, and H. Lynn. Emilio field - Anisotropy analysis from PP and PS data. *64th EAGE conference and exhibition, Florence, Italy*, 2002.

Zhijing Wang. Seismic anisotropy in sedimentary rocks. *Annual meeting of the Society of Exploration Geophysicists*, 2001.

D. F. Winterstein and B. N. P. Paulsson. Velocity anisotropy in shale determined from crosshole seismic and vertical seismic profile data. *Geophysics*, 55(04): 470–479, 1990.

J. Wright. Short note: The effects of transverse isotropy on reflection amplitude versus offset. *Geophysics*, 52(4):564–567, 1987.

Oz Yilmaz. *Seismic Data Analysis*. Society of Exploration Geophysicists, 2001.

J. Yuan. *Analysis of Four-component Seafloor Seismic Data for Seismic Anisotropy*. PhD thesis, University of Edinburgh, Scotland, 2001.

J. Yuan, X.-Y. Li, and A. Ziolkowski. Converted-wave moveout analysis in layered anisotropic media - a case study. *63rd Mtg. Eur. Assn. of Expl. Geophys.*, pages Session: L–27, 2001.

Y. Zhang. Nonhyperbolic converted wave velocity analysis and normal moveout. *66th Intern. Mtg. Soc. Expl. Geophys.*, expanded abstracts:1555–1558, 1996.

Y. Zhang and E.A. Robinson. Stacking P-SV converted wave data with raypath velocity. *62nd SEG annual meeting*, pages 1214–1217, 1992.

Appendix A

Further figures for chapter 3

Further figures for chapter 3 of the amplitude spectra of the stacked data set. Firstly for the whole data set and secondly focused on the reservoir area.

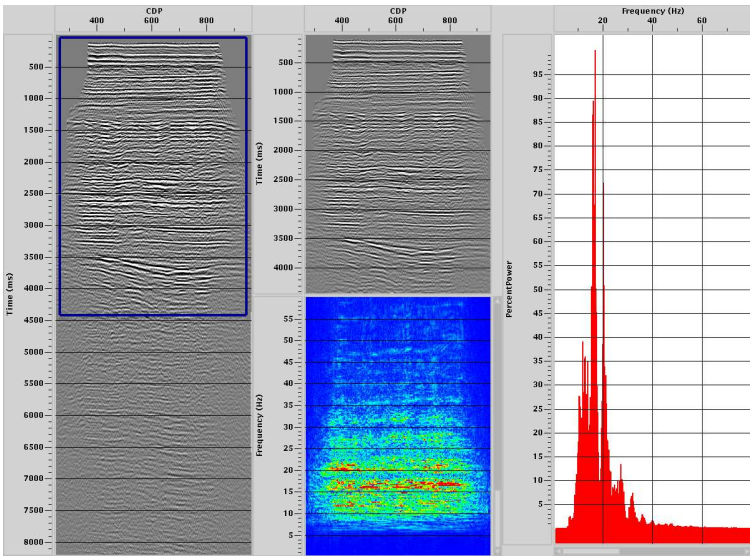

(a) P-wave

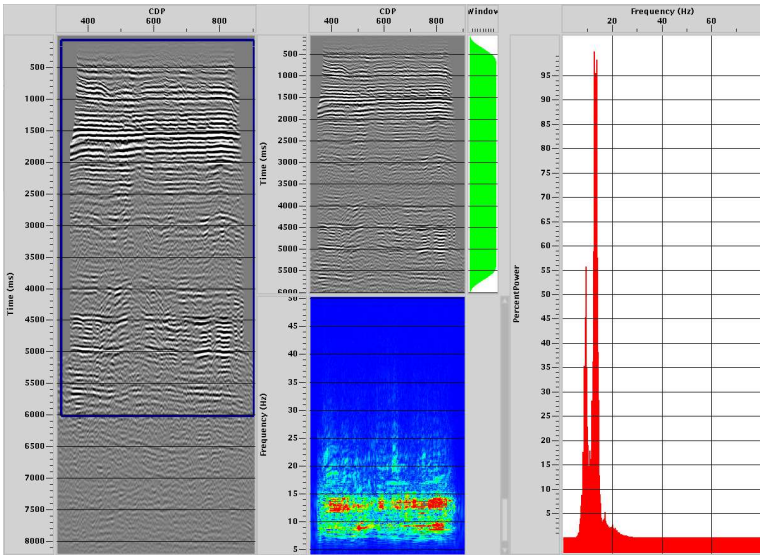

(b) C-wave

Figure A.1: Amplitude spectrum for the whole data set of (a) P-wave and (b) C-wave. On the left is the stack displayed, in the middle on top the zoom of the selected area (here the whole data), on the bottom the F-X power spectrum and on the right the average power spectrum.

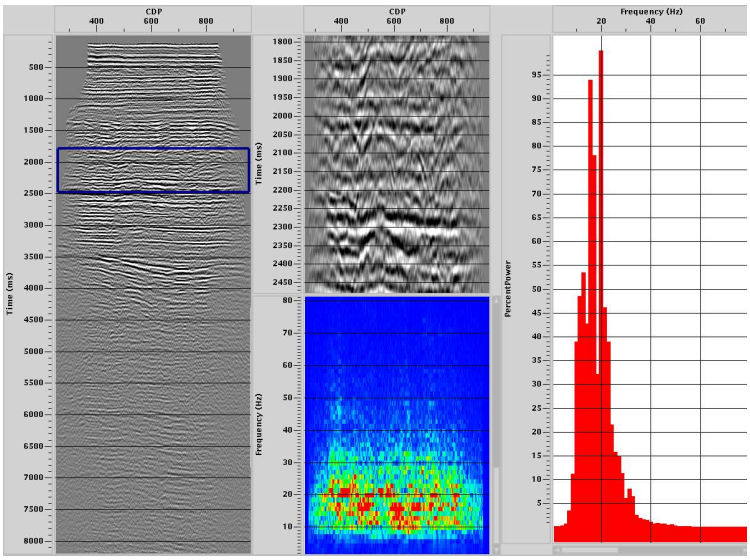

(a) P-wave

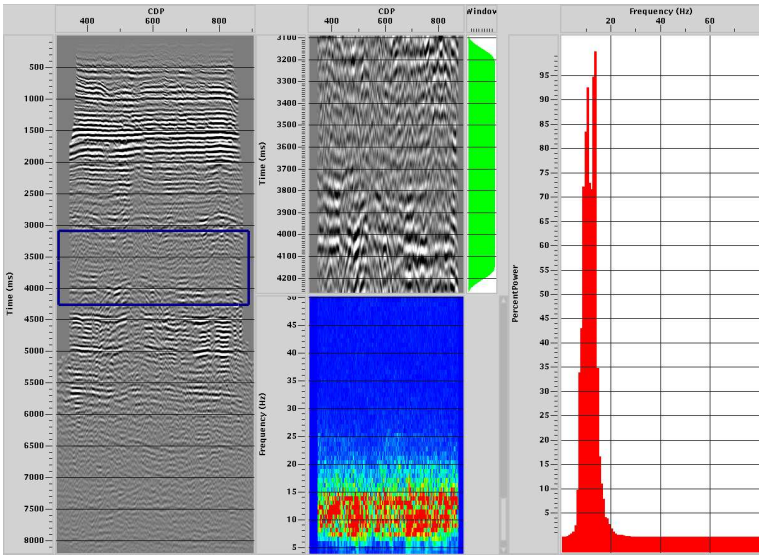

(b) C-wave

Figure A.2: Amplitude spectrum for the target area of (a) P-wave and (b) C-wave. On the left is the stack displayed with a blue rectangle indicating the selected area, in the middle panel on top the zoomed in area of the data, on the bottom the the F-X power spectrum and on the right the average power spectrum.

Appendix B

Further figures and tables for chapter 4

The tables list more model parameters, for example the stacking velocities, and further inversion results, such as the stacking velocites and their picking errors,for the reference model and its six model variations.
The figures show the result of the accuracy analysis for P- and C-wave for the model variations and the inversion results for the model variations are displayed for the C-wave when $x/z = 2.5$.
Further figures display the results for the accuracy analysis and inversion for the low S-wave model.

Model	V_{p2} (km/s)	V_{c2} (km/s)	V_{s2} (km/s)	γ_{eff}	σ
exact	2.622	2.004	1.696	0.957	0.938
V1	2.647	2.016	1.7	0.970	0.662
V2	2.635	2.008	1.694	0.968	0.782
V3	2.609	2.	1.697	0.945	1.133
V4	2.595	1.993	1.694	0.939	1.369
V5	2.595	1.995	1.696	0.936	2.342
V6	2.665	2.021	1.696	0.988	0.549

Table B.1: The stacking velocities V_{p2}, V_{c2} and V_{s2} for the reference model and its variations. The parameters γ_{eff} and σ change according to the model variations too.

Model	V_{p2} (km/s)	V_{c2} (km/s)	V_{s2} (km/s)	$\Delta_p V_{p2}$	$\Delta_p V_{c2}$	$\Delta_p V_{s2}$
exact	2.62	2.005	1.72	0.002	0.001	0.024
V1	2.65	2.01	-	0.003	0.006	-
V2	2.64	2.1	-	0.005	0.092	-
V3	2.61	2.0	-	0.001	0	-
V4	2.6	2.0	-	0.005	0.007	-
V5	2.6	1.99	-	0.005	0.005	-
V6	2.66	2.02	-	0.005	0.001	-

Table B.2: Summary of velocity inversion results and their picking errors (Δ_p =model - picked value) when compared with the model values.

	V_{p2} km/s	V_{c2} km/s	$\Delta_p V_{p2}$	$\Delta_p V_{c2}$
picked values ref.	2.26	1.26	0.005	0.003
picked values V1	2.24	1.25	0.002	0.007

Table B.3: Summary of velocity inversion results and their picking errors (Δ_p =model - picked value) compared with the model values for the low S-wave model.

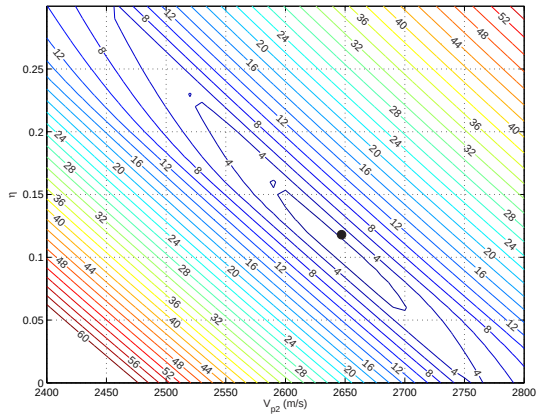

(a) V1, $x/z = 2$

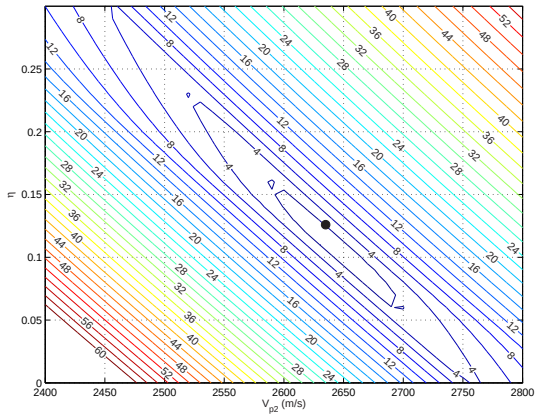

(b) V2, $x/z = 2$

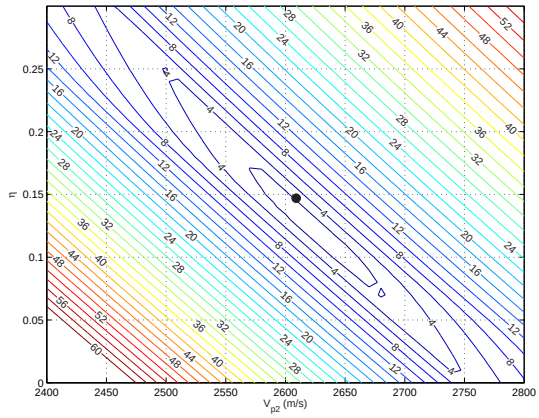

(c) V3, $x/z = 2$

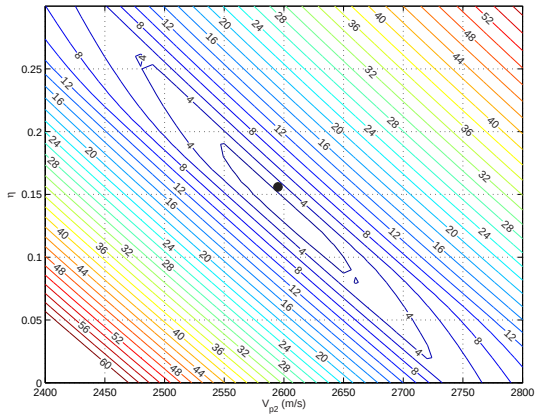

(d) V4, $x/z = 2$

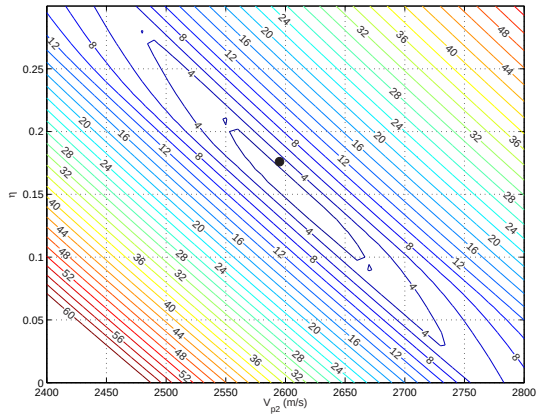

(e) V5, $x/z = 2$

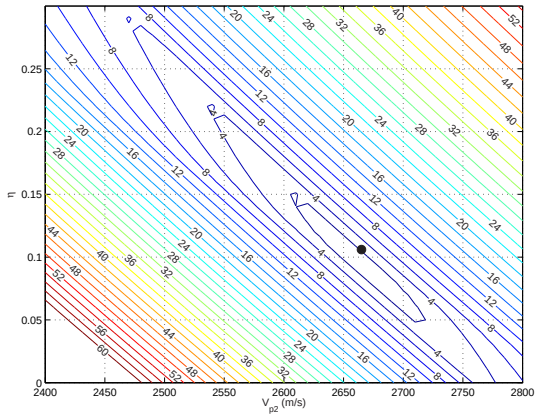

(f) V6, $x/z = 2$

Figure B.1: The influence of η and V_{p2} on the P-wave traveltime moveout from a single horizontal VTI layer. Contours display the maximum traveltime difference in ms between exact and approximated traveltimes Δt_{max} against an offset of 0-2000 metres. The black dot indicates the model values of $\eta - V_{p2}$ from the model variation. Shown are model variations (a) V1, (b) V2, (c) V3, (d) V4, (e) V5 and (f) V6.

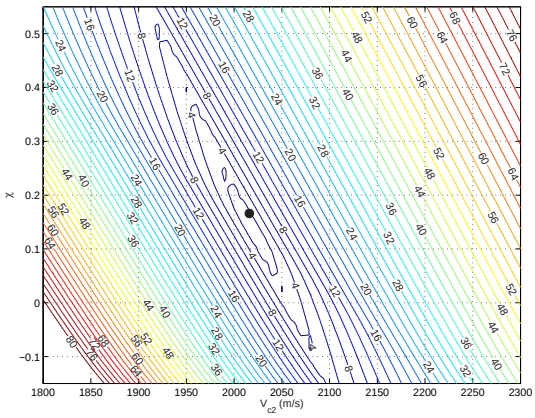

(a) V1, $x/z = 2$

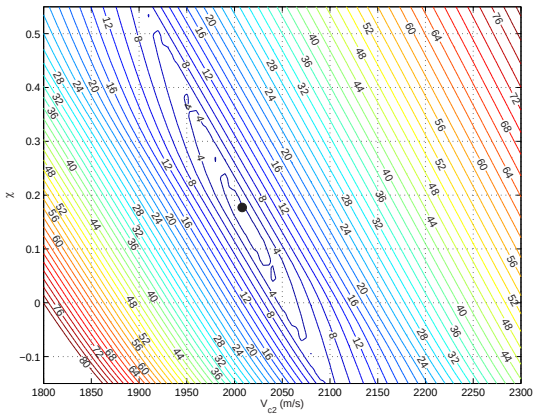

(b) V2, $x/z = 2$

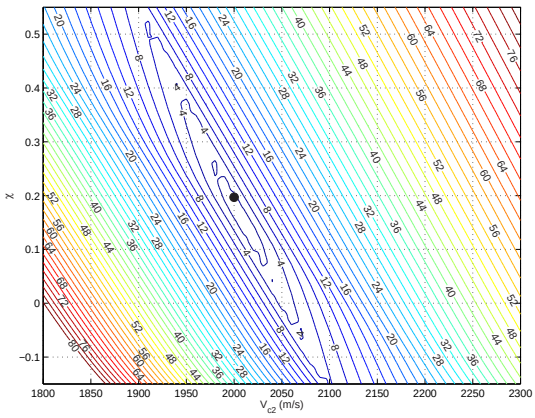

(c) V3, $x/z = 2$

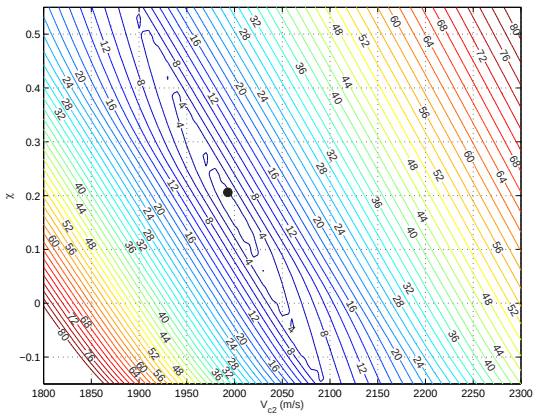

(d) V4, $x/z = 2$

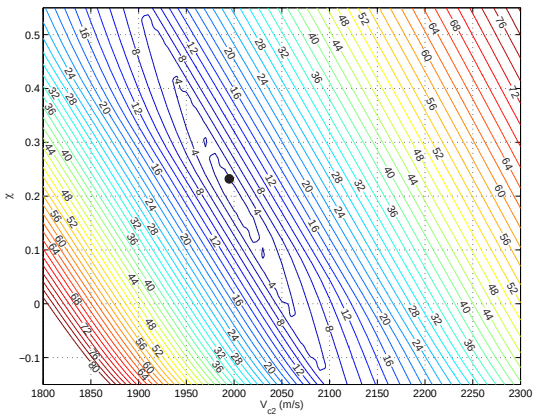

(e) V5, $x/z = 2$

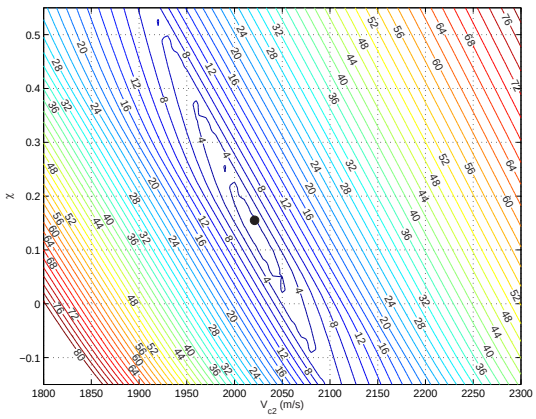

(f) V6, $x/z = 2$

Figure B.2: The influence of χ and V_{c2} on the C-wave traveltime moveout from a single horizontal VTI layer. Contours display the maximum traveltime difference in ms between exact and approximated traveltimes $\Delta t_{\max}$ against an offset of 0-2000 metres. The black dot indicates the model values of $\chi - V_{c2}$ from the model variation. Shown are model variations (a) V1, (b) V2, (c) V3, (d) V4, (e) V5 and (f) V6.

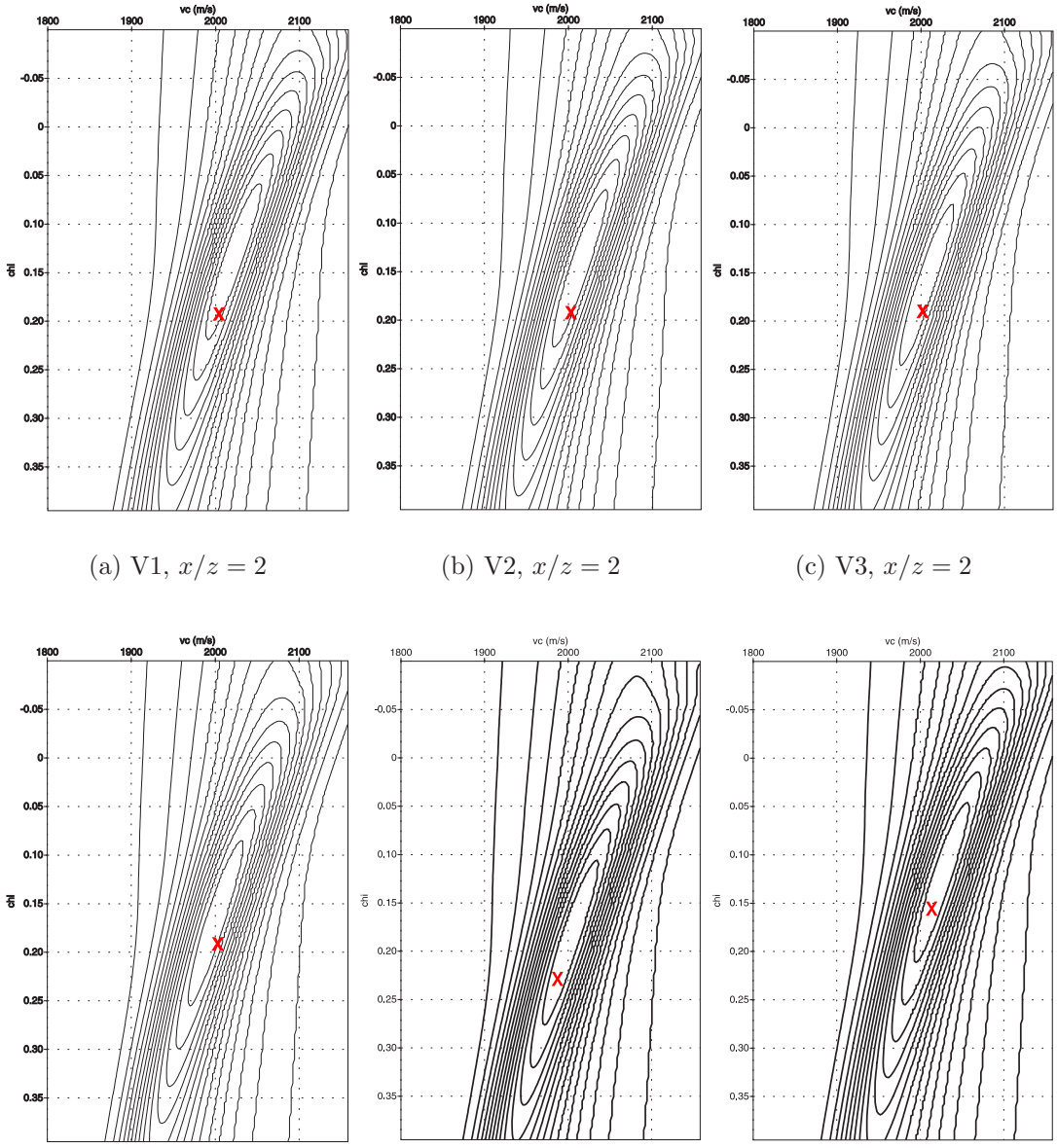

(a) V1, $x/z = 2$ (b) V2, $x/z = 2$ (c) V3, $x/z = 2$

(d) V4, $x/z = 2$ (e) V3, $x/z = 2$ (f) V4, $x/z = 2$

Figure B.3: Inversion results parameters $\chi - V_{c2}$ using a $x/z = 2.5$ for (a) model variation 1, (b) variation 2, (c) variation 3, (d) variation 4, (e) variation 5 and (f) variation 6. The crosses mark the individual model values.

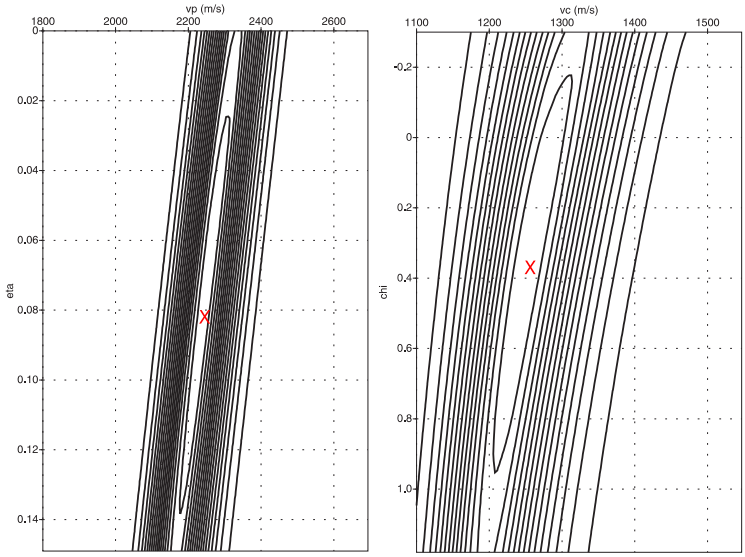

(a) V1, $x/z = 2.5$ (b) V1, $x/z = 2$

Figure B.4: (a) Inversion result for η and V_{p2} from the P-wave of the low S-wave velocity model. (b) Inversion result for χ and V_{c2} from the C-wave. The black dots indicate the model values.

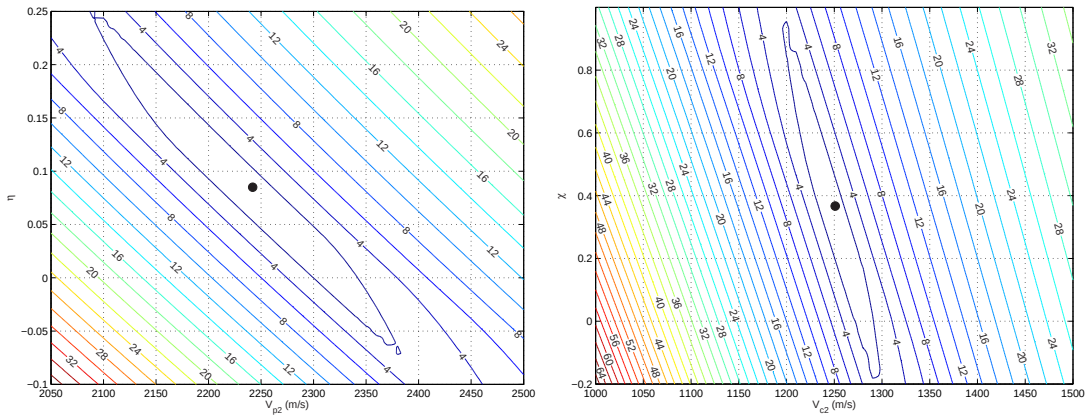

(a) $\Delta_{\text{inh}}\eta$ (b) $\Delta_{\text{inh}}\chi$

Figure B.5: (a) Influence of varying $\eta - V_{p2}$ displayed as Δt_{max} for an offset of 0-750 m for P-waves from the low S-wave velocity model V1. (b) Influence of varying $\chi - V_{c2}$ displayed as Δt_{max} for an offset of 0-600 m for C-waves. The dots indicate the model values.

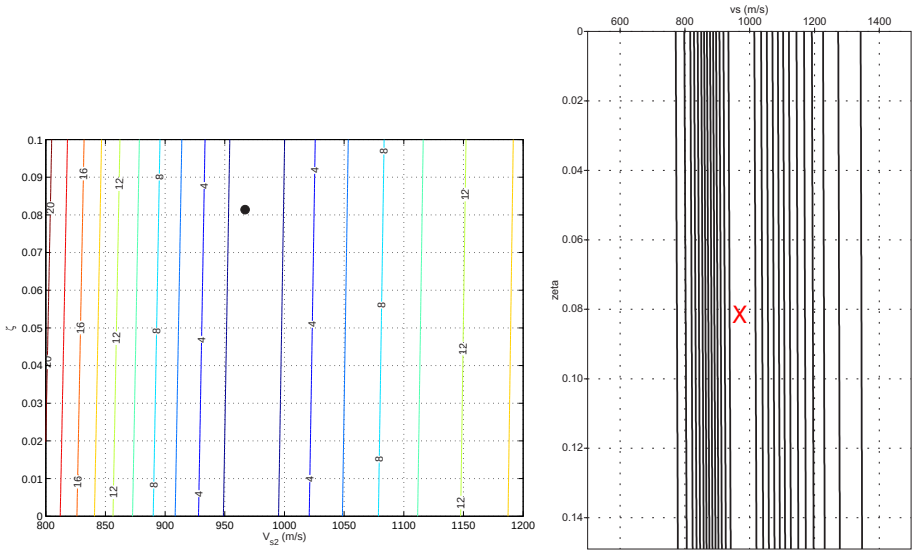

(a) $\Delta_{\text{inh}}\zeta$ (b) $\zeta - V_{s2}$ inversion

Figure B.6: (a) Influence of varying $\zeta - V_{s2}$ displayed as Δt_{max} for an offset of 0-350 metres (due to cusp) for S-waves from the low S-wave velocity model V1. (b) Inversion using double semblance analysis to estimate ζ and V_{s2} from C-wave data. For both analyses a $x/z = 1.1$ were used. The cross indicate the model values.

Appendix C

Further figures for chapter 5

Additional figures for chapter 5 display the effective reflection coefficients over angle of incidence for P- and C-wave for the different models.

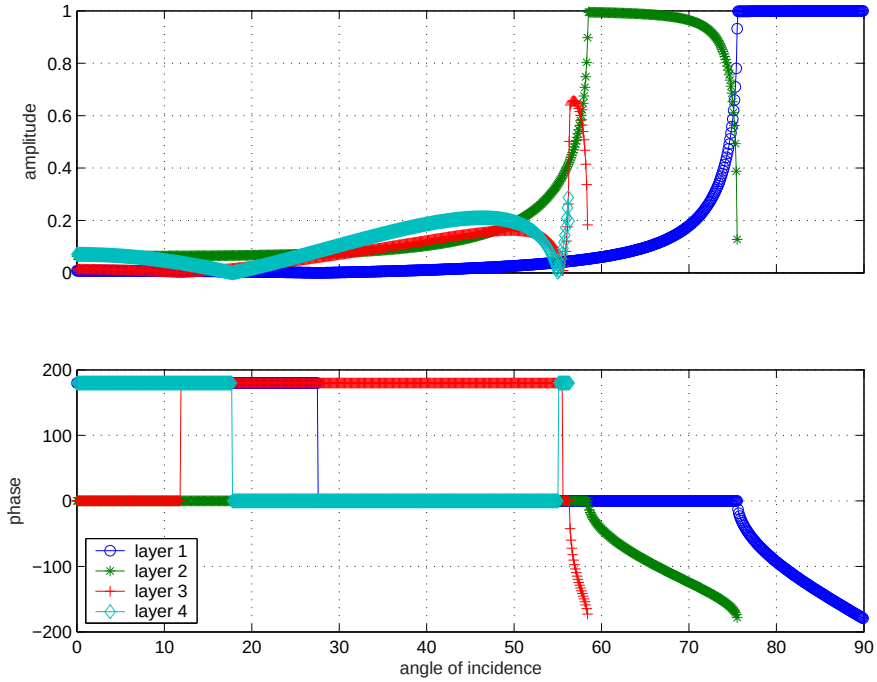

(a) PP

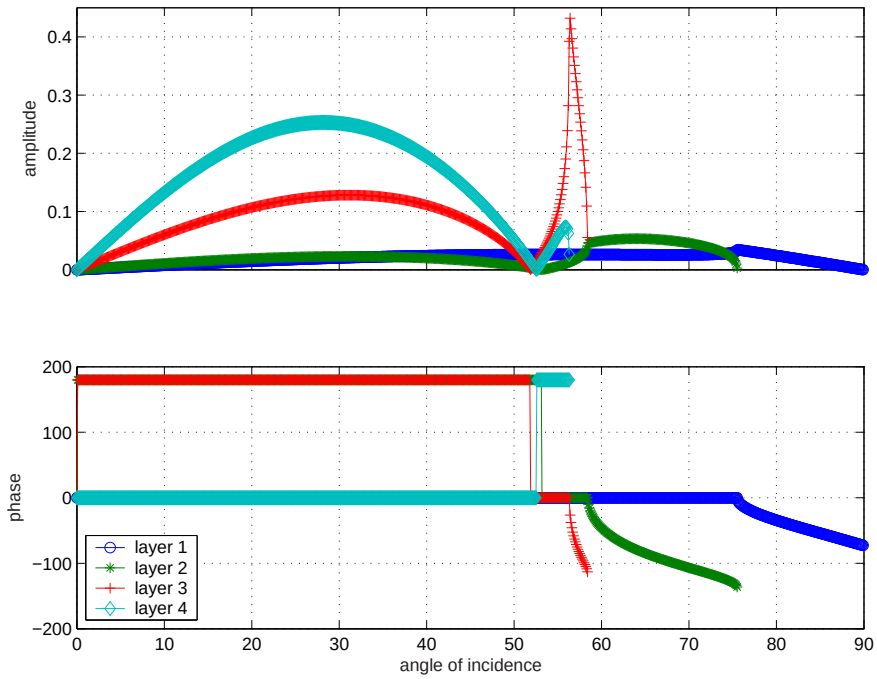

(b) PS

Figure C.1: Effective reflection coefficients for the isotropic model 1 are calculated for PP reflection (top) or PS conversion (bottom) on the bottom of the model layers and displayed over incidence angle. In each diagram, top: Effective reflection coefficient over incidence angle. Bottom: Corresponding phase behaviour.

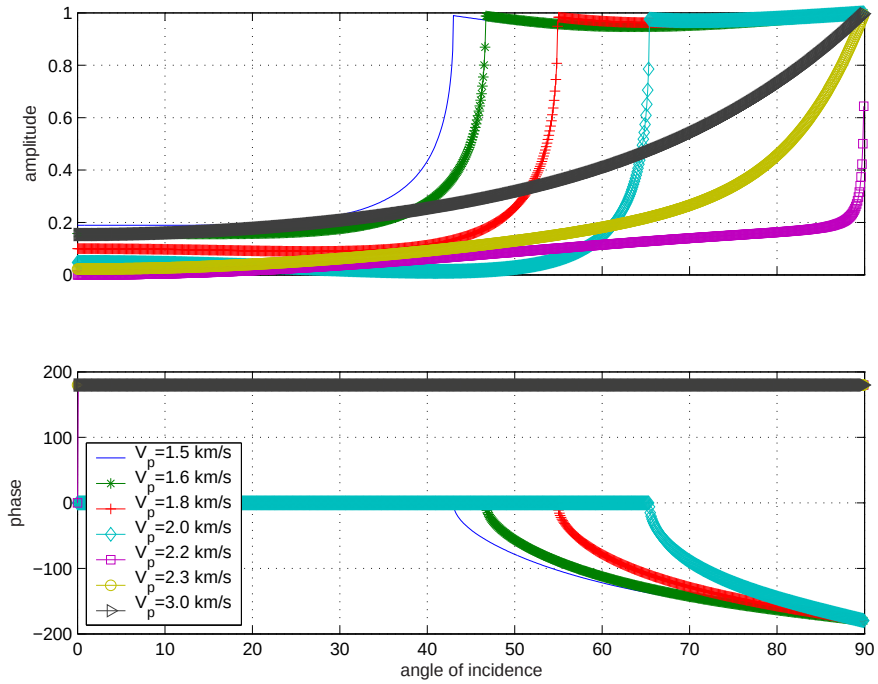

(a) PP

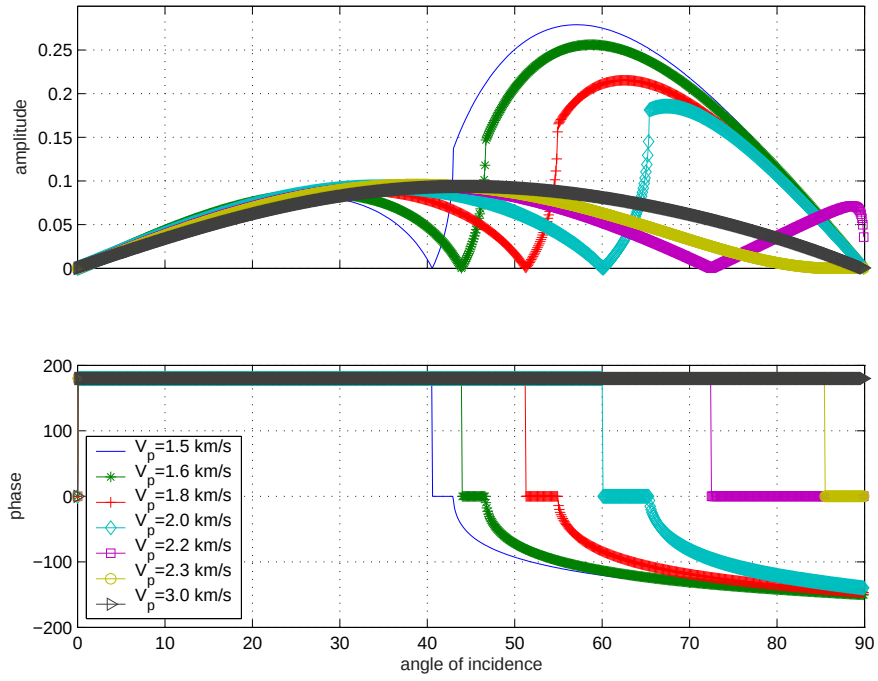

(b) PS

Figure C.2: Coefficients are calculated for a PP reflection at the bottom of the model layer. Top: Effective reflection coefficient for $V_s = 0.65$ km/s and varying P-wave velocity over angle of incidence. Bottom: Corresponding phase behaviour.

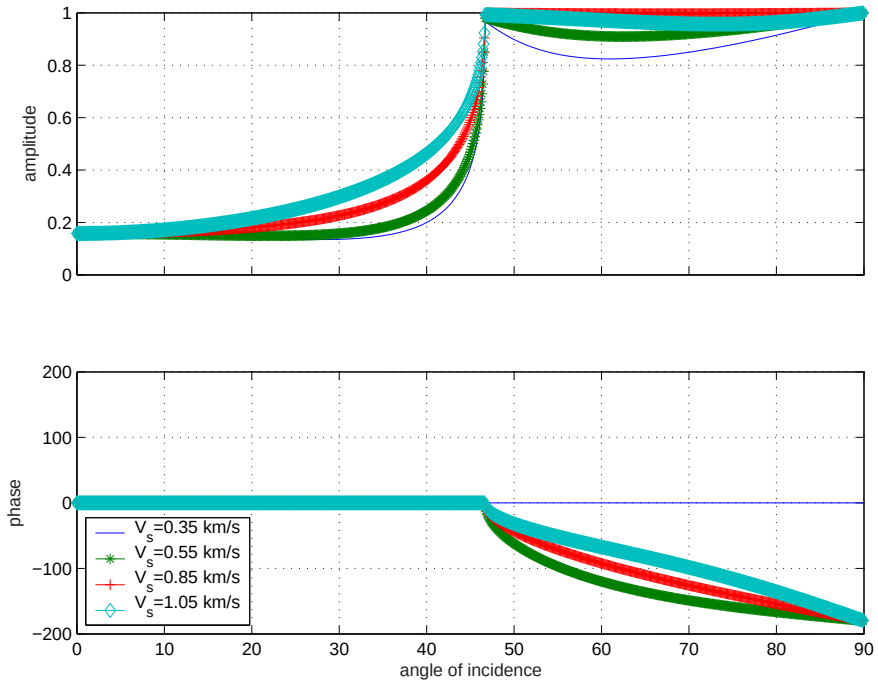

(a) PP

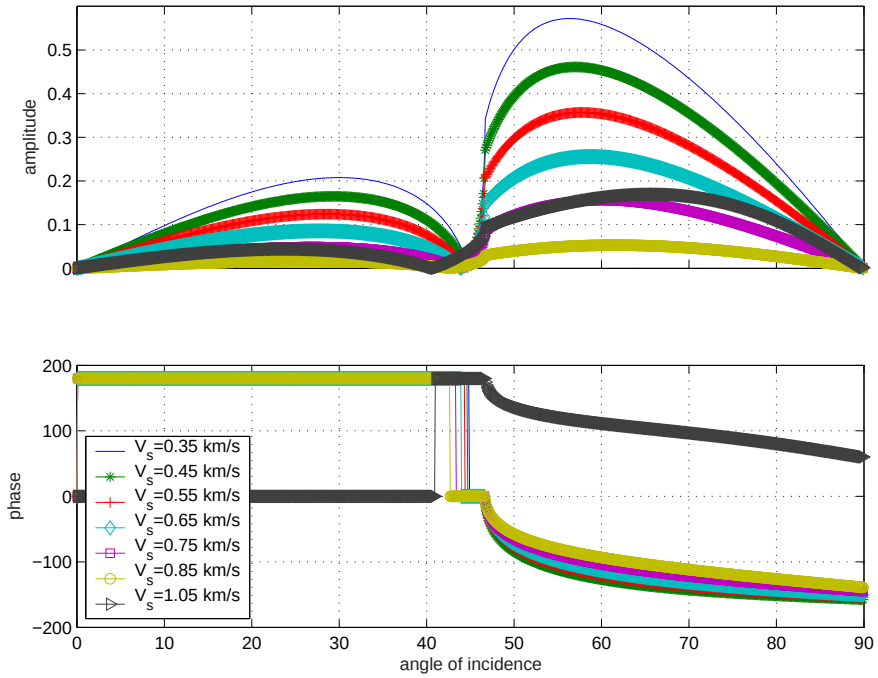

(b) PS

Figure C.3: Coefficients are calculated for PP reflection on the bottom of the model layer. Top: Effective reflection coefficient for varying S-wave velocity and constant $V_p = 1.6$ km/s over angle of incidence. Bottom: Corresponding phase behaviour.

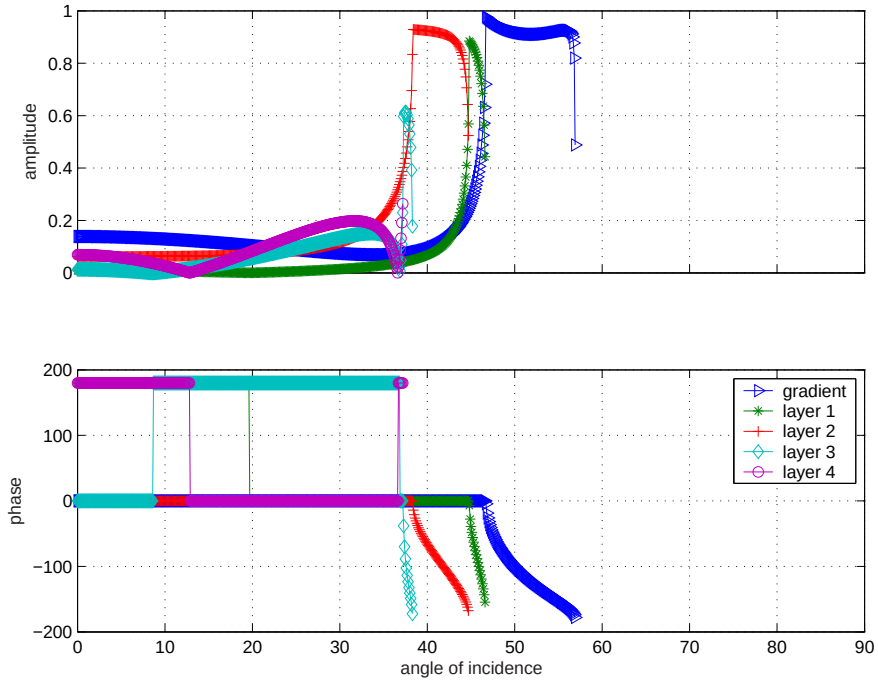

(a) PP

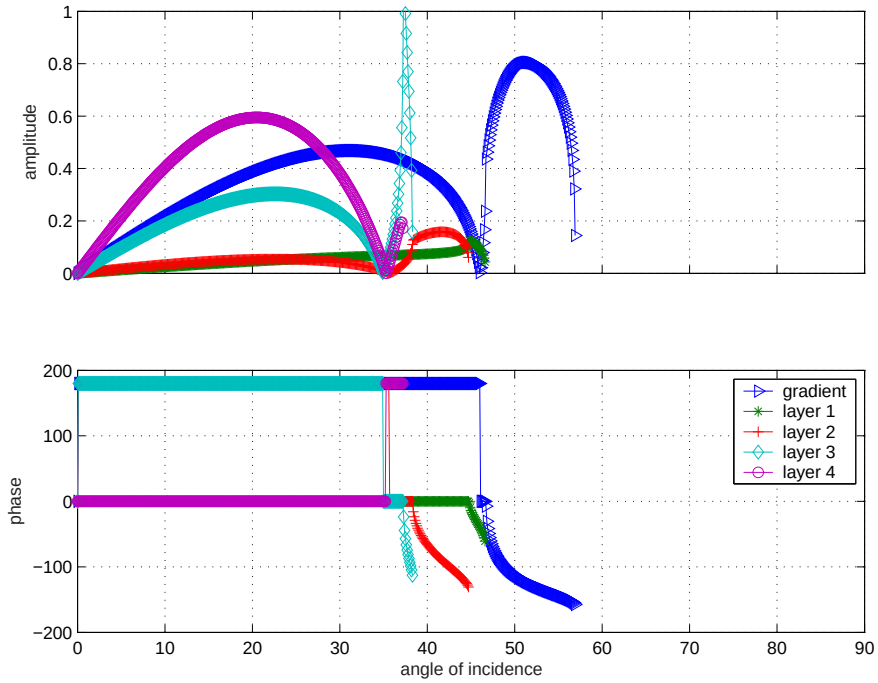

(b) PS

Figure C.4: The top 2 diagrams show coefficients calculated for PP reflection the bottom 2 diagrams for PS conversion. Coefficients are calculated for PP reflection on the bottom of each model layer underneath the gradient. Top: Effective reflection coefficient over offset. Bottom: Corresponding phase behaviour.

Appendix D

Further figures for chapter 6

The first figures display the NMO correction for further CDP and CCP gathers of the Alba data. Further, the instantaneous phase function for these gathers are displayed. Finally, the effective reflection coefficients over incidence angle for the Alba near-surface model are shown.

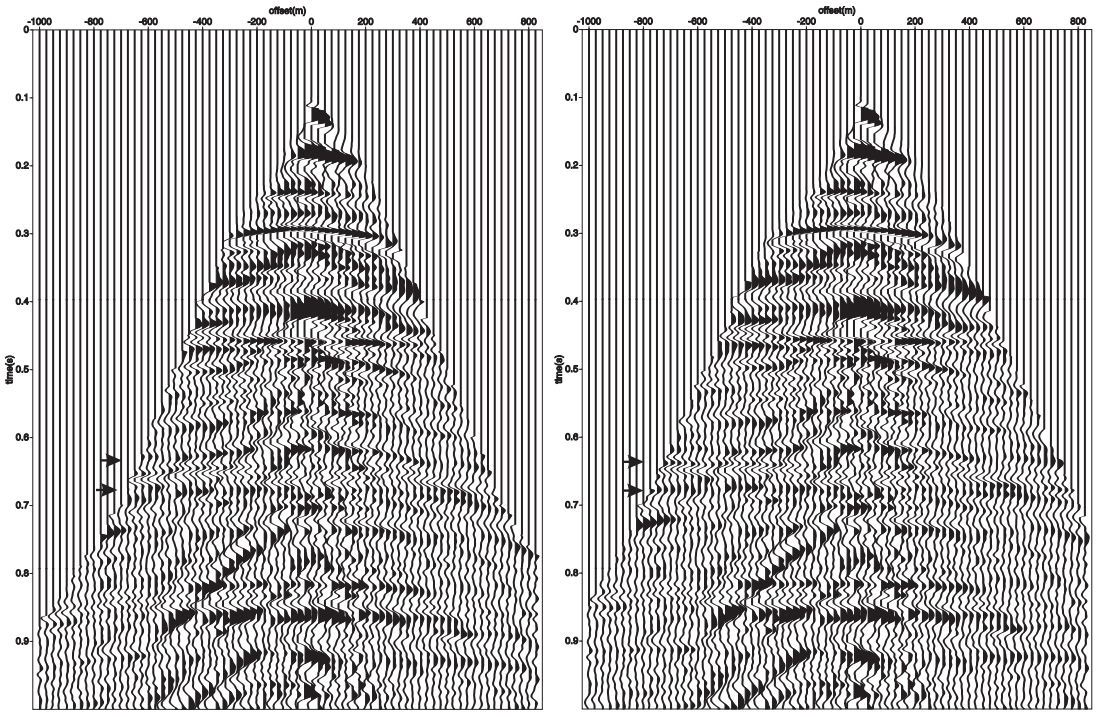

Figure D.1: (a) Anisotropic NMO using picked values (see Table 6.1) for CDP supergather 400. (b) Anisotropic NMO using η calculated from picked χ-values (see Table 6.3). The arrows indicate the events used for the parameter estimation.

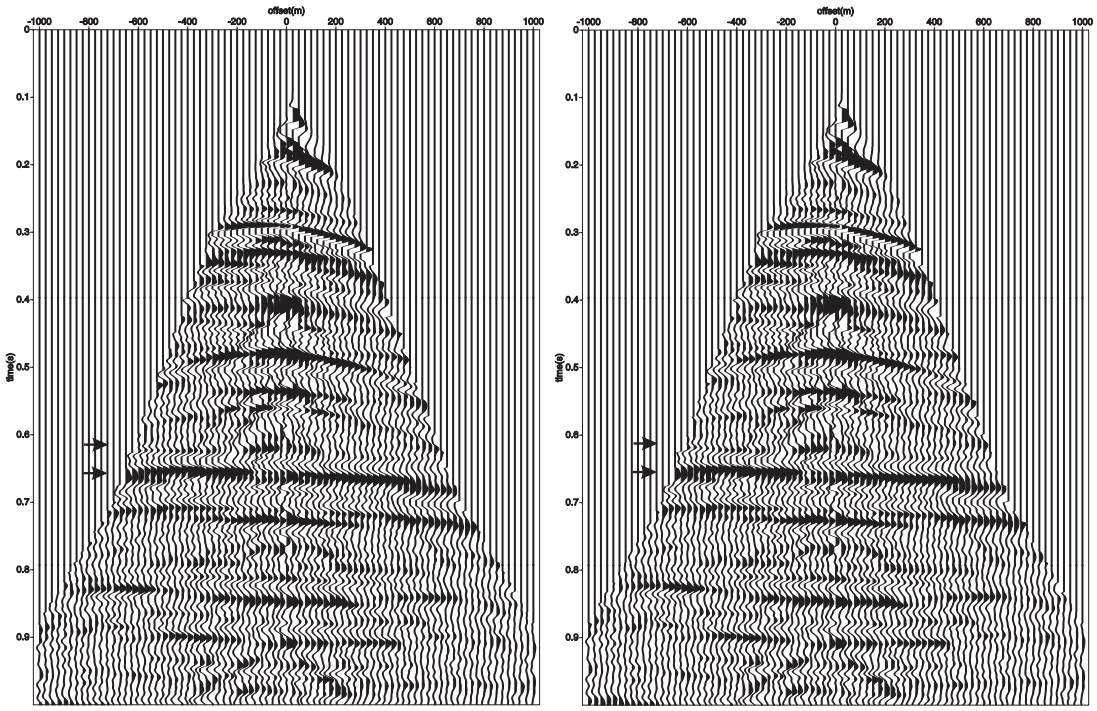

Figure D.2: (a) Anisotropic NMO using picked values (see Table 6.1) for CDP supergather 600. (b) Anisotropic NMO using η calculated from picked χ-values (see Table 6.3). The arrows indicate the events used for the parameter estimation.

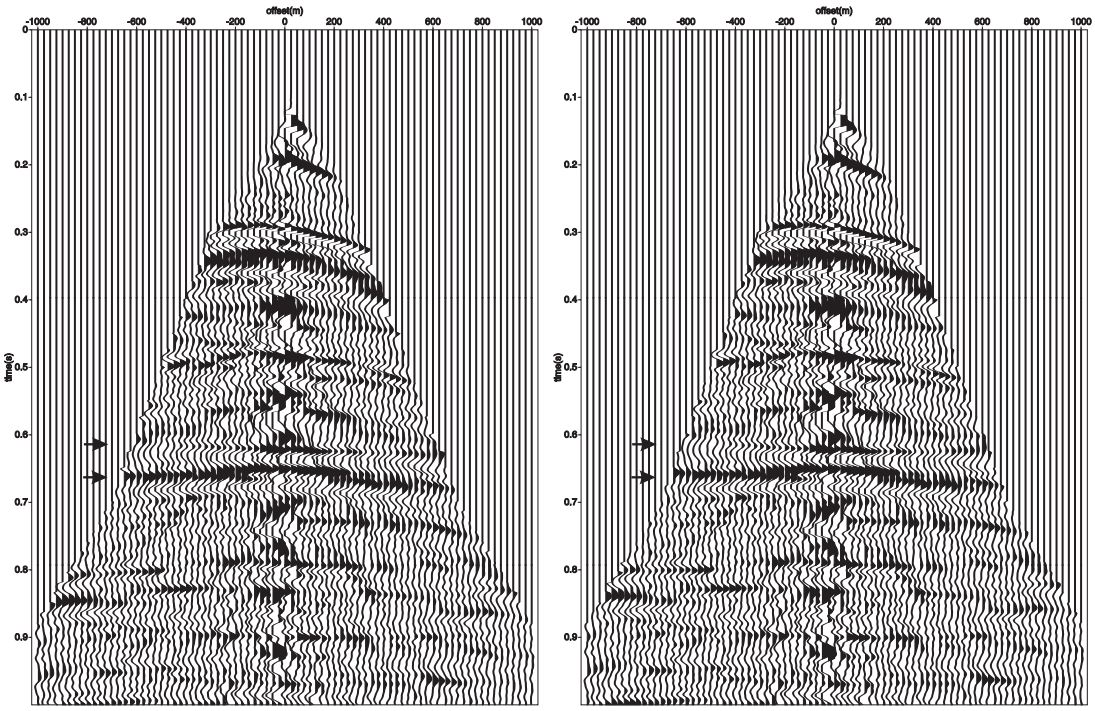

Figure D.3: a) Anisotropic NMO using picked values (see Table 6.1) for CDP supergather 700. b) Anisotropic NMO using η calculated from picked χ-values (see Table 6.3). The arrows indicate the events used for the parameter estimation.

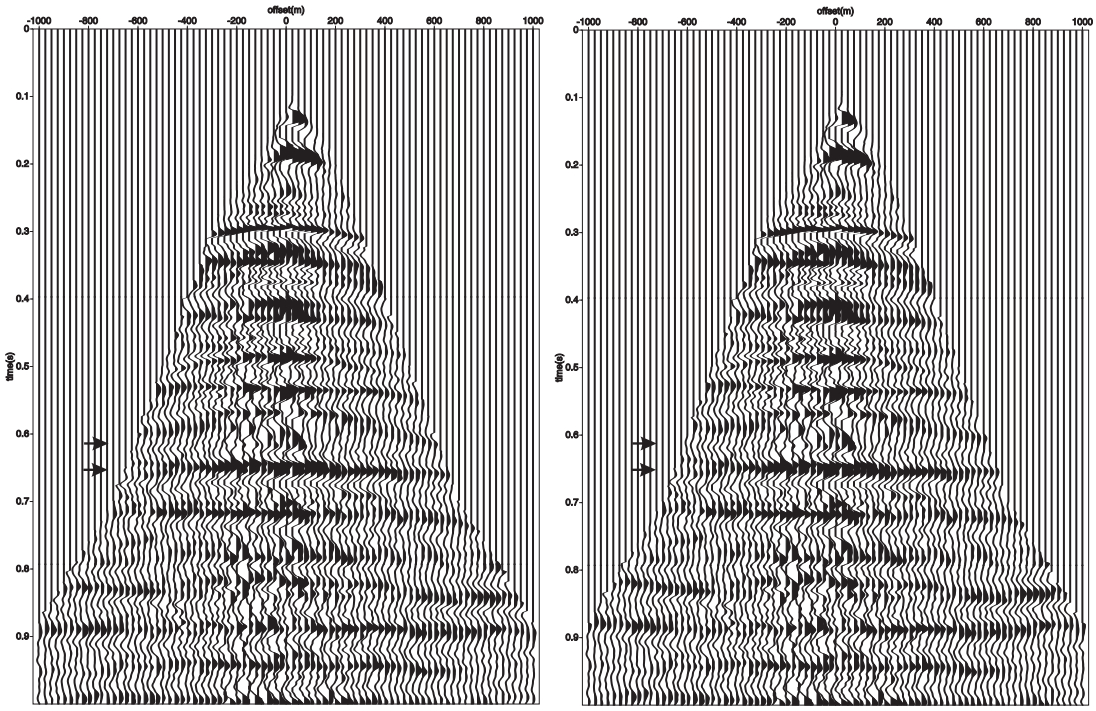

Figure D.4: (a) Anisotropic NMO using picked values (see Table 6.1) for CDP supergather 800. (b) Anisotropic NMO using η calculated from picked χ-values (see Table 6.3) for the same gather. The arrows indicate the events used for the parameter estimation.

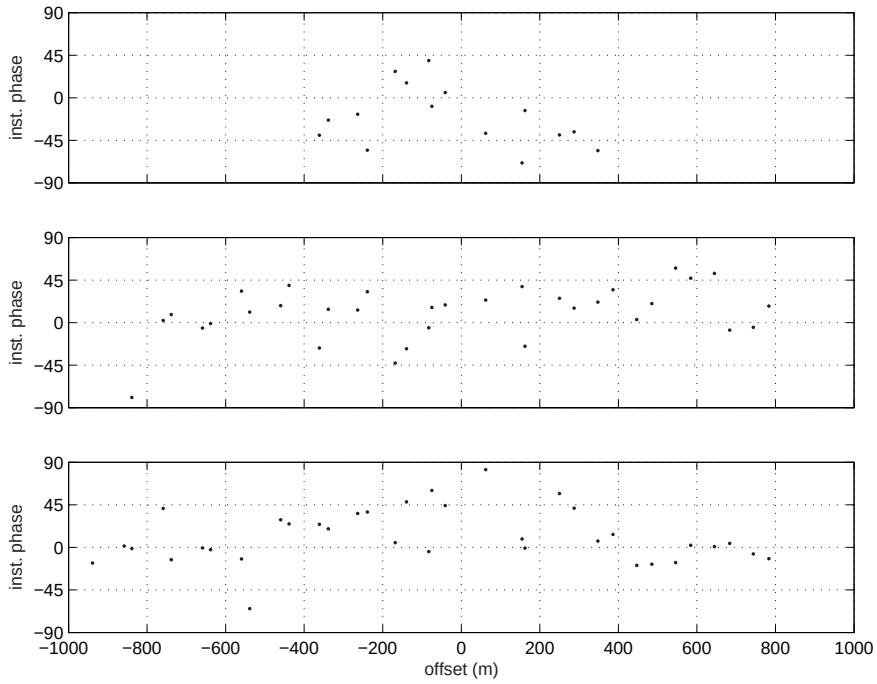

Figure D.5: Instantaneous phase function for 3 near surface events of CDP gather 400 of the vertical component of the Alba data.

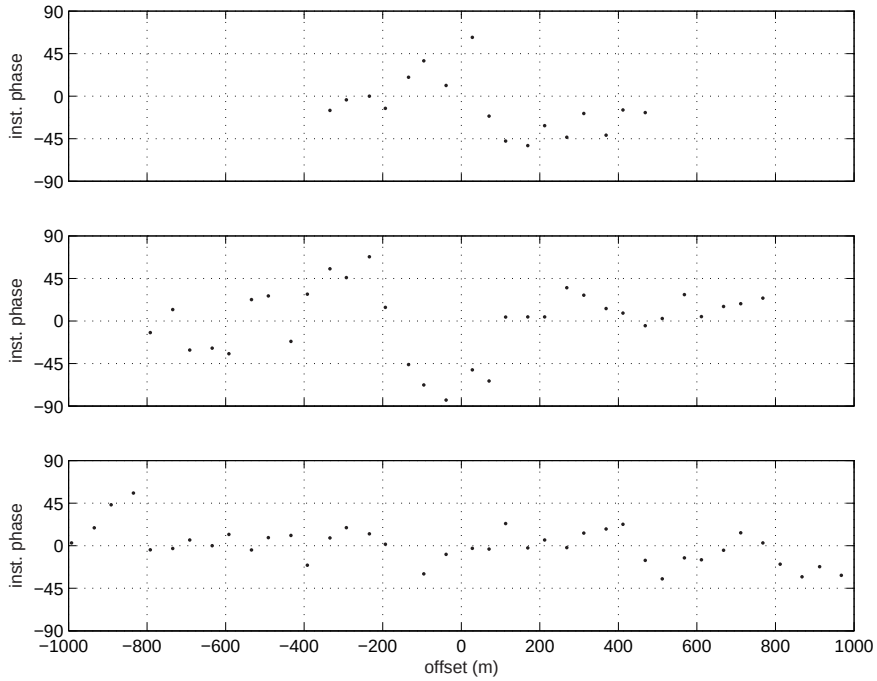

Figure D.6: Instantaneous phase function for 3 near surface events of CDP gather 600 of the vertical component of the Alba data.

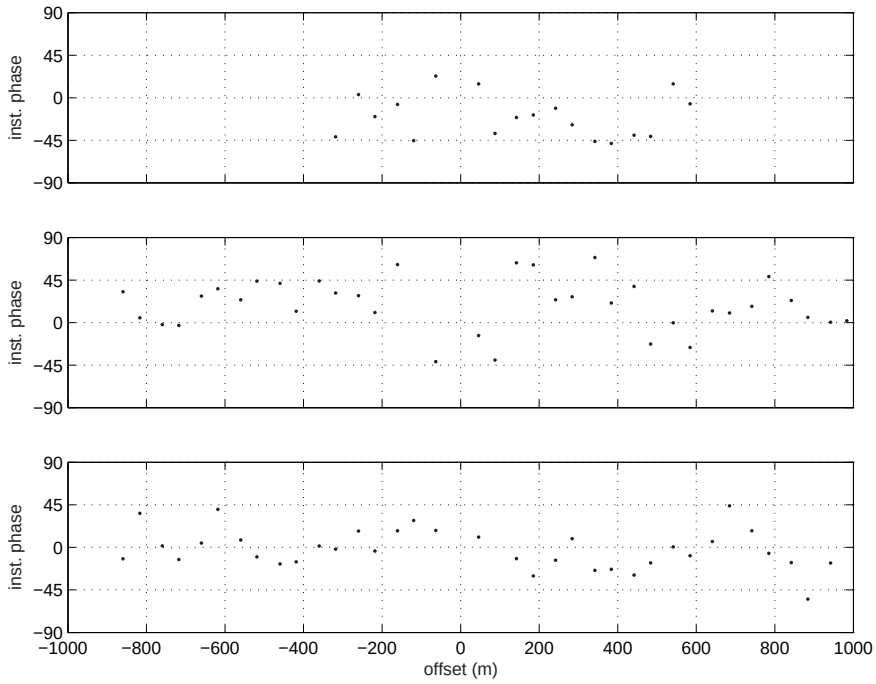

Figure D.7: Instantaneous phase function for 3 near surface events of CDP gather 700 of the vertical component of the Alba data.

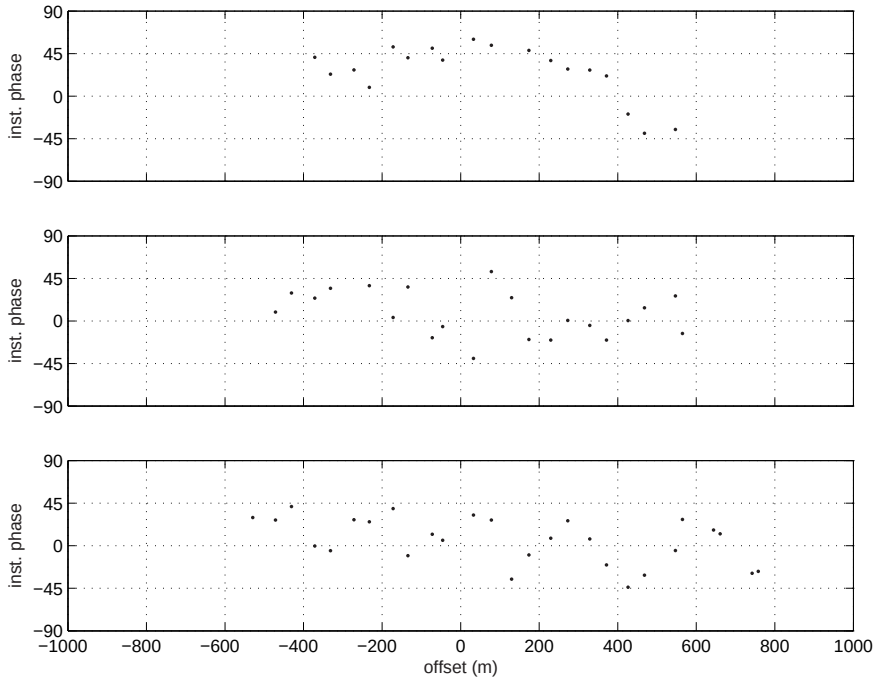

Figure D.8: Instantaneous phase function for 3 near surface events of CDP gather 800 of the vertical component of the Alba data.

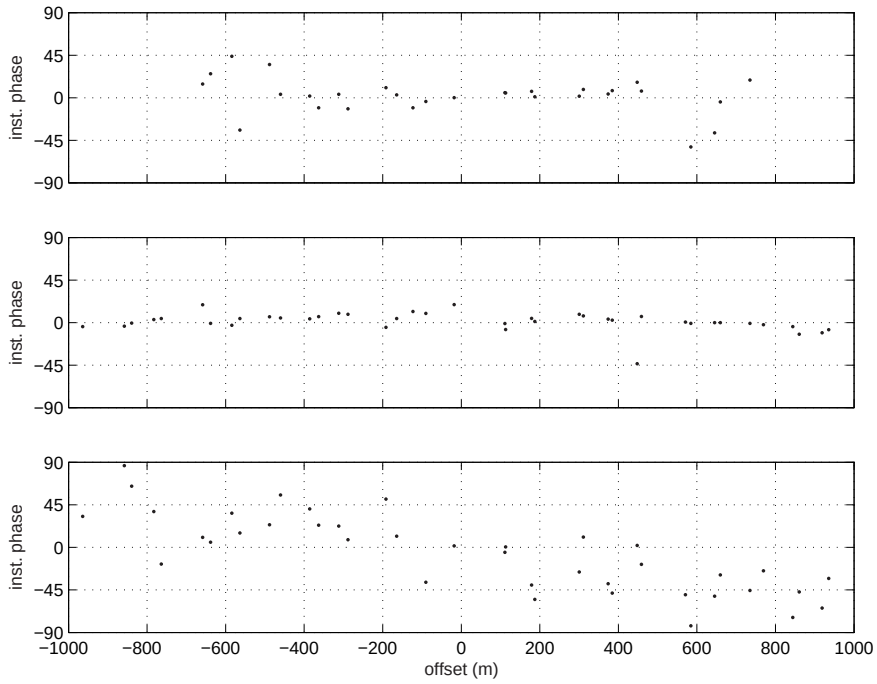

Figure D.9: Instantaneous phase function for 3 near surface events of CCP gather 400 of the vertical component of the Alba data.

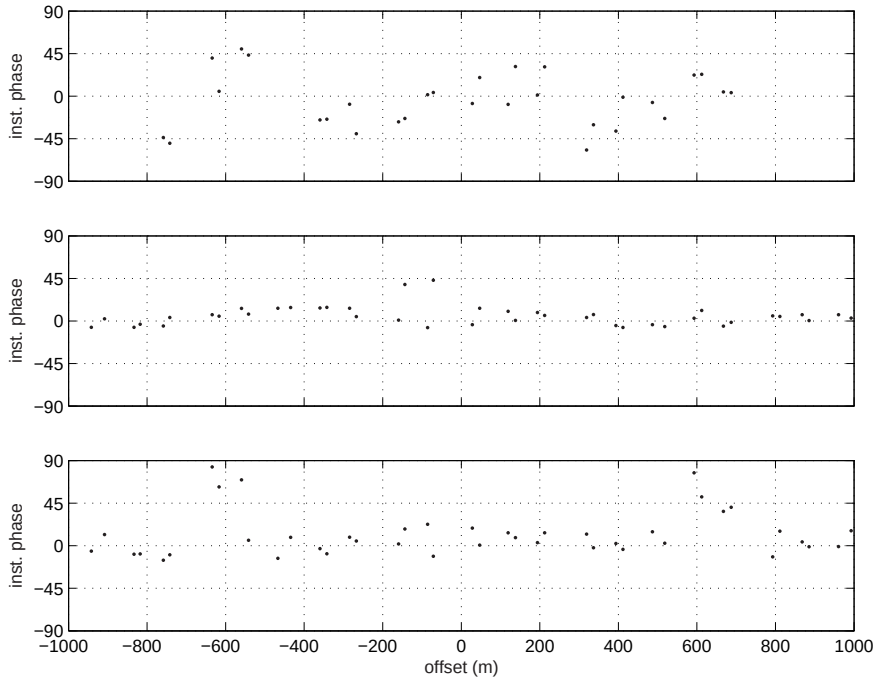

Figure D.10: Instantaneous phase function for 3 near surface events of CCP gather 600 of the vertical component of the Alba data.

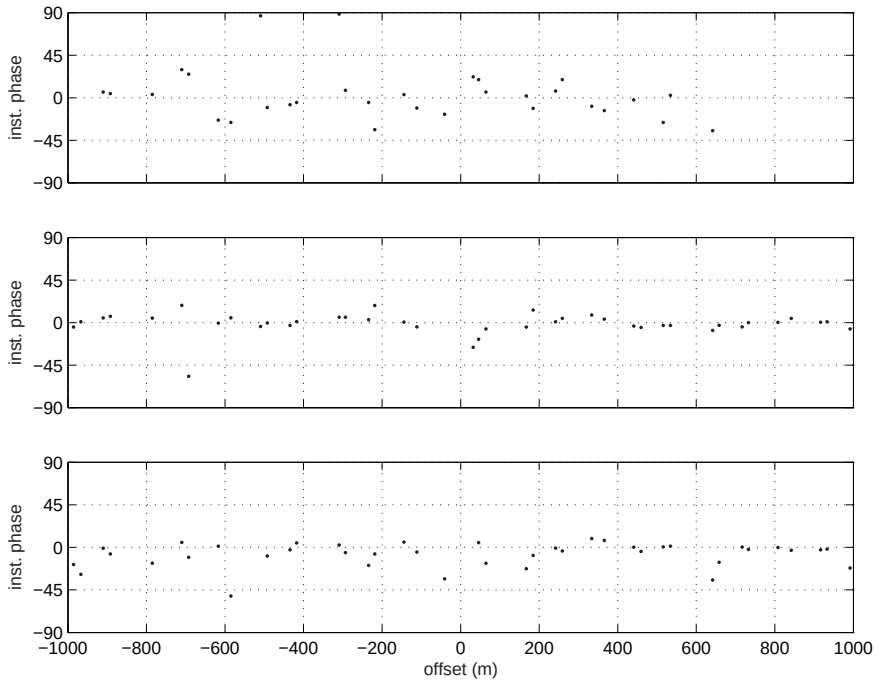

Figure D.11: Instantaneous phase function for 3 near surface events of CCP gather 700 of the vertical component of the Alba data.

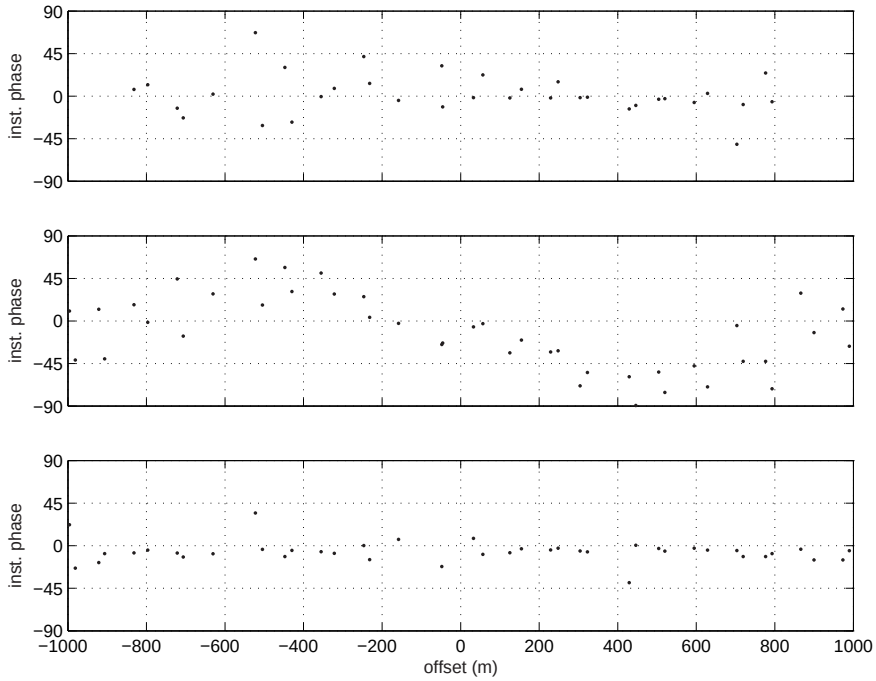

Figure D.12: Instantaneous phase function for 3 near surface events of CCP gather 800 of the vertical component of the Alba data.

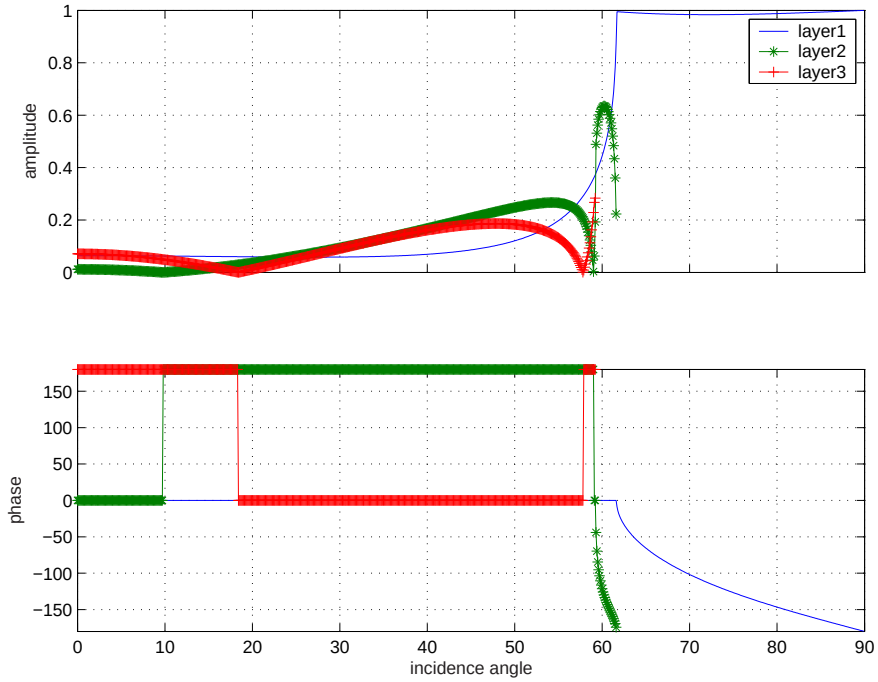

Figure D.13: Top: Effective reflection coefficient for the 3 interfaces in the Alba near-surface model for PP reflections over all possible incidence angles. Bottom: Corresponding phase behaviour.

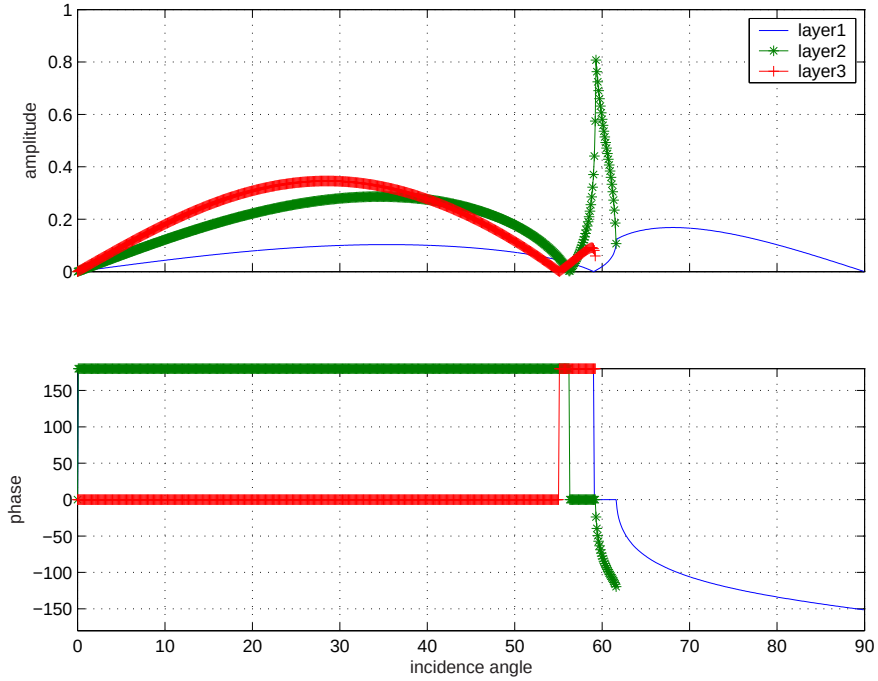

Figure D.14: Effective reflection coefficient for the 3 interfaces in the Alba near-surface model for P-S reflections over all possible incidence angles. Bottom: Corresponding phase behaviour.

Appendix E

List of Publications

Traub, B. and Li, X.-Y.: Sensitivity of anisotropic parameter estimation from 4C data: Modelling and a case study, *EAGE 64th Conference and Exhibition*, Florence, Italy, pages F018, 2002.

Traub, B. and Li, X.-Y.: Characterisation of near surface anisotropy using P- and converted wave data, *73th Ann. Intern. Mtg.: Soc. of Expl. Geophys.*, Dallas, USA, pages 797-800, 2003.

Traub, B. and Li, X.-Y.: Sensitivity of anisotropy parameter estimation from 4C data: Modelling and case studies, *EAGE 66th Conference and Exhibition*, Paris, France, pages E010, 2004.

Traub, B. and Li, X.-Y.: The effects of near-surface conditions on anisotropy parameter estimations from 4C seismic data, submitted to *Geophysical Prospecting*, 2004.